Fall 2017

Investigation of floodwave propagation over natural bathymetry using a three-dimensional numerical model

Daniel Vicente Horna Munoz
University of Iowa

INVESTIGATION OF FLOODWAVE PROPAGATION OVER NATURAL BATHYMETRY USING A THREE-DIMENSIONAL NUMERICAL MODEL

by

Daniel Vicente Horna Munoz

A thesis submitted in partial fulfillment
of the requirements for the Doctor of Philosophy
degree in Civil and Environmental Engineering in the
Graduate College of
The University of Iowa

December 2017

Thesis Supervisor: Professor George S. Constantinescu

Graduate College
The University of Iowa
Iowa City, Iowa

CERTIFICATE OF APPROVAL

_____

PH.D. THESIS

_____

This is to certify that the Ph.D. thesis of

Daniel Vicente Horna Munoz

has been approved by the Examining Committee for
the thesis requirement for the Doctor of Philosophy degree
in Civil and Environmental Engineering at the December 2017 graduation.

Thesis Committee: _____
George S. Constantinescu, Thesis Supervisor

_____
William E. Eichinger

_____
Witold F. Krajewski

_____
A. Jacob Odgaard

_____
Albert Ratner

To my family

The dream begins with a teacher who believes in you, who tugs and pushes and leads you to the next plateau, sometimes poking you with a sharp stick called “truth.”

Dan Rather

ACKNOWLEDGEMENTS

First and foremost, I offer my sincerest gratitude to my main supervisor, Prof. George Constantinescu, for believing in me and guiding me throughout these past years. I am grateful for your dedication and patience to meet with me whenever necessary. I learnt every time we met and you inspired me to keep learning on my own.

I am also greatly in debt to Prof. Witold Krajewski, not only for funding my thesis research but also for allowing me to be part of the Iowa Flood Center. Being part of the Iowa Flood Center allowed me to learn from some of the best people in the world who study floods. In every meeting I paid particular attention to your insights, comments, and perspective on what the future of flood modeling is. I simply cannot put in words how much I learn from being part of the Iowa Flood Center. I just wish I could have learnt soccer from you too.

I also would like to extent my gratitude to Professors Jacob Odgaard, William Eichinger and Albert Ratner for serving on my dissertation committee and for all your comments and ideas about how to improve my thesis work. I would like to thanks Prof. Jacob Odgaard, in particular, for being available and patiently meeting with me to guide me through parts of my research where the path was not clear.

During the duration of my Ph.D. studies I have met many great people at the University of Iowa, especially in IIHR-Hydroscience and Engineering. I have enjoyed every minute I have spent in this institute and I will not trade it for anything in the world. The success of my dissertation is also not without the help of Dr. Nate Young and Dan Gilles, for providing crucial information needed to run flood inundation models. I would also like to thank all the many friends that helped through this journey; friends from Peru, from the

University of Kansas, from Stanford University and from the University of Iowa. You all became more than friends; you all became family to me.

Last but not least I would like to thank my family. Papa, Mama, Diego, Tias, Tios, Abuelitas, Abuelitos, Primos y Primas. You all taught me that there is nothing like family's love, regardless of the distance. I wish my primo Carlos Andres, my abuelitos Juan y Mario y abuelitas Magda y Charo were still here with me. I just hope this thesis work makes you proud. Los llevo siempre en el corazon.

ABSTRACT

The current standard of simulating flood flow in natural river reaches is based on solving the 1-D or 2-D St. Venant equations or using hybrid 1-D/2-D models based on the same equations. These models are not always able to accurately predict floodwave propagation, especially around and downstream of regions where 3-D effects become important, or at times when the main assumptions associated with these models are violated (e.g. flow becomes pressurized due to presence of a hydraulic structure like a bridge or a culvert). A 3-D modeling approach, though computationally much more expensive, is not subject to such limitations and should be able to predict accurately predict floodwave propagation even in regions where 3-D effects are expected to be significant. This dissertation describes the development and validation of a 3-D time-accurate RANS-based model to study flood-related problems in natural environments. It also discusses how results from these 3-D simulations can be used to better calibrate lower order models. Applications are included where the flow becomes pressurized during high flow conditions and the sediment entrainment potential of the flow during the flooding event is estimated. Another important category of applications discussed in the present study are floodwave propagation induced by a sudden dam break failure. Results show that 2-D models show fairly large differences with 3-D model predictions especially in regions where 3-D effects are expected to be significant (e.g. near channel-floodplain transition, in highly curved channels, near hydraulic structures). The study also discusses the use of the validated 3-D model as an engineering design tool to identify the optimum solution for flood protection measures intended to reduce flooding in the Iowa River near Iowa City. 3-D simulation results are also used to discuss hysteresis effects in the relationship between bed shear stress

and the stage/discharge. Such effects need to be taken into consideration to accurately estimate erosion associated with the passage of a floodwave.

PUBLIC ABSTRACT

Historically engineers have been challenged with designing structures that should sustain possible undesired events such as floods or earthquakes. Due to climate change, large floods are expected to occur more frequently, affecting existing infrastructure and people as they pass through populated areas or regions containing critical infrastructure (e.g. nuclear power plants). For instance, eastern Iowa was highly affected by the Flood of 2008, which created losses in the order of billions of dollars. At flooding conditions, it is of crucial importance to know how the water will move. In other words, how high the water will be, which areas will become inundated and how fast the water will move. The current way of getting this information is based on using computer models that are based on solving a simplified set of equations. While they are able to provide a general representation of the floodwave propagation for many cases, they sometimes fail to replicate some important information (e.g. how fast a floodwave induced by a dam break event propagates, what is the erosion potential associated with the floodwave). A classic example is when the flow becomes pressurized over some regions. This thesis proposes a new way to compute floodwave propagation based on solving a fully 3-D Navier Stokes equations together with the free-surface position. It exemplified the use of the model to predict pressure scour effects associated with bridge deck submergence at high flow conditions during a flooding event and floodwave propagation induced by catastrophic dam failure. Using data from these computationally more expensive but more accurate simulations, one can test new modeling ideas in simpler 2-D or 1-D models or recalibrate these models to improve their accuracy.

TABLE OF CONTENTS

LIST OF TABLES

LIST OF FIGURES

CHAPTER 1 INTRODUCTION

1.1 Background

Flooding can have great repercussions on urban environments and can damage almost all structures placed in the floodplain. Knowledge of the flood extent and flood wave propagation velocity is of great importance for hydrologists and urban planners.

Cities affected by flooding have shown increasing concern about the impact of flooding on their infrastructure, which in turn mobilized efforts on improving flood-protection strategies as well as research initiatives to investigate flooding phenomena. Since flooding is both a hydraulic and a hydrologic phenomenon, the research goals were highly varied, ranging from scaling theory of peak flows or statistical analyses of floods to computational fluid dynamics models to simulate more accurately flood extents and durations.

Predicting flood extent and flood propagation information is usually obtained from numerical simulations. Several types of models can be used to simulate flooding. Flooding in riverine or coastal environments is a very complex hydrodynamic phenomenon, in particular because of the flow interaction between channel-floodplain and river/coastal (estuary) dynamics. The presence of hydraulic structures (e.g., dams, weirs) that can modify the flow regime over a certain region and of large obstacles (e.g., buildings) generally results in increase flow complexity (e.g., strong secondary currents in horizontal plane, flow separation, increased 3-D effects, sharp increase or decrease of the free surface). As such, numerical simulations of flooding in manmade or natural open channels and estuaries require the use of highly advanced numerical models to fully capture the fluid flow behavior, especially in areas where 3D effects such as flow separation or flow around a hydraulic structure are important. In addition, the numerical simulations should not just be able to predict the flow profile but also the corresponding free-surface elevation as a function of time. Therefore, the simulation of flooding is a highly 3D and time-dependent

phenomena which should require the use of a fully 3D numerical model with free-surface tracking capabilities. However, given that in practical applications one is interested to predict floods in relatively large domains (kilometers to hundreds of kilometers in both horizontal directions) and the time scales associated with natural flooding events are relatively large (days to months), numerical approaches based on the simplified (depth-averaged or shallow flow) equations of fluid flow are usually employed rather than solving the full 3D Navier-Stokes equations. The most popular approaches to predict floods in natural environments are based on the use of 1D St. Venant equations, 2D St. Venant equations (Shallow water equations) or hybrid 1D/2D St. Venant equations solvers with turbulence (roughness) parametrization based either on Chezy or Manning's coefficients.

Over the last two decades many attempts have been done to simulate flood extent and flood propagation using the aforementioned methods based on solving the shallow flow equations of motion. These simplified models are subject to limitations associated with the simplifications and assumptions inherent to depth averaging or section averaging the equations of motions. While relatively computationally inexpensive, these models were shown to often provide quite inaccurate predictions of the maximum flood levels during the propagation of the flood wave or of the dam break propagation speed (see Concerted Action on Dam-Break Modeling Final Report in 2000). As a result, one has to add large safety factors when results of these simulations are used in developing strategies to mitigate adverse flood effects. Moreover, the use of simplified methods (1D, 2D or hybrid 1D/2D St. Venant equations solvers) still calls for a good understanding of the 3D flow physics, which should also allow a better understanding of the main reasons why predictions using such simplified approaches are sometimes very inaccurate. For instance, 1D St. Venant model cannot simulate lateral flow into the floodplain accurately, whereas 2D St. Venant model cannot accurately predict flow in regions where separation and strong adverse pressure gradients are present (e.g., flow around hydraulic structures, flow in channels of high bank curvature). These limitations pose a strong case to the use of fully 3D non-

hydrostatic models with free-surface tracking capabilities to predict flood extent and flood wave propagation.

Reynolds-Averaged Navier Stokes (RANS) models would be the desired choice to simulate flooding in 3D, but their up-to-date application to flooding problems is very scarce. On the other hand, with the proliferation of computing resources and the increase of computer speed, application of 3D RANS models to predict flooding in natural environments is possible, at least for small to medium size domains (lengths of couple of kilometers in each horizontal direction). One of the advantages of employing such a model is a reduced level of calibration compared to a 1D or 2D models, since the turbulence is now modeled using advance turbulence closure models that capture the turbulent behavior of the flow. Moreover, accounting for roughness effects it is much easier and less empirical compared to St-Venant-based models which use Manning's formula to account for roughness effects. Eddy resolving models such as Large-Eddy simulation (LES), hybrid RANS-LES models such as Detached Eddy simulation (DES) or Direct Numerical simulation (DNS) are still, at the present time, too computational expensive to simulate flooding in real domains and over relevant time scales. With further increase of computer power and improvements in parallelization techniques, it is envisioned that such approaches will become feasible in the future.

1.2 Motivation

Several studies have shown that the frequency of flooding will increase under current changing climatic conditions (Milly et al. 2002) making flooding a crucial topic of research for future planning of cities and major industrial works (e.g., nuclear plants). Several cities have been affected by flooding in the last 20 years (e.g. 2008 flood in Cedar Rapids in Northeast Iowa, USA or 2013 North India floods) which not only caused an immense amount of material damage but also loss of human lives. The estimated cost of the 2008 flood in Eastern Iowa was approximately $64 billion while the estimated cost of

the 2013 North India floods was $27 billion and 102 lives. As a result, flood prediction and mitigation is a very active area of research. In turn, this requires using a code with advanced numerics that can capture the complex unsteady hydrodynamics associated with propagation of a flood wave over a complex domain.

The hydrodynamic behavior of floods cannot be accurately captured and understood using current, state-of-the-art approaches used for flood modeling that are based on solving the shallow flow equations in 1D or 2D. As already commented on, it is well documented that the flow behavior becomes highly 3-dimensional during unsteady events such as floods, especially in regions of high stream curvature, near the floodplain-main channel boundaries, and around man-made obstacles (e.g., hydraulic structures places in the main channel or in its immediate vicinity, constructions situated on the flood plain). As such, a much more accurate approach for simulating flooding is the use of a fully 3-D non-hydrostatic 3D Navier-Stokes model, provided that the model can also simulate the deformations of the free surface as part of the solution.

The increase of computing power over the last two decades makes the use of fully 3D numerical models an attractive option for flood prediction. However, the development of such numerical tools requires careful validation. This is not so much because of the basic Navier-Stokes solver using a state-of-the-art RANS turbulence model, for which the performance is fairly well known, but because of the deformable free surface module. Though different methods can be used to track the free surface, all methods are subject to errors and their performance for flooding simulations in simple and complex domains is not clear. Another big challenge is to determine the minimum level of grid refinement needed to obtain accurate predictions of floods. This level of mesh refinement is different in different parts of the domains (e.g., the level of refinement should be larger in regions where 3D effects are expected to be important). Simply using very fine meshes over the whole domain is not an option, given the huge computational costs required to simulate flood propagation even for relatively small regions. This motivates, the present research

work that tries to develop a numerical model to predict flood propagation in natural domains, to formulate clear recommendations on how the model should be used, and to apply the model for several important classes of applications related to flood propagation and dam break problems. These applications should show the superiority of using 3-D models over the standard approach based on using 2-D models.

Another motivation of the present work is the need to be able to assess the accuracy of standard 2-D St. Venant solvers used for flood propagation and dam-break problems. By performing 3-D and 2-D simulations for the same problem, one can compare the depth-averaging the 3-D data with the 2-D simulation results. This should allow getting a better idea of the level of accuracy of the 2-D simulations and especially of the regions where these errors are relatively high. Then, using the depth-averaged 3-D solution, one can try to better calibrate the 2-D model or to test the effectiveness of implementing additional models/modifications trying to account for effects that are not captured in standard versions of these simpler models (e.g., curvature effects, presence of weirs, dams in the domain). Thus, the present work is also relevant in the context of efforts devoted to improvement of 2-D St. Venant solvers, which will remain for some time the main tool to simulate floods and dam break problems over medium to large domains.

Another motivation of the present work is related to design of flood protection measures and estimation of maximum erosion that can be induced by the passage of a flood wave in a certain critical region (e.g., around a bridge site where bridge piers are present). Once the model is validated, one can run simulations corresponding to different designs (e.g., in terms of position and size of flood barriers) and use the model as a tool to optimize design of flood protection structures. Though, in principle, this can also be done using a 2-D solver, the accuracy of the predictions, especially those related to sediment entrainment capacity, should be much higher when a 3-D model is used, as the vertical distribution of the horizontal velocity is part of the solution in a 3D model. 2-D models simply assume a logarithmic distribution of the horizontal velocity in the vertical direction, which is

obviously wrong in regions where 3-D effects and secondary flow are important. Moreover, 2-D models predictions are basically worthless once flow changes regime from open channel flow to pressurized flow, a situation that can occur when hydraulic structures are placed along or across the main river channel (e.g., bridge piers, culverts).

1.3 Research goals and objectives

The present research tries to advance the state of the art in the field of numerical simulation of floods by using fully three-dimensional RANS models with a deformable free surface to predict flood wave propagation and flows triggered by dam breaks in natural environments.

The first major goal of this research is to develop, investigate the predictive capabilities of, and successfully validate a fully 3-D non-hydrostatic RANS model with deformable free-surface capabilities using the Volume-of-Fluid method to be used in the simulation of flooding events in natural environments. The model should be able to predict flood waves associated with naturally induced floods or by the sudden structural failure of a dam or flood protection structures, such as levees. The model will be developed within STARCCM+, a state-of-the-art general CFD software with advanced meshing capabilities and good scalability for RANS simulations performed on meshes with a large number of grid points.

A second main goal will be to assess the performance of commonly used 2-D shallow flow solvers and to propose better ways to calibrate these models by using results from the 3-D simulations. Data generated by the 3-D model can be used for validation of lower order models. This is crucial given the lack of detailed validation data provided from direct measurements during floods.

Previous applications of 3-D URANS-VOF applications for this type of problems was restricted to very short domain or to idealized cases (e.g., mostly steady flow in river reaches with natural bathymetry, sometimes containing hydraulic structures). The present

research will be a major step forward toward a wider application of such advanced methodologies for river flood research and flood hazard. As such, a related goal is to show that this approach can be successfully applied for several main types of problems in flood research.

As the 3-D model provides the whole 3-D flow field and a much more accurate estimation of the bed shear stresses compared to the standard 2D shallow flow equations based models, a related goal is to get more insight into the physics of these flows and to evaluate quantities of engineering interest that cannot be accurately estimated using lower order models. As such, a related goal will be demonstrate that 3-D model can be used to estimate erosion potential at bridge sites for scenarios where the bridge deck becomes submerged during the passage of the flood wave and pressure scour effects become important. This is of crucial importance to insure proper design for structural stability of bridges, as most of the erosion at bridge piers and abutments occurs during floods. Given the major flood damage that occurred during the floods of 2008, the state of Iowa has initiated major programs to estimate hazard due to sudden failure of hydraulic structures in the state. A related goal will be to illustrate the usefulness of the model to address such scenarios by applying the model to estimate hazard for a reservoir where a major structural failure has occurred. The model will be applied to model sudden dam break at two locations in the state of Iowa, near Des Moines and Iowa City, where most of the state population and major industrial sites are located.

The long term goal of this research is to develop and test state of the art numerical modeling tools to improve flood monitoring and flood prediction efforts that should eventually allow the development of more accurate Flooding Maps.

The main objectives of this study are:

- to validate the 3-D model for a series of test cases in idealized geometries for which validation data is available mostly from laboratory experiments. These cases will test the different modules of the code and how well the code performs for time-

accurate calculations. A related goal is to determine the mesh refinement requirements to get accurate results.

- to validate the 3-D model for simulating flow in river reaches with real bathymetry. The main tests will be to simulate flow in river reaches of lengths ranging from 1 to 18 km containing hydraulic structures (e.g., one or several hydraulic dams) for steady and unsteady (flood propagation) events. This will allow testing the model for cases where the flow regime changes between subcritical and supercritical and the implementation of the boundary conditions.

- to quantify the errors associated with results obtained using a calibrated 2-D depth-averaged model, commonly used for flood predictions in research and consulting, based on comparison with 3-D model results at low and high low conditions.

- to apply the 3-D model as a design tool for flood protection strategies, which include construction of flood protection walls or removal of river dams.

- to quantify the potential for sediment entrainment during the passage of a floodwave, including possible pressure scour effects during the submergence of a bridge deck.

- to quantify hysteresis effects on bed shear stress distributions associated with the passage of a flood wave in an open channel

- to demonstrate the capability of the 3-D model to simulate flooding induced by the structural failures of dams under realistic conditions

- to develop a methodology for recalibration of 2-D depth-averaged models to accurately capture the propagation of dam break floodwaves.

1.4 Structure of thesis proposal

The outline of the proposal is as follows. Chapter 2 provides a summary of current approaches to simulate flood propagation and dam break problems including 1-D, 2-D and

hybrid 1-D/2-D CFD approaches. In addition, current approaches for tracking the free-surface in 3-D CFD codes are reviewed. Chapter 3 describes the fully 3D Unsteady Reynolds-Averaged Navier-Stokes (URANS) model coupled with an advanced 2-equation k-ε turbulence model with deformable free-surface capabilities via the Volume-of-Fluid (VOF) method. The chapter provides a description of the mesh generation procedure and boundary conditions. Finally, validation of the model for different steady and unsteady test cases with idealized geometry is presented. Chapter 4 discusses several validation calculations of flow profiles in river reaches with lengths ranging from 1 km to 18 km for low and high flow conditions. Errors associated with 2-D depth-averaged models are also discussed as well as possible flood protection strategies based on 3-D results. Chapter 5 discusses the potential for sediment entrainment during the passage of a flood wave based on 3-D simulation results and possible pressure scour effects in channel/river reach containing a bridge induced during the times the bridge deck becomes submerged. Finally, Chapter 6 discusses 3-D and 2-D simulations of two realistic dam break scenarios for the state of Iowa and how to recalibrate 2-D models to better reproduce 3-D results.

CHAPTER 2 LITERATURE REVIEW

In recent years the cost-effective generation of spatially-distributed numerical river corridor models has been facilitated by advances in algorithm model development to solve the governing non-linear equations and massive parallel-computing algorithms, and increased computing power. The proliferation of high-resolution digital elevation maps, hydrographic data and constant development of numerical tools has resulted in the development of hydrodynamic models capable of producing quantitative assessments of flood risk at very fine spatial and temporal scales (Hunter et al. 2007).

2.1 Types of numerical hydraulic models

Hydraulic models are classified according to the number of dimensions in which they represent the spatial domain. The selection of a one-, two- or three-dimensional model depends on the complexity of the flow processes to be numerically simulated. The flow behavior is highly three-dimensional, especially in regions of high stream curvature, near the regions where a tributary joins the main river (confluence hydrodynamic zone), near hydraulic structures such as river dams, groynes bridge piers and bridge abutments, and during high-flow conditions in which flow occurs over the floodplain, which can induce strong secondary flow. Each of these models have their own unique equations of motions. The three-dimensional equations of incompressible constant-density fluid motion are called the Navier-Stokes equations. They consist of a total of 4 equations which describe conservation of mass or continuity, and conservation of momentum in the three directions. Starting from the incompressible Navier-Stokes equations, one can depth-average the equations to obtain the Shallow Water equations (continuity and momentum for the depth averaged horizontal velocities), also called the depth-averaged Navier-Stokes equations or the 2-D St. Venant equations. When depth-averaging, one direction is eliminated (vertical direction), therefore reducing the complexity of the problem and imposing limitations on the applicability of these equations. The Navier-Stokes equations can also be section-

averaged. In this case, the final product are a set of 2 equations, usually called the 1-D St. Venant equations.

2.2 One-dimensional numerical models

Models based on solving the 1-D St. Venant equations are still the most used approach for simulating flooding. Among the most popular 1-D models are general codes such as HEC-RAS, developed by the U.S. Army Corps of Engineers, and MIKE 11, developed by DHI (Bates and Roo 2000). The 1-D St. Venant equations are shown below:

$$\frac{\partial \hat{h}}{\partial t} + \frac{\partial\left(h\hat{\hat{U}}\right)}{\partial x} = 0 \tag{2.1}$$

$$\frac{\partial \hat{\hat{U}}}{\partial t} + \hat{\hat{U}}\frac{\partial \hat{\hat{U}}}{\partial x} + g\left(\frac{\partial \hat{h}}{\partial x} + S_f - S_0\right) = 0 \tag{2.2}$$

where $\hat{h}$ is the section-averaged depth of channel, $\hat{\hat{U}}$ is the section-averaged streamwise velocity, g is the gravity acceleration, S_f is the friction slope, S_0 is the bottom slope, t is time and x is the direction along the centreline of the channel.

Depending on the level of complexity, these equations can be classified as kinematic, diffusive and dynamic wave equations. The difference between these approximations are shown below:

$$S_f = S_0 \leftarrow \text{Kinematic} \tag{2.3}$$

$$S_f = S_0 - \frac{\partial \hat{h}}{\partial x} \leftarrow \text{Diffusive} \tag{2.4}$$

$$S_f = S_0 - \frac{\partial \hat{h}}{\partial x} - \frac{\hat{\hat{U}}}{g}\frac{\partial \hat{\hat{U}}}{\partial x} - \frac{1}{g}\frac{\partial \hat{\hat{U}}}{\partial t} \leftarrow \text{Dynamic} \tag{2.5}$$

The kinematic wave approximation (Equation 2.3) assumes that the friction slope (S_f) is equal to the bottom slope and that the flow is uniform. Both conditions can be

justified when the wave height is much smaller than the depth and when the mean channel velocity divided by depth and time scale is negligible compared to channel slope. This approximation is usually used in hydrologic models for channel flow routing such as HEC-HMS.

The diffusive wave approximation (Equation 2.4) adds another level of complexity and assumes that the inertial acceleration terms, both local and advective, are much smaller than the remaining terms. As a result, the friction slope balances the bottom slope and the pressure terms. This approximation is only valid when the flow is essentially subcritical. Some examples of codes that use this approximation are MIKE SHE and LISFLOOD-FP. The dynamic wave (Equation 2.5) describes the complete set of the 1-D St. Venant equations. It is the most challenging and numerically expensive form to solve when the 1-D approach is used, but it is valid for all channel flow scenarios, at least for cases when the simplified assumptions associated with the 1-D approach are valid. HEC-RAS and MIKE11 are just 2 examples of 1-D codes that solve the dynamic wave equation.

Some advantages of using a code based on the 1-D St. Venant equations is that they are computationally efficient, even when solving the dynamic wave equation. For example, such models can simulate streams with lengths greater of 100 km and are capable of simulating, albeit in a very approximate way, the effect of the presence of in-stream structures such as bridge deck and piers, culverts, low-head dams and lateral structures. However, they cannot simulate lateral diffusion of flood waves, discretization of the topography as sections instead of a surface (Hunter et al. 2007) and require extensive calibration for different flow conditions. Furthermore, cross-section location and orientation are decided by the modeler, which can lead to poor results if the modeler lacks experience (Bates and Roo 2000).

Flooding in riverine environments have been modelled extensively using 1-D models. HEC-RAS (Casas et al., 2006, Omer et al., 2003) and HEC-2 (Mohammed, 2006) in particular have been applied to flood inundation studies in non-urban environments. The

focus of these studies was to investigate how changes in topography resolution affect the flood inundation extent, discharge and water surface elevation and the sensitivity of the solution to Manning's coefficient. These studies concluded that 1-D models are highly sensitive to topography information. Mohammed (2006) used HEC-2 to develop a hydraulic model to predict flood levels in the Linggi River near the Seremban town, Malaysia for floods with different return periods ranging from 10 to 100 years. The calibrated model showed good agreement with respect to measured observations in terms of free-surface elevations that were predicted with errors in the order of 5% or smaller.

One-dimensional models have also been applied to model dam/levee break problems (Choi et al., 2001, Mambretti et al., 2008, Zhang et al., 1992). In the aforementioned cases, the 1-D St. Venant equations were applied to replicate simple configuration dam breaks (flat bed, rectangular column of water). It was found that the 1-D numerical model can replicate these phenomena with acceptable accuracy, as long as the geometries are simple and the ratio of flow depths upstream to downstream of the dam is moderate (less than 0.05).

2.3 Two-dimensional numerical models

The constraints of the 1-D St. Venant equations and the need for more information about the temporal and spatial evolution of the flood event led to the development and use of 2-D models. The solution of the 2-D Shallow Water equations can be divided, broadly speaking, in two main classes: Full solution of the Shallow Water equations and Simplified approximations called "Zero-Inertia" models. The 2-D Shallow-Water equations are shown below:

$$\frac{\partial h}{\partial t}+\frac{\partial\left(h\tilde{U}\right)}{\partial x}+\frac{\partial\left(h\tilde{V}\right)}{\partial y}=0 \tag{2.6}$$

$$\frac{\partial\tilde{U}}{\partial t}+\tilde{U}\frac{\partial\tilde{U}}{\partial x}+\tilde{V}\frac{\partial\tilde{U}}{\partial y}=-g\frac{\partial\left(z_b+h\right)}{\partial x}+\frac{1}{\rho h}\frac{\partial}{\partial x}\left(\tilde{\tau}_{xx}h\right)+\frac{1}{\rho h}\frac{\partial}{\partial y}\left(\tilde{\tau}_{yx}h\right)-\frac{\tau_{bx}}{\rho h} \tag{2.7}$$

$$\frac{\partial\tilde{V}}{\partial t}+\tilde{U}\frac{\partial\tilde{V}}{\partial x}+\tilde{V}\frac{\partial\tilde{V}}{y}=-g\frac{\partial\left(z_b+h\right)}{\partial y}+\frac{1}{\rho h}\frac{\partial}{\partial x}\left(\tilde{\tau}_{xy}h\right)+\frac{1}{\rho h}\frac{\partial}{\partial y}\left(\tilde{\tau}_{yy}h\right)-\frac{\tau_{by}}{\rho h} \tag{2.8}$$

where h is the water depth, $\tilde{U}$ is depth averaged velocity in the x direction, $\tilde{V}$ is the depth averaged velocity in the y direction, g is the gravitational acceleration, z_b is the bed elevation, ρ is density of fluid, $\tilde{\tau}_{xx}$, $\tilde{\tau}_{yy}$, $\tilde{\tau}_{yx}$ and $\tilde{\tau}_{xy}$ are the four components of the depth averaged shear stress tensor, and τ_{bx} and τ_{by} are the bed shear stress components.

In the Zero-Inertia models, the inertia terms are omitted. The solution of the full Shallow Water equations is subject to instabilities and convergence problems, therefore making the Zero-Inertia models an attractive alternative for practitioners. Moreover, the lack of inertial terms in the governing equations assumes that the inundation process is a slow phenomenon, thus the choice of a zero-inertia model is justified by the physical conditions, at least for many cases. (Hunter et al., 2007).

The Shallow Water equations are not free of limitations due to the simplifying assumptions made in their derivation. Their main disadvantage is the lack of ability to simulate pressurized flow making them not ideal to simulate flow in domains containing culverts and bridges (Frank et al., 2001; Verwey 2001). Calculations using 2-D models are computationally more expensive compared to 1-D models and they are prompt to instabilities and convergence problems. Generating high quality 2-D meshes in complex domains is not always an easy task and requires experience.

With the increase of computer power the application of the Shallow-Water equation model to simulate flood propagation has become the most attractive option and thus it has been applied to flooding in riverine, coastal and estuarine environments, as well as dam/levee break problems. For instance Musser and Dryer (2005) simulated flooding in a 4.6 mile reach of the Flint River at Albany, Georgia using FESWSMS. Their results showed good agreement with gage readings. Another simulation was performed by Wagner and Mueller (2001) using RMA-2. The model was used to simulate flooding in a reach of the Ohio River, Jefferson County, Kentucky. The model was calibrated for low flow conditions (35 000 cfs) and was successfully validated for high flow conditions (390 000 cfs). O'Brien et al. (1993) successfully used FLO-2D to simulate the 1993 mudflows in

Rudd Creek in Davis County, Utah. Their simulation results of area of inundation, maximum flow depth, frontal wave flow depths and velocities, and final deposits of mud compared well with measurements.

Some examples of application of 2-D depth-averaged CFD codes to dam break problems include the work of Xanthopoulos and Koutitas (1976) and Singh et al (2011). Singh et al (2011) developed a 2-D model and applied it to simulating the realistic Malpasset dam failure in the Reyran River, France in 1959. The solution showed that the errors in flood arrival time decreased with increasing distance downstream of the dam. The closest location for data comparison was located approximately 2 km downstream of the dam and showed 4% error whereas the points located approximately 6 and 7 km downstream of the dam showed errors less than 1%.

Hervouet (2000) also performed a comparison between 1-D and 2-D models applied to the realistic dam break case of the Malpasset dam. In order to obtain free-surface elevation measurements to be used for validation, a 1:400 scale model was constructed. It was found that the 1-D and 2-D codes gave overall comparable predictions. For example, the free-surface elevation differences between the predictions by the two models ranged from 10 cm to 10 m, the differences between the 1-D model and experimental results ranged from 30 cm to 11 m, while the differences between the 2-D model and the experimental results ranged from 14 cm to 7 m.

2.4 1-D/2-D coupled flow models

A compromise between 1-D and 2-D modeling approaches are hybrid 1D/2-D methods. Such methods were developed to reduce computation time while still maintaining the capability of simulating in-stream structures. The main idea is to model the channel flow using a 1-D model and the floodplain flow using a 2-D model. By assuming one-dimensional flow in the main channel, the grid cell size is no longer limited by the channel width, allowing the grid cell size to increase (Dhondia and Stelling, 2002) and therefore

reducing the computational cost. By assuming 2-D flow over the floodplain, lateral wave diffusion can be accurately accounted, especially in complex terrains and urban environments (Syme et al., 2004).

The linkage between the 1D and 2D models can be achieved in several ways. One of the most common ways is to link them laterally with a simple weir equation, which makes momentum not be conserved, such as is done in the MIKE FLOOD software (DHI, 2009). Another approach is to keep the free surface continuous across the linkage and to conserve the 1D-2D volume, such as in done in the Delft 1D-2D software (Frank et al., 2001).

Horrit and Bates (2002) performed a comparison between flood inundations models, namely HEC-RAS (1D), LISFLOOD-FP (Coupled 1D/2D) and TELEMAC-2D (2D). The models were applied to predict flooding in a 60-km reach of the Severn River, UK. It was concluded that both HEC-RAS and TELEMAC-2D are capable to represent flood extent and discharge. LISFLOOD-FP had to be calibrated against independent inundation area in order for it to obtain acceptable results. It was also found that both TELEMAC-2D and HEC-RAS are capable of making equally good predictions in terms of flowrates and flood inundation extent, with TELEMAC-2D having marginally better results than HEC-RAS. LISFLOOD-FP had consistently the poorest results amongst the three models and it required independent validation to obtain accurate results (calibration based on inundated area rather than based on the flowrate).

All 1-D, 2-D and coupled 1D/2D hydraulic models are sensitive to errors of measurements in rating curves, spatial resolution of elevation data, and the inherent simplifying assumptions of the governing equations. Flow boundary conditions are usually specified based on rating curves, developed by assuming uniform steady flow in the entire cross section of the channel. Such rating curves are subject to errors from measurement of cross-sectional geometry, which usually range from 4 to 6% (Sauer and Meyer, 1992) and from the assumption of uniformity of velocity in the cross section. In addition, under high

flow conditions, the errors in discharge measurements can be as high as 20 percent (Pappenberger et al., 2006) due to non-uniformity of overbank flow. Finally, roughness effects have to be calibrated and are mostly based on visual estimation, resulting in oversimplification of land cover heterogeneity.

2.5 Three-dimensional numerical models

Even though a fully 3-D numerical simulation of flood flows is the most accurate way to model the flood event, there are only a handful of attempts made in the literature. This is mostly due to their high computational costs related to using meshes with a large number of cells and sufficiently small time steps to insure convergence. For most practical applications, one needs to use parallel computing in order to obtain solutions in a reasonable amount of physical time. This, in turn requires a highly scalable code. The capability of the grid generator associated with the code to generate high quality meshes with regions of finer mesh refinement in critical flow regions and smooth transition toward the regions of coarser mesh refinement is another limiting factor in the widespread use of 3-D codes for flooding applications in natural environments.

During a flood event, the free surface is moving in time and space, which means that the position of the boundary between water and air is unknown and has to be determined as part of the solution. In the framework of 3-D models, free-surface flows are analyzed via three main types of methods: moving-grid methods, fixed-grid methods and particle methods (Floryan and Rasmussen, 1989). These methods are briefly described next.

2.5.1 Moving grid methods

Moving grid methods, as their name suggests, are Lagrangian methods that reshape the grid close to the free surface in order to make the grid fit the shape of the free-surface. Some examples of moving grid methods are strictly Lagrangian methods, free Lagrangian methods and mixed Lagrangian-Eulerian methods. For instance, in a strictly Lagrangian

method, the grid close to the interface is moved as long as the geometry is simple and the steepness is small (Hirt et al. 1970). When high deformation of the mesh arises, the elements must be switched and reconnected around the free surface. This is the principle behind Lagrangian methods with rezoning (Hirt et al. 1974).

As river and flood flows are generally shallow, the simplest way to implement a moving grid method in a structured mesh 3-D code is to keep the bed mesh fixed and to use vertical grid lines extending from the fixed bed to the moving free surface. The distribution of the points along these grid lines will change as the free surface moves but the number of points (cells) in the vertical direction will remain constant as points are just redistributed vertically at each horizontal location. The governing equations should contain some extra terms accounting for the temporal evolution of the cells. However, in some applications these terms can be neglected. In fact, using the standard fixed mesh governing equations with moving meshes is correct, if one is interested only in the final steady solution. Such an approach was used by Zeng and Constantinescu (2007) to simulate flow in a meandering channel and flow in highly curved open channels with fixed or deformed bed. In their work, the free-surface elevation was obtained implicitly by applying the kinematic free-surface boundary condition while the dynamic free-surface boundary condition was applied to provide boundary conditions for velocity and pressure. The deformable free-surface (moveable mesh) capabilities were validates mainly using two test cases: Flow in an S-shaped channel with trapezoidal cross section and Flow in a 193° degree channel bend with rectangular cross section. Both test cases assumed a fixed flat bed. The results, in terms of predicted transverse free-surface elevation and longitudinal free-surface elevation along the two banks, showed really good agreement with experimental data. Meselhe and Sotiropoulos (2000) applied a similar treatment of the free-surface to calculate the free-surface deflections, thus obtaining accurate results in channels containing medium to large curved bends. While adaptive mesh techniques for free-surface tracking have not been applied to rivers, they should in principle work.

2.5.2 Fixed grid methods

In the case of fixed grid methods, there is no need to change the grid in order to capture the location of the free surface, since the grid itself covers both the water and air regions. There are two subcategories of fixed grid methods: surface tracking and surface capturing methods. In the case of surface tracking methods, a set of pointers identifies the location of the free-surface, whereas in the case of surface-capturing methods, the free surface is identified by an iso-contour of a scalar value.

All fixed grid methods can work for cases when the boundary conditions are steady or unsteady. Most previous applications in hydraulics and river engineering report simulations conducted with steady boundary conditions in which the deformations of the free surface were induced mainly as a result of the pressure gradients induced by the flow (e.g., super elevation of the free surface at the outer bank of a bend or raising of the free surface close to the stagnation region of flow past a bridge pier). In such applications, the solution is generally steady. Another main category of applications are dam break simulations. Here again the inflow conditions are generally steady, though the solution is highly unsteady, and the deformations of the free surface are generally much larger compared to the previous type of applications. Very few applications were reported for cases when the boundary conditions are unsteady (e.g., a flood wave is introduced at the inlet). Some examples are the works performed by Shen et al. (2004) and Zhang et al. (2013).

2.5.2.1 Level set method

In the case of surface-capturing methods, the Level Set method (Osher and Sethian, 1988) is one of the most commonly employed. The scalar function used to track the location of the free surface is the distance perpendicular to the interface. This function is defined such that is positive in the water region, zero at the interface and negative in the air region. Equations 2.9 and 2.10 shows the basic equations of the Level Set method.

$$\frac{\partial \phi}{\partial t} + \vec{u} \cdot \nabla \phi = 0 \tag{2.9}$$

$$\phi = \begin{cases} -d & for \quad x \in \Omega_{gas} \\ 0 & for \quad x \in \Gamma (free\ surface) \\ d & for \quad x \in \Omega_{liquid} \end{cases} \tag{2.10}$$

where ϕ is the Level set function, $\vec{u}$ is the velocity vector, t is time and d is the perpendicular distance to the interface. Equation 2.9 expresses the kinematic free-surface boundary condition. However, Equation 2.9 does not preserve the perpendicular distance to the interface, d, at all times, since sharp gradients may arise. In order to preserve the perpendicular distance to the interface, the values of the Level Set function, ϕ, should be reinitialized. One solution is to solve a partial differential equation (e.g., see Sussman et al., 1994), as shown in Equation 2.11

$$\frac{\partial d}{\partial \tau} + s(d_0)(|\nabla d| - 1) = 0 \tag{2.11}$$

$$d_0(\mathbf{x}) = d(\mathbf{x}, \tau = 0) = \phi(\mathbf{x}, t) \tag{2.12}$$

$$s(d_0) = \frac{d_0}{\sqrt{d_0^2 + (|\nabla d_0|\varepsilon)^2}} \tag{2.13}$$

where d is the perpendicular distance to the interface, d_0 is equal to the computed Level Set function after computing the evolution of the Level Set (Equation 2.9), $s(d_0)$ is a smoothed signed function as shown in Equation 2.13, τ is an artificial time and ε is usually the length of one grid cell.

The main advantage of the Level Set method is that it is relatively easy to implement, even in 3-D codes. Moreover, the curvature of the free surface is easily captured. However, the signed distance function and the evolution of the Level Set induce significant numerical diffusion, which produces loss of mass over time. This is the most significant disadvantage of the Level Set method.

The Level Set method was applied for flows in open channels with deformable free surface, including for channels with realistic bathymetry and channels containing hydraulic structures. Several applications were reported by Kang et al. (2011) and Kang and Sotiropoulos (2012) for the case when the boundary conditions are steady. A 3D non-hydrostatic code in general curvilinear coordinates with free-surface evolution computed using the Level Set method was developed to simulate open channel flow with complex embedded hydraulic structures such as groynes, boulders and bridge piers.

One relevant 3-D case studied by Kang et al. (2011) was the free-surface flow past a rock structure in an open channel. A straight open channel was considered with an embedded rock structure, cross vane, typically used in river restoration projects (Figure 2.1). The computational results were compared with experimental results obtained in a 12 m long and 0.9 m wide flume located in St. Anthony Falls Lab. The cross vane was located midway in the channel. The average water depth and velocity were 0.17 m and 0.24 m/s respectively. The corresponding Reynolds and Froude numbers were 4.08×10^4 and 0.19 based on mean values for depth and velocity. Based on the physical values, the computational domain was created by considering the inlet and the outlet 3 m and 9 m downstream of the inlet of the flume, making the computational domain 6 m long, 0.9 m wide and 0.32 m high. The domain was discretized with 191 x 151 x 121 nodes in x, y and z directions respectively, making the total number of nodes approximately 3.5 million (Figure 2.2). Figure 2.3 shows the spatial distribution of streamwise velocity, free-surface elevation and local Froude number at the interface predicted by the 3-D simulation. The code was used to calculate a steady state RANS solution for this problem. One can see that the code can capture important 3-D effects such as the wake formed behind the cross vane near the two side walls. The elevation of the free-surface decreases as the flow goes through the cross vane, with the lowest free-surface elevation located right above the rocks near the sidewalls. These low free-surface elevation regions create in turn a change of the local Froude number from subcritical to supercritical, thus demonstrating the code capability on

dealing with complex local effects such as transcritical flow. In addition, the free-surface elevation was validated with experimental results as shown in Figure 2.4 and Figure 2.5, where it is clearly shown that the 3-D models results are in good agreement with experimental measurements.

A second relevant case calculated using the same code considered 3D free-surface flow in a meandering stream with complex natural bathymetry. The meandering channel used to conduct the experiment was installed in the St. Anthony Falls Laboratory Outdoor StreamLab (OSL). The bankfull discharge was 2.85×10^{-1} m^3/s with channel width and depth being approximately 3 m and 0.3 m, respectively. The corresponding Reynolds number was equal to 10^5, while the Froude number was equal to 0.4. The computational domain was discretized using 472 736 triangular elements with a grid point distribution of 191 x 51 x 96 nodes in the streamwise, transverse and vertical directions, respectively. Figure 2.6 shows the plan view of the computational domain with bathymetry elevation contours for reference. As in the previous case, the flow velocity (velocity magnitude), free-surface elevation and local Froude number were calculated. They are shown in Figure 2.7. As the flow enters the domain, the velocity is quite high in the straight region in which the cross sectional area is small. Once the flow enters the bend region, the core of high velocity moves towards the outer bank while the velocity magnitude decreases due to the increase of cross sectional area. Consistently, as the flow leaves the first bank and enters a straight region with small cross sectional area, the velocity magnitude increases and the core of high velocity moves towards the center of the channel. The flow then enters the second bend in which the behavior is consistent with the first bend. The sudden increase of velocity magnitude in the straight region between the first and second bend created in turn a decrease in free-surface elevation. Both effects combined made the flow transition locally from subcritical to supercritical. The prediction of the free-surface elevation in the steady state simulation was validated using experimental results as shown in Figure 2.8, in which good agreement between simulation and experiment was observed.

Level Set methods have also been applied to dam break problems in simple geometries, mostly in 2-D (e.g., Liang et al., 2011). Balabel (2015) performed an unsteady RANS with deformable free-surface captured using the Level Set method of a 2-D dam break. He considered a water column height of 10 cm and length of 1 m (Figure 2.9) inside a flume 25 cm long and 1 m high. Figure 2.10 shows the location of the bore as a function of the non-dimensional time, while Figure 2.11 shows the time evolution of the dam break. The results were compared with experimental results and it was shown that the Level Set method can accurately represent the location of the free-surface and complex topological changes of the turbulent flow. In addition, the influence of the density ratio between the fluids and the initial elevation of the water column was studied numerically. It was found that the higher the density ratio and the higher the initial column of water, the faster the gravity wave caused by the dam break travels (Figure 2.12).

The Level Set method has been successfully applied to problems with unsteady boundary conditions in which the location of the free-surface, as well as the pressure and velocity fields at a specified boundary, was changing in time. Chen and Yu (2009) successfully employed a fully 3D- non-hydrostatic unsteady Navier-Stokes solver coupled with the level set method to model wave-body interaction problems, such as a wave passing through a rectangular obstacle and pitch/heave motions of ships under wave action. Carrica et al. (2007) developed a 3-D unsteady RANS code coupled with a modified version of the Level Set method (single-phase version). The code was successfully validated with test cases that involved wave propagation.

2.5.2.2 Volume-of-fluid method

One of the most common surface-tracking methods for 3-D simulations in complex domains is the Volume-of-Fluid (VOF) method (Hirt and Nichols, 1981). In this method, the volume fraction occupied by the liquid (water) is tracked. Equation 2.14 shows the evolution of the volume fraction function.

$$\frac{\partial \alpha}{\partial t} + \vec{u} \cdot \nabla \alpha = 0 \tag{2.14}$$

where α is the volume fraction of the specified fluid, $\vec{u}$ is the velocity vector and t is time. As the volume fraction function is not smooth across the interface; therefore, the interface needs to be reconstructed in terms of the volume fraction. The first of the two most common techniques used to reconstruct the interface is the Simple Line Interface Calculation (SLIC) by Noah and Woodward (1976). In this technique, the interface propagates with the fluid and the lines are assumed parallel to one of the edges of the computational cell. The Hirt and Nichols VOF method (1981) employs a reconstruction similar to the SLIC, in which the interface is assumed as a straight line in which the location and slope are of the line depend on the average value of the volume fraction and the gradient of it in the neighboring cells. The second most common technique for interpolation is called Piecewise Line Interface Calculation (PLIC) by Young (1982), in which the slope of the interface is determined by the interface normal approaching the interface. During the reconstruction of the interface, the curvature of the free-surface becomes non-continuous. The VOF method conserves mass greatly and it is very robust, making it capable of dealing with a wide array of problems. On the other hand, due to the reconstruction procedure it is very difficult to implement and the curvature of the interface is non-continuous.

The VOF method has been the most popular approach for river engineering applications in which the free surface deformations are relatively large such that the commonly-used rigid lid approximation introduces large errors. One such application of flow in an open channel was reported by Ma et al. (2002). A fully 3D non-hydrostatic model with a VOF module was developed in FLUENT, a state-of-the-art CFD commercial code. The field site was situated on the River Calder, Todmorten, United Kingdom. The reach was 175 m long, 10 m wide and had vertical stone-sided walls of 3.5 m high with an average bed slope of 0.0035. A physical scale model was constructed with a 1:35 ratio,

making the model 5 m long, 0.3 m wide and 0.5 m deep. The scaled discharge was set to a constant 12.4 l/s which is equivalent to a discharge of 89.9 m^3/s with an approximate return period of 100 years in the actual river. Four different computational grids were tested: 101x11x8, 101x22x16, 202x22x16 and 202x22x32. Figure 2.13 shows the bathymetry used in the computational model, while Figure 2.14 shows a streamwise view of the computational grid. Experimental results are compared to numerical results obtained on the 202x22x16 computational grid. Figure 2.15 compares the streamwise and transversal free-surface elevations. The free-surface elevation shows very good agreement with experimental results. In terms of velocity profiles (Figure 2.16), the model performed fairly well based on general pattern of fluid flow and velocity magnitudes. The shift on the core of high velocity towards the left in the experimental results can be explained by the asymmetry of the inflow velocity, which is created by the asymmetry of bed topography prior to the start of the physical model. In conclusion, a fully 3D non-hydrostatic model coupled with the VOF module was able to accurately predict the free-surface elevation in both streamwise and transverse directions, as well as accurately representing the velocity field in an open channel of complex bathymetry under steady state conditions.

Other examples of VOF applications for river engineering problems include the work of Rodriguez et al. (2004), Endreny et al. (2011) and Fu et al. (2007). Rodriguez et al. (2004) successfully developed a fully 3D non-hydrostatic RANS model in FLOW3D to simulate flow in a highly sinuous river reach of approximately 50 m length (20-40 times the average depth of the channel). FLOW3D results were compared to depth-averaged results obtained using STREMR, a Shallow-Water equation solver developed by the Waterways Experimental Station of the U.S. Army Corps of Engineers. It was found that both FLOW3D and STREMR were capable of representing the mean flow profiles. Some differences were noted and they were attributed to the adverse pressure gradients created by 3D effects inside the curved parts of the channel and, in particular, by the secondary flows which cannot be well captured by 2-D models. Endreny et al. (2011) analyzed the

hyporheic response to hydraulic jumps created by river steps using a fully 3D non-hydrostatic code coupled with the Volume-of-Fluid method. It was found that the hydraulic jump affects extensively the flow patterns in the surface water and in the groundwater parts of the flow domain. They found that failure to represent the hydraulic jump accurately can lead to errors of approximately 75% in subsurface flow paths. Fu et al. (2007) used a 3D RANS model with the Volume-of-Fluid method to calculate the flow field and analyze the spawning sites for Chinese sturgeon near the downstream site of the Gezhouba dam, located in the Hubei province of China. Fu et al. (2007) were able to successfully identify the optimal locations for spawning sites which can be used as theoretical support for ecological conservation practices and proper management of the Three Gorges Reservoir.

Another main type of applications were the VOF method was used in river engineering is the calculation of unsteady flow induced by a dam break (Biscarini et al. 2010, Ozmen-Catagay et al. 2014, Ozmen-Catagay and Kocaman, 2011, Yang et al. 2010). Biscarini, Francesco and Manciolo (2010) made a detailed assessment of the capabilities of a fully 3-D non-hydrostatic RANS model with VOF developed in OpenFOAM, a free open source CFD code, to simulate dam-break flows. They discuss three test cases that are simplified versions of realistic dam-break scenarios. Moreover, a detailed comparison between results obtained using the 3-D model with VOF and a 2-D Shallow Water Equations model, CCHE2-D, was performed.

The first test case was a partial, instantaneous dam break over a flat-bed without friction. The setup was as follows: a 200 m square region contains a dam in the middle with an opening of 75 m asymmetrically positioned along the dam (Figure 2.17). Initially, the water elevation upstream of the dam was set to 10 m, while it was set to 5 m everywhere else. The results obtained with the 3-D model were compared to the numerical results obtained with the 2-D code proposed by of Fennema and Chaundry (1990) as well as with results obtained using a 2-D code, CCHE2-D. The time step was set to 0.02 s in both models. Figure 2.18 shows the distribution of the free-surface elevation 7.2 s after the

sudden collapse of the column of water. The free-surface elevations immediately upstream of the dam opening are lower in the 3-D model results than those predicted by the 2-D model, making the celerity of the gravity wave predicted in the 3-D simulation greater than the one predicted by the 2-D model (Figure 2.19). These observations are consistent with those made by De Maio (2004), who attributed these differences to the three-dimensionality of the gravity force during the initial stages of the event. Figure 2.20 shows the location of section E-E in the computational domain, the water depth time history at section E-E and the corresponding discharge hydrograph at this section. The 2-D model underestimates the peak water depth and the peak discharge by approximately 10% and 30%, respectively. Thus, it was concluded that 2-D models are inadequate in accurately simulating the generation and propagation of the gravity wave immediately after the collapse of the dam.

The second dam-break case considered flow over a triangular obstacle placed in a laboratory flume (Soarez-Frazao, 2002). The experimental setup is shown in Figure 2.21 and consists of a relatively shallow column of water of 2.39 m of length and 0.11 m of depth at rest inside a closed rectangular channel 5.6 m long and 0.5 m wide. The center of the bump was located 2.06 m downstream of the column of water and its dimensions are 0.065 m high, 0.9 m long with side slopes of 0.014. Downstream of the bump, a shallow pool of 0.065 m was present. Due to the small width of the channel, the test case can be considered basically two-dimensional. This allows to highlight the differences between the 3-D and 2-D models (Figure 2.22), as in principle 2-D models applied to a 2-D problem should perform as well as 3-D models. The simulations were carried with a constant time step of 0.01 s and with a spatial resolution of 0.5 m. Figure 2.23 shows the evolution of the free-surface elevation near the bump at 1.8 s, 3 s, 3.7 s and 8.4 s after the start of the flow. As the wave propagates and hits the bump, it creates a backwater effect due to the reflection of the wave on the obstruction. At the first snapshot it is clear that the 2-D model is incapable of representing the front wave location. At 3 s after the dam break, the wave has

already overcome the bump and is traveling downstream of it. The 3-D model clearly captures the bore propagating downstream of the bump, which is in good agreement with experimental data, while no bore is present in the 2-D model results. This is an indication that the bore predicted in the 2-D model simulation is late compared to both experimental results and the 3-D model results. At 3.7 s after the dam break, the wave has hit the back wall and is travelling upstream toward the downstream face of the bump. The 3-D model is able to capture this behavior more accurately than the 2-D model, which shows a relatively flat free-surface elevation. At 8.4 s after the dam break, the wave has reflected twice on the back wall and has made its way through the obstruction. Clear differences can be observed between both models. In general, the 2-D model overpredicts the free-surface elevation upstream of the bump and underpredicts it downstream. The shape of the free-surface elevation in the 2-D simulation is essentially flat compared to the 3-D simulation, which represents better the phenomena.

The third and last test case corresponded to an experiment of a dam break flow over a 90° bend performed by Frazao and Zech (2002). A 2.4 m^2 reservoir was connected with a 0.495 m wide L-shaped rectangular channel of 4 m length directly downstream of the reservoir followed by a 3 m extension after the 90° bend (Figure 2.24). The reservoir is initially filled up to an elevation of 53 cm, which is 20 cm above the L-channel bottom elevation. The shape of the downstream region of the dam is of great importance since it may create an increase of water elevation upstream and even slow down the front propagating wave. The simulations were performed with a constant time step of 0.02 s with a spatial resolution of 0.01 m. Figure 2.25 shows the temporal evolution of the free-surface elevation along the outer wall of the channel at 3 s, 5 s, 7 s and 14 s after the dam break in the experiment and numerical simulations. Figure 2.26 shows a 3-D view of the temporal evolution of the free surface in the experiment until 14 s after the dam break occurred. As soon as the column of water collapses, it starts to move downstream until it hits the 90° bend. Then, the water reflects and there is a backwater wave propagating upstream of the

bend towards the reservoir. The 3-D model is able to predict with high accuracy the free-surface elevation at all times during the simulation with respect to experimental results. Significant differences between 3-D model and the 2-D model were observed between 3 s and 7 s after the dam break occurred. However, at 14 s after the dam break, the differences were small. Such conclusions are in agreement with those of Soarez et al. (2002), who attributed such differences to the underestimation of the bore level by the 2-D model. This caused the propagation of the bore in the 2-D simulation to be slower compared to that observed in the 3-D simulation.

Overall, these 3 cases showed the superiority of using a 3-D model for dam break cases, even for test cases that can be considered to be close to two-dimensional.

The Volume-of-Fluid method, just as the Level Set method, has been successfully applied to problems involving unsteady forcing at the boundaries. Zhang et al. (2013) applied a 2-D unsteady RANS code coupled with the Volume-of-Fluid method to study the effects of solitary and random waves passing through a vegetation patch. In addition, Shen et al. (2004) used a 2-D unsteady RANS code with VOF to simulate cnoidal wave propagation over a submerged bar. Both of these studies found that the VOF method was capable of producing accurate results even when highly unsteady boundary conditions were used.

2.5.3 Particle methods

The last main type of methods that can be used to simulate free-surface flows are called Particle Methods. Particle Methods simulate the flow as a set of discrete interacting particles. Each particle contains its own mass, energy, momentum, velocity and position. The main attractive feature of Particle Methods is that the free-surface is explicitly associated with the particles, thus there is no need for interface tracking or capturing. The most popular Particle Method is called Smoothed Particle Hydrodynamics or SPH (Floryan and Rasmussen, 1989). The main concern with SPH is the treatment of the viscous forces

since, at the present moment, there is no clear way to account for viscous effects. SPH has been applied to a wide array of applications ranging from astrophysics hydrodynamics (Lucy, 1977) to environmental hydrodynamic problems. SPH has been successfully applied for simulating wave action on water works, mainly for coastal work and design (Dalrymple and Rogers, 2006; Gomez-Gesteira et al., 2005), design of fish passage facilities for the hydropower industry (Ferrand et al., 2013), modeling of floating oil dispersion (Violeau et al., 2007; Yang and Liu, 2013) and dam spill way design (Rebollo et al., 2010). It has also been applied to dam break problems as described in the work of Kao and Chang (2012) and Prakash et al. (2014). Kao and Chang (2012) successfully solved the 2-D Shallow Water equations using SPH, while Prakash et al. (2014) focused on simulating realistic dam breaks with SPH in 3D. Since the focus of this thesis is not on Particle Methods, a detailed description will not be presented. More details on SPH and applications using SPH are given in the monography by Violeau (Fluid Mechanics and the SPH Method: Theory and Applications).

Figure 2.1 Plan view of the cross vane installed in a St. Anthony Falls Laboratory flume. Flow is from left to right. Reproduced from Kang et al. (2011).

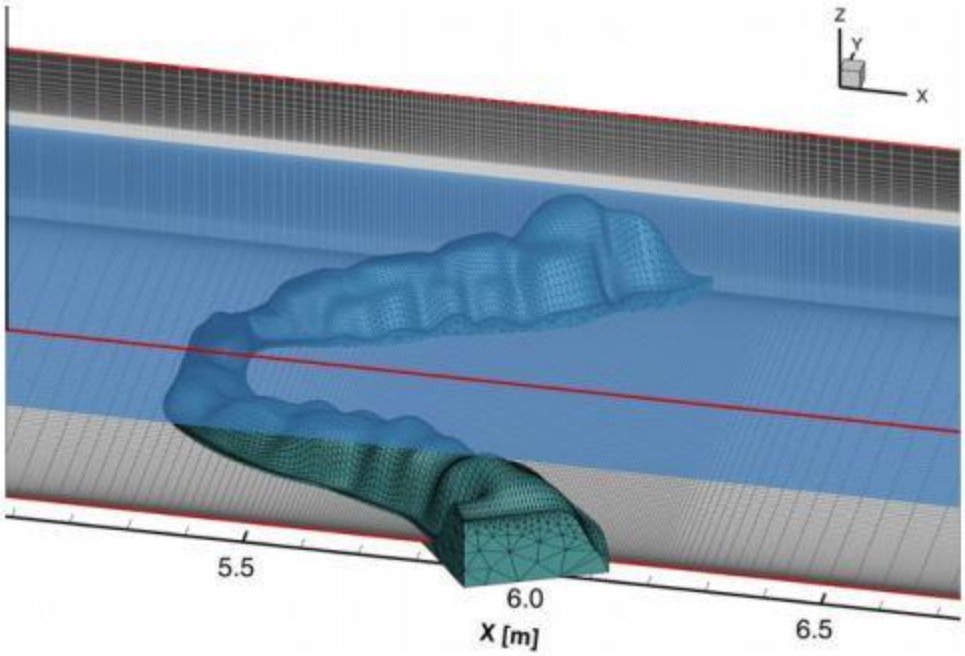

Figure 2.2 Computational grids near the cross vane and on the channel walls. Flow is from left to right. Reproduced from Kang et al. (2011).

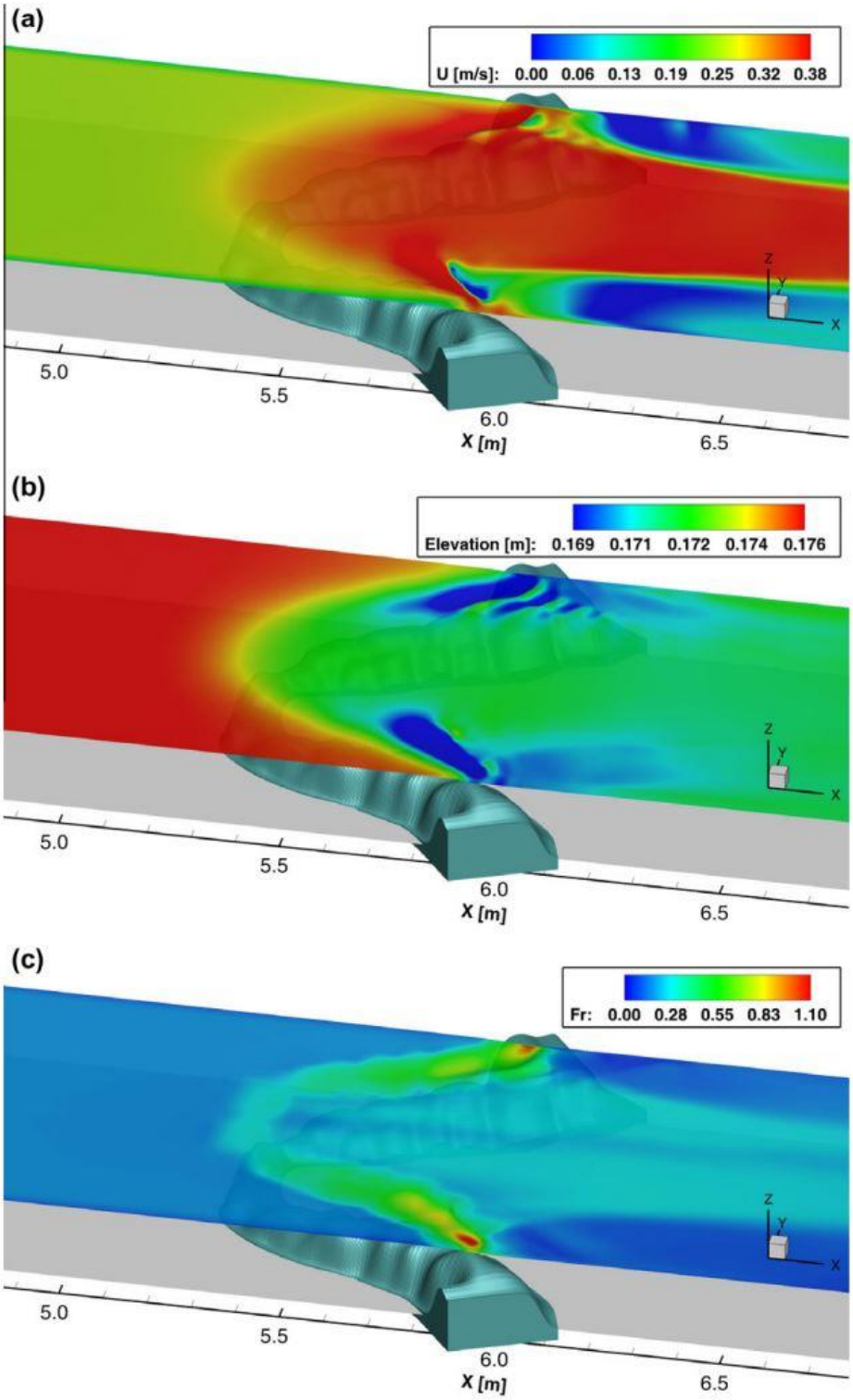

Figure 2.3 Contour plots of the computed (a) streamwise velocity; (b) free-surface elevation; and (c) local Froude number at the water surface ($\phi = 0$). Flow is from left to right. Reproduced from Kang et al. (2011).

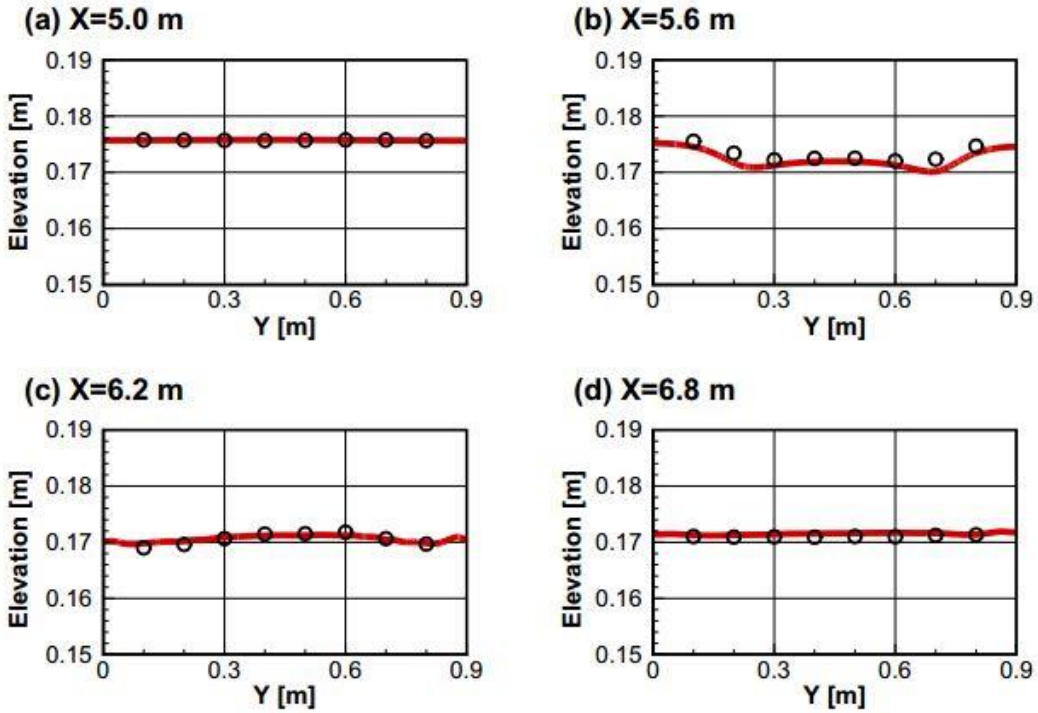

Figure 2.4 Comparison of the computed and measured transverse water surface profiles (solid line: computation, symbol: measurements). Reproduced from Kang et al. (2011).

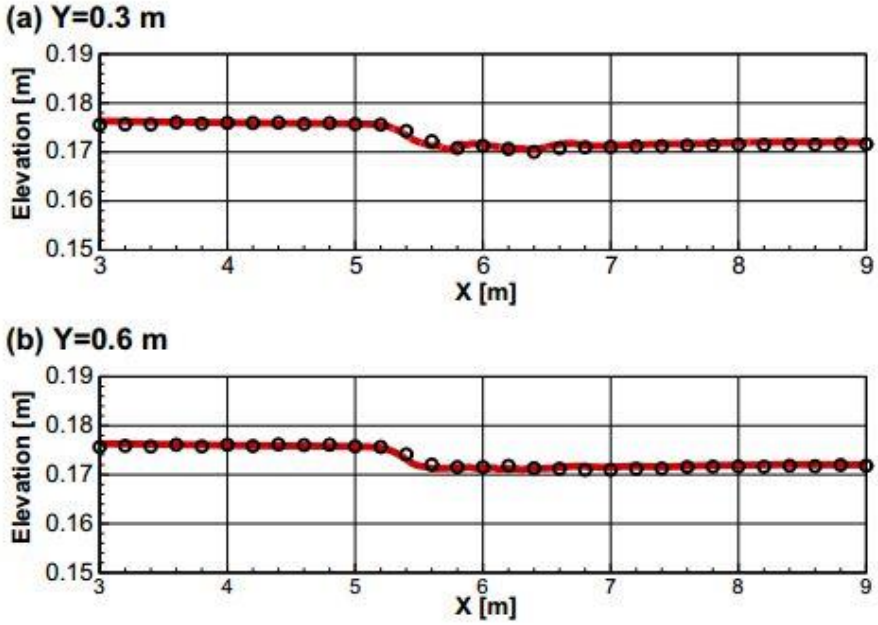

Figure 2.5 Comparison of the computed and measured streamwise water surface profiles (solid line: computation, symbol: measurements). Reproduced from Kang et al. (2011).

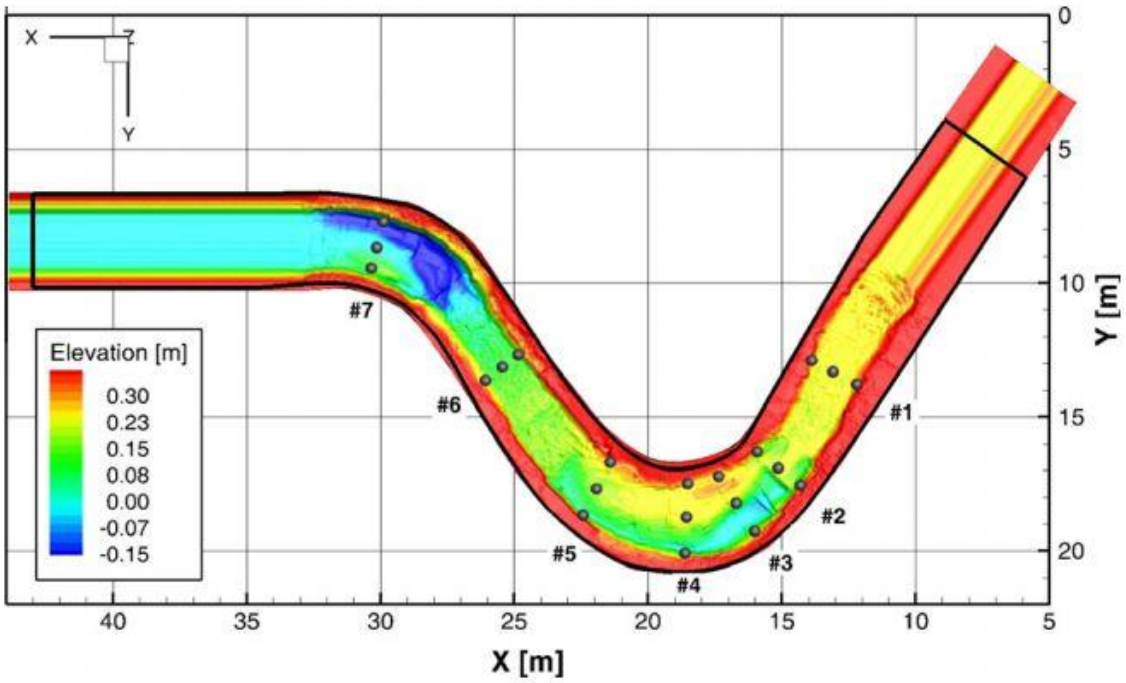

Figure 2.6 Plan view of the computational domain used in the simulation of flow in a meandering stream performed by Kang et al. (2011). Solid lines denote the boundaries of the background grid, contour plots show the immersed body reconstructed from the measured bathymetry, and symbols show the water surface measurement locations. Flow direction is from right to left. Reproduced from Kang et al. (2011).

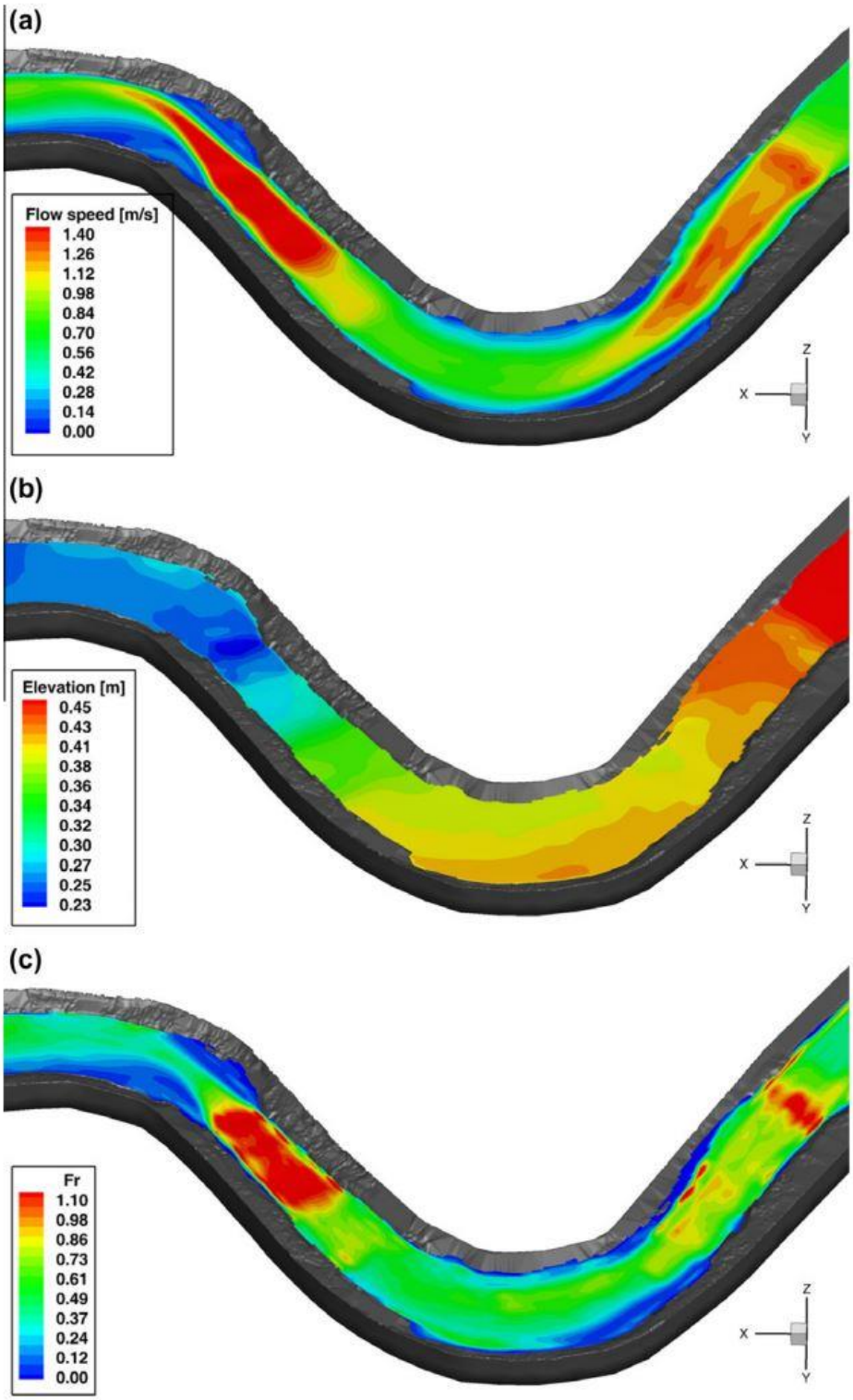

Figure 2.7 Contour plots of the computed (a) flow speed; (b) free-surface elevation; and (c) local Froude number at the water surface (ϕ=0) based on the simulation of flow in a meandering stream performed by Kang et al. (2011). Flow direction is from right to left. Reproduced from Kang et al. (2011).

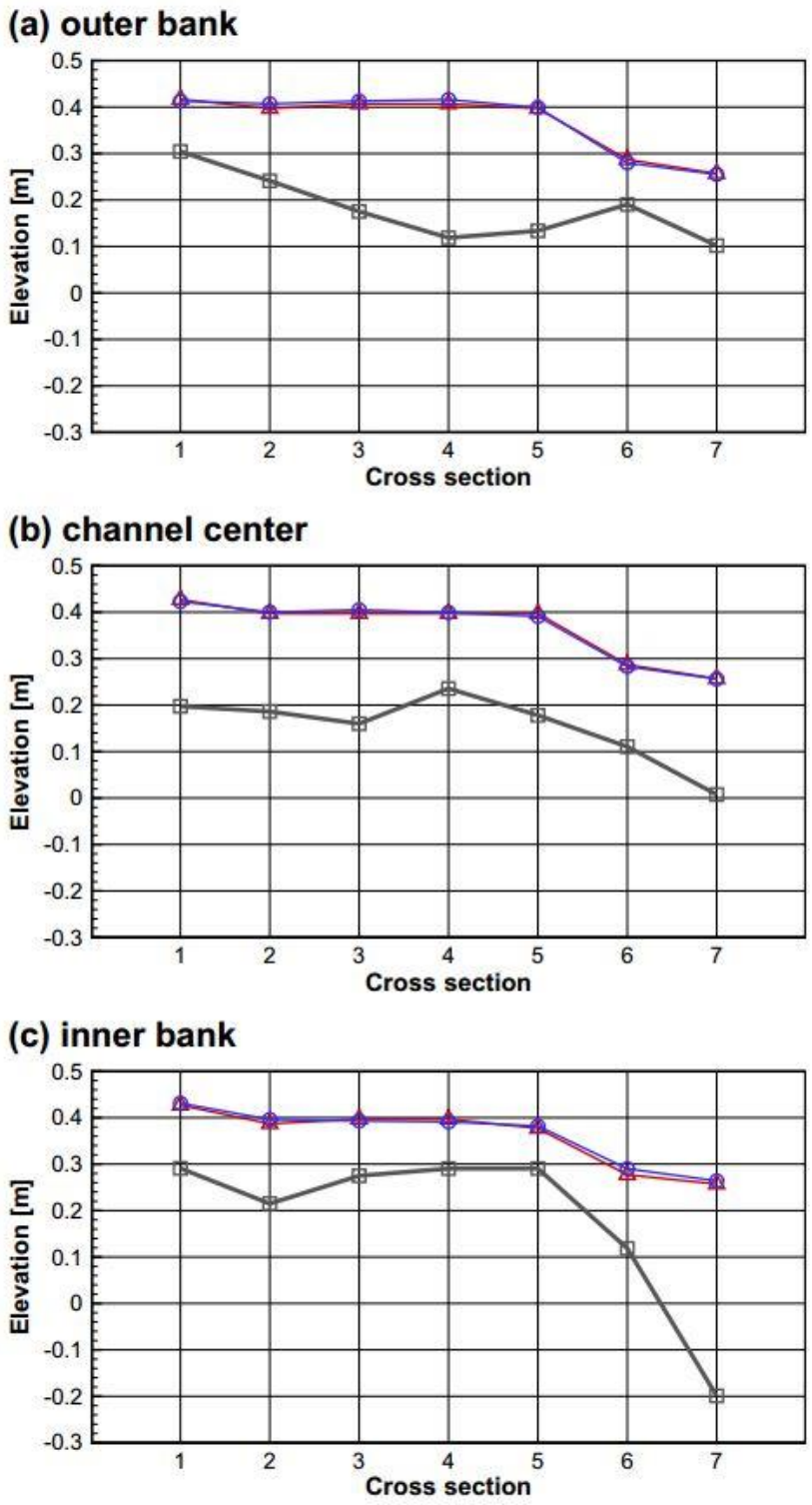

Figure 2.8 Comparison of the computed (blue line with circle) and measured (red line with triangles) free-surface elevation at several cross sections (gray line with square; bed elevation). The locations of the cross sections are shown in Figure 2.6. Reproduced from Kang et al. (2011).

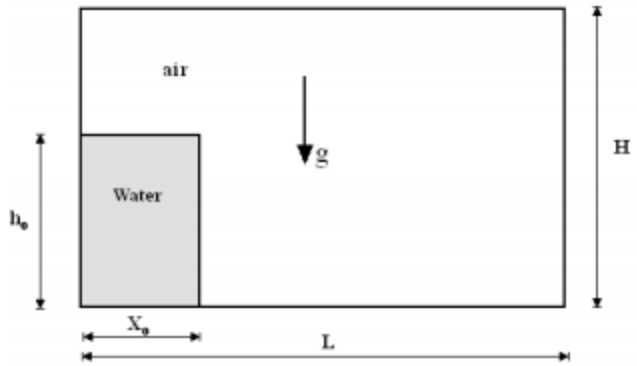

Figure 2.9 Computational domain of the dam break problem. H is the total domain height, L is the total length of the domain, ho is initial water column height, xo is initial water column length and g is the gravity acceleration. Reproduced from Balabel (2015).

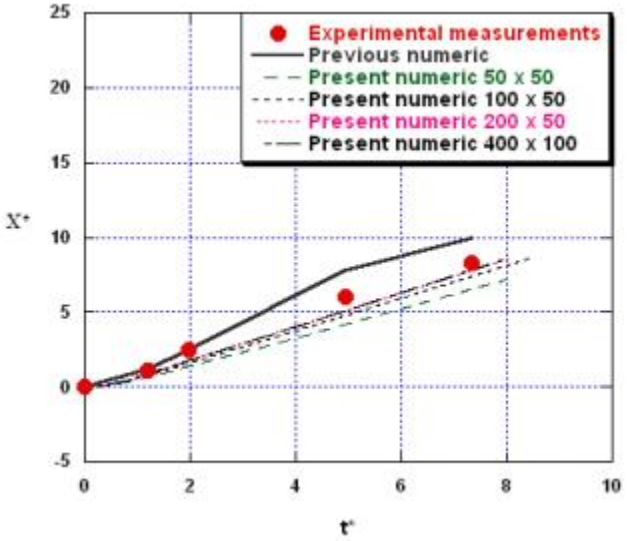

Figure 2.10 Comparison of the numerical predictions of the dimensionless horizontal displacement caused by the dam break with data from experimental measurements (Stanby et al., 1988) and previous numerical results (Shigematsu et al., 2004). Reproduced from Balabel (2015).

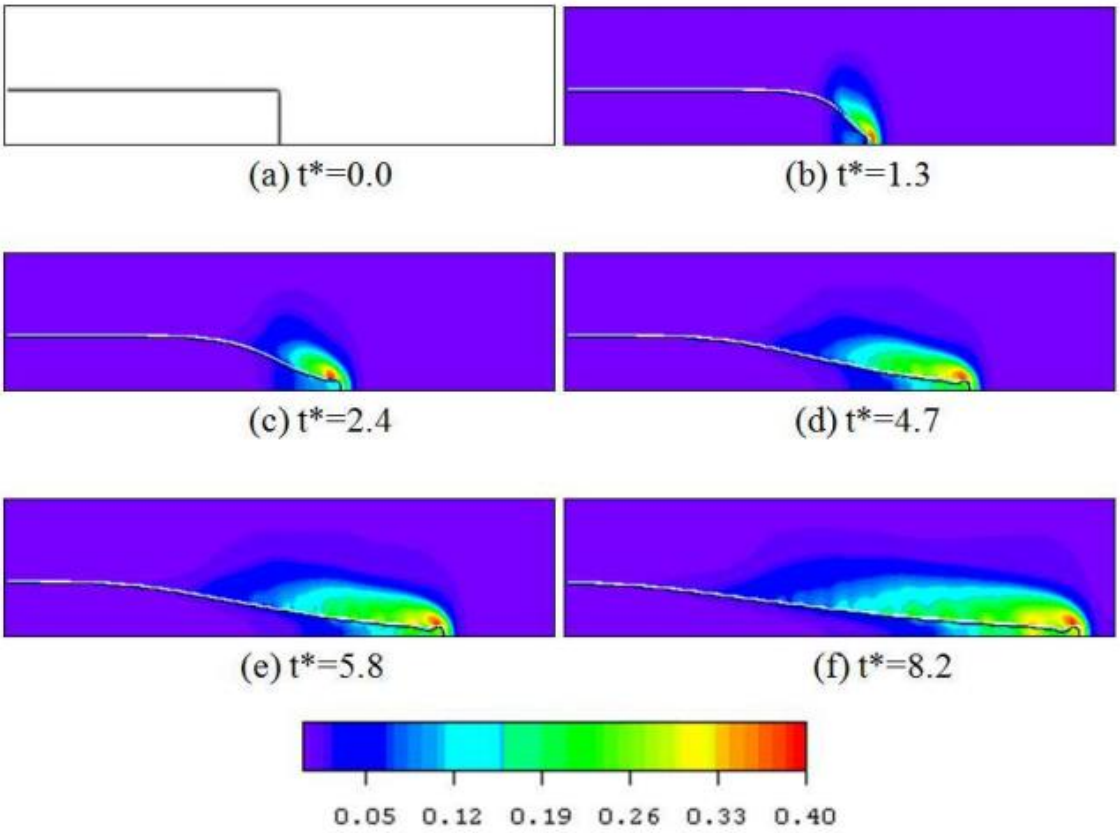

Figure 2.11 Transient free surface of the dam break along with the predicted turbulent kinetic energy at different dimensionless times. Reproduced from Balabel (2015).

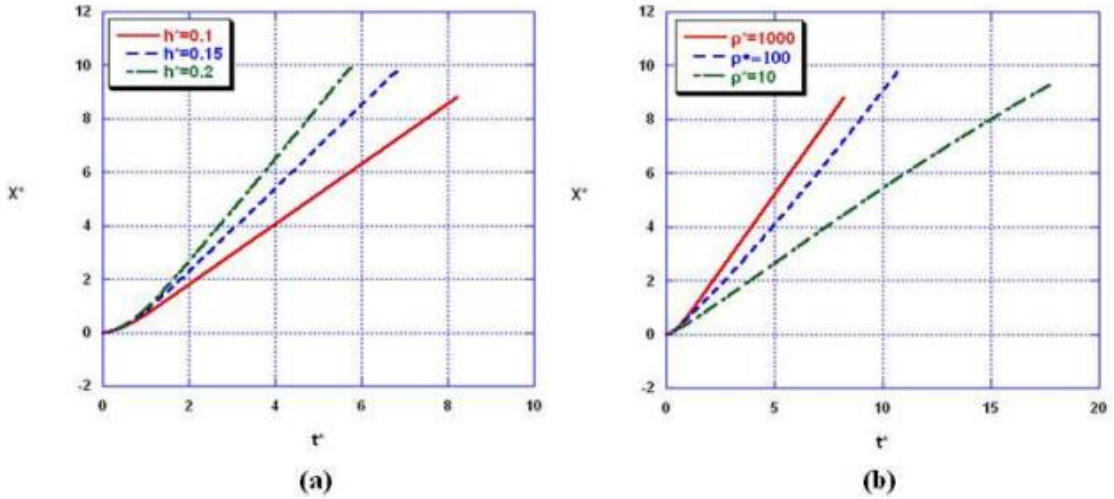

Figure 2.12 The effect of dam height (a) and density ratio (b) on the downstream movement of dam front. Reproduced from Balabel (2015).

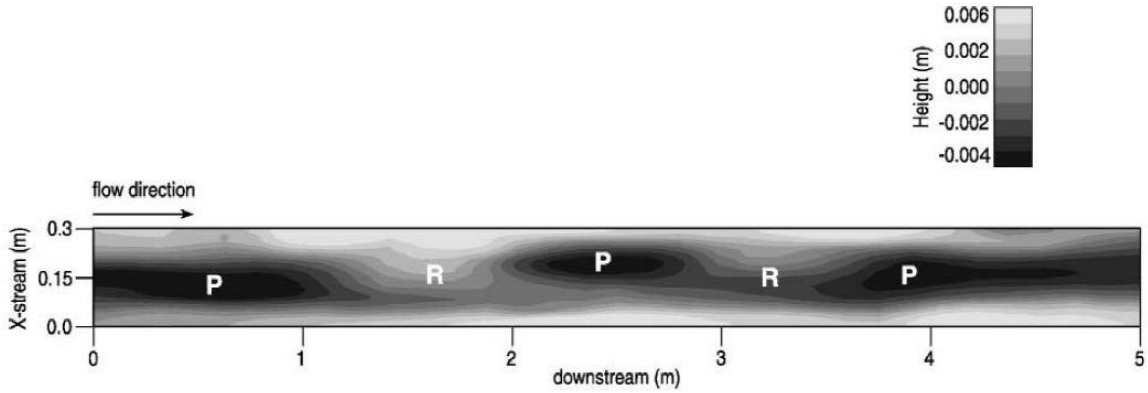

Figure 2.13 Flume bed topography produced of the Todmorten study reach scaled by 1:35 used in the simulation performed by Ma et al. (2002). Note the limited range in bed topography but also the clear demarcation of shallow pool (P) and riffle (R) sites. Reproduced from Ma et al. (2002).

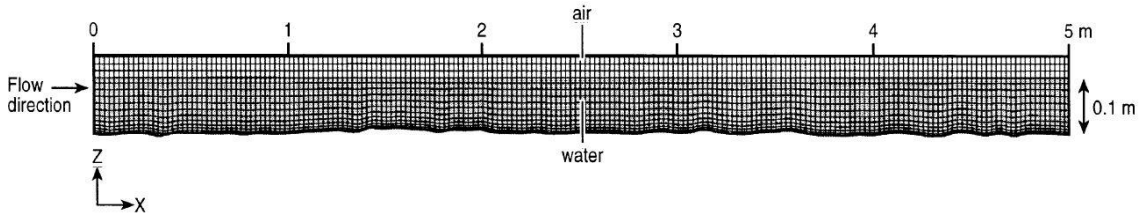

Figure 2.14 Computational grid employed by CFD model (202 x 22 x 16 including boundary cells) in the simulation of flow in the Todmorten study reach. Reproduced from Ma et al. (2002).

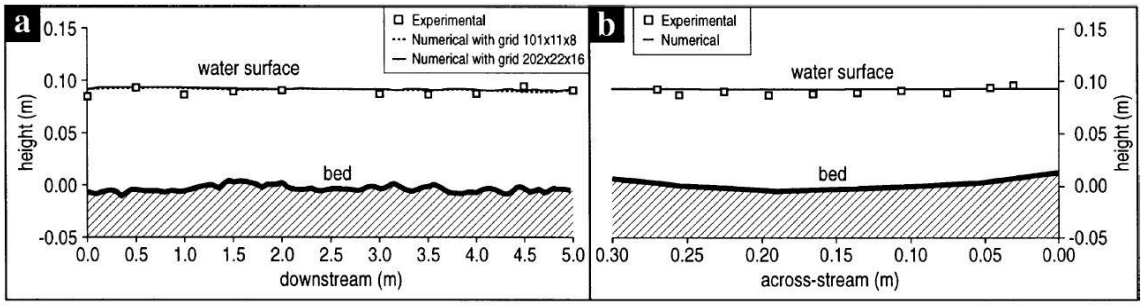

Figure 2.15 Position of the water surface measured in the 1:35 flume model and produced by the numerical model used by Ma et al. (2002) to simulate flow in the Todmorten study reach. (a) View downstream along the centerline of the channel and using 2 different grid sizes in the numerical model; and (b) view across the channel at a location halfway down the 5 m long model with the 202 x 22 x 16 grid only. Reproduced from Ma et al. (2002).

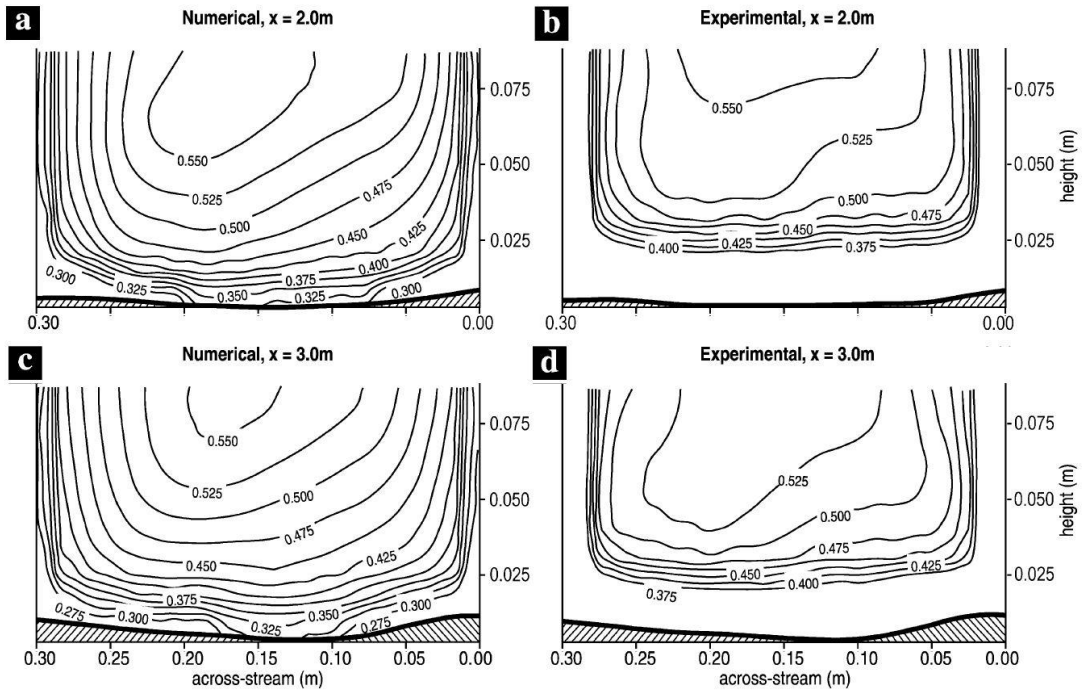

Figure 2.16 Streamwise isovels for two locations in the 5 m long flume and numerical model from the simulation of the Todmorten study reach reported by Ma et al. (2002). Isovels are shown for 0.025 m/s intervals. The view shown is looking downstream at the sections. The downstream positions of 2 m (a-b) and 3 m (c-d) correspond to a pool head and riffle respectively (Figure 2.13). Reproduced from Ma et al. (2002).

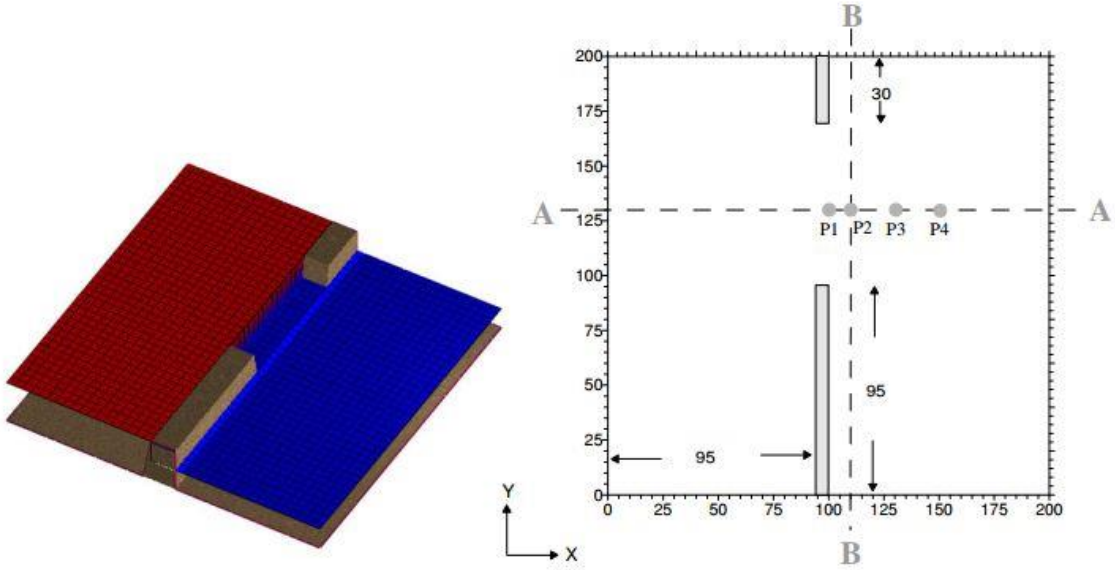

Figure 2.17 Plan view (dimensions in m) – Geometric schematization of dam break over flat bed without friction for the dam break test case calculated by Biscarini et al. (2010). In plan, Sections A-A, B-B, P1(100,130), P2(110,130), P3(130,130), P4(150,130) are shown. Reproduced from Biscarini et al. (2010).

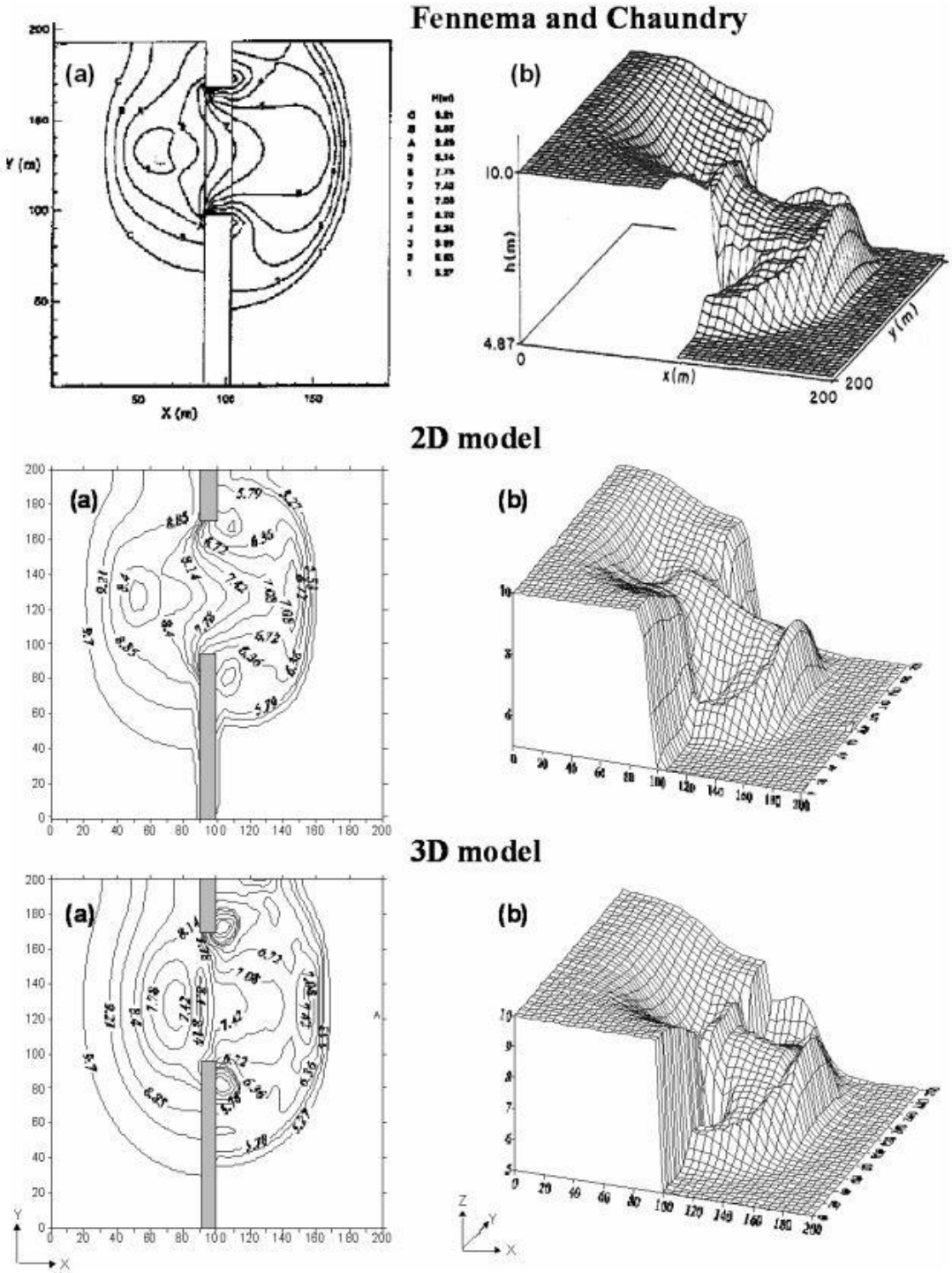

Figure 2.18 Comparison between the 2D model proposed by Fennema and Chaundry (1990), shallow water (CCHE2-D) and full Navier Stokes simulation performed by Biscarini et al (2010): (a) Contour levels at 5.2m, 5.7 m, 6.2 m, 6.7 m, 7.2 m, 7.8 m, 8.2 m, 8.7 m and 9.2 m; (b)Water surface wireframe (three-dimensional view) after 7.2 s from failure. Reproduced from Biscarini et al. (2010).

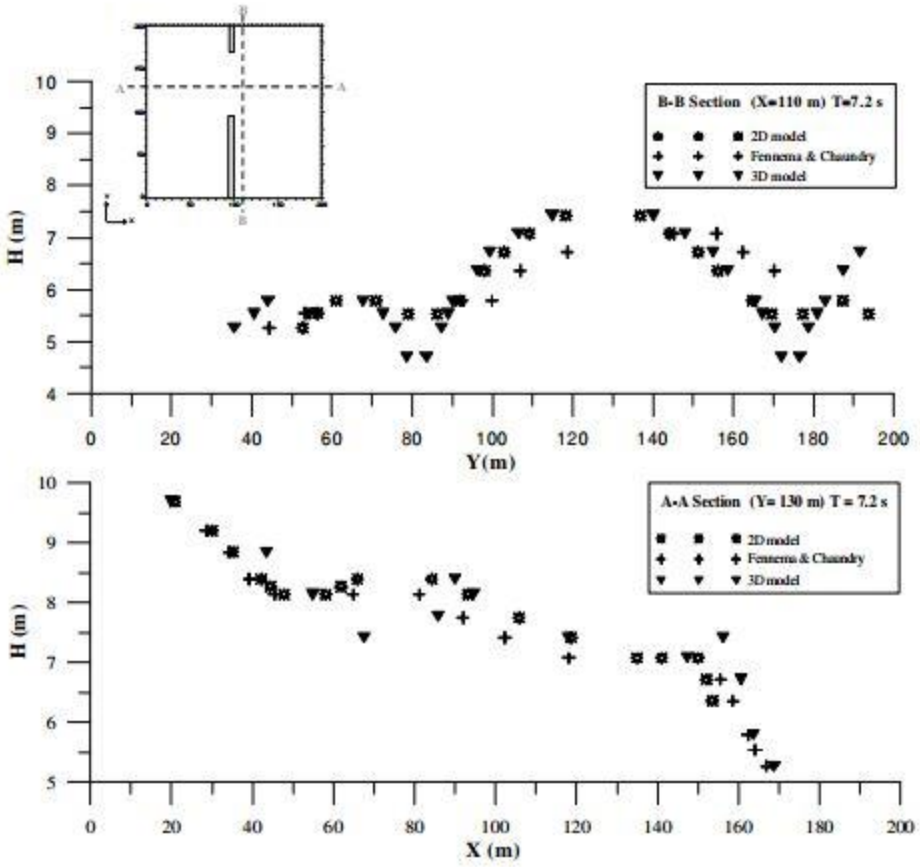

Figure 2.19 Comparison of water depth at 7.2 s after the gate collapse between the 2D results from Fennema and Chaundry (1990), 2D model (CCHE2-D) and the 3D simulation performed by Biscarini et al. (2010): Results shown for sections A-A and B-B . Reproduced from Biscarini et al. (2010).

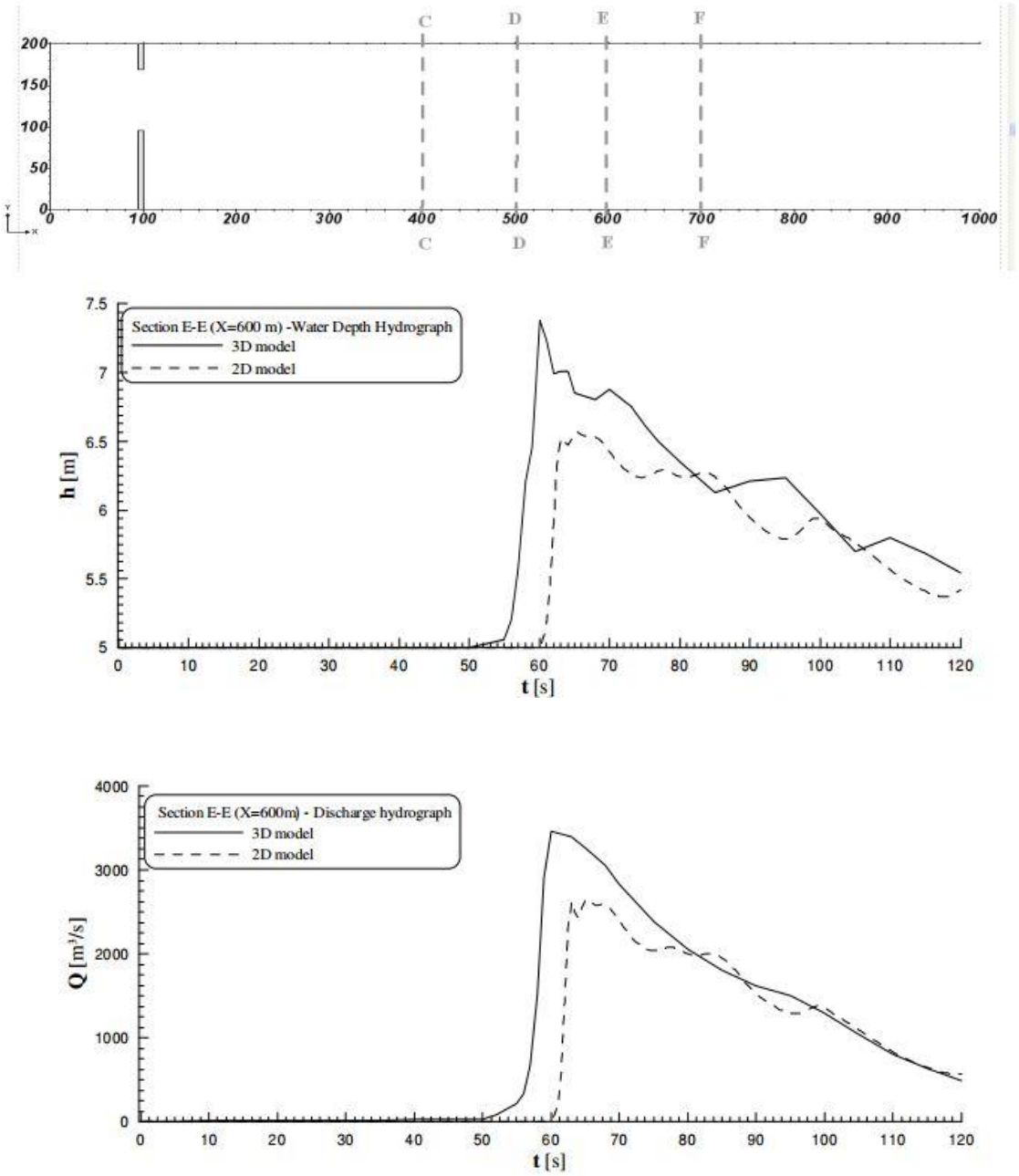

Figure 2.20 Water depth hydrograph and Discharge hydrograph at section E-E (x=600) in the dam break simulation of Biscarini et al. (2010) and the 2-D CCHE-D simulation. Reproduced from Biscarini et al. (2010).

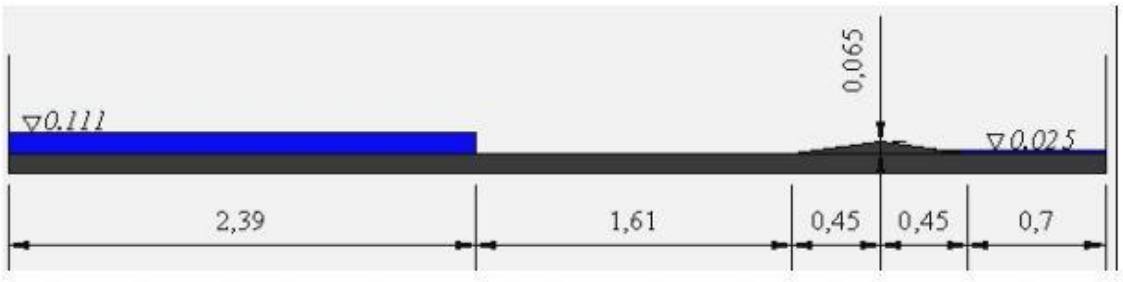

Figure 2.21 Experimental set-up and initial conditions in the lab experiment and numerical simulations of dam break flow advancing over a triangular obstacle considered in the 3-D numerical study of Biscarini et al. (2010). All dimensions in (m). Reproduced from Biscarini et al. (2010).

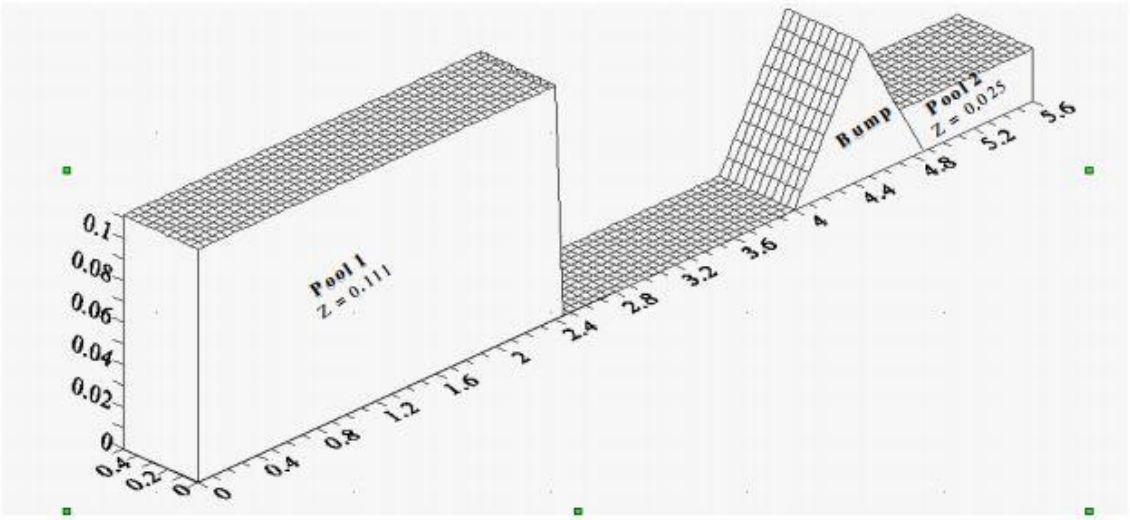

Figure 2.22 3-D isometric view and initial conditions for the bump test case (Soarez et al., 2002). Reproduced from Biscarini et al. (2010).

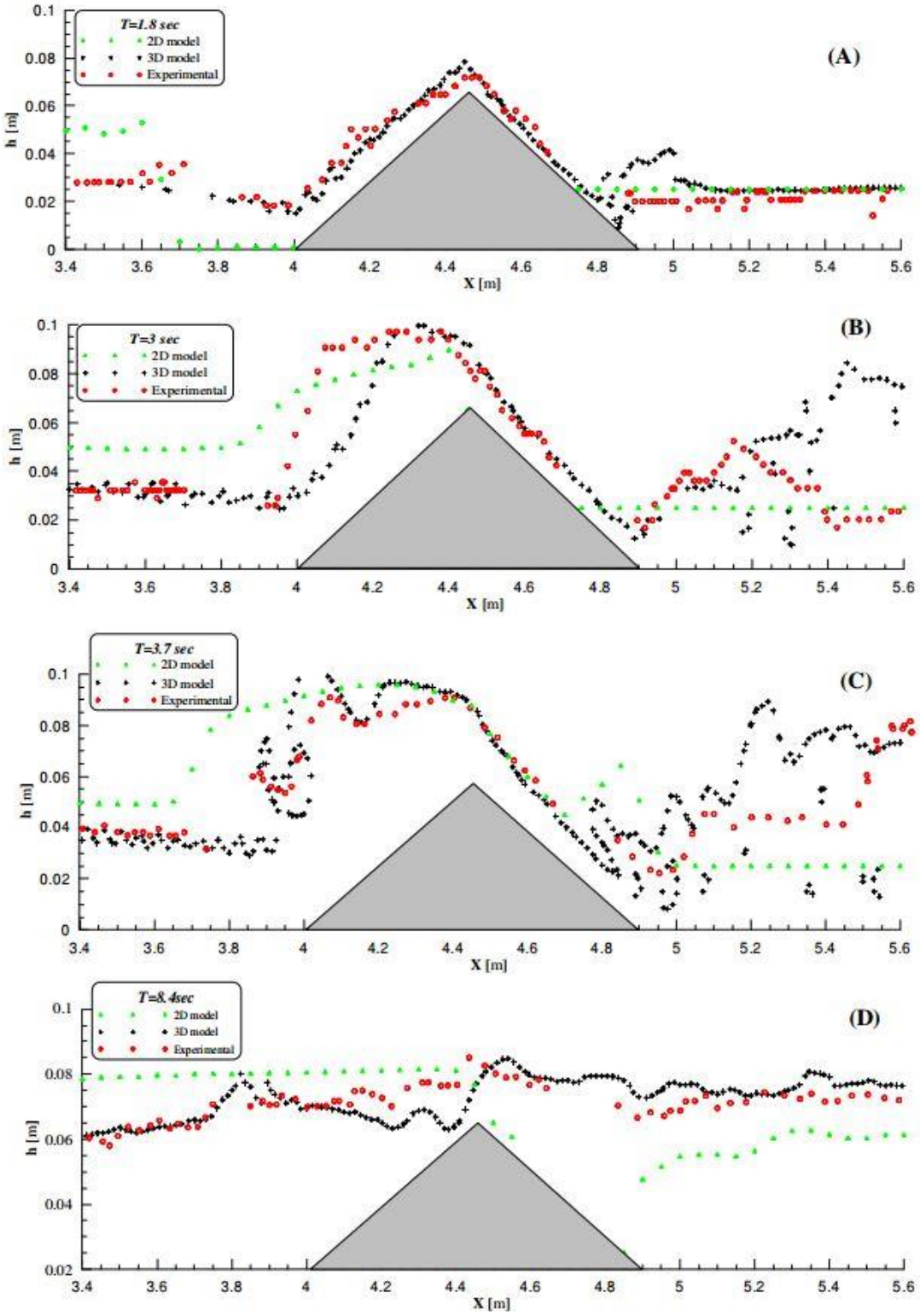

Figure 2.23 Water surface profile comparison between models and experimental results at (a) T=1.8 s, (b) T = 3 s, (c) T =3.7 s and (d) T = 8.4 s after the start of the flow in the dam break case studied by Biscarini et al. (2010). Reproduced from Biscarini et al. (2010).

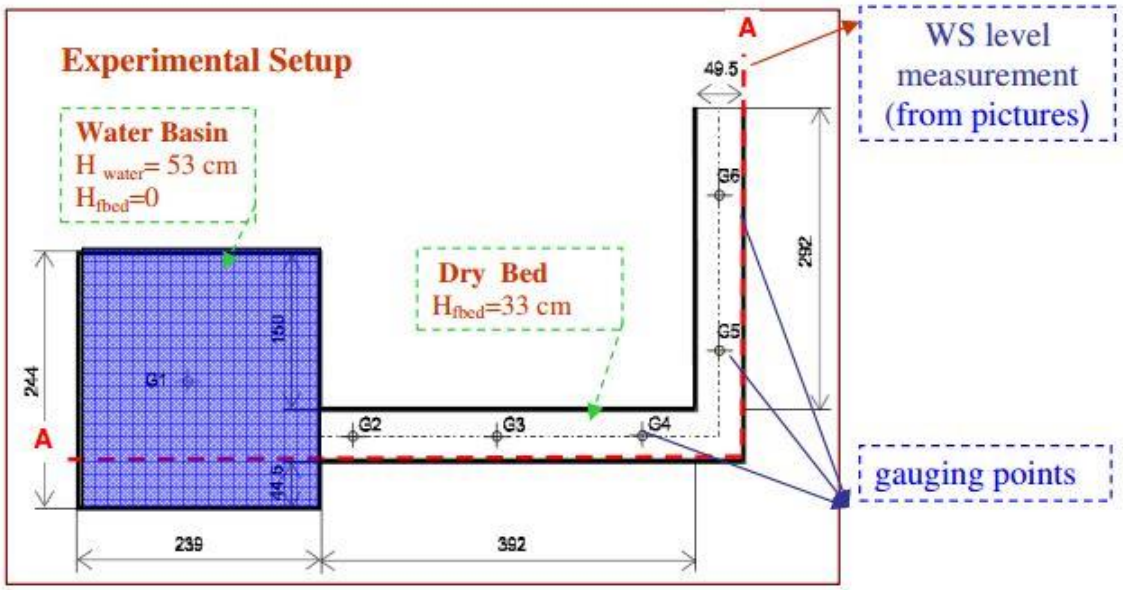

Figure 2.24 Experimental set-up and initial conditions for the dam break flood wave propagating in the 90○ bend test case considered by Biscarini et al. (2010). All dimensions in cm. The gauging points are denoted G1, G2, G3, G4, G5 and G6 (Soarez et al., 2002). Reproduced from Biscarini et al. (2010).

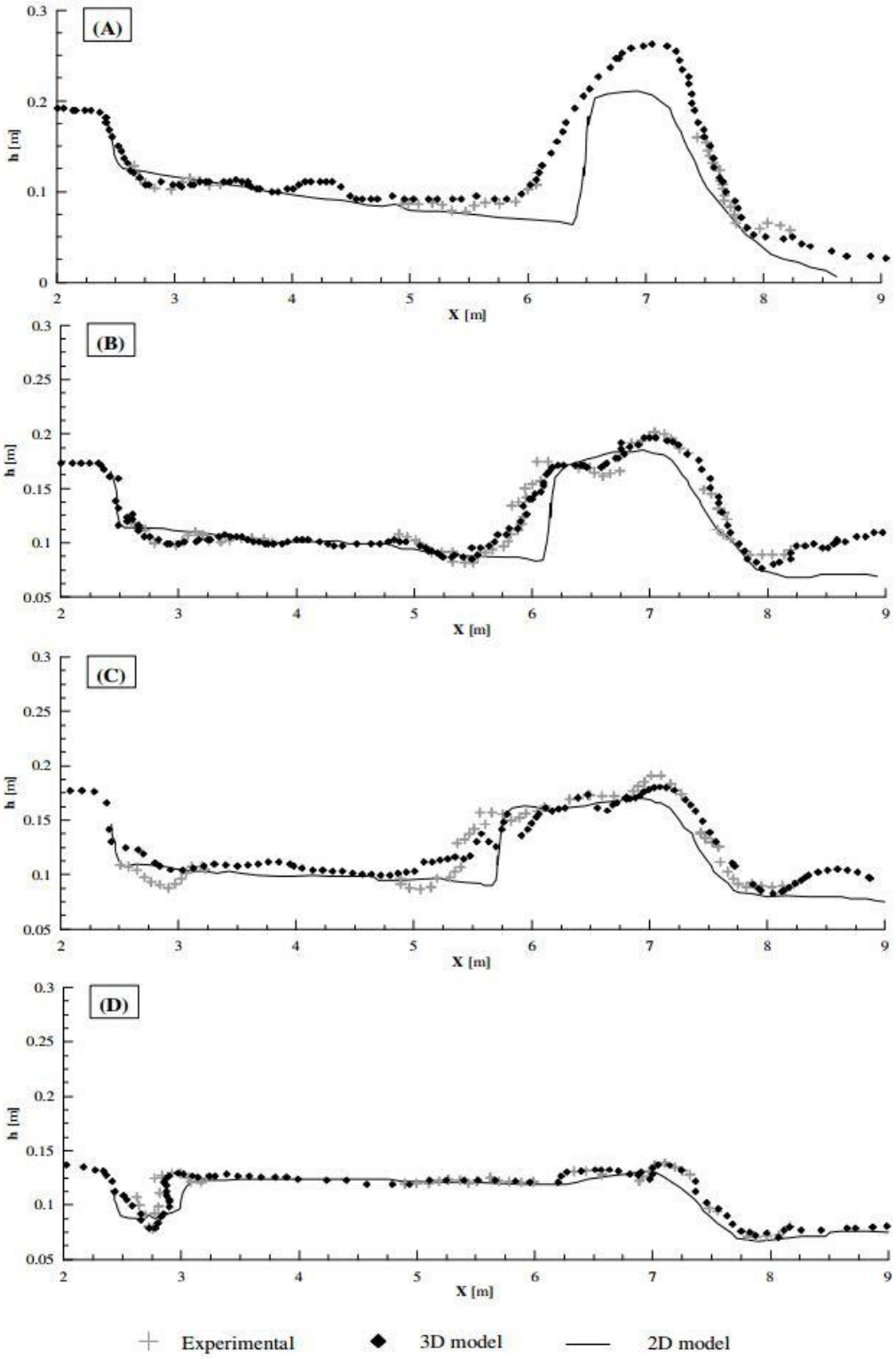

Figure 2.25 Comparison between computed and experimental free-surface profiles along section A-A (outer bank) for the dam break test case studied numerically by Biscarini et al. (2010). Results are compared in the 4 frames at different times after failure (a) T = 3 s, (b) T = 5 s, (c) T = 7 s and (d) T = 14 s. Reproduced from Biscarini et al. (2010).

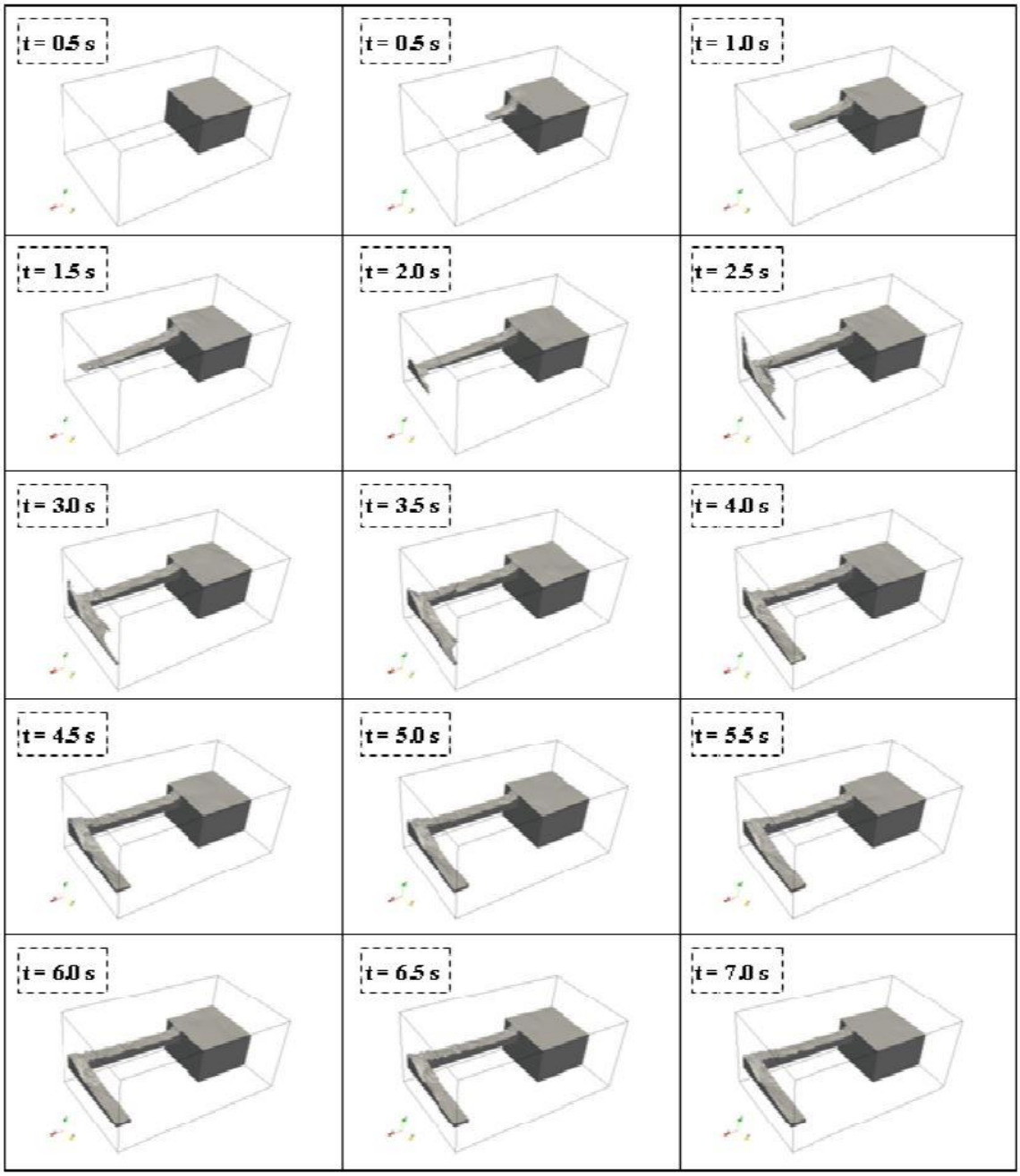

Figure 2.26 Temporal evolution of the flood wave propagation in a 90○ bend test case proposed by Biscarini et al. (2010). Visualization is based on the results obtained with the 3-D model used by Biscarini et al. (2010). Reproduced from Biscarini et al. (2010).

CHAPTER 3 NUMERICAL MODEL AND VALIDATION

3.1 Introduction

Flow in natural environments is almost always turbulent making turbulence modelling capabilities crucial for accurately representing the flow physics. The most common approach of modelling turbulence is to use the Reynolds Averaged-Navier Stokes (RANS) Equations. RANS is capable of capturing the mean effect of turbulence on the flow via the use of a turbulence model, and it is capable of simulating both steady and unsteady flows. The main disadvantage of RANS is that it cannot resolve all the energetically important eddies. By contrast, an eddy resolving-modelling technique is capable of capturing most of the energy-containing eddies in the flow. Among the eddy-resolving techniques, Large Eddy Simulation (LES) is the most common approach. LES resolve the most energetic eddies up to a certain size (cut off wavelength) and only models the combined effect of the smaller (least energetic) unresolved eddies on the resolved flow. Another example of a popular eddy-resolving technique is a hybrid RANS-LES approach called Detached Eddy Simulation (DES). DES reduced to an unsteady RANS near wall boundaries and to LES in the rest of the computational domain. Not having to resolve the near-wall coherent structures (wall streaks) reduces the computational cost of DES compared to well-resolved LES (no wall functions). Given the current computational power, LES is not feasible for modelling flow in river reaches of lengths in the order of 10-20 km over time periods of the order of hours to days. This is why, time-accurate RANS (URANS) is employed in the present study.

The time accurate RANS simulations of the riverine flooding in the present study were performed using STAR-CCM+, a state-of-the-art commercial CFD code developed by CD-Adapco. The main features of STAR-CCM+ include the ability to perform RANS, LES, DES simulations using a variety of advanced turbulence models and sub-grid scale models. Some examples of RANS turbulence models included in STAR-CCM+ are $k-\varepsilon$

, $k-\varpi$ and Spalart-Allmaras ($S-A$). The constant coefficient Smagorinski subgrid-scale model, the Dynamic Smagorinski model or the WALE model can be used for LES computations.

STAR-CCM+ contains a very powerful meshing capability in which an initial geometry can be imported, smoothed in such a way to improve computational efficiency and to obtain better results without loss of information. Once the geometry has been processed, a volume mesh is created with the desired meshing model in order to obtain a mesh which is acceptable to STAR-CCM+ requirements. Mesh topologies and mesh generation techniques include tetrahedral, hexahedral and polyhedral models with mesh refinement near boundaries. Additional refinement can be included near boundaries by producing high-aspect ratio, highly skewed cells named prism layers.

Multiple-phase flows can be simulated in STAR-CCM+ via three types of models: the Volume-of-Fluid method, the Multiphase segregated flow module and the Eularian Multiphase mixture model. The Volume of Fluid (VOF) method assumes that the phases are immiscible and the computational grid is capable of resolving the interfaces. In such cases, additional inter-phase interaction is not needed and single pressure and velocity fields can represent both phases. The multiphase segregated flow the phases need not to be immiscible or in thermodynamic equilibrium and each phase has its own pressure, velocity and temperature field. A phase interaction model is needed at each interface for the conservation equations to be closed. Finally in the Eularian Multiphase mixture model the multiphase mixture is treated as a single phase system (thermodynamic equilibrium), therefore having a single set of momentum, energy and mass conservation equations. The Eularian multiphase mixture is usually applied to solid suspension in liquids or for spray molecules dispersion. In the present work we deal only with constant temperature incompressible flows. The fastest and most robust approach for such computations is VOF.

Based on the available modules and the requirements related to the type of simulations considered in the present study, fully 3D unsteady RANS simulations were

performed using the realizable two-layer $k-\varepsilon$ model with deformable free-surface capabilities via the VOF method.

3.2 3D Unsteady RANS hydrodynamic model

The URANS equations are obtained by time-filtering (time-averaging over a time interval that is larger than the time scale of most of the turbulent eddies) the Navier-Stokes equations. This approach is highly attractive when dealing with riverine flooding given their highly unsteady nature. At the same time, capturing the eddy content of the flow is not needed for engineering applications, thus a state-of-the-art RANS model is a good option. Equation 3.1 shows the Continuity equation, which represents the mass conservation of the system, while equation 3.2 shows the conservation of momentum equations. The mean effect of turbulence on the flow is accounted for in the governing equations by including an additional viscous term that is proportional to the eddy viscosity provided by the RANS model.

$$\frac{\partial U_i}{\partial x_i} = 0 \tag{3.1}$$

$$\frac{\partial U_i}{\partial t} + \frac{\partial (U_i U_k)}{\partial x_k} = -\frac{1}{\rho}\frac{\partial P}{\partial x_i} + \frac{1}{\rho}\frac{\partial}{\partial x_k}\left[(\mu + \mu_t)\left(\frac{\partial U_i}{\partial x_k} + \frac{\partial U_k}{\partial x_i}\right)\right] - g\hat{k} \tag{3.2}$$

where U_i is the Reynolds Averaged velocity component along the i direction based on the original velocity component u_i, ρ is the density of the fluid, μ is the molecular dynamic viscosity, μ_t is the eddy viscosity predicted by the RANS model, P is the pressure, g is the gravity and $\hat{k}$ is the unit normal vector along the vertical direction.

The finite-volume solver solves the governing equations integrated over elementary control volumes. The advective terms are discretised using a second-order accurate in space upwinding scheme, while the transient (unsteady) term was second-order accurate in time based on an implicit representation. The diffusive term is discretised using a second-order central difference scheme. The pressure gradient term is discretised using a second order

accurate central difference scheme. The Pressure-coupling algorithm chosen was the SIMPLE algorithm. In the SIMPLE algorithm, an intermediate velocity is obtained by solving the momentum equations without the pressure gradient term which does not satisfy the continuity or mass conservation equation. A pressure correction algorithm is employed to modify the pressure field and in turn modify the mass fluxes and velocity fields in order for the corrected velocity field to satisfy mass conservation.

3.2.1 RANS $k-\varepsilon$ turbulence model

The $k-\varepsilon$ turbulence model is based on solving transport equations for the turbulent kinetic energy (k) and the turbulent dissipation rate (ε). Different versions of the $k-\varepsilon$ model are available. The most popular are the standard $k-\varepsilon$, realizable $k-\varepsilon$, two-layer $k-\varepsilon$, and many more. For the present study the realizable two layer $k-\varepsilon$ approach was chosen as this is the recommended model for the coupling of RANS with the Volume-of-Fluid method in STAR-CCM+. As its name suggests, the realizable two-layer $k-\varepsilon$ model combines both the realizable and the two-layer models; therefore both models will be briefly explained next.

3.2.1.1 Realizable $k-\varepsilon$ turbulence model

The Realizable $k-\varepsilon$ turbulence model solves the same equation for the turbulent kinetic energy (k) as the standard $k-\varepsilon$ model but solves a slightly modified equation for the turbulent dissipation rate (ε). In addition, the C_μ coefficient (shown below) is not assumed to be constant. Rather, it is a function of the mean flow and turbulence properties. This allows the realizable $k-\varepsilon$ model to satisfy certain mathematical constraints in the normal stresses which are consistent with the physics of turbulence (e.g., for boundary layer flows). The realizable $k-\varepsilon$ model provides as good as, or better, results in many applications compared to the standard $k-\varepsilon$ model. Equations 3.3 and 3.4 show the transport equations for the turbulent kinetic energy, k, and the turbulent dissipation rate, ε, respectively.

$$\frac{\partial \rho k}{\partial t}+\frac{\partial (\rho k U_j)}{\partial x_j}=\frac{\partial}{\partial x_j}\left[\left(\mu+\frac{\mu_t}{\sigma_k}\right)\frac{\partial k}{\partial x_j}\right]+f_c G_k+G_b-\rho\left(\left(\varepsilon-\varepsilon_0\right)+Y_M\right)+S_k \tag{3.3}$$

$$\frac{\partial \rho \varepsilon}{\partial t}+\frac{\partial (\rho \varepsilon U_j)}{\partial x_j}=\frac{\partial}{\partial x_j}\left[\left(\mu+\frac{\mu_t}{\sigma_\varepsilon}\right)\frac{\partial \varepsilon}{\partial x_j}\right]+ f_c C_{\varepsilon 1} S_\varepsilon+\frac{\varepsilon}{k}\left(C_{\varepsilon 1} C_{\varepsilon 3} G_b\right)-\frac{\varepsilon}{k+\sqrt{\nu\varepsilon}} C_{\varepsilon 2}\rho\left(\varepsilon-\varepsilon_0\right)+S_\varepsilon \tag{3.4}$$

where S_k and S_ε are user-specified source terms, ε_0 is the ambient turbulence value in the source terms and f_c is a curvature correction factor. G_k is the production of turbulent kinetic energy due to velocity gradients; its definition is given below.

$$G_k=\mu_t S^2-\frac{2}{3}\rho k\left(\nabla\cdot\vec{U}\right)-\frac{2}{3}\mu_t\left(\nabla\cdot\vec{U}\right)^2 \tag{3.5}$$

where S is the modulus of the mean strain rate tensor $\mathbf{S}$ defined as follows:

$$S=\left|\mathbf{S}\right|=\sqrt{2\mathbf{S}:\mathbf{S}} \tag{3.6}$$

$$\mathbf{S}=\frac{1}{2}\left(\nabla^2\vec{U}+\nabla^2\vec{U}^T\right) \tag{3.7}$$

G_b is the production of turbulent kinetic energy due to buoyancy effects and it is defined as follows:

$$G_b=\beta\frac{\mu_t}{\sigma_t}\left(\nabla^2 T\cdot\vec{g}\right) \tag{3.8}$$

where T is the temperature field, σ_t is the turbulent Prandtl number and $\vec{g}$ is the gravitational acceleration vector.

Y_M is the dilation dissipation to account for possible compressibility effects and it is defined as:

$$Y_M=\frac{C_M k\varepsilon}{c} \tag{3.9}$$

where C_M is equal to 2 and c is the speed of sound.

The relationship between k, ε and the turbulent viscosity, μ_t, is as follows:

$$\mu_t = \rho C_\mu \frac{k^2}{\varepsilon} \tag{3.10}$$

As explained previously the coefficient C_μ is no longer a constant and it computed based on the mean flow field and turbulent quantities. Therefore C_μ is computed as

$$C_\mu = \frac{1}{A_0 + A_s U^{(*)} \frac{k}{\varepsilon}} \tag{3.11}$$

where $U^{(*)} = \sqrt{\mathbf{S}:\mathbf{S} - \mathbf{W}:\mathbf{W}}$, $\mathbf{W}$ is the vorticity tensor and is defined as $\mathbf{W} = \frac{1}{2}\left(\nabla^2 \vec{U} - \nabla^2 \vec{U}^T\right)$. In addition A_0 and A_s are computed in the following way:

$$W = \frac{S_{ij} S_{jk} S_{ki}}{\left(S_{ij} S_{ij}\right)^{3/2}} \tag{3.12}$$

$$\phi = \frac{1}{3}\arccos\left(\sqrt{6} W\right) \tag{3.13}$$

$$A_s = \sqrt{6}\cos(\phi) \tag{3.14}$$

$$A_0 = 4.0 \tag{3.15}$$

Finally, the realizable $k-\varepsilon$ model constants are defined as $C_{\varepsilon 1} = \max\left(0.43, \frac{\eta}{5+\eta}\right)$ where $\eta = \frac{Sk}{\varepsilon}$, $C_{\varepsilon 2} = 1.9$, $C_{\varepsilon 3} = \tanh\frac{|\vec{v}_b|}{|\vec{u}_b|}$, where $\vec{v}_b$ is the velocity component parallel to the gravitational acceleration and $\vec{u}_b$ is the velocity component perpendicular to the gravitational acceleration, $\sigma_k = 1.0$ and $\sigma_\varepsilon = 1.2$.

The k and ε equations are discretised using a finite volume representation with first order upwind scheme for the convective terms. The temporal discretization is consistent with that of the RANS equations and so it is second order accurate in time. For the incompressible flow simulations discussed in the present study the density and temperature fields were constant, so the governing equations are simpler.

3.2.1.2 Two-layer approach for the $k-\varepsilon$ turbulence model

The two-layer approach allows the $k-\varepsilon$ turbulence model to be applied inside the viscous sublayer by dividing the computation in two regions or layers: one close to the wall and one away from it. In the layer close to the wall, the turbulent dissipation rate, ε, and the turbulent dynamic viscosity, μ_t, are defined as functions of the wall distance. The values of the turbulent dissipation rate obtained in the near wall layer are then blended smoothly with the values obtained in the outer region where the transport equation for ε is solved. The two-layer approach is only used for the turbulent dissipation rate, while the transport equation for the turbulent kinetic energy, k, is solved everywhere in the domain.

Three two-layer approaches have been implemented in STAR-CCM+: two for shear-driven flows and one for buoyancy driven flows. In the present study we deal with shear driven flows. The two proposed approaches for shear-driven flows are the Wolfstein and the Norris-Reynolds formulas, both of which give comparable results. The two-layer approach is available for the Standard $k-\varepsilon$ and for the Realizable $k-\varepsilon$ models and the chosen two-layer formulation was the Wolfstein formulation.

3.2.2 Volume-of-fluid model

The VOF method is based on the advection of the volume fraction, α. The VOF version used in STAR-CCM+ is a modified version of Equation 2.15, in which the VOF has been extended for more than 2 phases. Additionally, source and sink terms can be included if needed and compressibility effects can be accurately accounted for.

$$\frac{\partial \alpha_i}{\partial t} + u_j \frac{\partial \alpha_i}{\partial x_j} = S_i - \frac{\alpha_i}{\rho_i} \frac{D\rho_i}{Dt} \tag{3.16}$$

where α_i is the volume fraction of the i-th phase, S_i is the source or sink term of the i-th phase, ρ_i is the density of the i-th phase with its material derivative noted equal to $\frac{D\rho_i}{Dt}$. Finally, the densities, viscosities and specific heats satisfy the following relationships:

$$\rho = \sum_i \rho_i \alpha_i \tag{3.17}$$

$$\mu = \sum_i \mu_i \alpha_i \tag{3.18}$$

$$c_p = \sum_i \frac{(c_p)_i \rho_i}{\rho} \alpha_i \tag{3.19}$$

where ρ_i, μ_i and $(c_p)_i$ are the density, molecular dynamic viscosity and specific heat of the i-th phase.

The Volume-of-Fluid equations are discretised using the finite-volume representation with second-order upwind scheme for the advection term. The temporal discretization is also second order accurate. The second-order upwind scheme is often sufficiently accurate to capture a sharp interface. However, if a more refined interface is needed, a sharpening factor can be included in the VOF formulation which reduces the numerical diffusion and creates a more accurate representation of the free surface. For the scope of this research no sharpening factor was included as well as no source of sinks.

3.2.3 Grid generation procedure

In order to increase computational efficiency and obtain more accurate results, all computational grids were created within the mesh generator available in STAR-CCM+. To

create the computational grid, the domain boundaries should be imported as surfaces into STAR-CCM+. This was accomplished by first post-processing the geometries (e.g., bathymetry of the channel) using Tecplot and Pointwise V17, thus obtaining the boundaries in the required format. The boundaries were then imported into STAR-CCM+ and a meshing continua was created. Within this meshing continua, the user can select the desired meshing options.

Before creating the volume mesh, the surface has to be smoothed to get rid of unnecessary details and geometrical features that can create numerical instabilities (e.g. sharp corners). This can be accomplished by two methods: Surface Wrapper and Surface Remesher, out of which the Surface Remesher was chosen since its procedure is easy to understand and manipulate. Surface Remesher creates a surface mesh in each boundary with the user defined level of representation. For example, if one were to model hydraulic structures located within the river reach, a boundary can be created around the structure so that it is individually represented with more refinement compared to the outer domain. If no special level of refinement is needed, then the Surface Remesher creates a surface mesh with the same level of resolution everywhere in the domain. This is an important step, since a surface mesh is needed in order to create a volume mesh. In the proposed RANS model, the level of refinement is in decreasing order (most refined to least refined) as one goes from regions situated close to hydraulic structures to the river channel and finally to the floodplains and outer regions (e.g., regions containing air).

The second step in the mesh generation procedure is to define the boundary conditions for each of the boundaries imported. This is needed because during the volume mesh generation the type of boundary condition are taken into account when generating a high quality mesh consistent with the required boundary condition. The boundary conditions will be explored in more detail in the next subsection.

The third and final step is to create the volume mesh. After the surface mesh has been created with the desired level of resolution, the user can select the desired volume mesh modules. STAR-CCM+ is capable of generating tetrahedral, hexahedral and polyhedral unstructured meshes. In the present study, hexahedral meshes were generally chosen, since the control over the size and number of cells becomes more intuitive due to the cell shape (i.e. cube like). Tetrahedral cells, on the other hand, are created by generating pyramid-like cells, making the control of the size and number of cells difficult.

Hexahedral meshes are created by selecting the Trimmer meshing module in STAR-CCM+. Trimmer creates cube-like cells based on the specified cell size in the surface mesh. It is also possible to create cells with different edge sizes in each direction (x, y and/or z). This feature makes Trimmer highly suitable to deal with river/floodplain flow, since the mesh can be refined in the vertical direction while maintaining relatively large edge sizes in the horizontal directions. The anisotropic cells are created in the same specified regions during the surface re-meshing procedure, making the surface mesh consistent with the volume mesh. The horizontal mesh resolution near hydraulic structures is between one-half to one-fourth of the horizontal mesh resolution in the river channel, while the horizontal mesh resolution in the floodplains is twice the horizontal mesh resolution of the river channel. In contrast, the vertical resolution in the three regions previously mentioned is about the same. The mesh resolution in the outer regions was set to a number 16 times larger than the mesh size in the river channel. This was done to minimize the total number of cells, while maintaining a good overall resolution. Figure 4.1 shows an example of mesh refinement near the main channel of the river compared to the floodplain. It is clearly observed that the Trimmer mesh refinement is done by creating cells which are half the size of the outer cell. In addition Figure 4.2 (a) shows an example of how a Trimmer mesh looks in a cross-sectional view.

Special attention needs to be given to regions close to the walls, since the mesh resolution must be capable of capturing the effects of the boundary layer. If the user were to use a pure Trimmer mesh, the number of cells would become extremely large. An attractive alternative is to use the Prism Layer meshing module. This module creates high aspect ratio, highly-skewed cells parallel to any specified wall-boundary condition. The number of cells and their height are directly specified by the user. The height of the first Prim Layer cell created in each mesh is equivalent to y^+=100, unless an equivalent roughness height is specified. STAR-CCM+ relaxes the y^+ requirement in the presence of roughness, making the desired wall spacing equal to twice the roughness height. Since the typical Reynolds number in realistic river flows are in the order of 1 million or larger, an assumption of y^+=100 would produce very thin layers near the wall thus compromising the model's numerical stability. In order to input an equivalent roughness height sediment data, in particular the values of d_{50} and d_{90}, are needed since the equivalent roughness height can be calculated from the mentioned parameters. By including sediment data, the height of the Prism Layers is increased. This reduces the total number of cells and improves numerical stability. Figure 4.2 (b) shows a close-up to the Prism Layers generated near the wall.

The described procedure does not always guarantee a computational mesh that is of sufficiently high quality. In order to avoid convergence problems, the mesh should be regenerated as many times as needed. If the problem still persists, STAR-CCM+ can solve the problems in two ways. The first option, which is also the desired option, is to activate the Cell Quality Remediation module. This module selects the cells which are producing unrealistic results and does not allow the results to propagate out of those cells. The second option, which is less recommended, is to remove cells from the computational domain. STAR-CCM+ instead, creates voids with slip boundary conditions at all faces. In the RANS simulations discussed in the present study, the Cell Quality Remediation model was always active as an insurance policy against unrealistic results.

3.2.4 Boundary conditions

For each of the imported surfaces in the meshing procedure (Section 3.2.3), a boundary condition is needed. The boundary conditions that have to be specified are problem dependent, but for open channel flow applications the types of boundary conditions are fairly limited (inlet, outlet, wall boundary, symmetry).

The inlet boundary condition was specified on each imported surface whose purpose is to push water into the computational domain. The inlet boundary condition can be specified via a Velocity Inlet boundary condition or Mass Inlet boundary condition. For the following test cases, inlet boundary conditions were specified using the Velocity Inlet boundary condition, in which the velocity magnitude and the free-surface level are required. Velocities and free-surface elevations were known for each test case, since the inlet sections are either located in a lab setup or near a river gaging station.

An outflow boundary condition was specified on each surface where water/air is wanted to leave the domain of interest. In the case of water-filled domain, the outflow boundary condition is located in the river/floodplain domain. In the case of air-filled domain, the outflow boundary condition is located where the air is in contact with the open atmosphere. The outlet boundary conditions can be specified using a Pressure Outlet boundary condition or a Flow-Split outlet boundary condition. The Pressure outlet was chosen in all subsequent test cases since a desired Pressure and Volume Fraction of Water (free-surface elevation) can be directly specified. In the case of an open channel outlet, either extrapolation of pressure and volume fraction (zero gradient boundary condition) or a desired pressure and volume fraction distribution were specified. In the case when air is present next to the outlet boundary, the pressure outlet boundary condition was given a pressure equal to 0 Pa and a volume fraction of water equal to 0. This was done to simulate an open atmosphere boundary condition.

A wall boundary condition was specified on each surface that represents a solid surface, such as bathymetry/topography surface, bridge deck surface, etc. The wall boundary condition allows the user to specify a rough or a smooth wall, slip/no slip conditions and the velocity of the wall surface. Since the surfaces are fixed in space, the velocity at the wall was set to 0 m/s in the simulations. The wall was assumed to be a no-slip surface. The walls were assumed to be smooth in all laboratory test cases while the walls were assumed to be rough in all test cases corresponding to field applications. The specified roughness height was set to $2d_{50}$.

If the simulation was performed for a single phase (only water or air present in the domain), then the Volume Fraction module was not active. When dealing with a single phase problem, the setup of the problem changes slightly, since there is no surface (boundary) open to the atmosphere. Instead, a surface with a symmetry boundary condition is placed either at the location of the free surface. This approach is commonly known as the rigid lid approximation. The rigid lid approximation was used in order to do a comparison between results obtained with and without the free-surface module.

3.3 2-D shallow water equations model

In a subsequent chapter (Chapter 4), the results obtained with the 3-D Unsteady RANS STAR-CCM+ model are compared to results obtained with a 2-D Shallow Water Equation code, SRH-2D. SRH-2D solves the full 2-D shallow water equations in conservative form.

$$\frac{\partial h}{\partial t}+\frac{\partial\left(h\tilde{U}\right)}{\partial x}+\frac{\partial\left(h\tilde{V}\right)}{\partial y}=0 \tag{3.20}$$

$$\frac{\partial\left(h\tilde{U}\right)}{\partial t}+\frac{\partial\left(h\tilde{U}\tilde{U}\right)}{\partial x}+\frac{\partial\left(h\tilde{V}\tilde{U}\right)}{\partial y}=-gh\frac{\partial\left(z_b+h\right)}{\partial x}+\frac{\partial}{\partial x}\left(\tilde{T}_{xx}h\right)+\frac{\partial}{\partial y}\left(\tilde{T}_{yx}h\right)-\frac{T_{bx}}{\rho} \tag{3.21}$$

$$\frac{\partial\left(h\tilde{V}\right)}{\partial t}+\frac{\partial\left(h\tilde{U}\tilde{V}\right)}{\partial x}+\frac{\partial\left(h\tilde{V}\tilde{V}\right)}{y}=-gh\frac{\partial\left(z_b+h\right)}{\partial y}+\frac{\partial}{\partial x}\left(\tilde{T}_{xy}h\right)+\frac{\partial}{\partial y}\left(\tilde{T}_{yy}h\right)-\frac{T_{by}}{\rho} \tag{3.22}$$

where h is the water depth, $\tilde{U}$ is depth averaged velocity in the x direction, $\tilde{V}$ is the depth averaged velocity in the y direction, g is the gravitational acceleration, z_b is the bed elevation, ρ is density of fluid, $\tilde{T}_{xx}$, $\tilde{T}_{yy}$, $\tilde{T}_{yx}$ and $\tilde{T}_{xy}$ are the four components of the depth averaged shear stress tensor, and T_{bx} and T_{by} are the bed shear stress components.

While Equation 3.20 is identical to Equation 2.6, Equations 3.21 and 3.22 show some differences compared to Equations 2.7 and 2.8 respectively. Equations 2.7 and 2.8 can be obtained by using the chain rule of the derivative starting with Equations 3.21 and 3.22 and by finally dividing the equations by h.

The bed shear stresses are estimated based on a Manning's coefficient (n) formulation which takes into account the bed roughness in a single parameter.

$$T_{bx} = \rho\left(\frac{gn^2}{h^{1/3}}\right)\tilde{U}\sqrt{\tilde{U}^2+\tilde{V}^2} \tag{3.23}$$

$$T_{by} = \rho\left(\frac{gn^2}{h^{1/3}}\right)\tilde{V}\sqrt{\tilde{U}^2+\tilde{V}^2} \tag{3.24}$$

The depth-averaged turbulent stresses are defined as follows:

$$T_{xx} = 2\frac{\mu+\mu_t}{\rho}\frac{\partial\tilde{U}}{\partial x} \tag{3.25}$$

$$T_{yy} = 2\frac{\mu+\mu_t}{\rho}\frac{\partial\tilde{V}}{\partial y} \tag{3.26}$$

$$T_{xy} = 2\frac{\mu+\mu_t}{\rho}\left(\frac{\partial\tilde{U}}{\partial y}+\frac{\partial\tilde{V}}{\partial x}\right) \tag{3.27}$$

The eddy viscosity can be calculated using one of the two turbulent models available in SRH-2D: the parabolic and the $k-\varepsilon$ model. For simplicity, the parabolic turbulence model was chosen and therefore it is the only turbulence model described next. In the case of the parabolic turbulence model, the eddy viscosity is calculated as

$$\mu_t = \rho C_t U_* h$$

(3.28)

where U_* is the shear velocity defined by

$$U_* = n\sqrt{\frac{g}{h^{1/3}}}\sqrt{\tilde{U}^2 + \tilde{V}^2} \tag{3.29}$$

The model constant, C_t can range from 0.3 – 1.0 with a default value of 0.7.

3.4 Validation of the numerical model

The hydrodynamic model developed in STAR-CCM+ needs to be first validated based on standard test cases before it is applied to flow in natural environments (i.e. natural river reaches). A systematic validation was performed in this study, in which three validation test cases were chosen to test the accuracy of the RANS model to simulate free-surface elevation and velocity profiles within the water domain. The validation starts with a series of dam break scenarios for validation. Such step is of crucial importance since the proposed 3-D model will eventually be used to simulate realistic dam break scenarios (Chapter 7). The first test case is a standard 2-D dam break case, which is used to assess the accuracy of the solver and to estimate meshing requirements for unsteady flows with high free-surface deformations. The second and third test cases correspond to dam break flow over a triangular obstacle and dam break flow over a 90° bend, respectively. These test cases are used to assess the accuracy of the solver when dealing with dam break flows. The fourth test case corresponds to flow in an S-shaped channel under subcritical flow conditions. This case is used to test the capability of the code to accurately predict channel velocity profiles and free-surface deflections in man-made curved channels. The last test case corresponds to flow in a 193° open channel bend under subcritical flow conditions. This case is used to test the accuracy of the model when high free-surface deflections in the channel are expected.

3.4.1 2-D dam break test case

In the hypothetical abrupt failure of a dam bordering a lake/reservoir, the blocked column of still water spreads suddenly into the adjacent region downstream of the lake/reservoir. The most idealized case that mimics such an event is the one in which a rectangular column of water collapses on a flat horizontal surface. Martin and Moyce (1952) studied this problem experimentally by collapsing a square column of water of length a = 2.25 in. into an 11.25 in. long by 2.8125 in. high channel of rectangular cross section. The parameters tracked during the experiment were the front surge position and the remaining water column height. Both variables give information about the spreading of the gravity wave.

The computational domain size is 5a x 1.25a, which is consistent with the computational domain employed by Kelecy and Pletcher (1997) and with the experiment performed by Martin and Moyce (1952). Figure 3.3 shows the general layout of the 2-D dam break test case. The results obtained were non-dimensionalized taking the initial column height as the length scale (i.e. 2.25 in) and the velocity scale equal to the characteristic velocity of a surface gravity wave (i.e. $\sqrt{ga}$). Several uniform meshes were employed to assess the performance of the numerical model as a function of mesh refinement. The four computational meshes employed contained 100x25, 200x50, 400x100 and 800x200 mesh points, respectively.

Figure 3.4 shows the mass conservation for the computations performed on the four meshes. It is observed that the mass conservation errors are below 7% for all cases. It comes as no surprise that the coarser mesh (i.e. 100x25) shows the highest mass conservation error due to the reduced ability to accurately characterize the water region and the corresponding interface location. Figure 3.5 and Figure 3.6 show the front surge position and the remaining water column height as a function of non-dimensional time. Agreement with experimental data is excellent (less than 5%) and independent of mesh resolution in terms of front-surge position and remaining water-column height.

Figure 3.7 shows snapshots of the water motion and it is used as supporting evidence on the physicality of the results obtained with the developed model. Figure 3.7 shows a typical gravity wave propagation. One can thus conclude that the model can produce accurate results for cases when high deformations of the free-surface are expected during the simulation.

3.4.2 Dam break flow over a triangular obstacle

The second test case deals with dam break flow over a straight channel including a triangular obstacle, as performed in the experiment conducted by Soarez-Frazao, 2002. Initially, a column of water of 0.111 m by 2.39 m (H x L) was set 1.61 m left to the triangular obstacle. In addition, to the right of the triangular obstacle a pool of still water can be found with a height of 0.065 m, as shown in Figure 3.8. At t=0 the column of water is left free to collapse. The flood wave advances toward the triangular obstacle, thus creating a dam break flow scenario with added complexity.

The size of the computational domain is consistent with that of the experimental setup used by Soarez-Frazao, 2002. The accuracy of the simulation will be assessed based on comparing the free-surface elevation profiles in the experiment and simulation, as well as comparing photographs of the flood wave with present numerical results, as well as results of the 3-D simulation conducted by Biscarini et al., 2010.

Figure 3.9 shows the free-surface elevation profile plot along the center of the channel at 4 different times: 1.8 s, 3.0 s, 3.7 s and 8.4 s after the collapse of the column of water. Both 3-D models perform quite similarly in all four times. A slight improvement in the accuracy of the predictions can be observed at t = 3 s where the present 3-D model captures the second crest induced by a backward propagating wave left of the triangular obstacle. The present 3-D model matches the experimental results slightly better than the simulation conducted using the numerical model proposed by Biscarini et al., 2010.

The conclusions drawn from in Figure 3.9 are confirmed by analyzing the pictures showing the flood wave structure in the experiment and the corresponding visualizations based on the numerical results (Figure 3.10). The 3D model proposed by Biscarini et al., 2010 captures a sharper interface, allowing it to simulate air entrainment near wave breaking. This phenomenon can be clearly observed at t=1.8 s, 3.0 s and 3.7 s. While this air entrainment phenomenon usually happens when waves break, it cannot be clearly observed in the pictures taken during the experiment at the corresponding times. On the other hand, the present 3-D model simulation captures a more diffused interface. Air entrainment is not captured by this simulation. Visual comparison of the experimental and numerical visualizations of the flood wave confirms that the position of the free surface is better captured by the present 3-D model compared to the 3-D model proposed by Biscarini et al., 2010.

3.4.3 Dam break flow over a 90○ bend

The third test case considers a dam break flow advancing in a 90° L-shaped channel, as performed in the experiment conducted by Soarez-Frazao and Zech, 2002. The downstream channel shape plays a crucial role in the propagation of the flood wave. For instance, the interaction of the flood wave with the outer wall of the L-shaped channel can cause backwater effects or may cause the front to slow down. Initially, a 2.44 m x 2.39 m reservoir is connected to a 0.495 m high, L-shaped rectangular channel. The upstream reach of the L-shaped channel is 4 m long. The downstream reach is 3 m long. The L-shaped channel is connected to the rectangular reservoir 0.33 m above the bottom surface of the reservoir. The reservoir is filled 0.2 m above the channel bottom. The experimental setup is shown in Figure 3.11. At t=0 the reservoir is left free to discharge into the channel.

The computational domain is consistent with the experimental setup used by Soarez-Frazao and Zech, 2002. The free-surface elevation profiles predicted by the 3-D

simulation are compared with experimental measurements and numerical results obtained using the 3-D model proposed by Biscarini et al., 2010.

Figure 3.12 shows the free-surface elevation profiles along the outer bank of the channel at t=3 s, 5 s, 7 s and 14 s after the release of water from the reservoir into the channel. Both 3-D models perform quite similarly at all four times. In fact, the model proposed by Biscarini et al., 2010 seems to perform slightly better than the present 3-D model especially at t=5 s, 7 s and 14 s near the outlet of the domain where the present 3-D model predicts a clearly defined dip in the free surface elevation at a distance of approximately 8.5 m from the reservoir. The simulation results of Biscarini et al., 2010 show no dip in the free-surface elevation and matches the experimental results better. Besides the aforementioned differences, the present 3-D model simulation matches very closely the experimental results in the other parts of the domain.

.

3.4.4 Flow in a curved S-shaped channel

The S-shaped channel comprises two identical 90° bends in opposite directions connected by a small straight reach with a trapezoidal cross sectional geometry with side slopes of 1:1 and with a bottom width of 1.83 m. The radius of curvature of each bend is 8.54 m. Figure 3.13 shows a top view of the channel, while Figure 3.14 shows the cross sectional geometry. The mean inlet velocity is 0.692 m/s and the water depth at the inlet is 0.156 m. The parameters of the simulation are summarized in Table 3.1. The validation was carried out by comparing the numerical results to measurements provided by Yen (1967) in his experiment number 3.

Table 3.1 Main parameters of free-surface open channel flow experimental (Yen, 1965) and numerical studies conducted in an S-shaped channel

Velocity at the inlet (m/s)	0.692
Average water depth (m)	0.156
Bottom width of the channel (m)	1.83
Froude number	0.6
Reynolds number	1.0×10^5
Number of grid cells	550 000

The results were non-dimensionalized by using the inlet velocity as the velocity scale and the average water depth as the length scale. Figure 3.15 shows the measured and computed non-dimensional streamwise velocity profiles over the depth at Section S0. Results are plotted at five different locations along the transverse direction (η/B), where η is measured from the center of the channel. Overall, it is found that the velocity profiles predicted by the simulation are in good agreement with experimental data (less than 10% error), with the most noticeable difference at location (a). At location (a), the simulation underpredicts the streamwise velocity consistently across the depth (~20%). Location (b) underpredicts slightly the streamwise velocity close to the free surface and location (e) overpredicts it slightly. While some differences are noted at locations (d) through (e), the simulation results show very good agreement with experimental data (less than 10% difference).

Figures 3.16 and 3.17 show the transverse free-surface profiles at four specific cross sections and the longitudinal free-surface profiles along the two banks of the channel, respectively. In Figure 3.16 it is observed that the transverse free-surface profiles predicted by the simulation are in good agreement with experimental data at all the four specified cross-sections. In Figure 3.17, a positive free-surface deflection is observed at the outer bank while a negative deflection is observed at the inner bank. Such behavior is consistent

with what is expected for open channel bends. The computed longitudinal free-surface profiles show the same trend as the measured data with errors increasing as one moves downstream. The differences become more noticeable as the flow approaches the end of the second bend. These errors, however, are relatively small.

The validation performed for the flow in an S-shaped channel proved that the numerical model is capable of accurately simulating open channel flow problems when mild to moderate free-surface deflections are expected.

3.4.5 Flow in a 193○ open channel bend

In this test case, the channel geometry was the one used by Blanckaert (2002) and is shown in Figure 3.18. The channel consists of a single 193◦ bend with a radius of curvature of 1.7 m, with two straight channels before and after the bend of 9 m and 5 m long, respectively. The total channel length is 22.7 m along the centerline. The cross-section shape is rectangular with a channel width of 1.3 m. The mean inlet velocity is 0.43 m/s and the water depth at the inlet is 0.159 m. The parameters of the simulation are summarized in Table 3.2.

Table 3.2 Main parameters of the experimental (Blanckaert, 2002) and numerical studies corresponding to flow in a 193○ open channel bend

Velocity at the inlet (m/s)	0.43
Average water depth (m)	0.159
Bottom width of the channel (m)	1.3
Froude number	0.38
Reynolds number	6.8×10^4
Number of grid cells	385 000

Two simulations were performed. The first simulation was a single phase simulation using the Rigid Lid approximation. The second simulation was a two-phase flow simulation using the VOF method. Figure 3.19 shows the cross sectional geometry used in the Rigid Lid simulation, while Figure 3.20 shows the cross sectional geometry used in the VOF simulation. The results obtained using the Rigid Lid approximation will only be used to validate streamwise velocity and vorticity distributions, but not free-surface profiles. The free-surface deflections will be validated by comparing the results obtained in the VOF simulation with experimental results of Blanckaert (2002).

Figure 3.21 shows streamwise velocity distribution at 6 cross-sections located in bend. No major differences can be observed by visual inspection between the simulations using the Rigid Lid approximation and the VOF method. The flow pattern is very similar in the two simulations. However, differences tend to increase as one moves downstream. In Section D30 and D60 the differences are negligible while at section D180 the differences are more noticeable. The streamwise vorticity distributions (Figure 3.22) show the same patterns in the two simulations at the cross sections. The biggest differences are observed at the section D90 situated near the center of the bend, where the core of high vorticity in the simulation using the Rigid Lid approximation diffuses from the inner bank to the center of the channel away from the bottom surface. The VOF simulation shows that the core of streamwise vorticity diffuses toward the center of the channel but remains close to the bottom wall.

Figure 3.23 shows the transverse free-surface profiles for the same 6 cross sections for which the streamwise velocity and vorticity comparison was performed. Overall, the transverse free-surface profiles show very good agreement with experimental data. A noticeable difference is shown at cross-section D30 at the inner bank, where the VOF simulation is unable to reproduce the free-surface deflection observed in the experiment, resulting in an error of approximately 30% near the inner bend. The VOF simulation predicts a significant negative free-surface deflection that is not consistent with the

experimental results. This inconsistency is not present in the subsequent cross sections. At the other cross sections, the errors are quite small, less than 5%. This is the case especially for sections D90, D120 and D150. At section D180, the free surface is underestimated consistently across the cross section by a small amount.

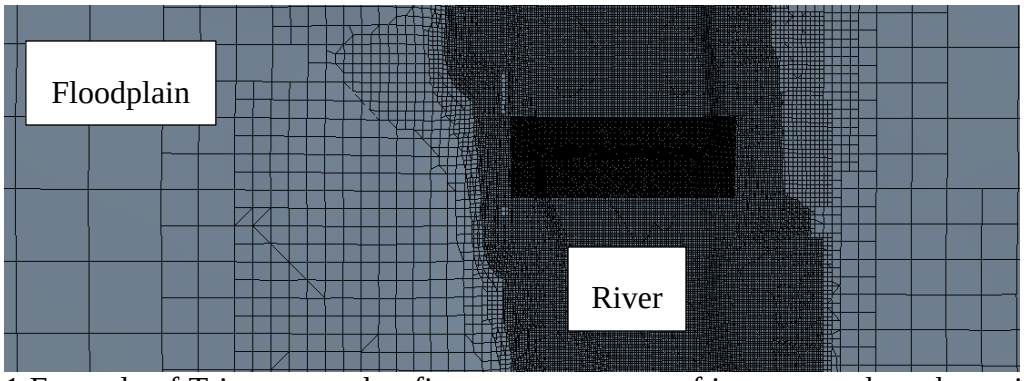

Figure 3.1 Example of Trimmer mesh refinement near areas of interest, such as the main channel of the river and its floodplain.

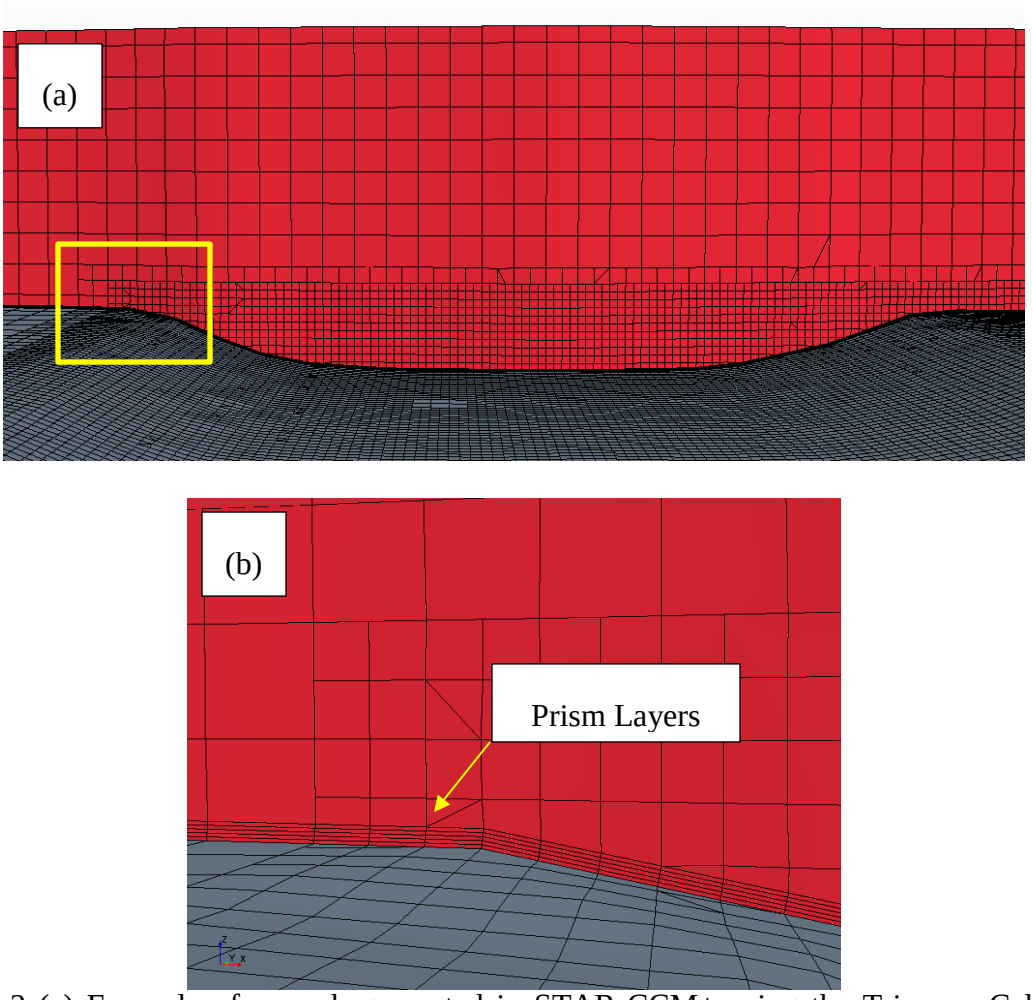

Figure 3.2 (a) Example of a mesh generated in STAR-CCM+ using the Trimmer Cell mesher and the Prism Layer mesher. (b) Close-up view of the Prism Layers near the wall boundary.

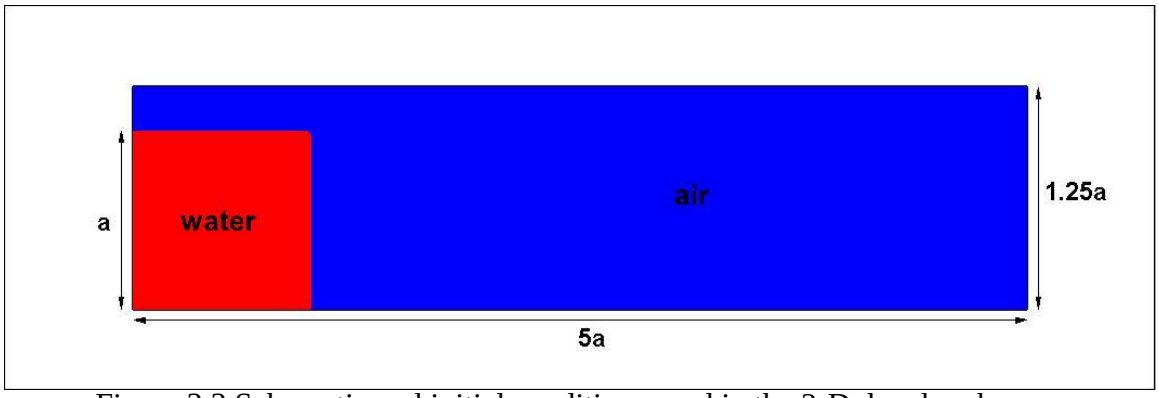

Figure 3.3 Schematic and initial conditions used in the 2-D dam break case.

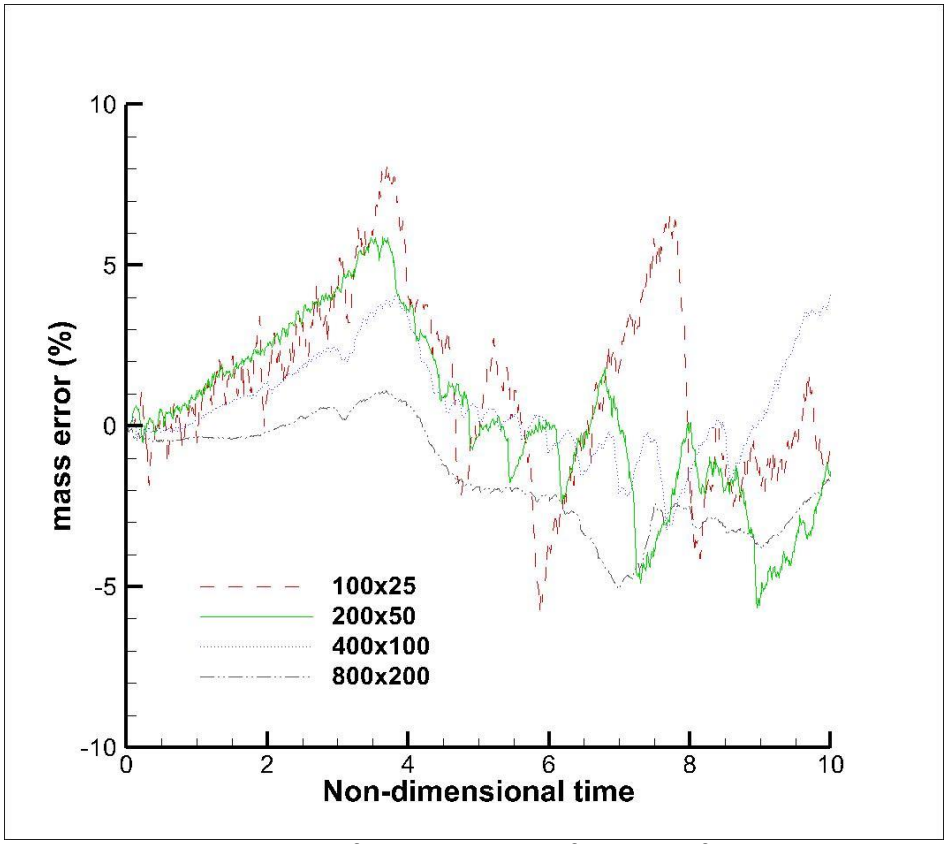

Figure 3.4 Time history of mass error as a function of mesh resolution.

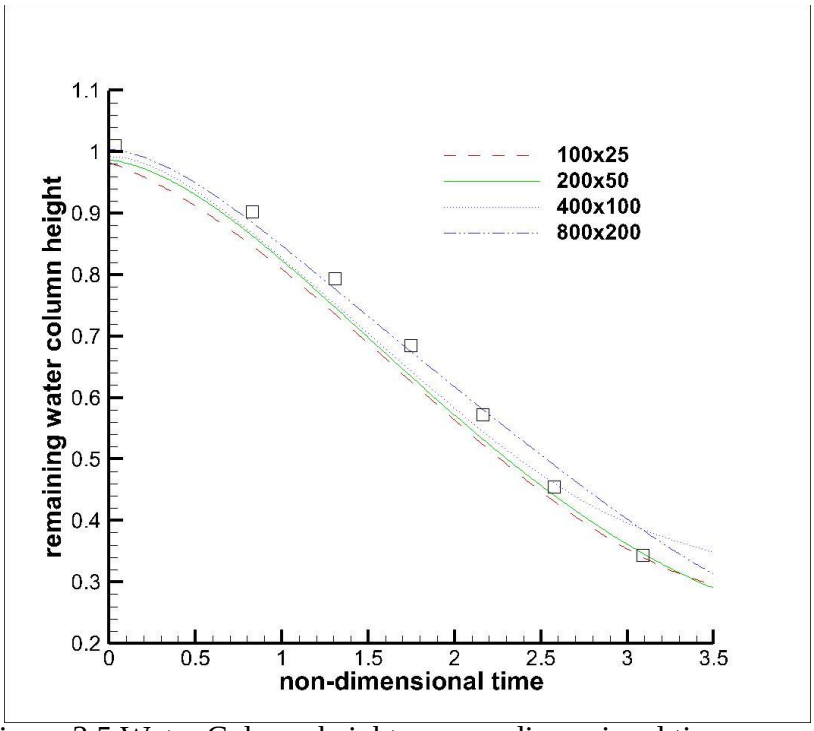

Figure 3.5 Water Column height vs. non-dimensional time.

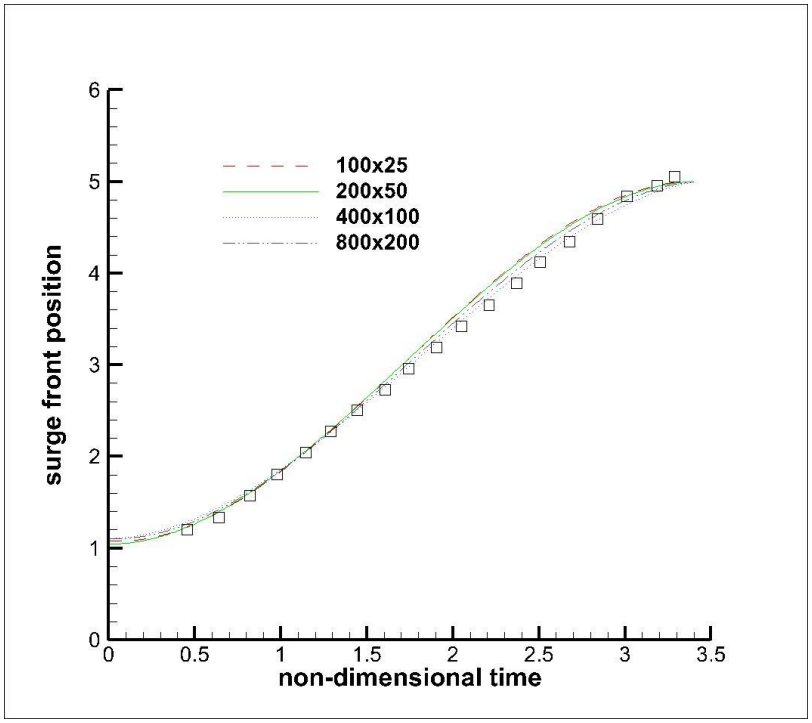

Figure 3.6 Front surge position vs. non-dimensional time.

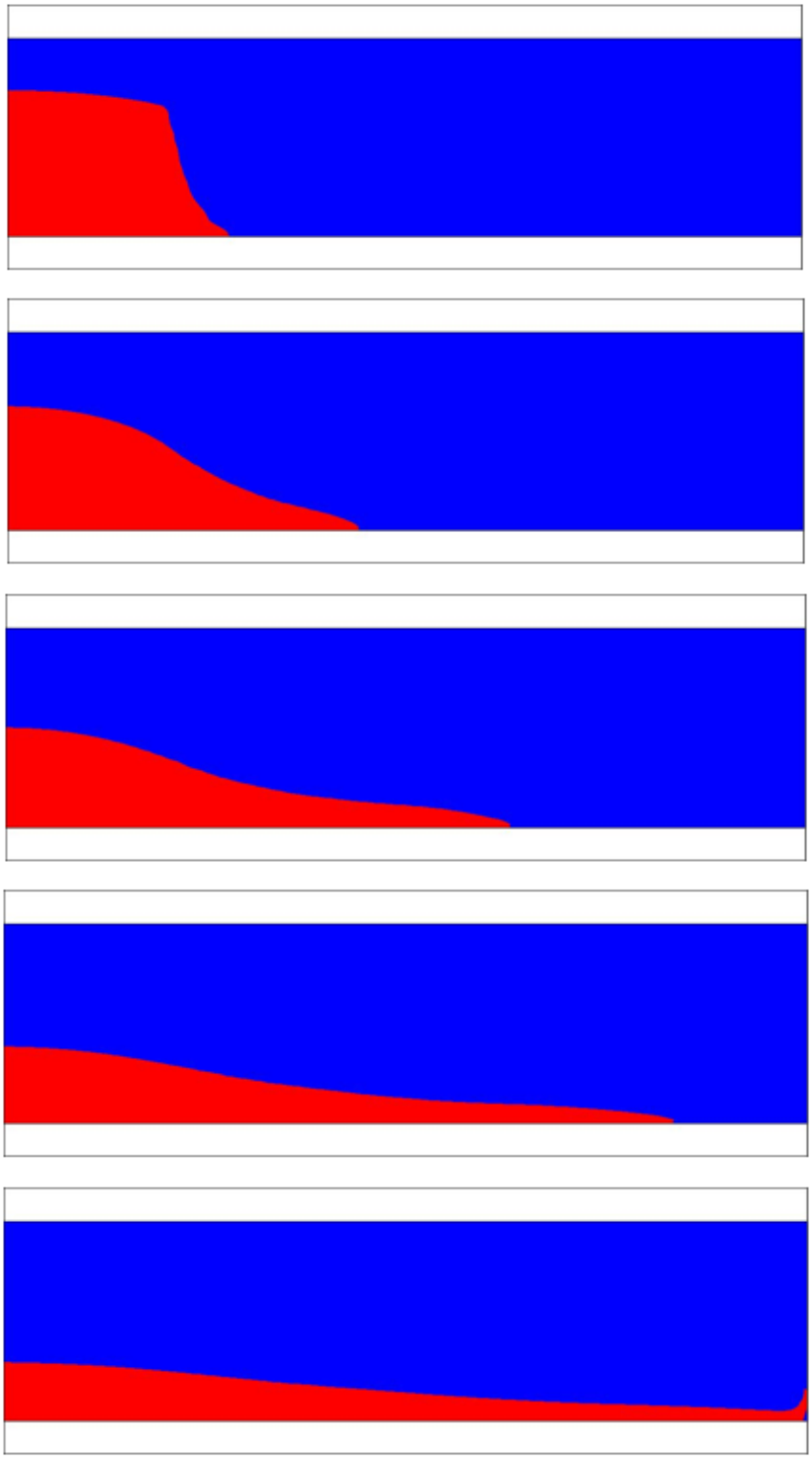

Figure 3.7 Free-surface position at selected non-dimensional times equal to 0.6, 1.2, 1.8, 2.4 and 3.0 obtained on the 200x50 grid. Red (dark) areas represent the water.

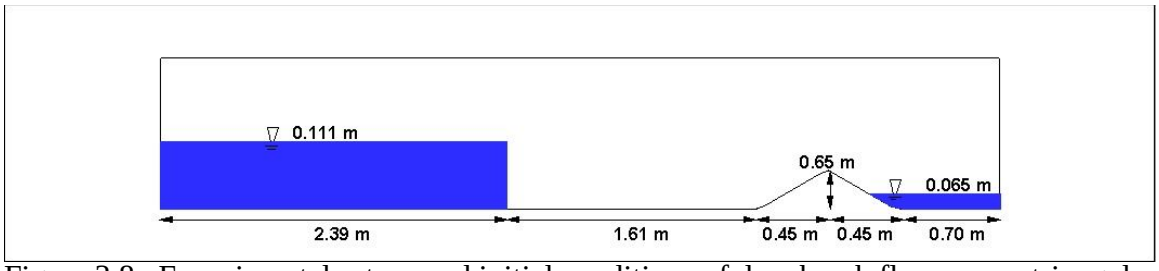

Figure 3.8 . Experimental set-up and initial conditions of dam break flow over a triangular obstacle test case as described in Soarez-Frazao, 2002.

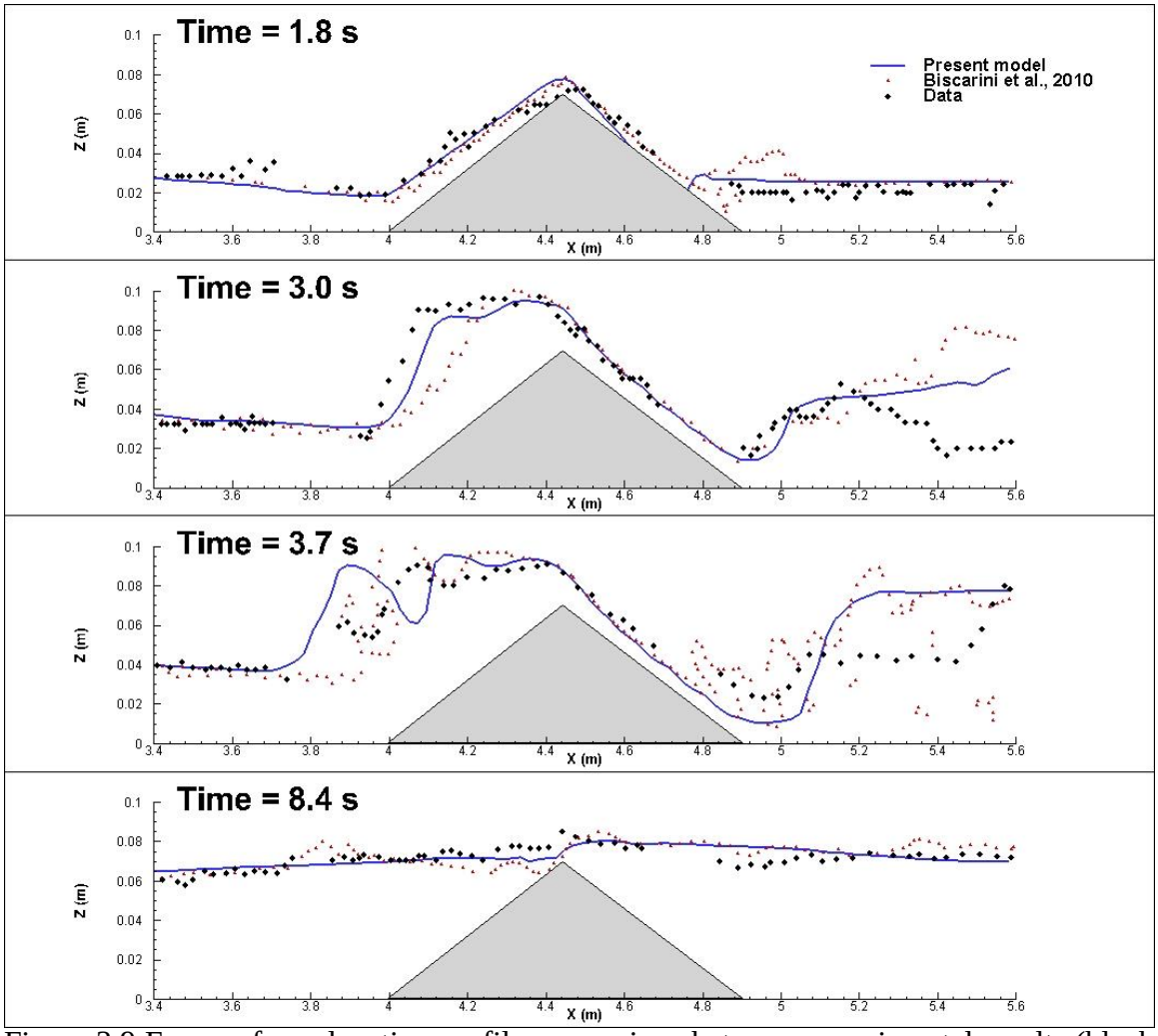

Figure 3.9 Free-surface elevation profile comparison between experimental results (black circle), numerical results obtained with the model proposed by Biscarini et. al., 2010 (red triangles), and results obtained the current proposed model (blue line) for the dam break flow over a triangular obstacle. Reproduced from Biscarini et. al., 2010.

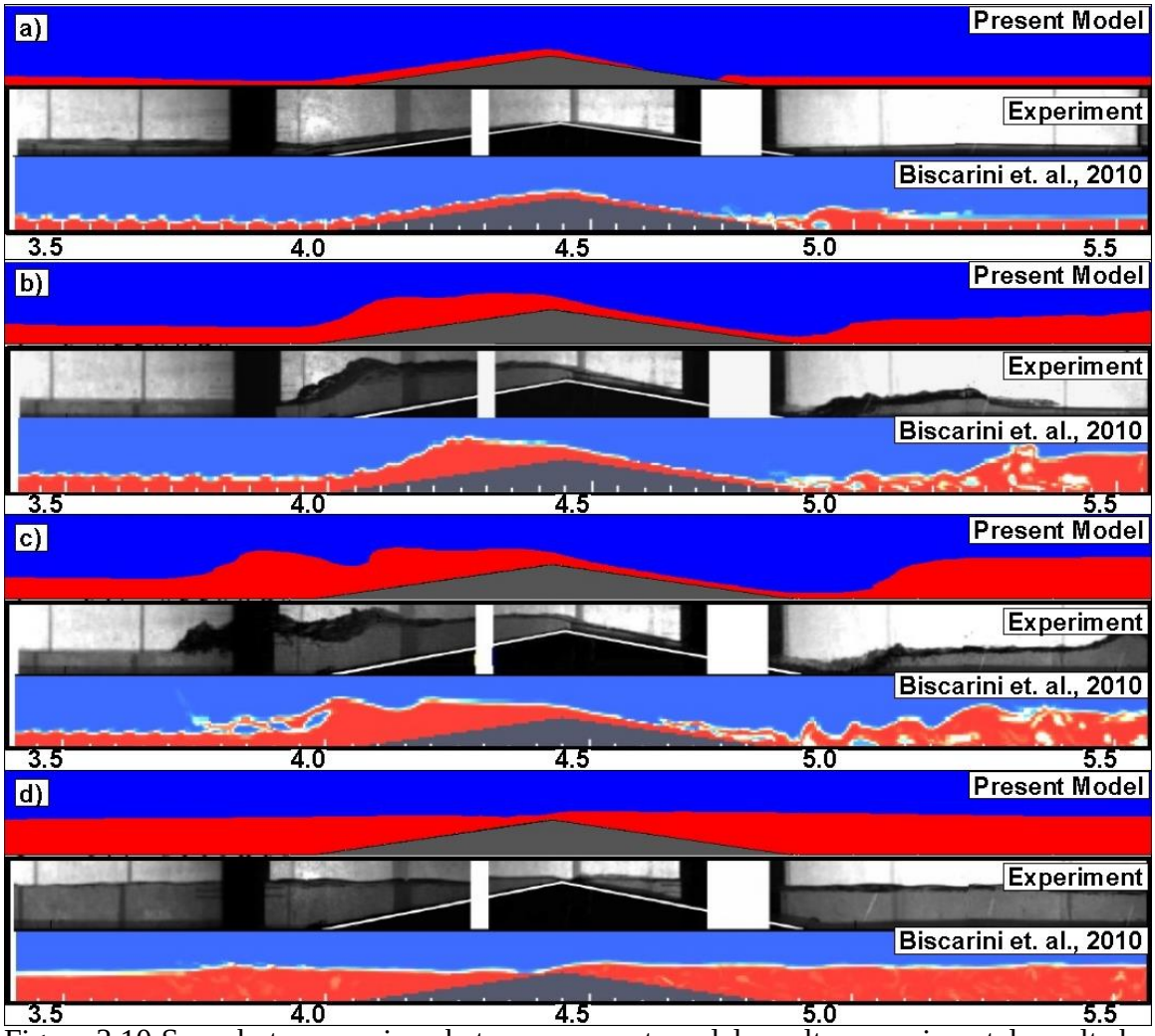

Figure 3.10 Snapshot comparison between present model results, experimental results by Soarez-Frazao, 2002, and numerical results obtained by Biscarini et. al., 2010 at four different times after the start of the dam break flow. a) Time = 1.8 s, b) Time = 3.0 s, c) Time = 3.7 s; and d) Time = 8.4 s. Reproduced from Biscarini et. al., 2010.

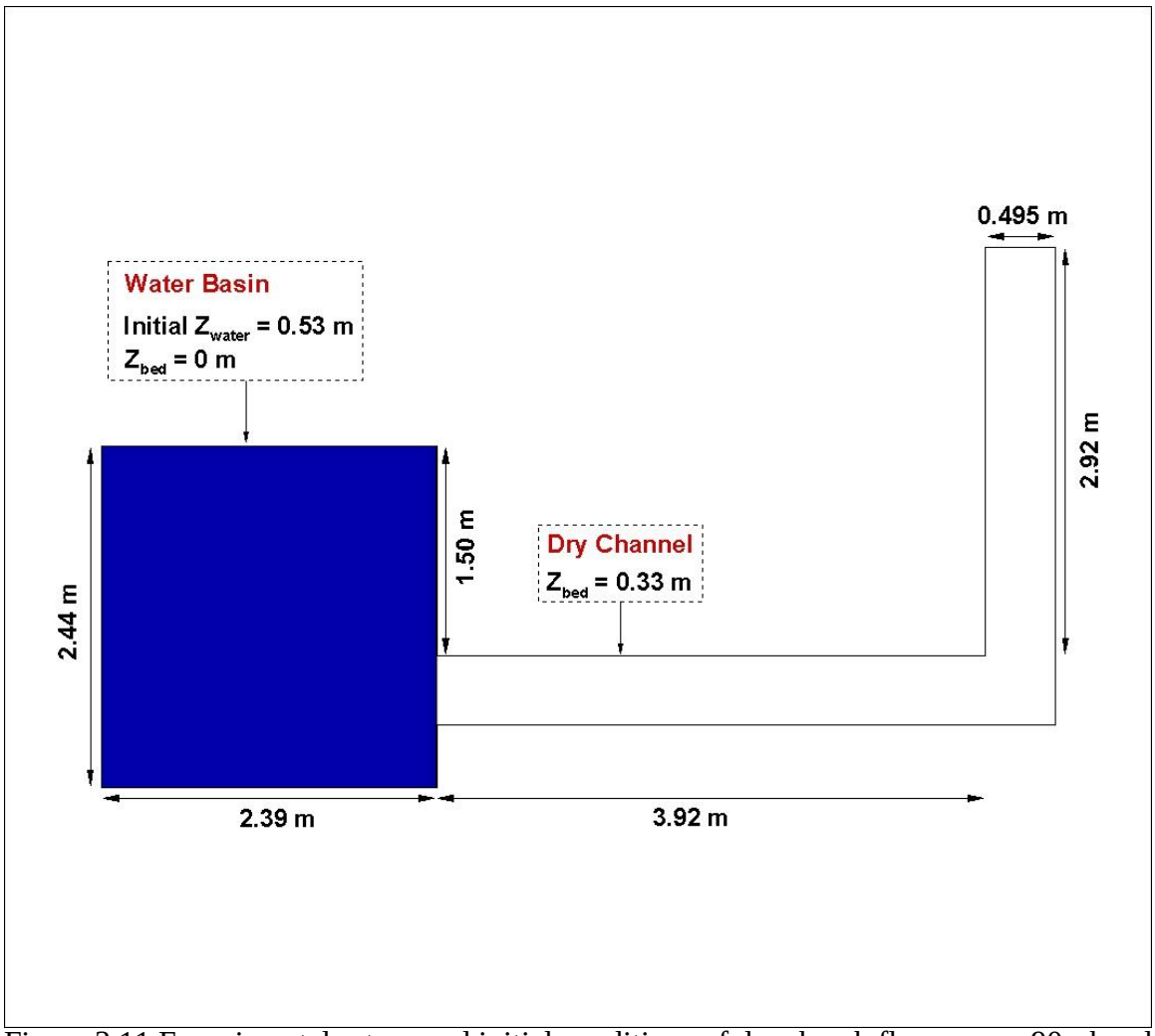

Figure 3.11 Experimental set-up and initial conditions of dam break flow over a 90○ bend test case as described in Soarez-Frazao and Zech, 2002.

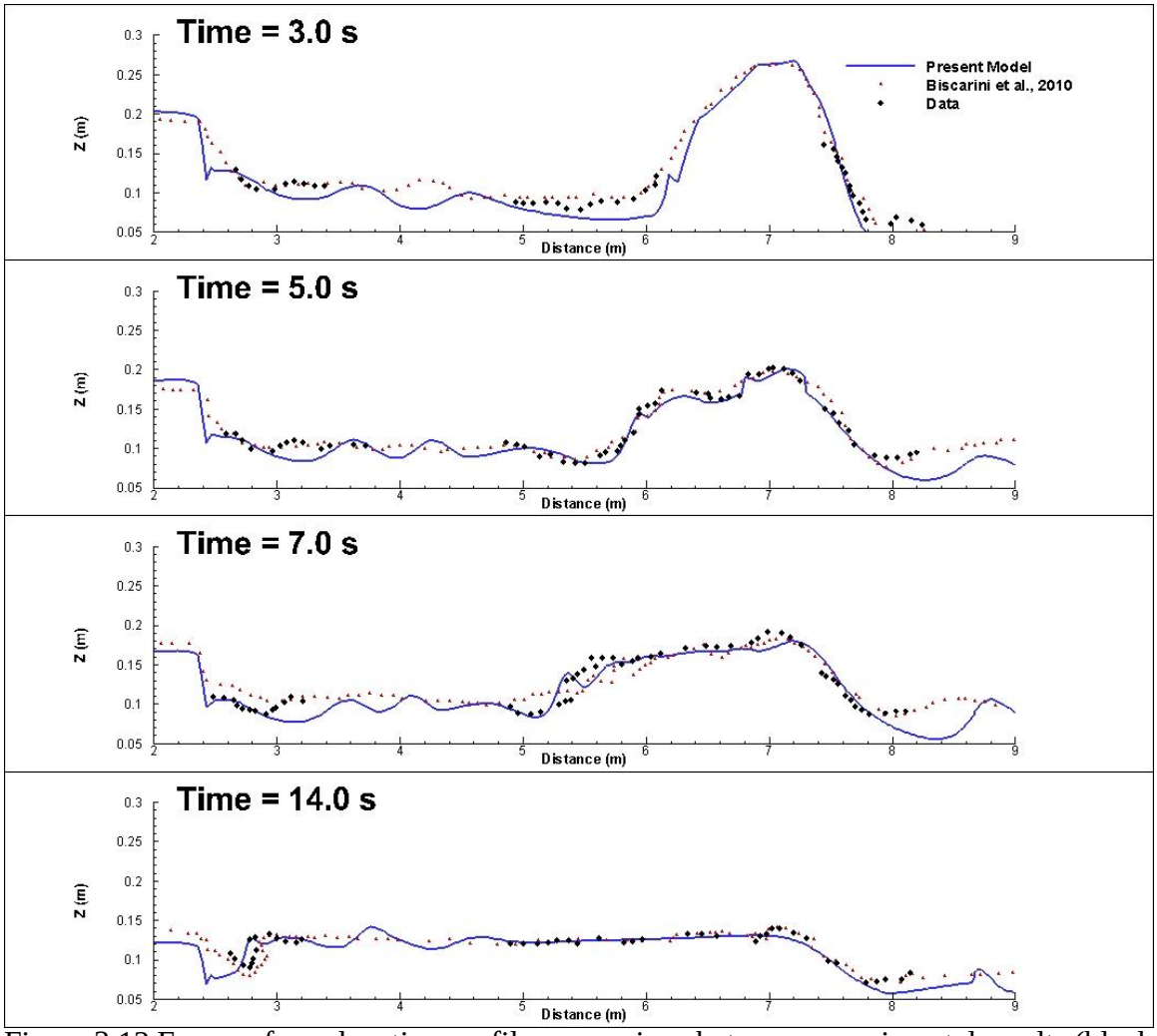

Figure 3.12 Free-surface elevation profile comparison between experimental results (black circles), numerical results obtained with the model proposed by Biscarini et. al., 2010 (red triangles), and results obtained the current proposed model (blue line) for the dam break flow over a 90○ bend. Reproduced from Biscarini et. al., 2010.

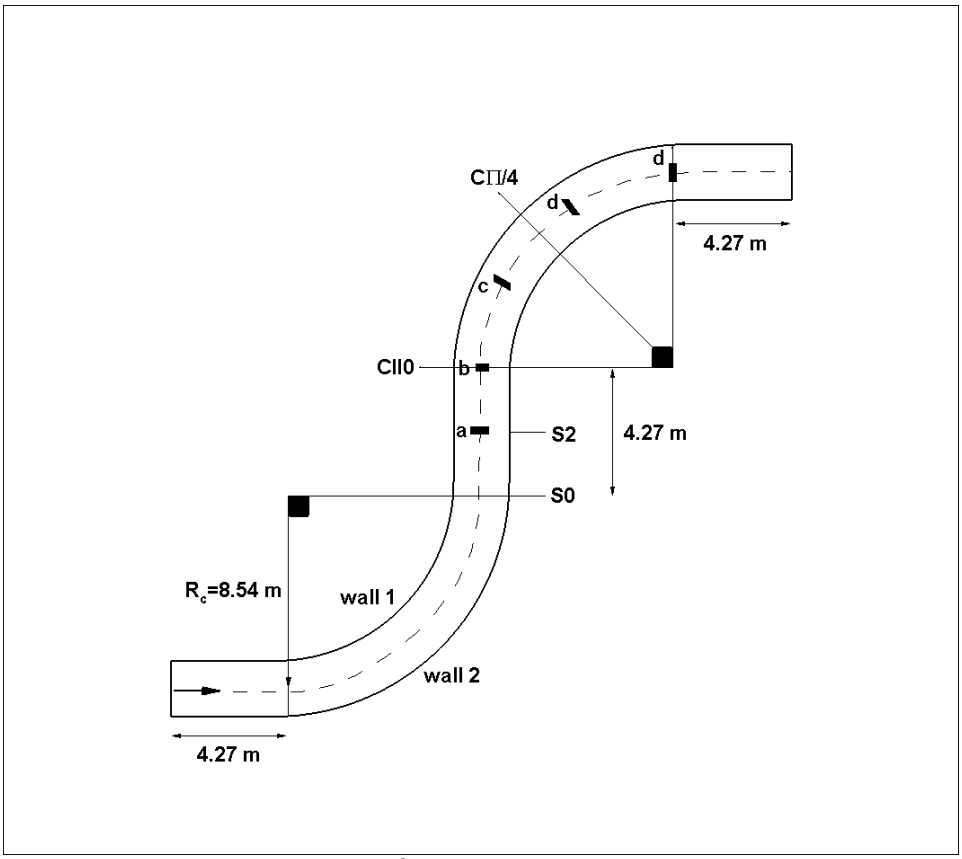

Figure 3.13 General experimental layout of the S-shaped channel experiment conducted by Yen (1967).

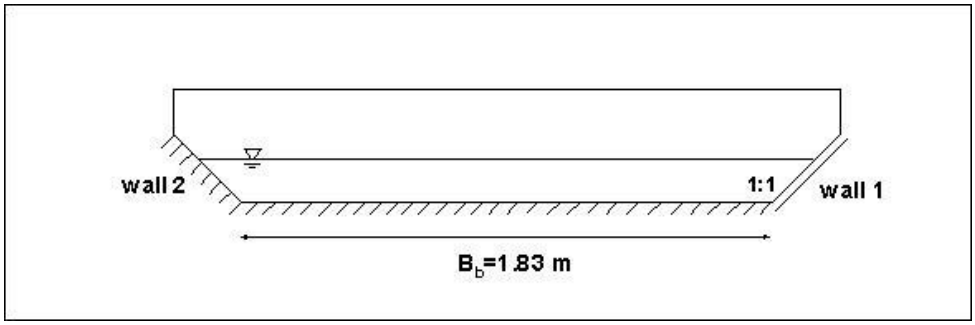

Figure 3.14 S-shaped channel cross-section geometry.

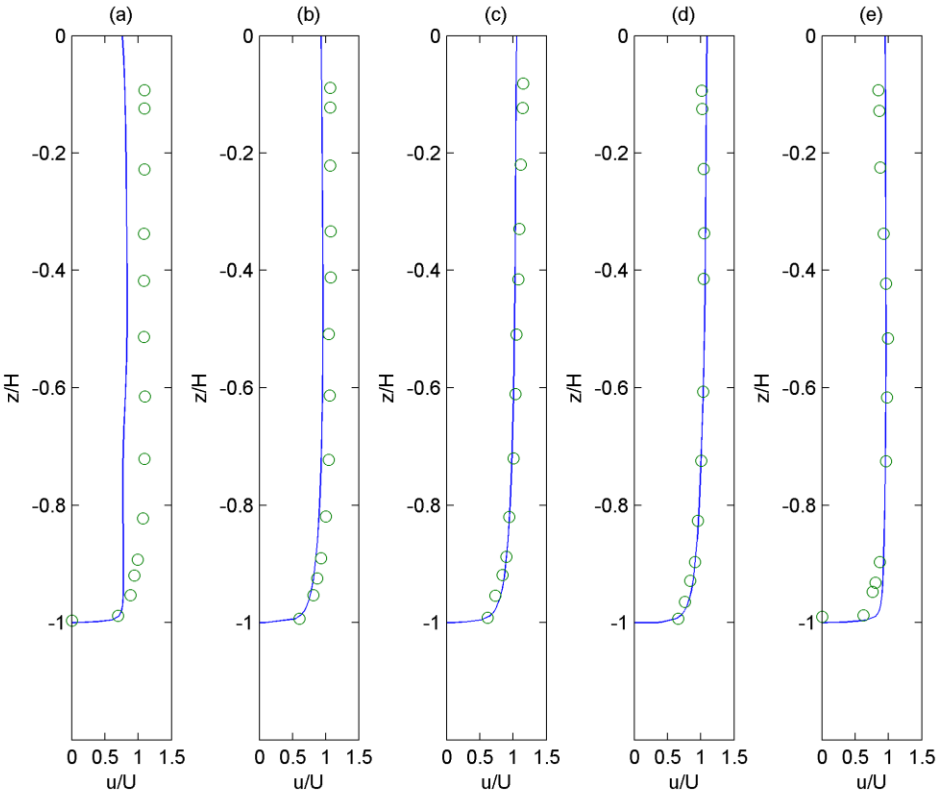

Figure 3.15 Streamwise velocity profiles at section S0 a) η/B=-0.461; b) η/B=-0.307; c) η/B=0.0; d) η/B=0.307; e) η/B=0.461 ○ = experimental data. blue line = numerical model.

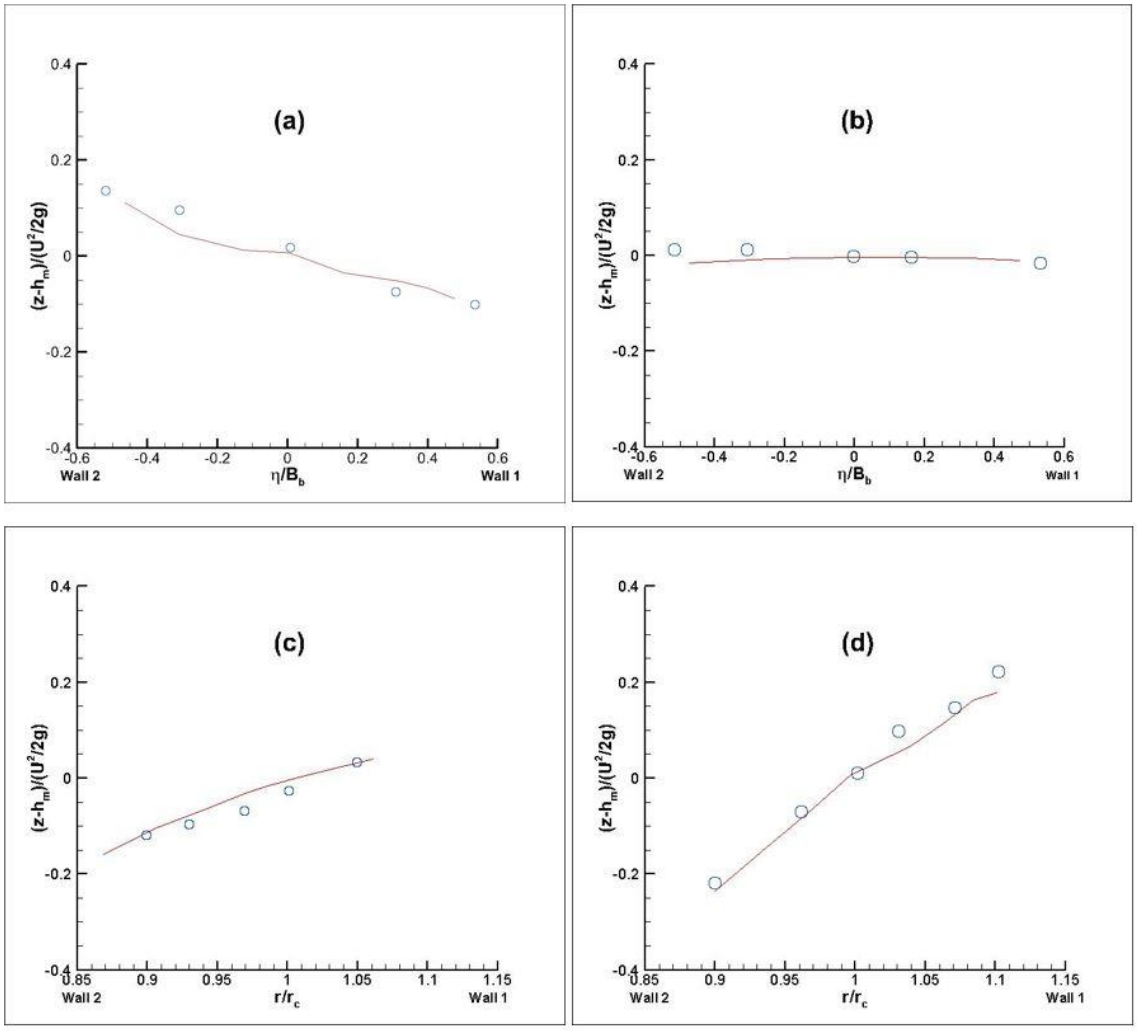

Figure 3.16 Transverse free-surface profiles a) Section S0; b) Section S2; c) Section CII0; d) Section $\pi/4$. ○ = experimental data. blue line = numerical model.

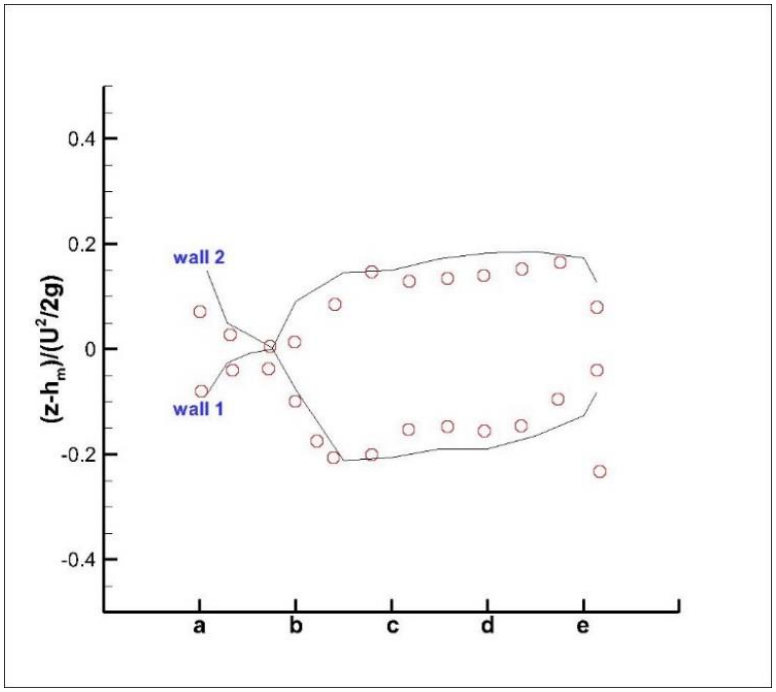

Figure 3.17 Longitudinal free-surface profiles near the two channel banks.○ = experimental data. lines = numerical model.

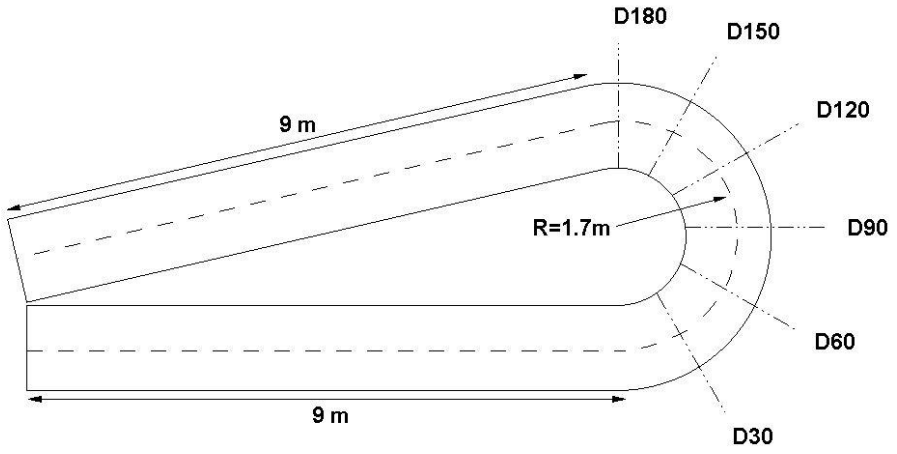

Figure 3.18 General Layout of the 193○ open channel bend experiment of Blanckaert (2002).

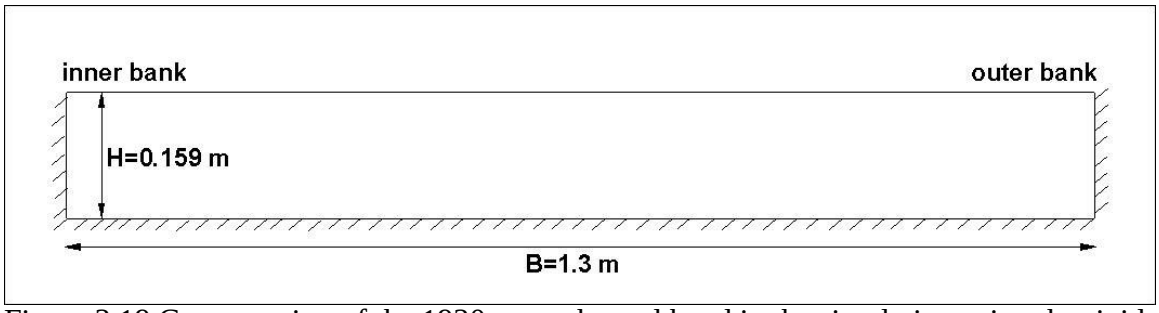

Figure 3.19 Cross-section of the 1930 open channel bend in the simulation using the rigid-lid approximation.

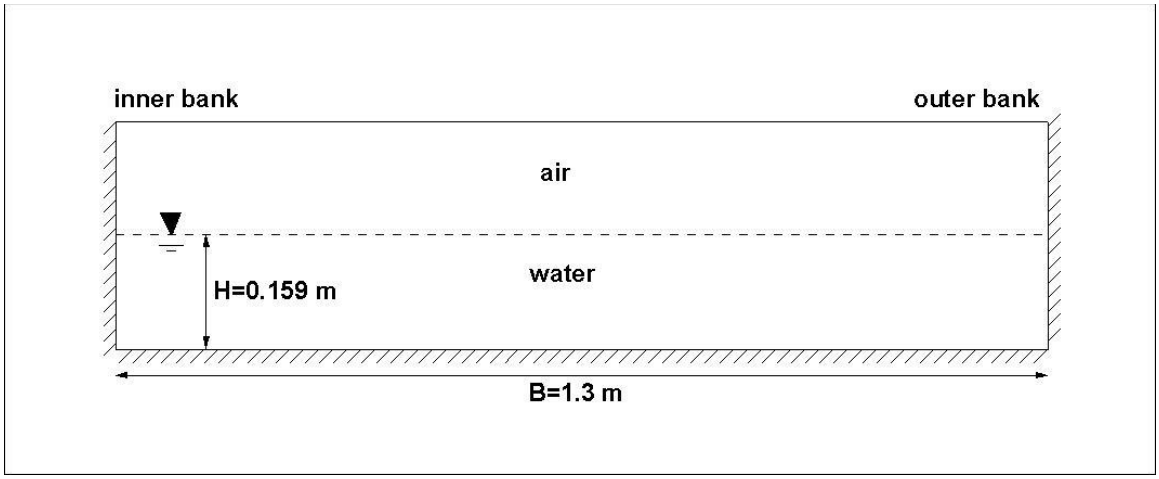

Figure 3.20 Cross-section of the 1930 open channel bend in the simulation using the VOF model.

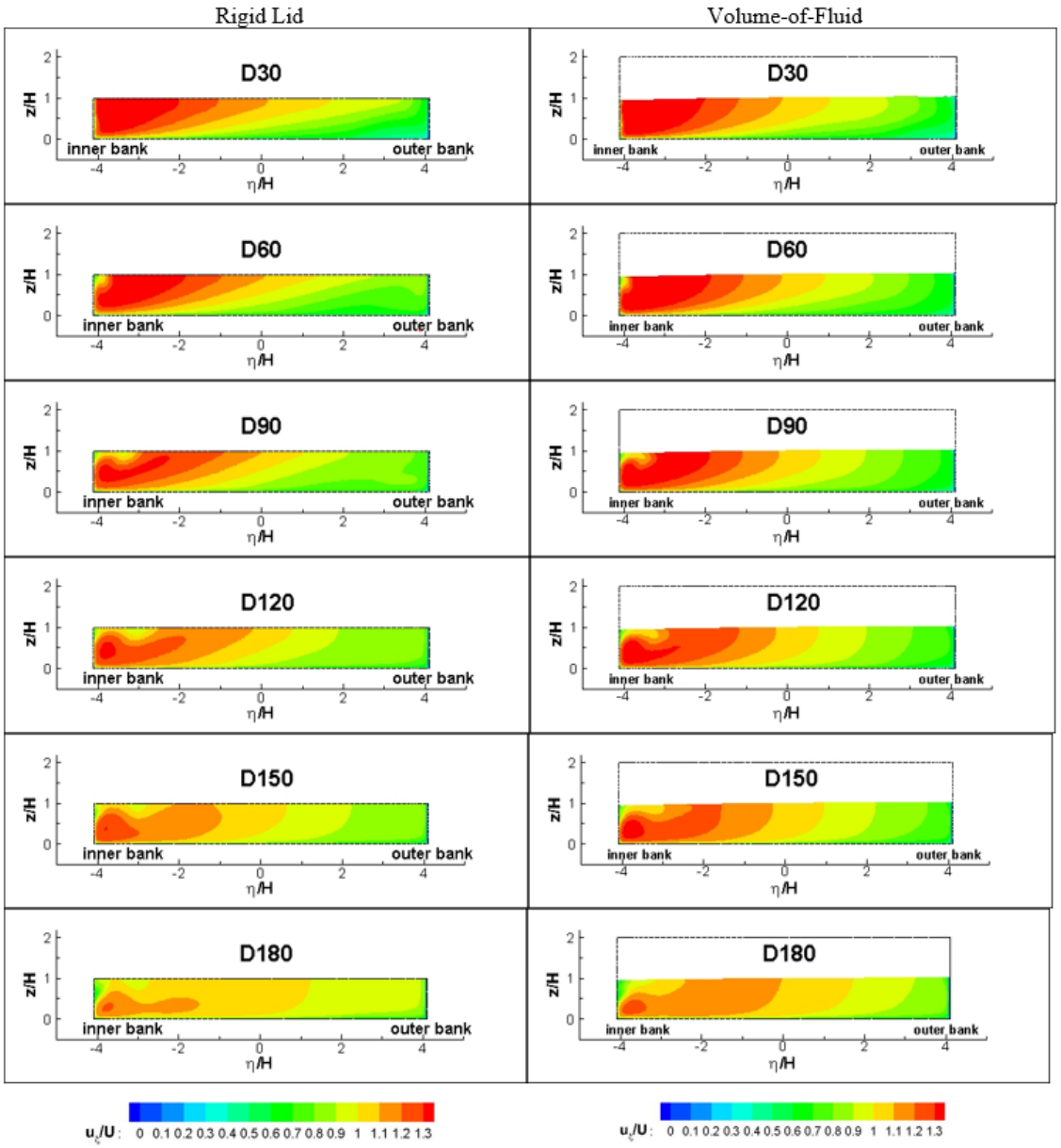

Figure 3.21 Streamwise velocity distributions at specified cross sections in the simulations using the rigid lid approximation and the VOF model.

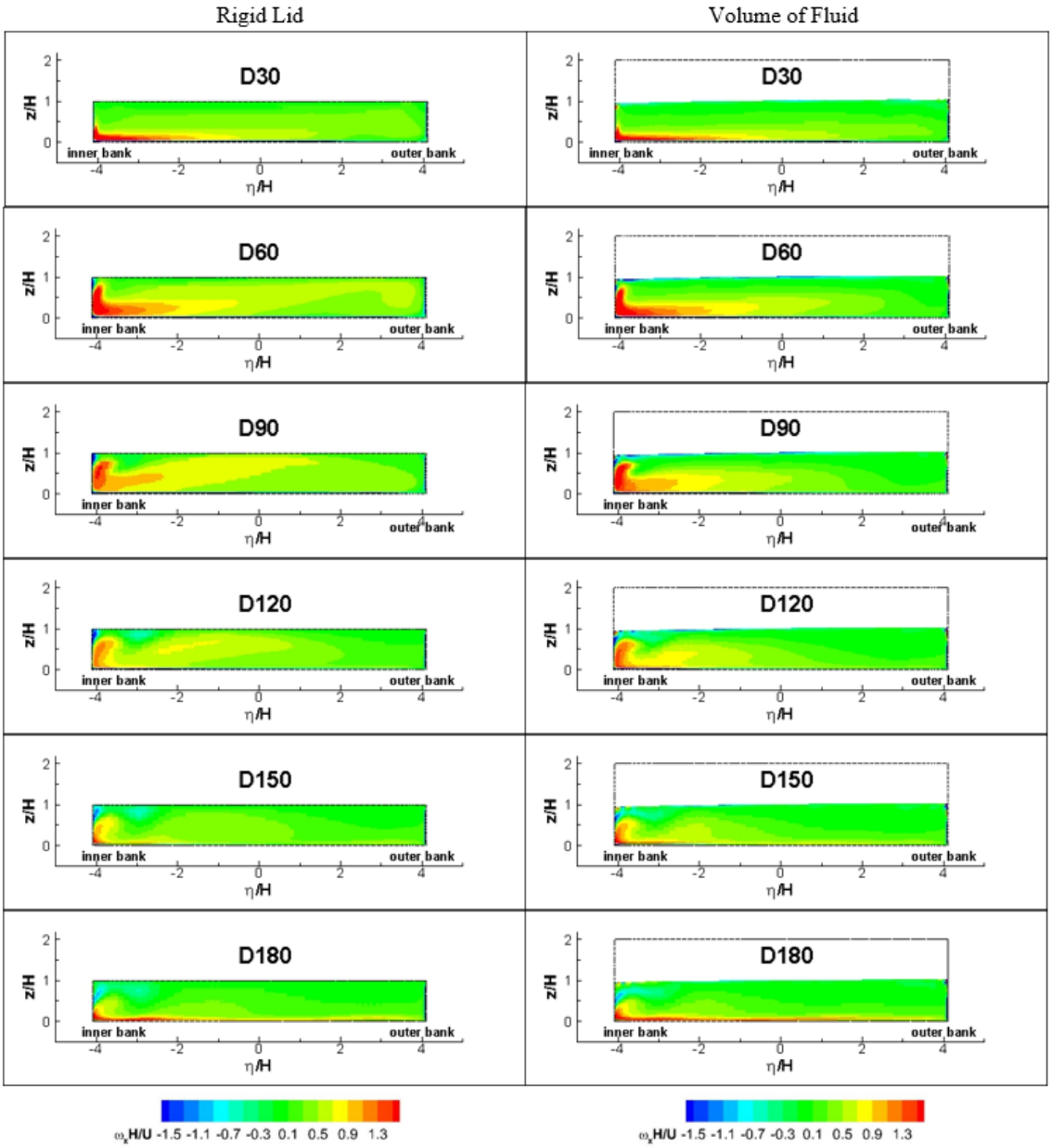

Figure 3.22 Streamwise vorticity distributions at specified cross sections in the simulations using the rigid lid approximation and the VOF model.

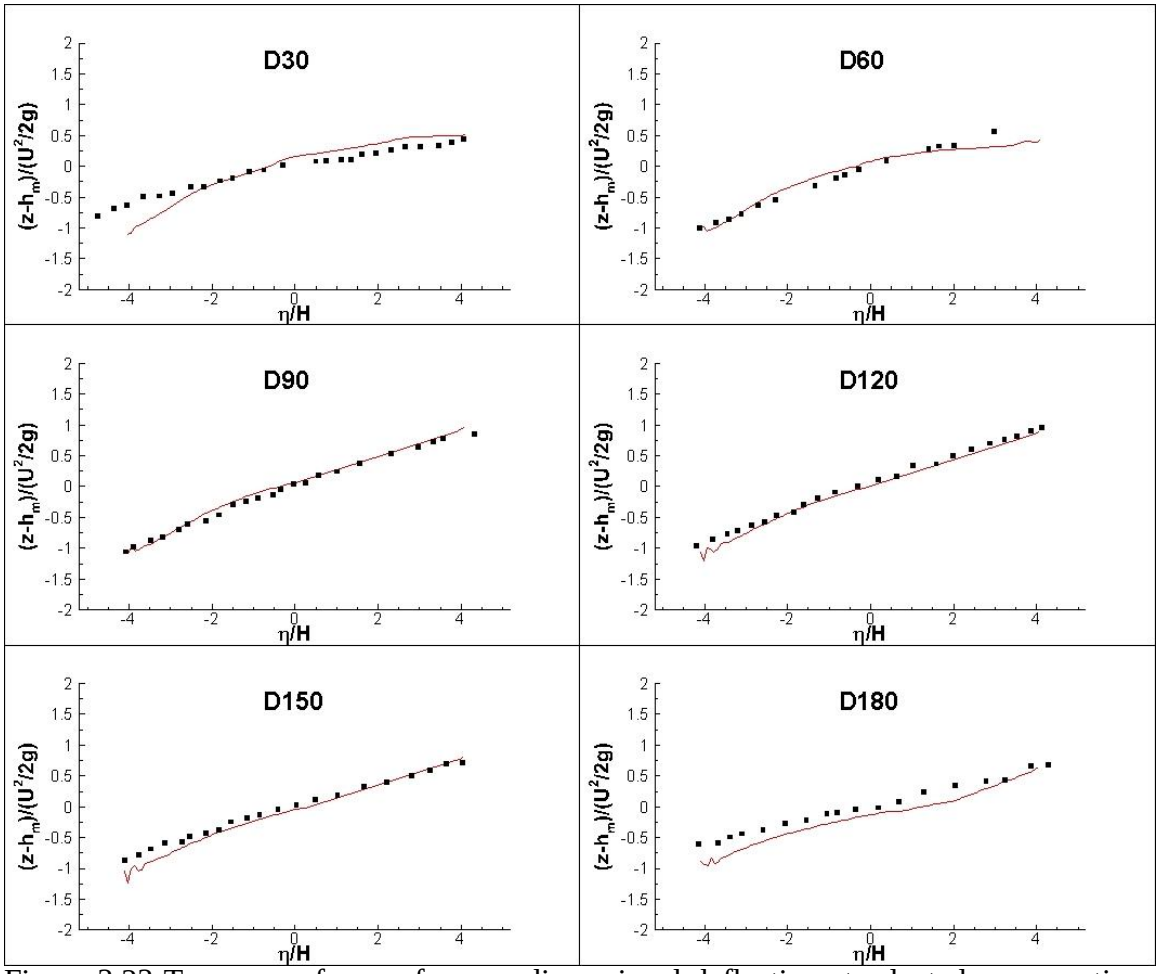

Figure 3.23 Transverse free-surface nondimensional deflection at selected cross sections in the VOF simulation and in the experiment.

CHAPTER 4 APPLICATION OF THE DEVELOPED 3-D MODEL TO PREDICT FLOW IN NATURAL RIVER REACHES

While the developed 3-D model was shown to be able to simulate realistic flow profiles and free-surface deflections in laboratory test cases with simple open channel geometries, its capabilities of accurately simulating flow in natural streams containing hydraulic structures and, in some cases, changes in the flow regime (e.g., from subcritical to supercritical and vice versa) is yet to be investigated. The main objective of the following simulations is to test the model capabilities to simulate flow in river reaches of lengths ranging from 1 km to 18 km under both steady and unsteady state conditions. The complexity of the problems being investigated is increased systematically. Additionally the results obtained with the developed 3-D model are compared to results obtained with other state-of-the-art 3D models as well as 2D depth-averaged models.

The first test case focuses on simulating one of the most common scenarios found in natural river reaches, which is subcritical flow in a river bend. The bend is located within a 1-km reach of the Iowa River near Iowa City. This test case is used to determine what boundary conditions and computational setup work the best for cases when the flow remains subcritical, including at the exit boundaries. The second test case considers flow in a 2-km reach of the Iowa River near Iowa City, with 1 river dam present inside the domain. The objective of the second test case is to test the capabilities of the 3-D model to simulate cases with a hydraulic structure in place that forces the flow to transition from subcritical to supercritical rapidly within the domain of interest. The first and second test cases simulate the flow under steady state conditions. Results are compared with those obtained using other state-of-the-art CFD codes such as FLOW-3D and FLUENT respectively.

The third test case considers the flow in an 18-km reach of the Iowa River near Iowa City in which both steady and unsteady events are simulated. The purpose of this test

case is to assess the accuracy of 2-D depth-averaged solvers to predict flow in river reaches at low flow conditions. The fourth test case considers the flow in a 7-km reach of the Iowa River near Iowa City. Both steady state and unsteady events are simulated at high flow conditions. This test case will serve as a benchmark for assessing the accuracy of 2-D depth-averaged solvers to predict flow and free-surface profiles at high flow conditions when floodplain/main channel interaction becomes important. The chapter ends with an investigation of the efficiency of several flood protection strategies (i.e. installing floodwalls, river dam removals) using the developed 3-D model of the Iowa River near Iowa City.

4.1 Steady flow in a 1-km river reach with realistic bathymetry

A river reach of approximately 1 km of the Iowa River near Iowa City, for which detailed free-surface measurements are available under close to steady state conditions, was selected as the first validation test case. The presence of a flood protection dam (Section 1-1 in Figure 4.1a) upstream of the reach provides accurate information on the temporal variation of the flow discharge. Two other river dams are present at sections 2-2 and 3-3 in Figure 4.1a. As seen from Figure 4.1b, the simulated river reach starts some distance downstream of the flow control dam (Section 1-1) at section 1'-1' and extends until section 2'-2', situated some distance upstream of the first river dam (Section 2-2). Since the first river dam (Section 2-2) is not included in the computational domain, the downstream boundary condition has to be modified to take into account the influence of this first river dam. In addition, a straight extension of approximately 1 km was placed at the end of the 1-km reach to eliminate the recirculating flow convergence problems at the outlet section of the computational domain. Thus, the total length of the computational domain is close to 2 km. Results, however, will only be presented for the first 1 km of

physical domain corresponding to the actual river reach. Figure 4.2 shows the contour plot of the bathymetry elevation of the computational domain.

The main parameters of the simulation are shown in Table 4.1. The Froude number and the Reynolds number are defined with the mean velocity and mean water depth at the inlet section. The simulated flowrate corresponds to low flow conditions with all the flow remaining inside the main channel. The total number of grid cells of the computational mesh is close to 2 million and the Courant number is approximately 0.2.

Table 4.1 Main geometrical and flow parameters for the 1-km Iowa River reach simulation

Flowrate (m^3/s)	167.4
Velocity at the inlet (m/s)	0.44
Depth at the inlet (m)	4.82
Length of main channel (km)	0.85
Length of extension (km)	1
Time step (s)	0.5
Courant number	0.2
Froude number	0.06
Reynolds number	2.12×10^6
Number of grid cells	2.0×10^6

The first task was to explore what boundary conditions need to be employed to accurately predict the free-surface elevation for the given flow conditions. Since the location of the river reach is right upstream of the first river dam (Section 2-2 in Figure 4.1b), the effect of the first river dam on the flow should be accounted for. Two approaches were investigated.

The first approach was to use a zero gradient boundary condition for the pressure and volume fraction function, in which the values are extrapolated at the outlet boundary. The second approach consisted of specifying the volume fraction and pressure distribution at the outlet, which means that one can control the position of the free-surface elevation at

the outlet. Figure 4.3 shows the variation of the free-surface elevation along the centerline of the channel with the two proposed outlet boundary condition treatments, as well as the field data (symbols). When the pressure and volume fraction values are extrapolated to the outlet, the 3-D model is unable to accurately predict the free-surface elevation. The errors are approximately 1.2 m, which is equivalent to 25% of the mean water depth in the channel. This is an indication that the hydraulic structures present in the channel control to a large extent the flow distribution and free-surface profiles.

When the volume fraction and pressure distribution are specified at the outlet boundary, the errors decrease to approximately 2 cm, which is, by practical standards, negligible (less than 0.1%). The predictions are in very good agreement with the field measurements of the free surface elevation when the flow depth is specified at the outlet. This may look as the model needs additional information to obtain the correct solution. However, this is not the case given that the flow is subcritical and controlled from downstream (first river dam). For such cases specifying the flow depth at the outlet boundary is justified.

Figure 4.4 visualizes the distribution of the streamwise velocity at specified cross-sections situated inside the bend part of the channel. Consistent with the pattern generally observed in curved channels, the core of high streamwise velocity moves gradually from the inner bank at the entrance into the region of high curvature to the outer bank toward the exit from the same region. The core of high streamwise velocity is approximately situated over the deepest part of the cross section, as usually observed in bends with scoured bed. Figures 4.6 and 4.7 show the streamwise velocity distribution at 10 representative cross sections. It can be observed that the 3-D model predicts that the core of high stream velocities is situated near the center of the channel in Sections 1 through 3, where no significant curvature effects are experienced by the flow. The core of high velocity starts moving towards the inner bank as the high curvature region is approached (Sections 4 through 8), which is consistent with patterns generally observed in curved channels. As the

flow leaves the bend (Sections 9 and 10), the core of high velocity moves towards the outer bank, where the deepest regions of the channel are also located.

Figure 4.8 shows the mass conservation capabilities of the developed 3-D model in STAR-CCM+. The maximum mass conservation error was close to 8% of the inlet discharge, which is reasonable. It can be concluded that the 3-D model is able to accurately predict the free-surface elevation and streamwise velocity profiles without significant mass conservation errors in curved river reaches with natural bathymetry.

4.1.1 Comparison with FLOW-3D

The developed 3-D model has matched well the limited field experimental data. Comparison with results using other CFD codes can give an indication on which 3-D model performs better for flow in natural river environments applications. The results obtained with the STAR-CCM+ model are next compared with results obtained using FLOW-3D, a state-of-the-art commercial CFD software with deformable free surface capabilities via the VOF method.

The FLOW-3D simulation setup was the same as the one used in the STAR-CCM+ simulation. The inlet boundary was set as a velocity inlet with a specified free-surface elevation; the bottom-left wall and bottom-right wall surfaces were set as wall boundary conditions; the top surface was set as a pressure outlet open to the atmosphere; and the outlet boundary condition was set as a pressure outlet with a fixed free-surface elevation. The number of cells was close to 2 million and the time step was 0.5 s, which corresponded to a CFL number of approximately 0.2.

Figure 4.5 shows the free-surface elevation along the centerline predicted by STAR-CCM+ and FLOW-3D. Both codes predicts a free-surface elevation in excellent agreement with the field data, with errors lower than 0.5%.

Figures 4.6 and 4.7 show the streamwise velocity distributions at the same ten cross sections analyzed in the previous subsection. At Sections 1 through 3, the streamwise

velocity distribution given by STAR-CCM+ predicts that the core of high velocity is situated near the center of the channel, while FLOW-3D predicts the core of high velocity is located closer to the outer bank. Sections 1 through 3 are located in the straight region of the channel, upstream of the bend region. Their cross sections are fairly regular with no significant changes in the bathymetry. There is no evidence to suggest that the core of high velocity should be located near the outer bank. In Sections 4 through 8, the core of high streamwise velocity moved toward the inner bank, even though the deepest parts of the channel are located close to the outer bank. The flow in these sections is adjusting to the local channel bathymetry right downstream of the dam, as the flow is subcritical. This behavior can be observed in both STAR-CCM+ and FLOW-3D solutions. Finally, as the flow leaves the bend region, it moves towards the deepest parts of the channel. The flow has a slight tilt towards the outer bend due to the adverse pressure gradients caused by the bend. It can be concluded that both STAR-CCM+ and FLOW-3D are capable of capturing this effect.

Even though the streamwise velocity distributions are comparable in the solutions obtained using the two CFD codes, their mass conservation capabilities differ greatly. The legend of the contour plots of Figures 4.6 and 4.7 shows that the streamwise velocity values predicted by FLOW-3D are greater than the ones calculated by STAR-CCM+. A more compelling argument is presented in Figure 4.8 in which the mass errors are shown at each cross section for the STAR-CCM+ and FLOW-3D solutions. STAR-CCM+ shows a maximum mass error of 8%, while FLOW-3D has a maximum mass error of approximately 50%. It is expected that these errors can be reduced by reducing the time step of the simulation, increasing the number of subiterations per time step and/or refining the computational mesh in the region of interest (i.e. main channel of the river). However these approaches significantly increase the computational cost for the simulation. Due to the mass conservation problem found for the FLOW-3D solution, one can conclude that STAR-CCM+ is the better code for this type of applications.

4.2 Steady flow in a 2-km river reach with an inline hydraulic structure

A river reach of approximately 2 km of the Iowa River near Iowa City was selected as the second validation test case for applications in natural river reaches. The flow conditions are the same as in the previously discussed test case. As seen from Figure 4.9a, the simulated river reach starts some distance downstream of the first river dam at section 1'-1' and extends until section 2'-2', situated some distance downstream of the second river dam (3-3). A close-up of the location of the computational domain is shown in Figure 4.9b. Since the flow after the second river dam is subcritical, the downstream boundary condition needs to be modified to accurately predict the free-surface elevation. Consistently with the previous test case, an extension of approximately 1 km was included at the end of the 2-km reach to get rid of recirculating flow problems at the outlet section of the domain. The total length of the computational domain is close to 3-km. The results will only be presented for the first 2-km. Figure 4.10 shows a contour plot of the bathymetry/topography elevation data used to create the computational mesh. Figures 4.11 and 4.12 show the bathymetry distribution upstream and downstream of the river dam, respectively. The region around the river dam is characterized by a sudden drop in the bathymetry elevation, making the bathymetry upstream and downstream of the river dam to have very different elevation levels.

The main parameters of the simulation are shown in Table 4.2. The Froude number and the Reynolds number are defined with the mean velocity and mean water depth at the inlet section. The total number of grid cells of the computational mesh is close to 3 million and the Courant number was close to 0.2.

Table 4.2 Main geometrical and flow parameters for the 2-km Iowa River reach domain

Flowrate (m^3/s)	167.4
Velocity at the inlet (m/s)	0.44
Depth at the inlet (m)	4.82
Length of main channel (km)	0.85
Length of extension (km)	1
Time step (s)	0.5
Courant number	0.21
Froude number	0.06
Reynolds number	2.12×10^6
Number of grid cells	2.0×10^6

Two types of outlet boundary conditions are tested. The first method extrapolates the values of the pressure and the volume fraction function to the outlet boundary, therefore assuming uniform steady flow. The second approach differs from the one used in the previous test case. When specifying a free-surface elevation at the outlet, one implicitly assumes that the flow is uniform and steady. Under most conditions, this holds true. However, if one were to deal with highly unsteady flows and/or channel/floodplain compound flow, those assumptions may be broken. A more flexible way was sought that would be able to simulate a larger range of flow conditions. In the second approach, a small negative slope was included in the 1-km extension at the end of the domain of interest. By including such negative slope, the free-surface elevation needs to increase in order to overcome this smooth obstruction in the flow. With this approach, the variables at the outlet are extrapolated as usual. It was found that the second approach reproduced the streamwise free-surface elevation with higher accuracy (maximum error of 4 cm). The results obtained with the latter outlet treatment are shown in Figure 4.13.

To explain the flow features, streamwise velocity distributions and vector plots are analyzed next. Figure 4.14 shows the streamwise velocity distributions at eight cross

sections located upstream of the river dam. Figure 4.15 visualizes the streamwise velocity distribution in four cross sections located downstream of the river dam. Figures 4.16, 4.17 and 4.18 show vector plots throughout the domain. It is observed that when water enters the domain, the velocity distribution is very regular, with the core of high velocity situated near the center of the channel. Some flow disturbances are observed in Sections 1 and 2, but they might be due to their location close to the inlet where the flow is still adapting to the bathymetry. As the flow moves downstream, it encounters a big depression. As a result, the core of high velocity moves towards the deepest part of the channel. This creates recirculating regions on both banks of the channel, as observed in Figure 4.16. As the flow leaves the depression region, the core starts moving towards the center of the channel, as observed in Sections 3 through 8. While doing so, a shallow region is encountered at the right bank, which creates recirculating flow right downstream of this shallow region (Figure 4.17). This region can also be observed in Section 5 in Figure 4.19. Once the flow had fully readjusted from the effects of the bed depression and the shallow region near the right bank, the core of high velocity is again situated near the center of the channel.

Right after Section 8, the flow encounters the river dam. The river dam causes the flow to become supercritical, inducing a hydraulic jump right downstream of it. A typical hydraulic jump creates a significant recirculating flow region near the free surface, while the core of high velocity travels near the bed and eventually resurfaces some distance downstream. Moreover, the hydraulic jump in this specific test case occurs in a region where the channel width decreases, especially near the right bank, as seen in Figure 4.13. The deepest parts, which are located near the center of the channel, have a lower velocity magnitude compared to the shallower regions, which are located near the banks This is due because the velocity induced by the sudden drop of elevation at the dam is distributed over a larger depth in the deeper regions compared to the shallower regions. Thus, the center of the channel will experience slower velocities compared to the banks. Furthermore the contraction of the channel width increases the velocity near the banks, as seen in Sections

9 and 10 in Figure 4.20. These features eventually fade away and the flow transitions to a more typical open channel cross-sectional distribution, with the core of high velocity located near the center of the channel, as shown in Sections 11 and 12 in Figure 4.20.

4.2.1 Comparison with FLUENT

Even though the present 3-D (STAR-CCM+) model showed a better performance in the previous test case when compared to FLOW3D simulation results, it is of interest to investigate how its performance compares to other industry standard CFD codes. FLUENT, just as FLOW3D, is a state-of-the-art CFD code with deformable free-surface capabilities via the Volume-of-Fluid method.

The setup of the FLUENT model was very similar to the setup used in the STAR-CCM+ model. While the boundary conditions were the same as the ones used in STAR-CCM+, the flow modules were slightly different, since the implicit unsteady solver available in STAR-CCM+ had to be replaced by the explicit unsteady solver in FLUENT. Explicit unsteady simulations are highly restricted by the time step, since they are conditionally stable and are prone to numerical instabilities. On the other hand, implicit schemes are much more stable, thus relaxing the time step constraint, which may be a huge practical advantage. FLUENT, in turn, uses a variable time step that adjusts automatically to the flow conditions. In the present solution, the time step was allowed to increase to the maximum value beyond which the solution starts diverging. The fixed time step used in STAR-CCM+ was 0.5 s while the maximum time step for which the FLUENT solution remained stable was 0.05 s, which is 10 times smaller. The number of grid cells was around 2 million cells in both simulations.

Figure 4.13 compares the streamwise free-surface elevation among STAR-CCM+, FLUENT and field data. FLUENT performs slightly better than STAR-CCM+. However, the differences are small. The maximum error in terms of predicting the free-surface elevation was approximately 4 cm in the STARCCM+ solution. The FLUENT solution

showed a maximum error of 0.8 cm. This comes as no surprise, since a lower time step guarantees a more exact solution for all flow variables.

Figures 4.19 and 4.20 compares the streamwise velocity distributions at twelve representative cross sections. Sections 1 and 2 show significant differences. Around Section 1, FLUENT predicts the core of high streamwise velocity is situated near the bottom of the channel, close to the left bank. A similar patterns is observed at Section 2. In the STARCCM+ solution, Sections 1 and 2 show that the core of high velocity is situated near the center of the channel. There is no physical evidence to support the behavior shown by FLUENT. These differences might be due to the small distance to the inlet section, indicating that the flow is still adjusting to the inlet boundary condition. Sections 3 through 5 show similar streamwise velocity distribution with very small differences between the STAR-CCM+ and FLUENT solutions. This indicates that both CFD codes are able to reproduce the flow physics created by the sudden changes in bathymetry present in this region of the river reach. The velocity distributions look more physical in STAR-CCM+ since they are able to better capture the boundary layer effect near the wall. Sections 6 through 8 show some differences, even though both STAR-CCM+ and FLUENT predict that the core of high streamwise velocity is situated near the center of the channel. FLUENT is unable to predict accurately the boundary layer effect and distributes the velocity more evenly in the channel compared to the STAR-CCM+ results. STAR-CCM+ predicts a more concentrated core of high velocity and captures better the boundary layer effect on the velocity distribution.

Sections 9 through 12 are located downstream of the first dam. In Sections 9 and 10, both STAR-CCM+ and FLUENT predict that the core of high streamwise velocity is situated near the banks. This supports the fact that these features are caused mainly by bathymetry changes and by the hydraulic jump, both of which are captured by FLUENT and STAR-CCM+. Sections 11 and 12 show significant differences. STAR-CCM+ predicts that the flow started reattaching in Section 11 and has fully reattached at Section 12.

FLUENT, on the other hand, predicts that the flow is not reattaching and the magnitude of the near-bank cores of high velocity are increasing. This creates negative velocities near the bottom center of the channel (global mass conservation). Such behavior is extremely rare in natural river environments. Based on the above discussion, one can conclude that STAR-CCM+ better predicts the flow in a river reach with hydraulic structures in place, such as a river dam, even when the flow regime changes in the channel (e.g., subcritical to supercritical or vice versa).

4.3 Flow in a 18-km river reach with two inline hydraulic structures and one tributary

The third test case considered is an 18-km reach of the Iowa River near Iowa City. The main hydraulic features, such as the two hydraulic structures (i.e. river dams) and the main tributary, are included in the model. Figure 4.21 shows the location and extent of the computational domain. As seen from Figure 4.21, the computational domain starts right downstream of the flood control dam (Section 1-1) where a river gaging station is present (Section 1'-1'). The gage provides accurate measurements of stage and discharge over time. The end of the computational domain is located some distance downstream of the second river dam (Section 2'-2'), which is close to the south city limit of the city of Iowa City. The arrow points at Clear Creek, the main tributary feeding into the Iowa River near Iowa City. The inclusion of Clear Creek is of great importance due to the significant backwater effect from the Iowa River into Clear Creek during high flow conditions. Finally, a second river gaging station is also found within the domain of interest, approximately 100 m downstream of the second river dam.

The main parameters of the simulation are shown in Table 4.3. The Froude number and the Reynolds number are defined with the mean velocity and mean water depth at the inlet section (low flow). The total number of grid cells is close to 12 million and the Courant number is close to 0.2. The computational grid had to be optimized significantly to limit

the number of grid cells (i.e. in the order of 10 million) needed to mesh the domain. The optimization was accomplished by coarsening the horizontal grid resolution while maintaining enough vertical grid resolution in areas of interest (main channel and floodplain).

Table 4.3 Main geometrical and flow parameters for the 18-km Iowa River reach test case

Flowrate (m^3/s)	245
Velocity at the inlet (m/s)	0.51
Depth at the inlet (m)	5.45
Length of main channel (km)	18
Length of extension (km)	1
Time step (s)	0.5
Courant number	0.2
Froude number	0.07
Reynolds number	2.78×10^6
Number of grid cells	12.0×10^6

The model used to perform 2-D simulations of the same case was SRH-2D. The extent of the domain in the 2-D simulation was the same as the one used in the 3-D simulation. The 2-D model was provided by the Iowa Flood Center (IFC) and was calibrated for both low and high flow conditions. The outlet boundary condition is based on a specified rating curve at the outlet. The biggest differences between the two models are the geometry near the river dams and the fact that the 2-D model has included buildings/obstructions in the computational domain. The 3D model takes into account the exact shape of the dams based on old construction blueprints, while the 2-D model accounts for the presence of the dams by including a bump in the geometry with the same crest elevation as the constructed river dams. The 2-D model also has empty regions that are

used to represent existing buildings over the floodplain and bridge piers in the main channel.

The bathymetry/topography information is shown in Figure 4.22. It also includes the locations of 29 cross sections that will be used to analyze the solution. The cross sections are approximately equally spaced across the domain. Sections 1 through 15 are located upstream of the first river dam. Sections 16 through 27 are located downstream of the first river dam and upstream of the second river dam. Section 28 and 29 are located downstream of the second river dam. Figure 4.23 shows the locations of the two river dams and of Clear Creek, the main tributary, within the domain of interest.

For this specific test case, the main comparison that can be performed is in terms of the free-surface elevation between the 3-D and 2-D models. Figure 4.24 shows the free-surface elevation along the centerline of the channel for the 18-km reach predicted by the two models, as well as field data measurements. Between the inlet boundary and the first river dam, the 2-D model clearly underestimates the free-surface elevation with respect to field data, whereas the 3-D model (STAR-CCM+) follows very closely the field data, especially in regions close to the inlet. Around halfway in between the inlet boundary and the first river dam, the predicted free-surface elevation by the 3-D model starts to underestimate the elevation of the free surface. In between the first and second river dam, it is unclear which model represents the best the position of the free surface. The 3-D model overestimates the elevation close to the first river dam and it underestimates it in regions situated close to the second river dam. The 2-D model follows very closely the field data near the first river dam and it underestimates the free-surface elevation close to the second river dam. Finally, downstream of the second river dam the 3D model predicts the level of the free surface with more accuracy compared to the 2-D model, which consistently underestimates the free-surface elevation in the same region. On average the errors associated with the 3D model were in the order of 5% whereas the errors of the 2D model were in the order of 8% with respect to field data. Overall, it is concluded that the 3-D

model is able to predict the location of the free surface in a river reach of approximately 18 km with arguably better results compared to a calibrated 2D model.

While the location of the free surface is of most importance for flood modelling, an analysis of the velocity distribution is also relevant. Such task can be accomplished by examining the streamwise velocity distributions in the 3-D simulation, and by comparing velocity vectors, depth-averaged velocity profiles and unit-discharge profiles between the two simulations. Velocity vectors at the free-surface can be used as evidence to single out regions where the two solutions look very different. The 3-D and 2-D model results show visually no striking differences. This is why only vector plots at the free surface corresponding to the 3-D model results are shown (Figure 4.25 through Figure 4.33). These plots will be used to show where a specific cross section is situated within the domain of interest. The velocity vectors showed in the 3-D model correspond to vectors plotted on the isosurface of the volume fraction of water equal to 0.9. If one were to use the isosurface defined by a volume fraction of water being equal to 0.5, the vectors would be influenced by the air velocity profile. The bathymetry shown in the 3-D model vector plots is blanked inside regions with a volume fraction of water greater than 0.9, to make the results consistent with the vector isosurface. In addition, regions situated near the two river dams were omitted since the geometries differ in the two models.

The fact that the vector plots show little to no difference, does not necessarily guarantee the behavior of the flow is quasi 2-D at all locations. 3-D effects can become more noticeable when analyzing the streamwise velocity distributions at different cross sections. In order to do a one-to-one comparison, the 3-D velocity profiles were depth-averaged and the comparison can be made in terms of depth-averaged velocity profiles and/or in terms of unit discharge (depth-averaged streamwise velocity * depth). The main drawback of comparing depth-averaged velocity profiles is that they can differ significantly if the free-surface elevations predicted by the two models is not the same. The unit discharge, however, provides information on how the flowrate is distributed along the cross

section and takes into account both depth-averaged velocities, as well as water depth, which is a function of free-surface elevation; thus it was chosen as the desired function for comparing the two numerical results. Overall it was found that 22 out of the 29 cross sections showed really good agreement between the 3-D and 2-D unit-discharge profiles (less than 0.5% difference), meaning that in most of the Iowa River near Iowa City, the river behaves as a shallow environment. In order to understand the differences found at the 7 cross sections that showed some noticeable disagreement (between 5% and 20% difference) between the two simulations, several quantities were calculated and are shown in Table 4.4.

Table 4.4 Summary of agreement between 3-D and 2-D results for the specified 29 cross sections

Section number	**Straight/Curved**	**Location within bend**	**Main Channel Width/Depth**	**Main Channel Radius/Width**
2	Curved	Middle	25	2.5
8	Curved	End	15	2.5
9	Curved	Start	18	5
11	Curved	End	18	5
12	Curved	Start	18	2
13	Curved	Middle	20	2
14	Curved	End	18	2

The width to depth ratio gives a sense of the shallowness of the cross section. Usually it is assumed that shallow conditions are established when the width to depth ratio (W/D) is greater than 25; however no clear cutoff can be made. The ratio of the radius of curvature to the channel width (R/W) gives an indication of how curved the bend is. The lower the value, the more curved the bend is. Typically an R/W value less than 4 means very strong curvature effects, R/W between 4 and 8 means moderate curvature effects and greater than 8 means low curvature effects (Zeng et. al., 2010). Finally, Table 4.4 also

shows if the cross section is located in a straight or a curved reach and if it is located at the start, middle or end of the bend. This information can help explain the differences between the 3-D and the 2-D solutions.

Good agreement is expected at all cross sections located in straight reaches within the domain of interest and some differences are expected in cross sections located within and/or in the vicinity of bends. However, this is not always the case. Out of all cross sections located within bends, only cross sections 2, 8, 9, 11, 12, 13 and 14 shows noticeable differences between the 3-D and 2-D unit-discharge profiles. This would suggest that in the remaining cross sections, the curvature effects are not strong enough to make the 2-D results deviate from the 3-D (depth-averaged) solution. The W/D ratio in all these cross sections ranges from 15 to 25, indicating that the flow in that region is fairly shallow. Therefore the differences can be attributed to strong curvature effects, which for curved open channels are generally observed when the curvature radius to width ratio is less than 4. It was no surprise to find that in the cross sections that showed good agreement between the 3-D and 2-D models for the unit-discharge profiles the Curvature Radius to Width ratio was larger than 5 and the Width to Depth ratio was greater than 25. This means that a 2-D Shallow Equations solver can accurately capture the flow as long as the geometry is shallow (large Width to Depth ratio) and secondary flow induced by channel curvature is fairly weak.

4.3.1 Unsteady wave propagation

During the June-July 2008 period Eastern Iowa experienced the biggest flood in its history causing significant damage to several cities, including Iowa City. In the days previous to the flood event, the flow in the Iowa City reach of the Iowa River was quasi-steady with a flowrate equal to the one used for the previous steady state simulation. Once the flooding event started, it lasted for approximately a whole month. However, for validation purposes, only the first three days of the unsteady flooding event will be

analyzed. The hydrographs of three gaging stations located near the inlet section, right downstream of the second river dam and in Clear Creek are shown in Figure 4.34, as well as 11 time instances that will be used later for a more detailed analysis of the solution.

When dealing with a realistic flooding event, it is important to capture the time to peak of the event. If a proposed flood inundation model is unable to capture accurately the time to peak of a flood event, its results are of little to no use since the time to peak is directly related to the peak inundation being experienced. Therefore, the first validation will be in terms of the hydrograph reproduced near the USGS gaging station located approximately 100 m downstream of the second river dam. This location was chosen since the other two gaging stations were used to specify the inlet boundary conditions for the Iowa River and Clear Creek. As seen from Figure 4.34, the 3-D solution is capable of accurately predicting the flowrate at the same location of the USGS gaging station. The time to peak for the two peaks observed in the hydrographs were accurately captured with no clear delay or rush with respect to the recorded flow rates. However, the flowrates exhibit fluctuations around the desired values. The nature of these fluctuations is unknown, but most likely they are caused by the way the VOF method works. During an unsteady event, cells are being filled or emptied with water as the simulation progresses and so the flowrates and volume of water stored in the domain are directly related to the grid cell size. For the simulation in question, the grid cells size are relatively large implying that emptying and/or filling up of cells have a noticeable influence on the flowrates and total volume of water. Since the flow is mainly controlled by the presence of the two river dams, it can be safely assumed that when the flowrate is increased, the river dams will create a backwater effect to regions situated upstream of them. This backwater effect can propagate as a wave and so the emptying/filling up of the cells could have a wave-like behavior. This is most likely the explanation of the observed fluctuations of the predicted flowrates.

During the unsteady hydrograph propagation detailed free-surface elevation data was only available for the initial conditions (steady state conditions). Thus, the comparison

will be performed between the 3-D and 2-D results. Figure 4.37 shows the free-surface elevation at the 11 specified time instances during the unsteady event, as well as at steady state. To assess the performance of the two models, the relative error between the 2-D simulation with respect to the 3-D simulation was calculated in three regions of the computational domain: upstream of the first river dam, in between the first and the second river dam, and downstream of the second river dam. The errors are shown as percentages of the depth predicted by the 3-D model, since it is assumed that the 3-D model is more accurate than the 2-D model based on the preliminary test cases. The letters O and U mean "overestimate with respect to the 3-D model" or "underestimate with respect to the 3-D model" respectively. For instance, O(1%) means that the free-surface elevation predicted by the 2-D model overestimates by 1% of the mean channel depth with respect to the 3-D model prediction. At steady state (Time 0), the 2-D model is, on average, underestimating by approximately 8% the mean channel depth predicted by the 3D model. As the unsteady wave passes through the domain and the flowrates increase, this behavior starts to switch in the other direction. A small, but consistent, trend is observed, in which the depths predicted by the 2-D model become larger than the ones predicted by the 3-D model. At the latest time (Time 11), the 2-D model is consistently overestimating with respect to the 3-D model. While the percentages of overestimation at the latest time look relative low, the overall percentage change from Time 0 to Time 11 is quite noticeable, being as high as 10% with a mean value of 9%. The analysis of the time evolution of the free-surface elevation concludes that the 2-D model tends to overestimate the water elevation as the flowrates increase compared to those obtained using a 3-D model.

When comparing the unit-discharge profiles, it was found that cross sections that showed good agreement at steady state conditions also showed good agreement throughout the duration of the unsteady event. Figure 4.35 shows the unit-discharge profiles at 8 cross sections that showed good agreement at initial conditions, as well as at peak flowrate conditions during the unsteady event. It is observed that at both times the agreement

between both computational results is outstanding. However, Figure 4.36 shows that the agreement between the two simulations decreases with increasing flowrate at the cross sections that showed bad agreement between the two simulations at initial conditions.

Overall, only 7 cross sections out of a total of 29 showed clear differences between the velocity profiles in the two simulations for relatively low flow conditions. The differences are attributed to the level of curvature of the curved parts of the river reach. At high flow conditions, the reason for the differences can be multiple due to three-dimensional effects caused by the shear layer induced by the interaction between the main channel and its floodplain, which increases the overall three dimensionality of the flow field. While the Iowa River near Iowa City tends to acts mostly as a 2-D environment for low flow conditions, its behavior for high flow conditions is yet to be investigated and it is the focus of the next test case.

4.4 Flow in a 7-km river reach with two inline hydraulic structures and one tributary

To better investigate the accuracy of 2-D depth averaged models for flood propagation, simulations at high flow conditions were conducted. While simulating the full extent (18 km) would be the optimum choice, a sub-section of the entire domain was chosen due to computational constraints. When choosing the desired sub-section several considerations were taken into account. The first consideration was that all main hydraulic features of the full Iowa River domain had to be present in the smaller domain. The second consideration was that the desired shorter reach should show good agreement between 3-D and 2-D depth-averaged velocity profiles for low flow conditions such as to clearly observe any possible new differences. The third and final consideration was that the agreement between the predicted free-surface elevations by the 3-D and 2-D models should be very good. A section of 7-km of the Iowa River near Iowa City that satisfied these considerations was chosen for the following analysis (Figure 4.38). The 7-km reach starts

some distance upstream of the first river dam and extends some distance downstream of the second river dam. Figure 4.38 also shows the location of 8 cross sections that will be used for a more detailed analysis.

Figure 4.39 shows the bathymetry/topography information used in the 3-D and the 2-D models, respectively. The bathymetry/topography data used in the 3-D model had a constant resolution of 5 m inside the main channel and a variable resolution of 10-20 m over the floodplain. On the other hand, the 2-D model used a variable resolution between 5-20 m everywhere in the domain. The 2-D model also includes the presence of several buildings on the floodplain. It is expected, however, that these structures will not affect the free-surface elevation and velocity profiles in the main channel significantly. The mentioned buildings can be observed in Figure 4.39 (b), as they are represented as empty spaces in the domain. The lateral extent of the 2-D model is somewhat smaller than the lateral extent of the 3-D model. This difference will not affect the results, since the extent of the 2-D model includes most possible inundation scenarios.

Steady-state conditions were simulated for a flowrate of approximately 1150 m^3/s, which corresponds to flow conditions close to the peak flowrate experienced during the flood of 2008. The average velocity at the inlet was approximately 2.5 m/s with a corresponding depth of approximately 7 m. The CFL number was kept constant at 0.2 by decreasing the time step to 0.1 s to maintain numerical stability. Table 4.5 shows the main parameters of the simulation. Once steady state results were obtained, a sinusoidal unsteady wave with a flowrate amplitude of 600 m^3/s was propagated into the domain (Figure 4.40).

Table 4.5 Main geometrical and flow parameters for the 7-km Iowa River reach 3D simulation

Flowrate (m^3/s)	1150
Velocity at the inlet (m/s)	2.43
Depth at the inlet (m)	6.95
Length of main channel (km)	7
Length of extension (km)	1
Time step (s)	0.1
Courant number	0.2
Froude number	0.3
Reynolds number	16.9×10^6
Number of grid cells	8×10^6

Detailed free-surface elevation data were not available for steady state conditions. The only available information available was data from the USGS gage located 100 m downstream of the second river dam. For the specified flowrate, a corresponding free-surface elevation can be obtained for the location of the gage. While only a single point is used for data comparison, the comparison can provide valuable information on the accuracy of the numerical models. Figure 4.41 shows the free-surface elevation distribution along the centerline of the main channel for the 7-km reach obtained using the 3-D and 2-D models for both steady state and peak flood extent, as well as the relative location of the USGS gage and the corresponding free-surface elevation point for steady state conditions. Both the 3-D and 2-D models predict a free-surface elevation value very close (within 5 cm) to corresponding elevation obtained using the USGS rating curve. However, the free-surface elevation profile varies noticeably between the two simulations. On average, the 2-D simulation predicts a higher elevation compared to the 3-D simulation. The differences

are up to 0.4 m for distances between 3500 m and 5000 m. This behavior is consistent with what was concluded based on analysis of the evolution of the free-surface elevation during the unsteady wave propagation for low flow conditions. In that case, it was observed that the higher the flowrate, the more the 2-D model tends to overpredict the location of the free surface with respect to the 3-D model.

During the propagation of the unsteady wave, the differences become larger at peak flood extent (Time = 3.5 hr) compared to steady state results (as high as 0.75 m) across the entire domain. For instance, at approximately the same location (Distances between 3500 m and 5000 m), the differences grow from 0.4 m at steady state to 0.75 m at peak flood extent. Most likely, the differences are due to the reduction of cross sectional area caused by the inclusion of buildings in the 2-D model geometry, as well as the mesh resolution in the vertical direction in the 3-D model. The inclusion of buildings not only decreases the cross sectional area available for channel flow, it also decreases the available space for inundation. These two effects combined means that for the same flowrate, the 2-D model needs to inundate more in order to have a higher free-surface elevation and increase the corresponding cross-sectional area available in regions where buildings are present. On the other hand, the vertical mesh resolution in the 3-D model determines the resolution of the free-surface elevation, which is function of the cell size in the vertical direction.

While looking at the streamwise distribution of the water elevation gives a sense on how the two models compare, it tells little about the areas inundated in the tow simulations. Aerial pictures of the extent of flooding are presented in Figure 4.42 for the predictions obtained with the 3-D and 2-D models, as well as aerial photographs taken after the peak of the flood of 2008 at approximately the same discharge. When comparing the extent of flooding, the agreement between both numerical models and the aerial photograph is outstanding. Only slight differences can be observed throughout the domain where the 2-D model inundates slightly more than the 3-D model. For example, this happens between Section 1 and the 1st dam and between Section 2 and 3. Overall, the 2-D model

overestimates the flood extent by approximately 7% when compared to the 3-D model results. When comparing both numerical results to the aerial photograph, an exact extent of the flooded area cannot be delineated in the aerial photograph. The small contrast between the color of water in the river (light brown) and the ground (shades of green) and the visual obstruction of canopies forced us to delineate an approximate flooding extent using a red line (Figure 4.42 c). Both solutions are able to predict the approximate flooding extent captured from the aerial photograph, with the 3-D model predictions giving better visual agreement with respect to the aerial photograph compared to the 2-D model predictions.

During the propagation of the unsteady wave, both numerical models performed, visually, quite similarly. At peak flood extent (Figure 4.43), for instance, the 3-D and 2-D models predict similar peak flood extents; though the 2-D model actually predicts a larger extent (by 9%) of the inundated region when compared to the 3-D model prediction. Since the unsteady wave was an artificial sinusoidal wave, no comparison can be made with flooding extent that actually occurred.

Streamwise velocity distributions predicted by the 3-D model were analyzed at the 12 representative cross sections. The distributions looked qualitatively correct at these cross sections. Therefore, they are not presented. The unit-discharge profiles where differences between the 2-D and 3-D simulations were noticeable are shown in Figure 4.44. At steady state, significant differences were observed in Section 1, 6, 11 and 12. In Section 1, which is located in a region of high curvature, right before the 1st dam, the 2-D model the location and magnitude of peak unit discharge within the section is very different from the 3-D model prediction. In Section 6, which is located in the area influenced by the buildings, the 2-D model predicts a more spread-out distribution of the unit discharge compared to the 3D model. Thus, the 3-D model predicts higher values of unit discharge in the main channel. Section 11 is located in a straight reach upstream of the 2nd river dam. In principle, Section 11 should not present any difference between the two numerical

solutions. However, this is not the case. A shallow region is present on the east side of the cross section, which in turn creates recirculating flow. The 2-D model is unable to accurately capture this phenomenon and so it predicts a fairly symmetric and close to uniform unit discharge distribution away from the two banks. By contrast, the 3-D model predicts a distribution skewed towards the west side of the channel. Finally, Section 12 is located downstream of the 2nd river dam, where the flow is highly influenced by the hydraulic jump caused by the river dam. Given that the flow is highly three dimensional around the hydraulic jump, the 3-D and 2-D solutions are very different from each other in this region. The 3-D model predicts 2 peaks of the unit discharge at Section 12, whereas the 2-D model predicts a fairly uniform unit discharge distribution. The peak unit discharge magnitude difference are 20%, 25%, 8% and 16% for Sections 1, 6, 11 and 12 respectively.

At peak flood extent, the shapes of the unit discharge profiles predicted by the 3-D and 2-D models do not change significantly compared to the ones predicted at steady state. The main differences found at steady state between the predictions of the two models are also present at peak flood extent (Figure 4.44). The actual errors in term of magnitude of peak unit discharge are found to be equal or lower than the ones predicted at steady state, with values of 13%, 12%, 8% and 12% for Sections 1, 6, 11 and 12 respectively.

An in-depth analysis of the differences between the 2-D model predictions with respect to the 3-D model concluded that both models perform quite similarly in terms of flood extent, free-surface elevation and unit discharge profiles. However the 2-D model is unable to reproduce the exact free-surface elevation and unit discharge profiles predicted by the 3-D model. These differences are mainly caused by 3-D effects generally associated with regions of high stream curvature of the river reach and high flow conditions where main channel-floodplain shear layers are generated. The 3-D model proves to be a more flexible and accurate tool to predict flow in natural streams.

4.4.1 Assessment of possible flood protection strategies

Flood protection strategies refers to all methods used to reduce or prevent effects of flooding. Some examples of flood protection strategies for a river environment are levees, temporary flood protection walls, flood prevention dams, or construction of ponds. In the case of the Iowa River near Iowa City, the favored current approach of reducing the effect of detrimental flood waters is the deployment of temporary flood protection walls. Such walls do not allow water to flow into certain areas but severely constrict the available area for flow passage, thus increasing the three-dimensionality of the flow behavior. The 3-D model is used to assess the effectiveness of existing, as well as possible future, flood protection strategies. They include deployment of temporary flood protection walls in new zones of interest, as well as removal of one of the two, or both river dams located in the domain of interest. Due to the fact that these structures are only active at high flow conditions, they will only be tested in the 7-km reach of the Iowa River near Iowa City discussed in the previous subchapter.

The strategies that will be studied are shown in Table 4.6. Currently, Iowa City under flooding conditions deploys floodwalls that extend from halfway between Sections 8 and 9, until Section 12. These floodwalls will be called FW3 in the present document. Additional floodwalls are proposed to be installed to protect regions situated near Section 1 and the 1st Dam (FW 1), and between Section 3 and halfway between Sections 5 and 6 (FW 2). Additionally two dam removal strategies are proposed: one in which only the 2nd river dam is removed and one in which both river dams are removed.

Table 4.6 Flood protection strategies considered

Scenario 1	FW 3
Scenario 2	FW 1 + FW 3
Scenario 3	FW 2 + FW 3
Scenario 4	FW 1 + FW 2 + FW 3
Scenario 5	Removal of 2nd dam
Scenario 6	Removal of both dams

Steady state and unsteady wave solutions were obtained for the same flow conditions as in the previous subchapter (Table 4.5, Figure 4.40). Consistently with the analysis performed in the previous subchapter, the comparison between Scenarios 1 through 6 will focus on the free-surface elevation profiles, flood inundation extent and unit discharge profiles, with special emphasis on estimating the percent reduction of flooded areas since this variable directly correlates with the efficiency of each strategy in protecting against flooding.

Figure 4.45 shows the flood extent at steady state conditions, as well as the peak flood extent for all cases where floodwalls were installed in the computational domain (case scenarios 1 through 4), including the case where no floodwalls were present (Base Case). Floodwalls FW 3 are shown in red lines, whereas FW 1 and FW 2 are shown in blue. Inclusion of floodwalls FW 3 in the domain does protect areas in the direct vicinity of these flood protection structures from flooding at peak flood extent without having much effect upstream of the structures. A slight increase of the flood extent is observed between Section 1 and the 1st dam, as well as between Sections 2 and 3. The slight increase of the flood extent between Section 1 and the 1st dam and between Sections 2 and 3 is greatly overshadowed by the reduction of the flood extent in the vicinity of FW 3, resulting in a net flood extent reduction of approximately 8% at both steady state and peak flood extent.

Case Scenario 2 (FW 1 + FW 2) protects efficiently against flooding near Sections 1 and 2 at both steady state and peak flood extent. These areas were not protected in case scenario 1. Case Scenario 2 would be very beneficial to Iowa City since the floodwalls will

protect heavy development areas where, for instance, hospitals, hotels and restaurants are found. At steady state, the flood extent reduction is approximately 18%. At peak flood extent, the flood extend reduction is close to 19%. Case Scenario 3 (FW 2 + FW 3) significantly reduces flooding between Section 3 and Section 6, at both steady state and peak flood extent, without protecting areas previously protected in Case Scenario 2. In contrast to Case Scenario 2, Case Scenario 3 would protect a major residential area in Iowa City. The flood extent reduction for case Scenario 3 is approximately 15% under steady state conditions and 14% at peak flood extent. Case scenario 4, which includes all floodwalls (FW 1 + FW 2 + FW 3) would protect the same areas that the previous test cases protect, making it the more efficient among the four flood protection strategies considered. It would reduce flooding by 25% under steady state conditions and 26% under peak flood extent. It is important to mention that for Case Scenarios 1 through 4 the reduction of the flood extent is about the same for both steady state and peak flood extent conditions. The percentage reduction of the flooded area at peak flow conditions is expected to decrease with increasing flowrates for really large flows (i.e., when overtopping of floodwalls occurs).

Figure 4.46 shows the free-surface elevation profile along the centerline for all flood protection strategies that include floodwalls (case scenario 1 through 4), as well as for the Base Case. No significant differences can be observed at both steady state and at peak flood extent among Case Scenarios 1 to 4 and the Base Case. However, Case Scenarios 1 to 4 show an increase of the free-surface elevation downstream of the 2nd dam by about 0.3 m (1 ft). This should be mentioned since when implementing flood protection strategies, the flooding can be reduced in the areas of interest but can be enhanced in areas downstream or upstream of them. Therefore, flooding will be increased by about 1 ft. of water downstream of FW 3, though the effect should not extend significantly away from FW 3 since the flow should adjust to normal flow fairly rapidly.

Figure 4.47 compares the unit-discharge distributions at 6 cross sections that showed the biggest differences between the Base Case and Case Scenarios 1 to 4 at steady state and peak flood extent conditions. Figures 4.48 through 4.50 will also be used as an aid to explain the differences found in Figure 4.47. At Section 1, which is located near floodwalls FW 1, all profiles look quite similar at steady state. Case Scenarios 2 and 4 show a recirculating region (negative unit discharge) near the left bank, which is not found in the other cases. At peak flood extent, however, Case scenarios 2 and 4 show a significant increase of the peak unit-discharge, by approximately 30% with respect to the Base Case. This is due to the reduction in cross sectional area caused by inclusion of FW 1.

Section 2 (located downstream of FW 1 and the 1st dam) shows a similar trend in which little differences are observed at steady state conditions but differences arise at peak flood extent conditions. In particular, this is the case for Case Scenarios 2 and 4, where an increase of the peak unit discharge of approximately 10% is observed. This is explained by the reduction of the cross sectional area upstream (i.e. Section 1), which forces the flow in a particular direction that is not consistent with that observed in the Base Case. When the flow reaches Section 2 it does not have enough space to adjust and so differences are observed with respect to the Base Case.

Sections 4 and 5 (located near FW 2) show big differences, mostly in the shape of the unit discharge profile at both steady state and, mainly, at peak flood extent conditions. Case scenario 3 and 4 show a sharp increase of the unit discharge near the transition between the main channel and left floodplain. This difference in the shape of the unit discharge is explained by the presence of floodwalls FW 2. Figure 4.48 and 4.49 show the streamwise velocity distribution at Sections 4 and 5. The presence of FW 2 reduce the cross sectional area and changes the distribution of the streamwise velocity in these sections. At Section 5, a clear amplification of the streamwise velocity magnitude is observed. Case Scenarios 3 and 4 show an increase of the peak unit discharge of about 15% and 12% for Section 4 and 5 respectively.

Section 6 displays a similar pattern as Section 5, where Case Scenarios 3 and 4 show an increase of the peak unit discharge of approximately 20% (compared to 10% at Section 5), though this increase is not located near FW 2. Floodwalls FW 2, similarly to FW 1, force the core of high streamwise velocity toward a different location compared to the Base Case. FW 2 moves the core of high velocity towards the main channel of the Iowa River. This can be observed in the streamwise velocity distribution at Section 6 (Figure 4.50).

Finally, Section 11 shows the smallest difference between Case scenarios 1 to 4 and the Base Case. The core of high unit discharge moves closer to the left bank. This is caused by the presence of floodwalls FW 3 that force the core of velocity to have a different location compared to the Base Case. In turn, Case Scenarios 1 to 4 show an increase of the peak unit discharge by approximately 20%.

Reduction in the flood extent can also be achieved by removing the existing river dams in the domain. Such scenarios are studied in Case scenarios 5 and 6. Figure 4.51 shows the flood inundation extent comparison between Case Scenarios 5 and 6 and the Base Case for both steady state and peak flood extent conditions. At steady state, the flooding between Section 10 and 12 is reduced significantly in Case Scenario 5. Flooding in this region is influenced by the backwater effect caused by the 2nd river dam. This effect is highly local and does not propagate significantly upstream, where only a small reduction of the flood extent is observed near the 1st river dam. On the other hand, when both dams are removed (Case Scenario 6), the flood extent is greatly reduced not only between Sections 10 and 12, but also near Section 1 and the position of the 1st river dam. The free-surface elevation profile along the centerline of the main channel confirms these findings for steady state conditions (Figure 4.52). It is also concluded that the removal of the river dams will not have any effect on flood extent downstream of the 2nd river dam. This result makes sense, as the flow is supposed to achieve normal flow conditions in the absence of any obstruction (i.e. river dams). The percent reduction of the flood extent at steady state

conditions for Case scenarios 5 and 6 are 11% and 19% respectively, with respect to the Base Case.

At peak flood extent, however, small differences are observed between Case Scenarios 5 and 6 with respect to the Base Case. This indicates that the effectiveness of the dam removal measures becomes of lesser value at higher flowrates. Such decay in effectiveness is not surprising, since under higher flowrates flow obstructions (e.g., river dams) play a less important role. Figure 4.52 confirms this finding. The free-surface elevation profile at peak flood extent conditions shows only small differences near the river dams. The flood extent reduction at peak flood extent conditions for Case Scenarios 5 and 6 are 9% and 11% respectively, compared to 11% and 17% at steady state conditions, confirming the decrease of their capability to limit flood extent at higher flowrates.

In terms of unit-discharge profiles, only Sections 1, 2, 10 and 12 show significant differences between the Base Case and Case Scenarios 5 and 6. In particular, Section 1, shows a significant difference between the Base Case and Case Scenario 6. The region of high unit discharge of the unit discharge profile for Case Scenario 6 is now situated closer to the left bank compared to the Base Case and Case Scenario 5. This is explained by the fact that removing the dam creates a new path of less resistance. The peak magnitudes of the unit discharge at Section 1 in Case Scenario 6 is 15% larger compared to both Base Case and Case Scenario 5 at both steady state and peak flood extent.

At Section 2, an amplification of the core of high unit discharge is observed for Case Scenario 6, but no shift of its location compared to the Base Case. The amplification of the peak unit discharges is approximately 30% with respect to both the Base Case and Case Scenario 5. The amplification in the magnitude of the peak unit discharge at both Sections 1 and 2 for Case Scenario 6 is explained by the decrease of free-surface elevation (Figure 4.52). This reduces the cross sectional area and increases the magnitude of the streamwise velocities in the cross section (Figure 4.54 and Figure 4.55).

Section 10 shows practically no differences between the Base Case and Case Scenarios 5 and 6 at steady state conditions. At peak flood extent, differences are observed for the magnitudes of the unit-discharge profiles inside the main channel. Case Scenarios 5 and 6 show an increase of approximately 15% with respect to the Base Case, while the unit-discharge profile has a qualitatively similar shape. This increase is explained by the decrease of the free-surface elevation that increases the magnitude of the streamwise velocities at Section 10, as seen in Figure 4.56.

Finally, Section 12 shows major differences in the shape of the unit-discharge profiles. Case Scenarios 5 and 6 shows a fairly symmetric profile, while a two peak distribution is predicted in the Base Case. As explained previously, this distribution of the unit discharge is caused by the hydraulic jump forming downstream of the 2nd river dam. When the 2nd river dam is removed, the level of three-dimensionality of the flow in this region decreases and the flow achieves a fairly symmetric distribution of the unit discharge at both steady state and peak flood extent conditions, as seen from Figure 5.45.

4.5 Conclusions

The 3-D model developed in STAR-CCM+ was used to predict flow in realistic river reaches of lengths ranging from 1 km to 18 km for steady and unsteady flow conditions, as well as for low- and high-flow conditions. It was found that the newly-developed 3-D model is capable of predicting flow in realistic river environments. The model predictions were as good or better than the ones obtained with other state-of-the-art 3-D CFD codes such as FLOW-3D and FLUENT.

From the analysis performed for low- and high-flow conditions and for steady state and unsteady events it is concluded that while a standard 2-D model gives a somewhat accurate representation of the flow and flood development, it fails to predict the flow behavior everywhere, especially in areas where 3-D effects are important (e.g. due to high

curvature effects of the main river reach, sharp changes in the bathymetry, main channel / floodplain transition region at high flow conditions).

In the case of the 18-km river reach test case with steady low-flow conditions, the presently developed 3-D model was able to predict the free-surface elevation more accurately compared to a standard 2-D model. In terms of the unit-discharge profiles significant differences between the 3-D and 2-D models were observed in the cross-sections influenced by strong curvature effects. When an unsteady hydrograph was propagated into the domain, the 3-D model was able to reproduce the hydrograph recorded by a gaging station located within the domain with small differences. In terms of free-surface elevation, it was observed that the 2-D model is very sensitive to changes in flow conditions and so it starts to overestimate the free-surface elevation with respect to the 3-D model. At higher flowrates the differences between the 3-D model and 2-D model predictions switched from an underestimation by approximately 9% to an overestimation of 1% (10% difference) of the free surface elevation. In addition, the cross sections that showed differences in the unit-discharge profiles at initial conditions also showed differences at all times during the unsteady event. These differences were found to increase with increasing flow conditions. On the other hand, cross sections that showed good agreement at initial conditions also showed good agreement during the unsteady wave propagation.

Under high flow conditions present in the 7-km river reach test case, the floodplain becomes flooded. This adds an additional challenge for the 2-D model because of the formation of shear layers at the interface between the main channel and the floodplains, where 3-D effects and secondary flows are stronger. In terms of free-surface elevation at steady state conditions, it was found that both the 2-D model and the 3-D model were able to predict within 5 cm the free-surface elevation at the USGS gage, though they predicted quite different free-surface elevation profiles upstream of it. Consistent with what was observed for low flow conditions, these differences increased with increasing flowrate,

reaching up to 0.75 m. In terms of flood extent, the solutions predicted by the two models looked quite similar. In terms of the surface flooded, the differences between the 2D model and the 3D model predictions were 7% and 9% for steady state and peak flood extent, respectively. The unit discharge profiles showed significant differences at several cross sections.

The newly developed 3-D model was then used to asses flood protection strategies based on the inclusion of flood protection walls and removal of existing river dams. One of the scenarios tested predicted a flood extent reduction of about 25% both for steady state and peak flood extent conditions. The inclusion of the floodwalls induced a significant growth (up to 30%) of the magnitude of the peak unit discharge in several regions. When the flood protection strategy was based on removing existing dams, the most efficient solution was the one in which both dams present in the simulated river reach were removed. However, the impact of removing the dams decreased significantly at high flood conditions. Thus using floodwalls appears to be a better and less expensive solution in the case studied in this chapter. One concern in the implementation of any flood protection measures is the increase of the peak unit discharge. This, in turn, is expected to increase the rate of sediment erosion.

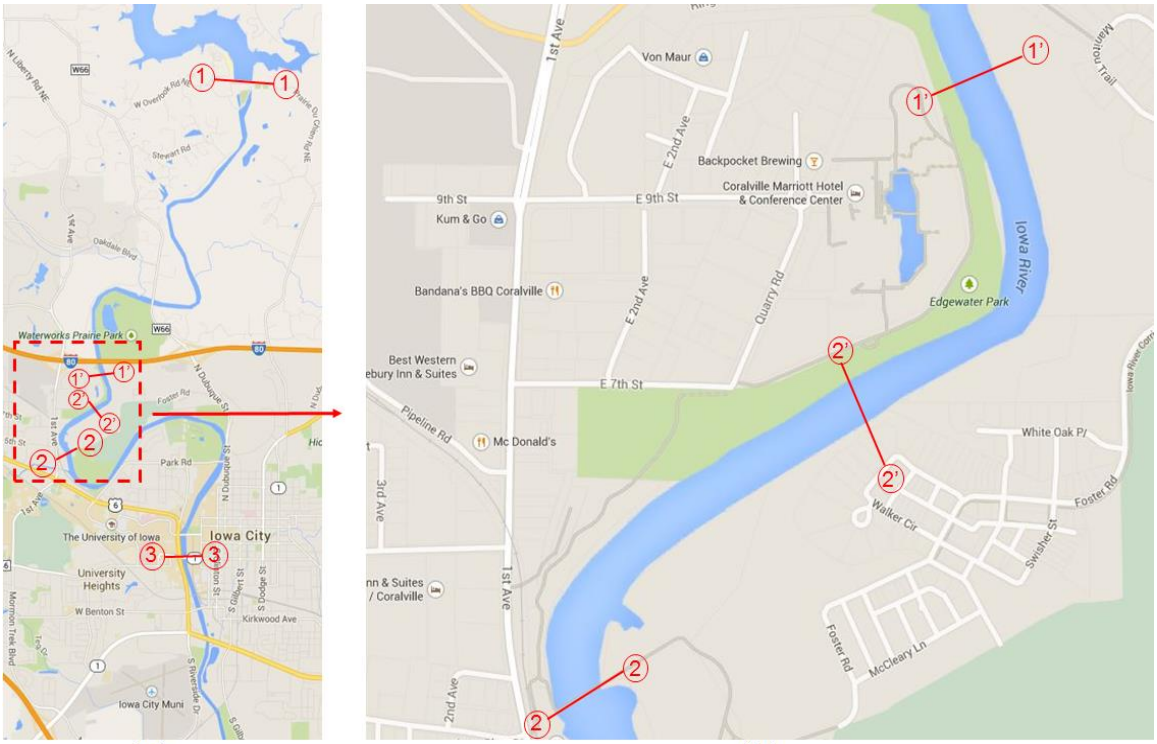

Figure 4.1 (a) Iowa River near Iowa City, Iowa, USA showing the flood control dam (1-1), the first river dam (2-2) and the second river dam (3-3). The start and end of the computational domain are shown in sections (1'-1') and (2'-2') respectively. (b) Close-up view showing the start of the computational domain (1'-1'), the end of the computational domain (2'-2') and the location of the first river dam (2-2) that is not part of the computational domain.

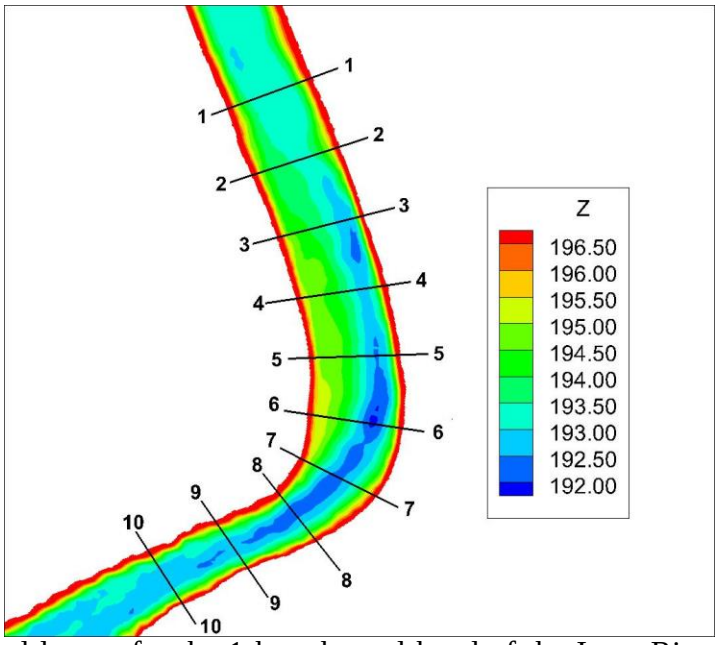

Figure 4.2 General layout for the 1-km channel bend of the Iowa River near Iowa City. Bathymetry contours are shown.

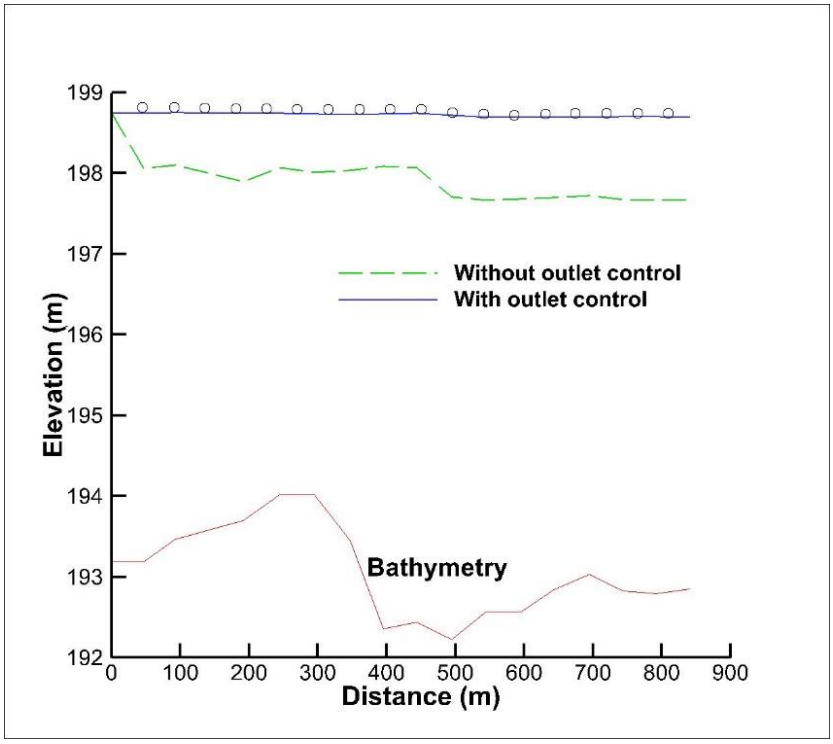

Figure 4.3 Free-surface profiles along the centerline of the 1-km channel bend with two different outlet boundary condition treatments. The symbols correspond to field data measurements.

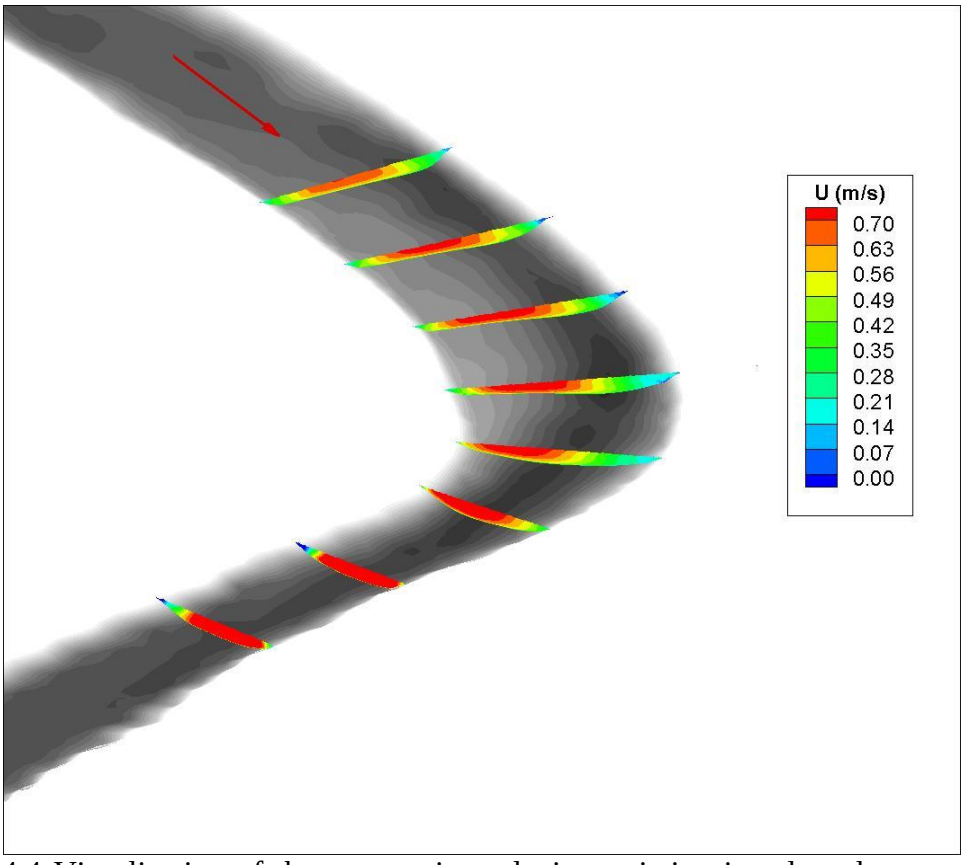

Figure 4.4 Visualization of the streamwise velocity variation in selected cross sections along the 1-km channel bend.

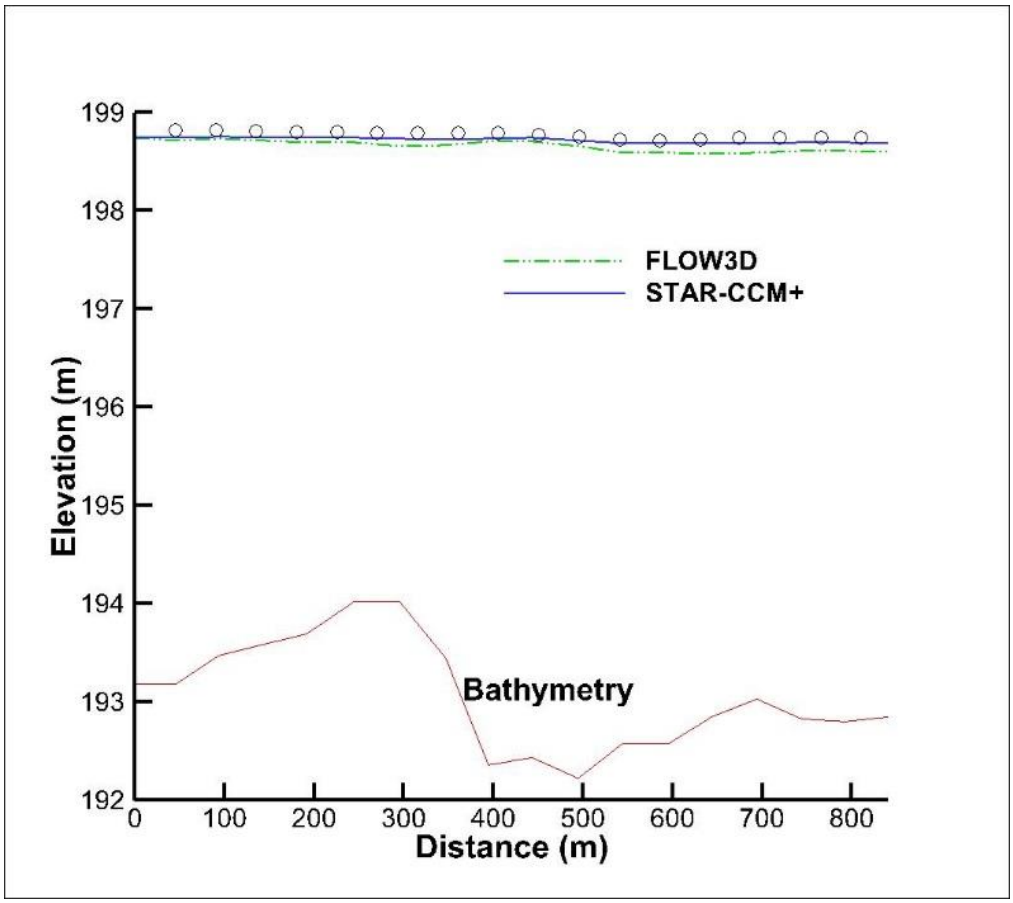

Figure 4.5 Free-surface profile comparison between STAR-CCM+ and FLOW-3D for the 1-km channel bend.

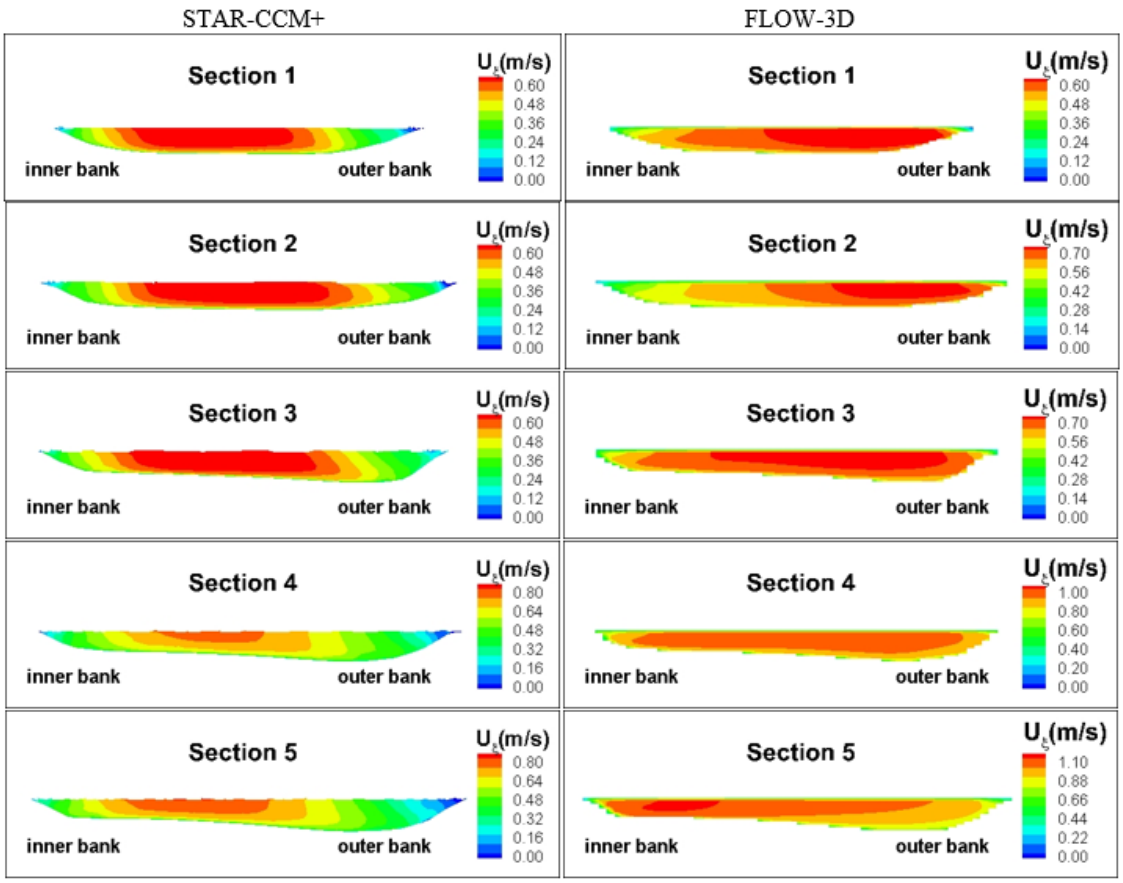

Figure 4.6 Streamwise velocity distribution comparison between STAR-CCM+ and FLOW-3D in sections 1 to 5.

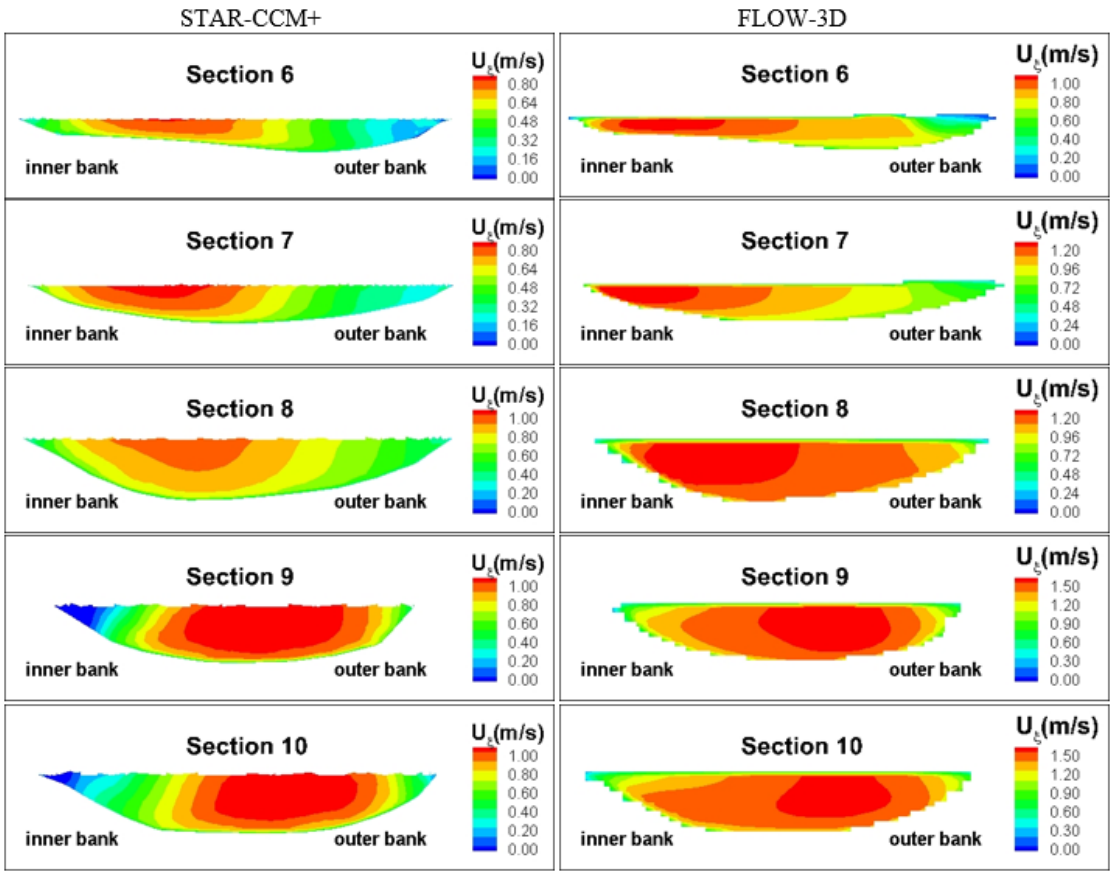

Figure 4.7 Streamwise velocity distribution comparison between STAR-CCM+ and FLOW-3D in sections 6 to 10.

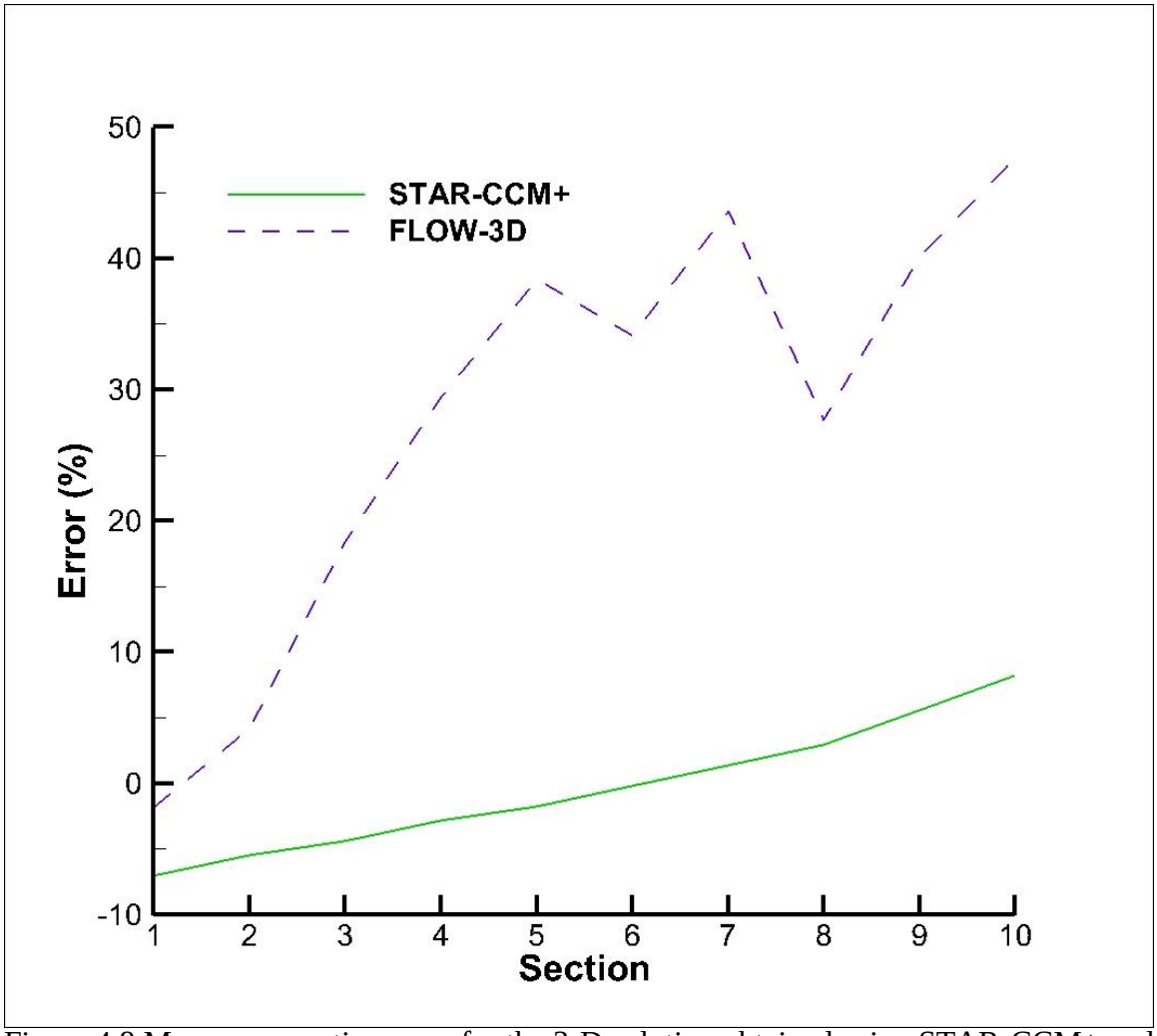

Figure 4.8 Mass conservation error for the 3-D solution obtained using STAR-CCM+ and FLOW-3D.

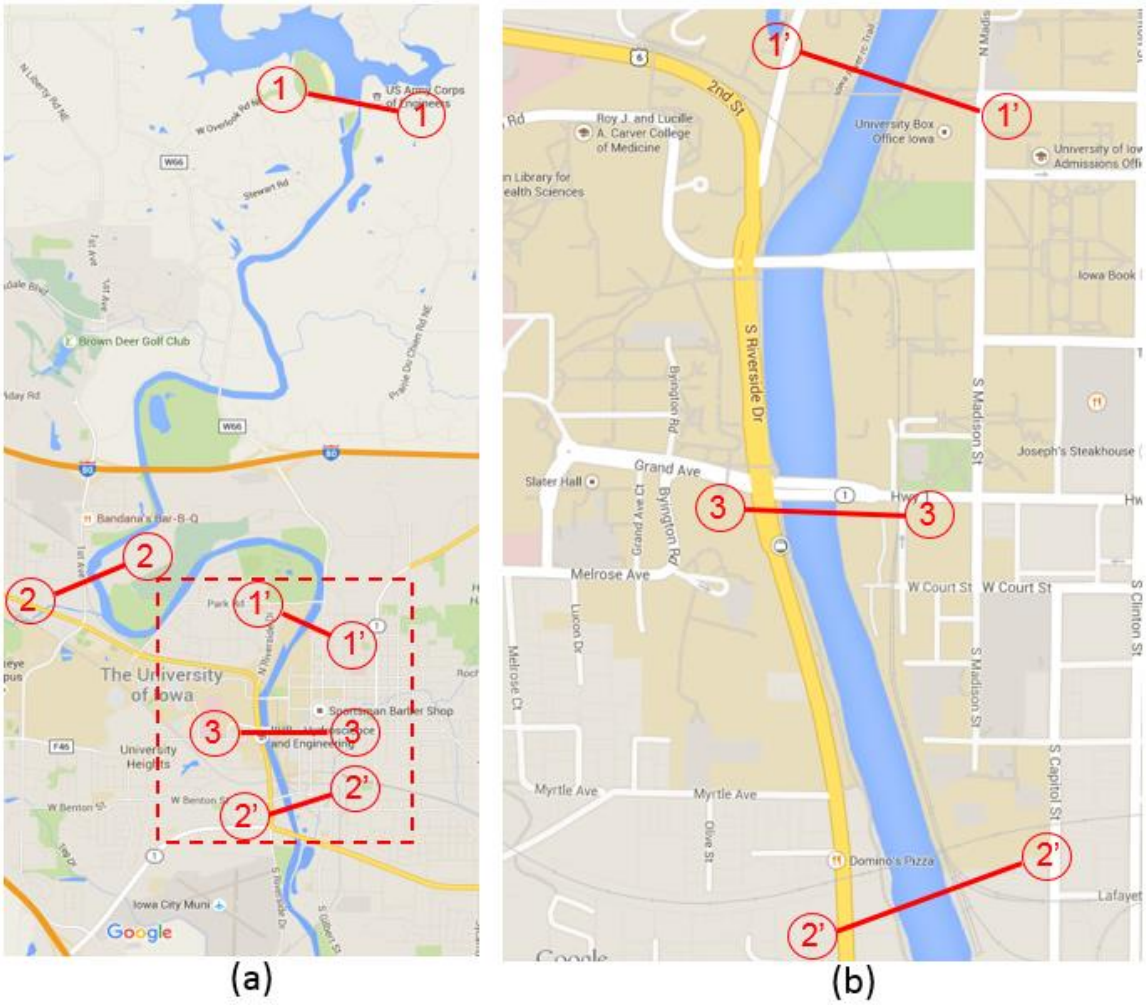

Figure 4.9 (a) Iowa River near Iowa City, Iowa, USA showing the flood control dam (1-1), the first river dam (2-2) and the second river dam (3-3). The start and end of the computational domain are shown in sections (1'-1') and (2'-2') respectively. (b) Close-up view showing the start of the computational domain (1'-1'), the end of the computational domain (2'-2') and the location of the second river dam (3-3).

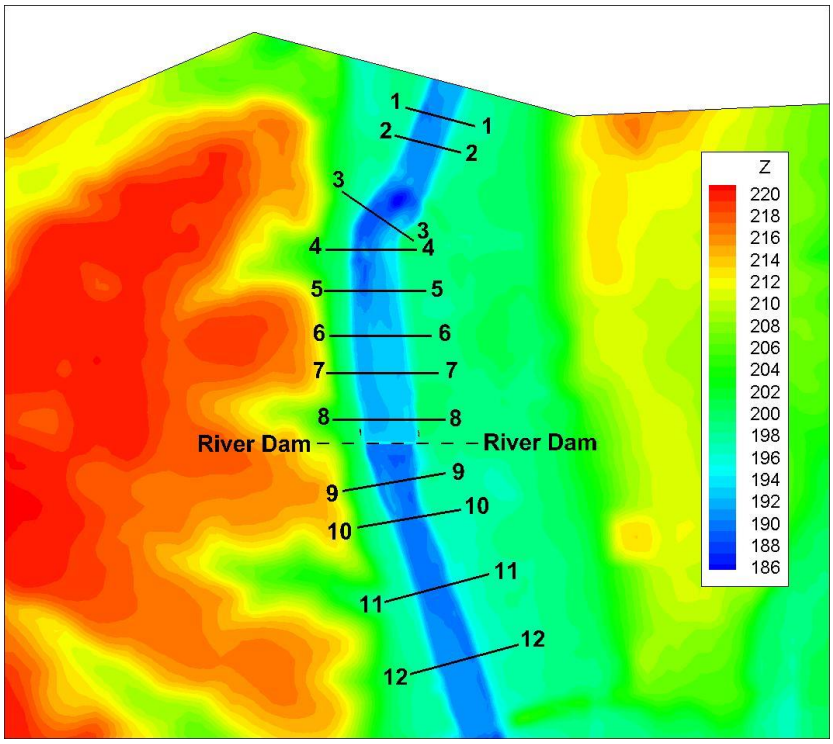

Figure 4.10 General layout of the 2-km river reach with bathymetry/topography contours.

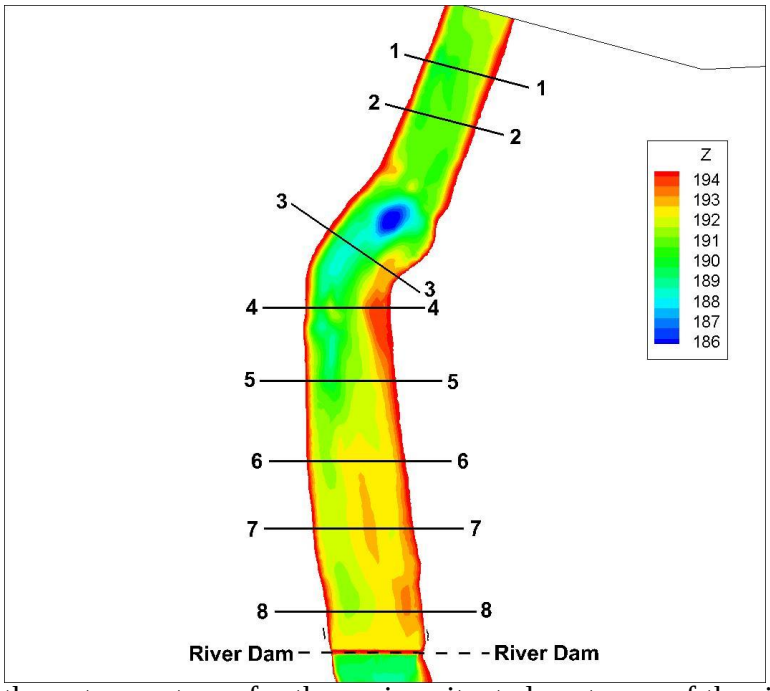

Figure 4.11 Bathymetry contours for the region situated upstream of the river dam in the 2-km river reach domain.

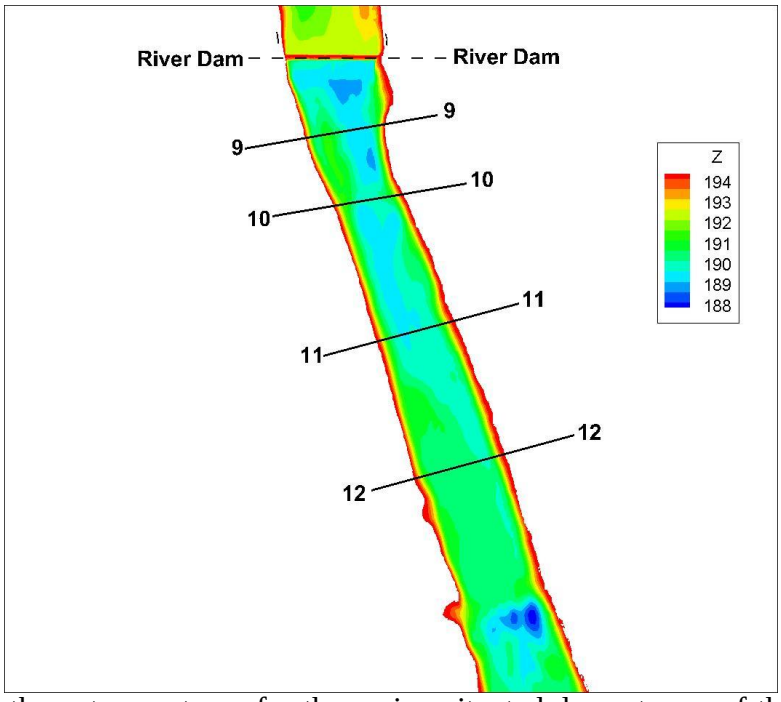

Figure 4.12 Bathymetry contours for the region situated downstream of the river dam in the 2-km river reach domain.

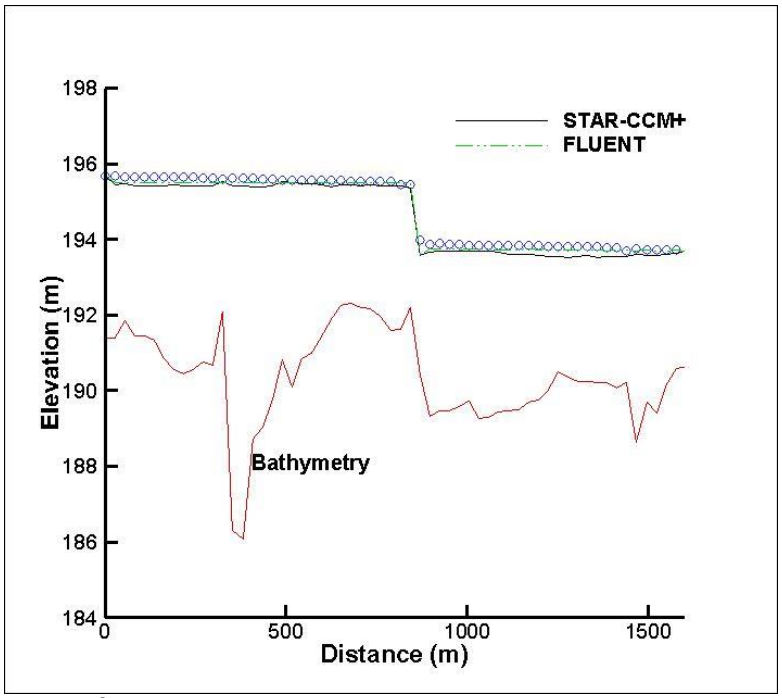

Figure 4.13 Free-surface elevation comparison between STAR-CCM+ and FLUENT predictions for the 2-km river reach. The field data is shown using symbols.

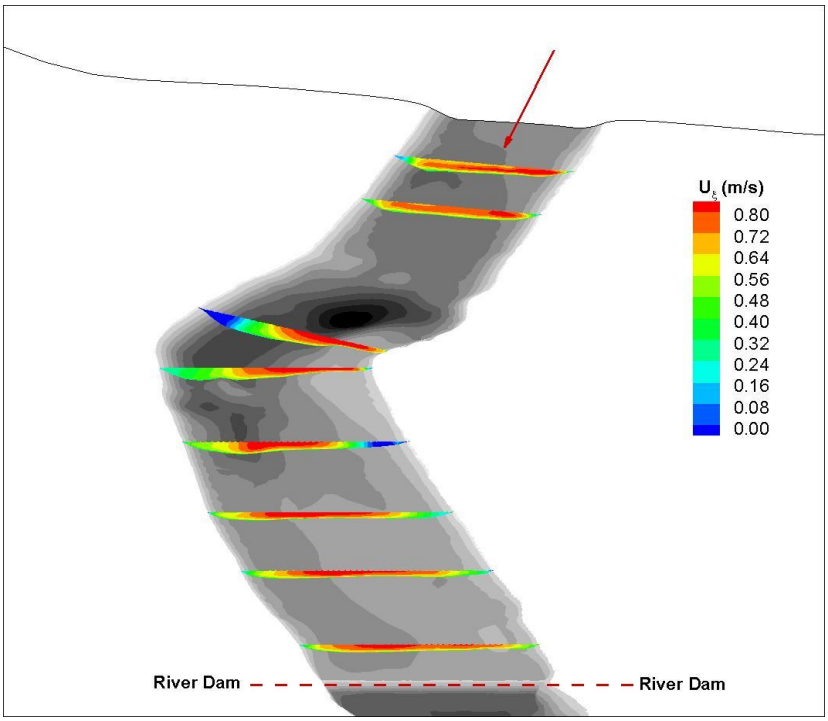

Figure 4.14 Streamwise velocity distribution in selected cross sections situated upstream of the dam for the 2-km river reach.

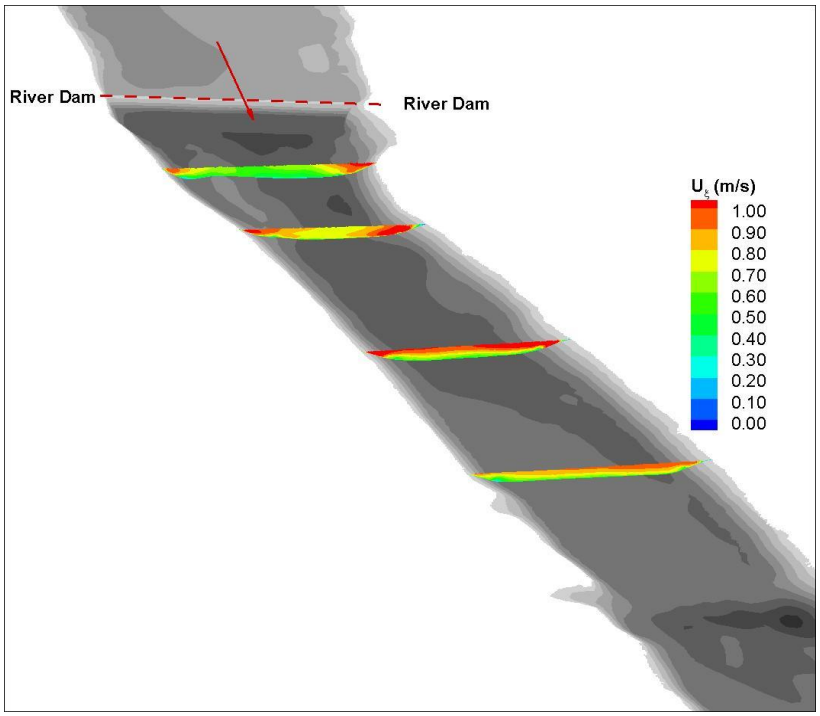

Figure 4.15 Streamwise velocity distribution in selected cross sections situated downstream of the dam for the 2-km river reach.

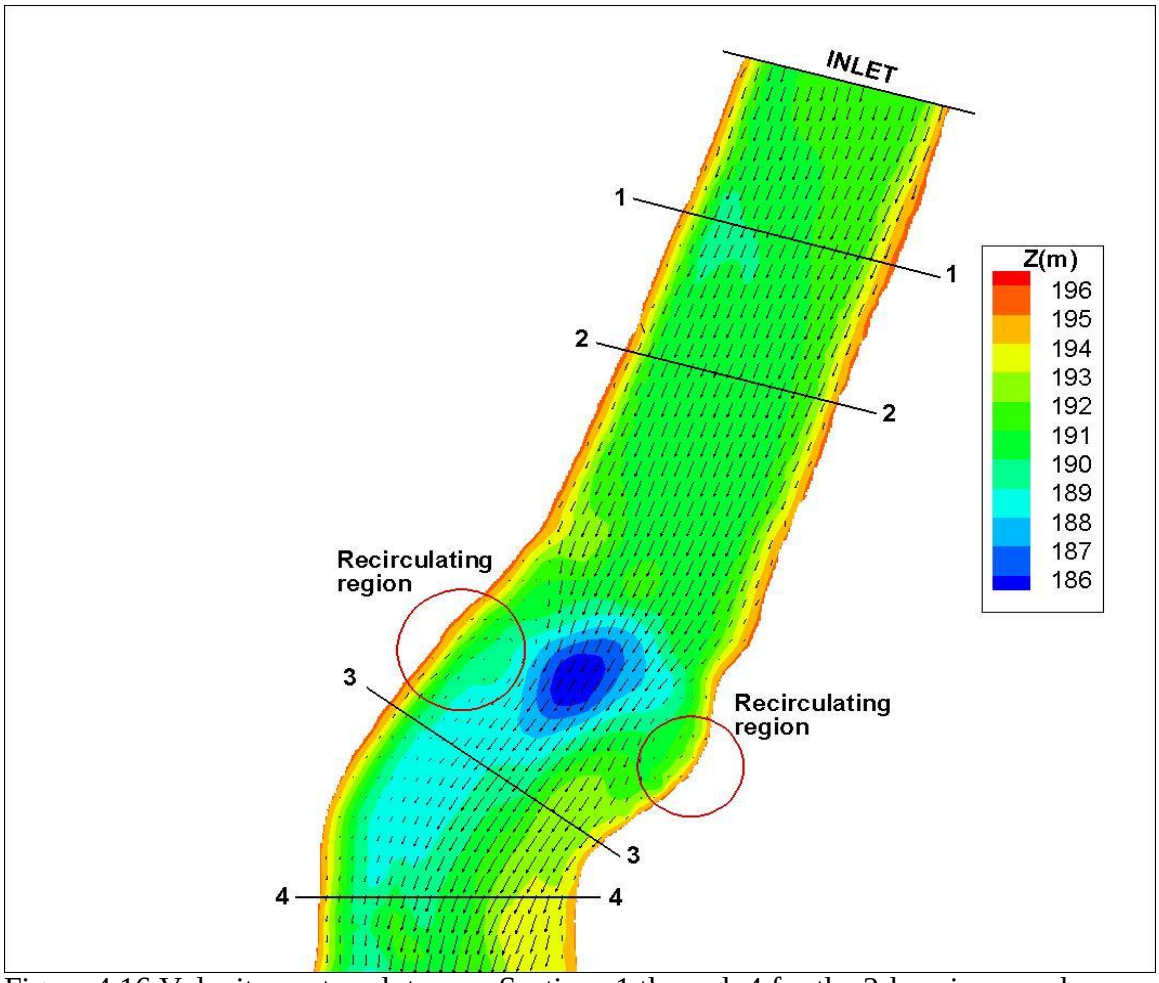

Figure 4.16 Velocity vector plots near Sections 1 through 4 for the 2-km river reach.

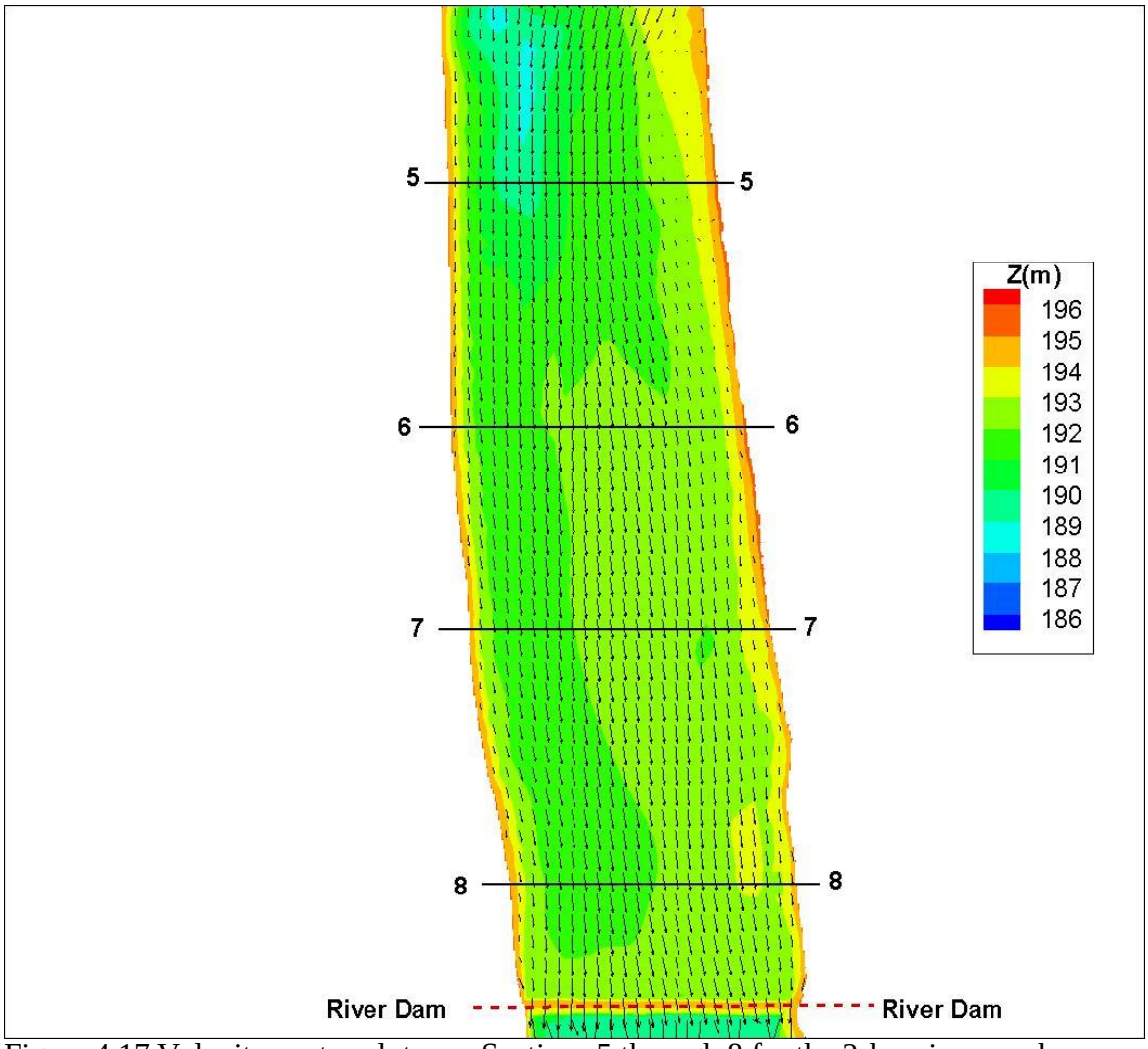

Figure 4.17 Velocity vector plot near Sections 5 through 8 for the 2-km river reach.

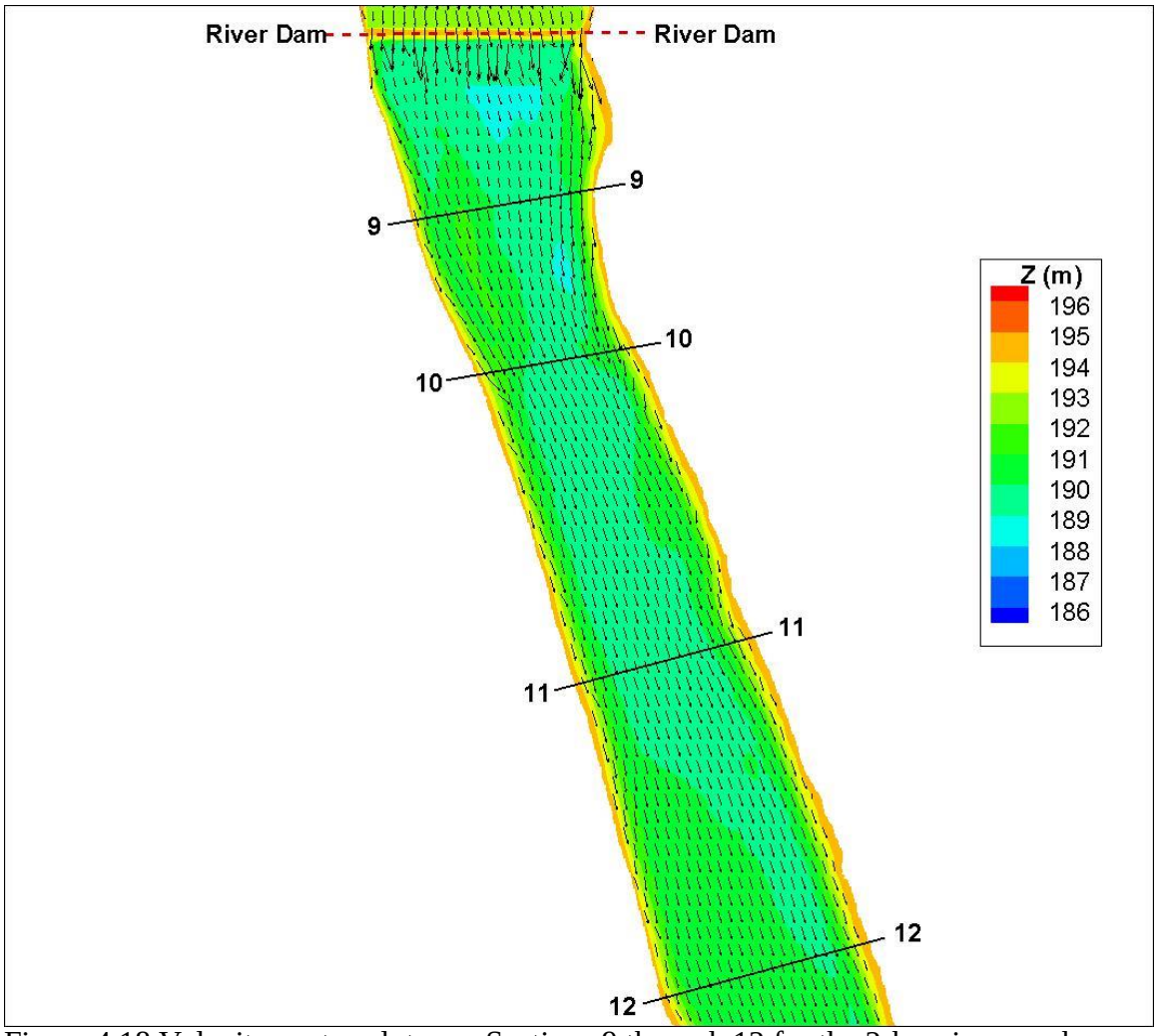

Figure 4.18 Velocity vector plot near Sections 9 through 12 for the 2-km river reach.

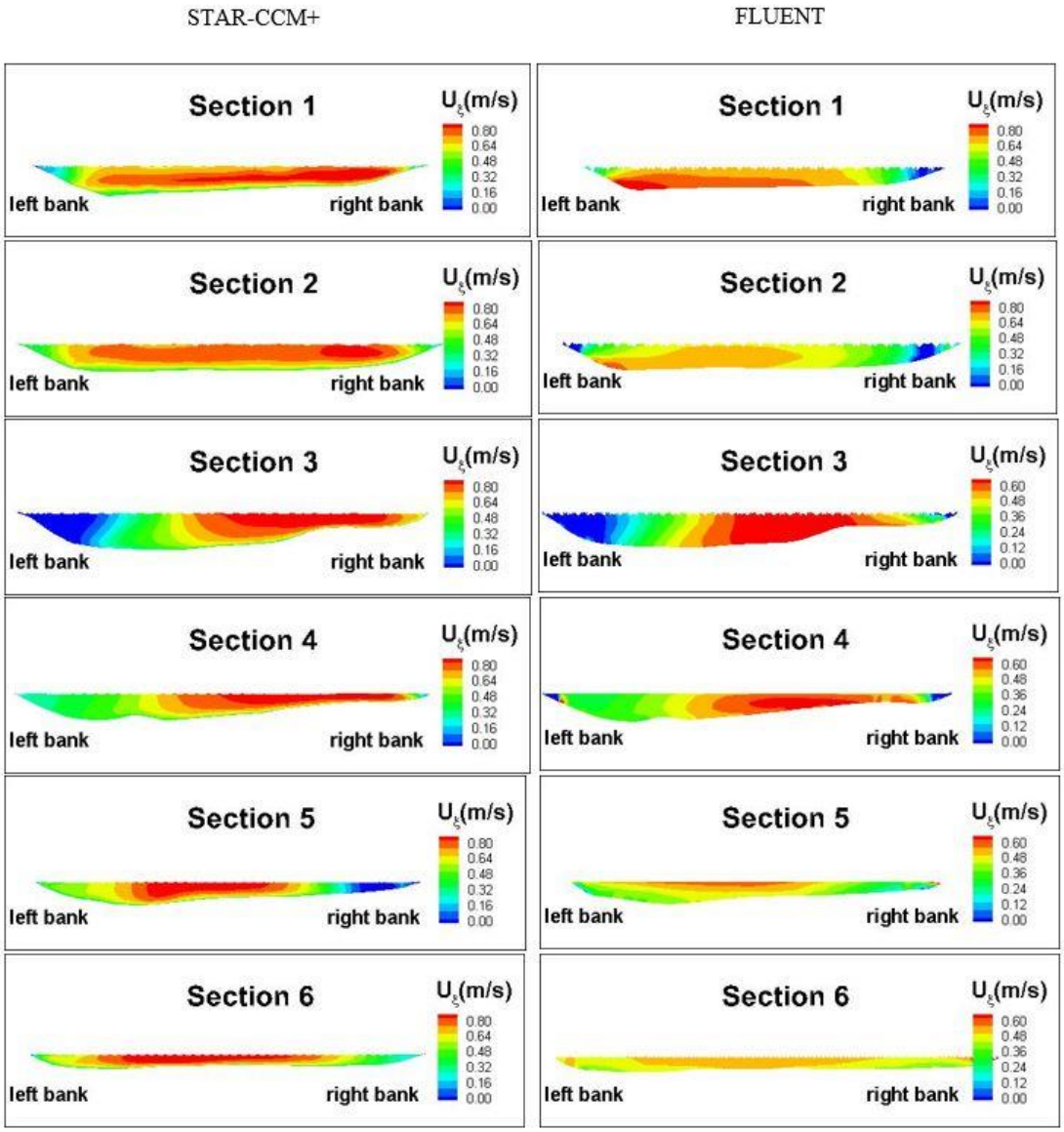

Figure 4.19 Streamwise velocity distribution comparison between STAR-CCM+ and FLUENT predictions in Sections 1-6 of the 2-km river reach.

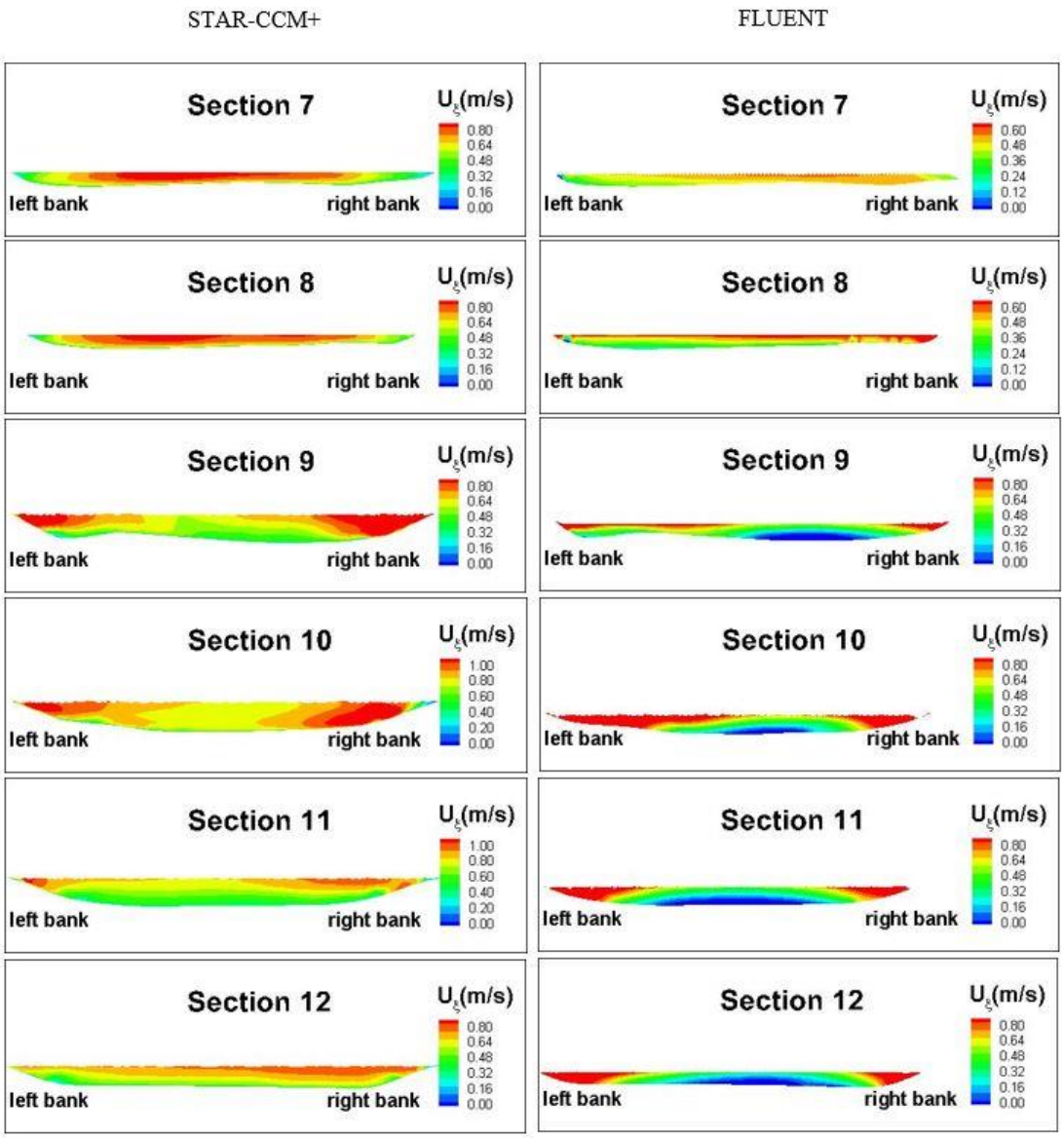

Figure 4.20 Streamwise velocity distribution comparison between STAR-CCM+ and FLUENT predictions in Sections 7-12 of the 2-km river reach.

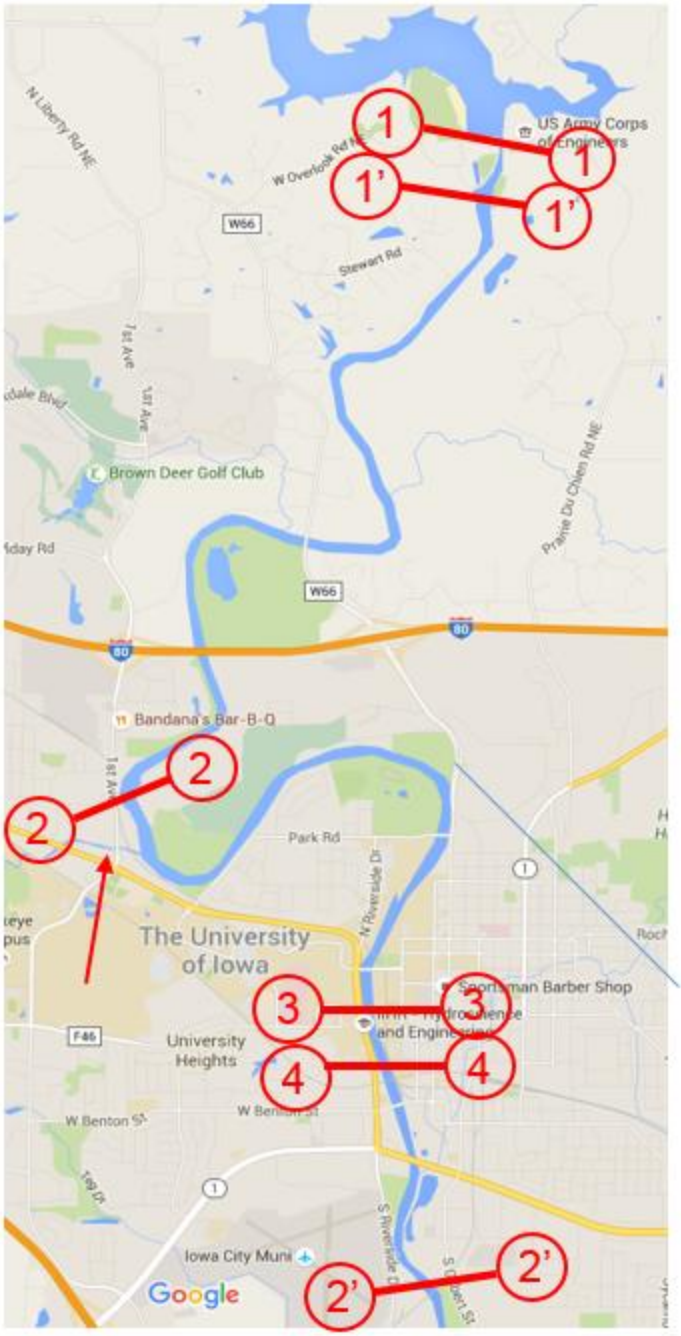

Figure 4.21 Iowa River near Iowa City, Iowa, USA showing the flood control dam (1-1), first river dam (2-2), second river dam (3-3) and USGS gage (4-4). The start and end of the computational domain are shown in sections (1'-1') and (2'-2') respectively. Arrow points to Clear Creek, the main tributary of the Iowa River near Iowa City.

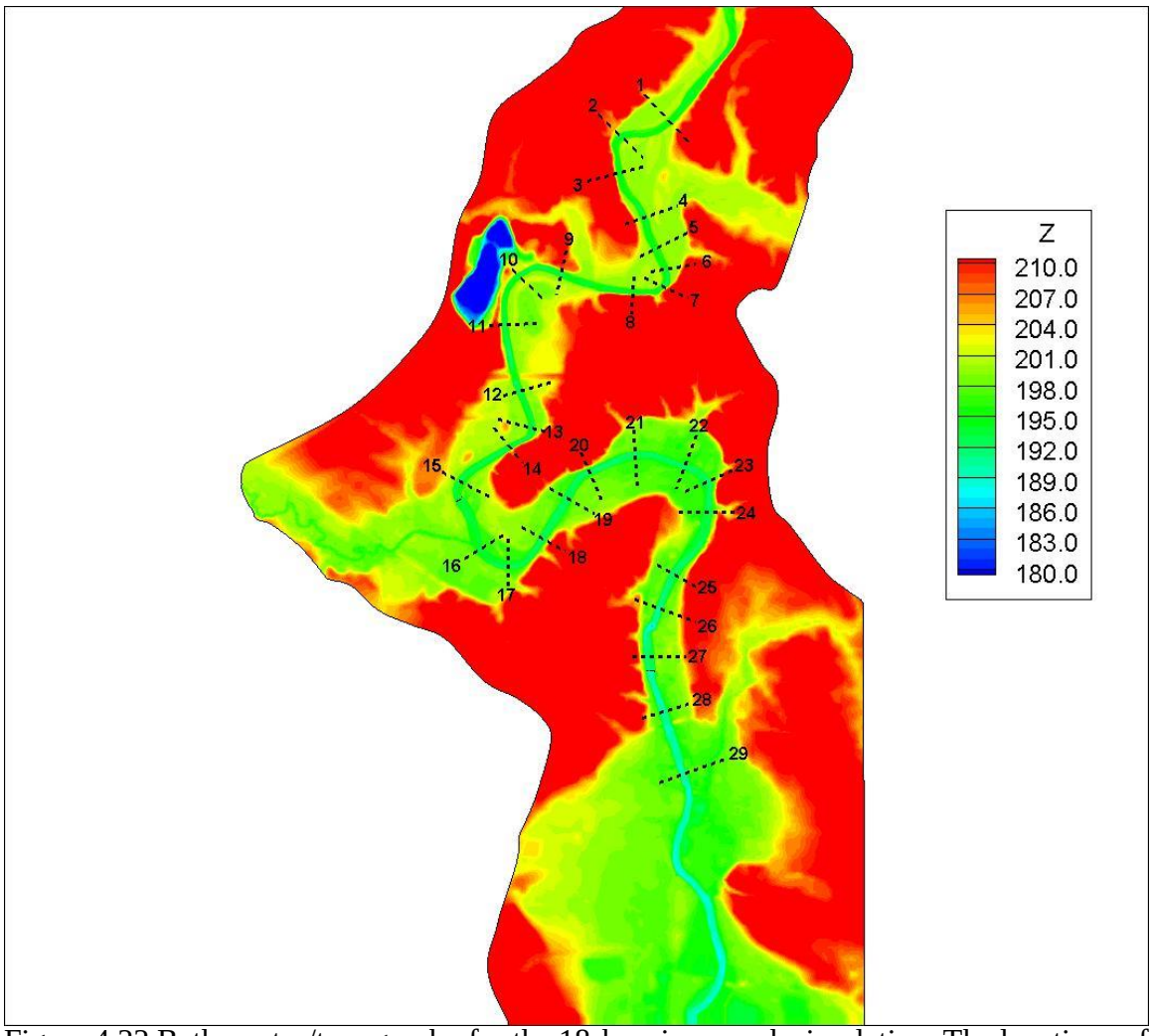

Figure 4.22 Bathymetry/topography for the 18-km river reach simulation. The locations of the 29 cross sections are also shown.

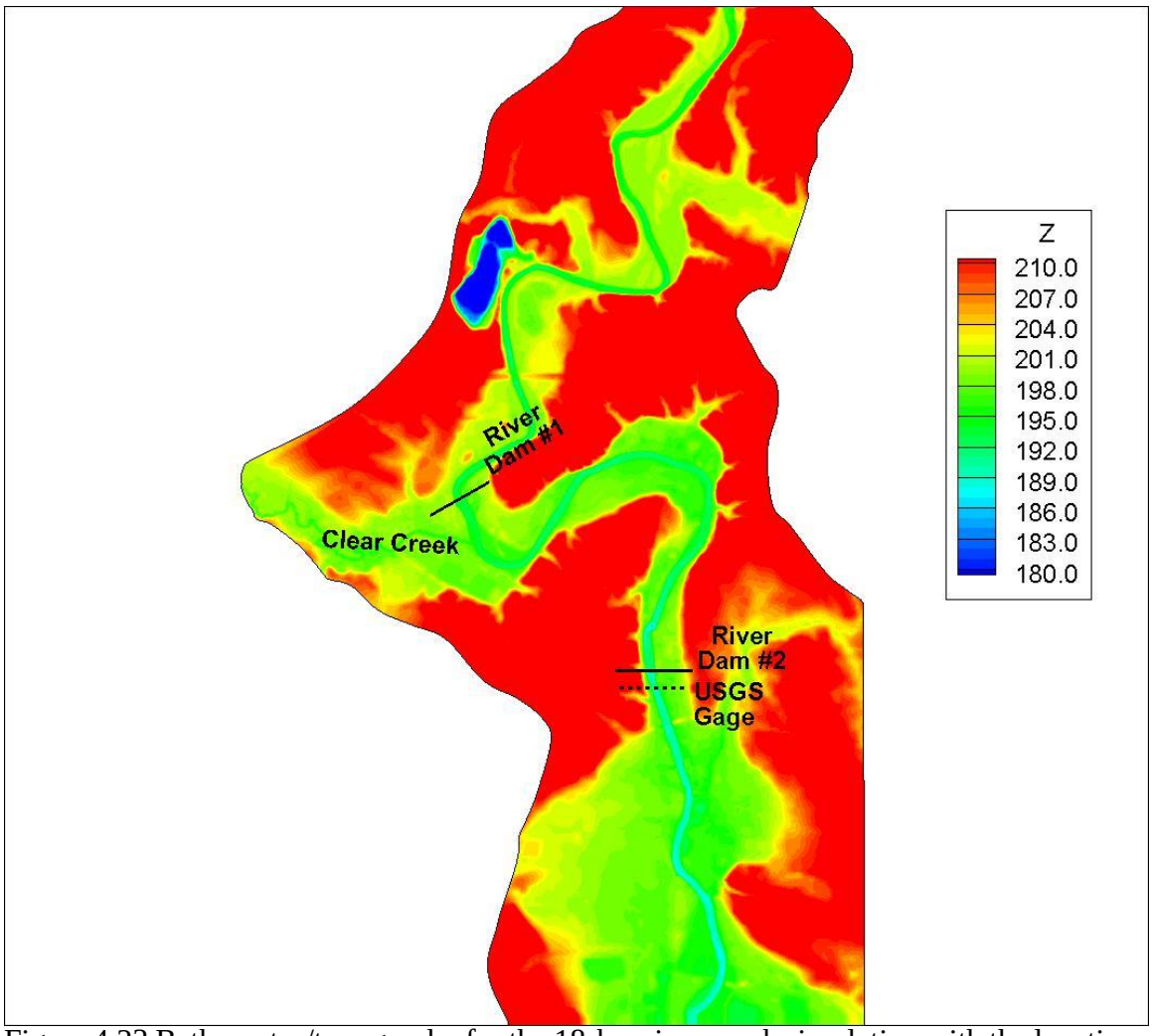

Figure 4.23 Bathymetry/topography for the 18-km river reach simulation with the locations of the two main hydraulic structures, the main tributary and the location of the USGS gage.

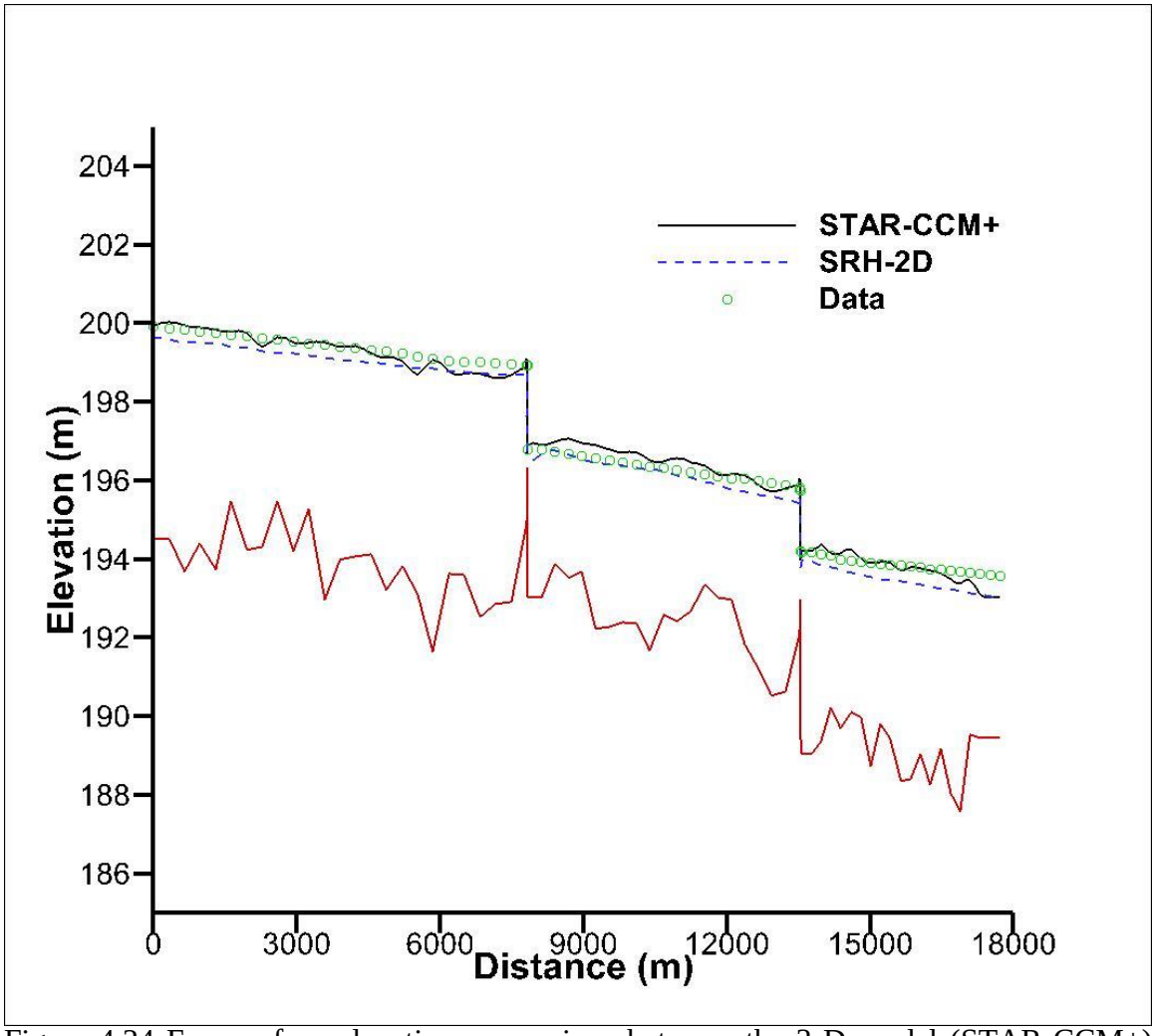

Figure 4.24 Free-surface elevation comparison between the 3-D model (STAR-CCM+) predictions, the 2-D model (SRH-2D) predictions and field data (symbols) for the 18-km river reach simulation of the Iowa River near Iowa City.

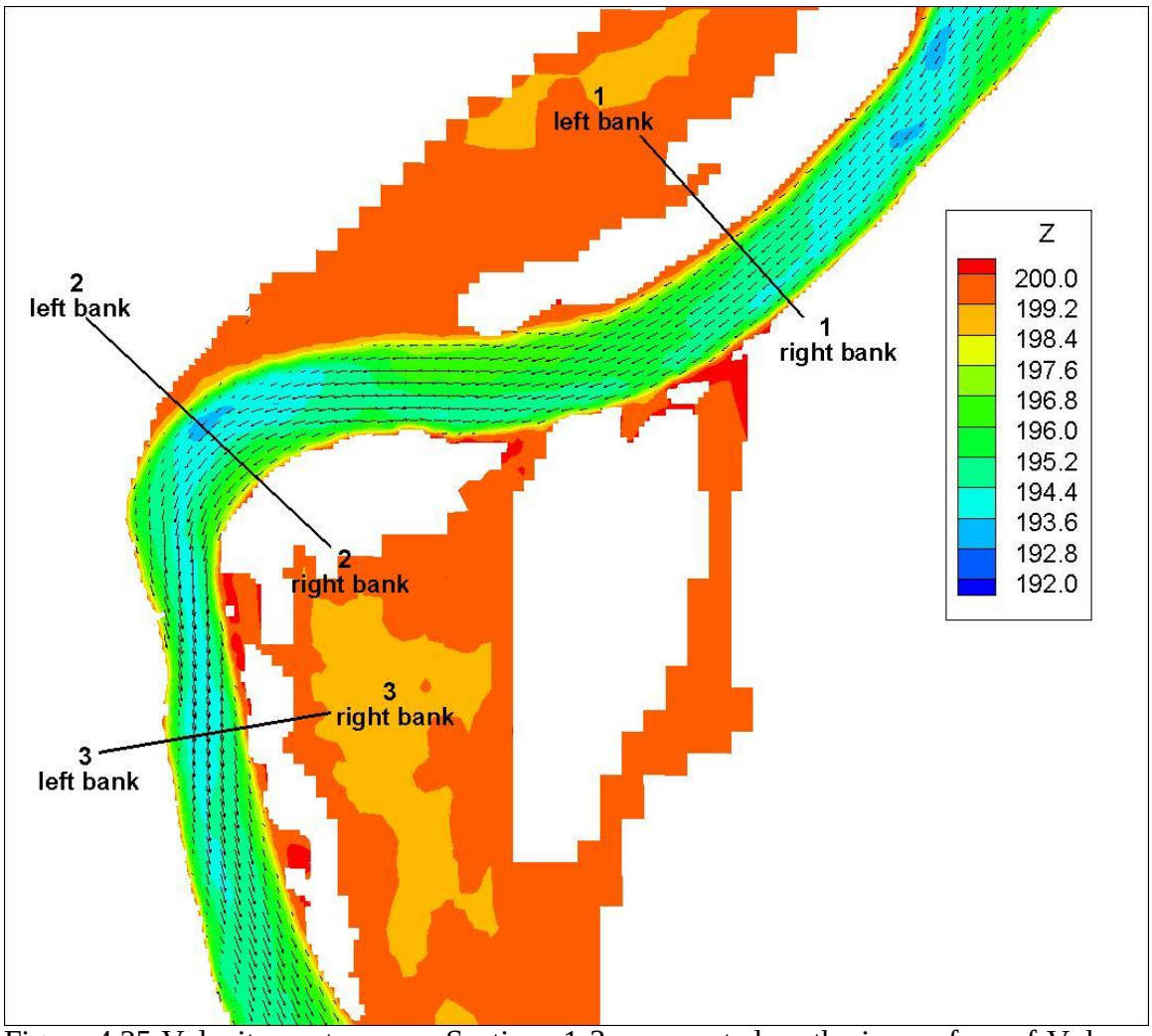

Figure 4.25 Velocity vectors near Sections 1-3 represented on the iso-surface of Volume Fraction of water equal to 0.9. Results are shown for the 3-D simulation of the 18-km river of the Iowa River near Iowa City. Velocity vectors were blanked for values of the Volume Fraction of water greater than 0.9.

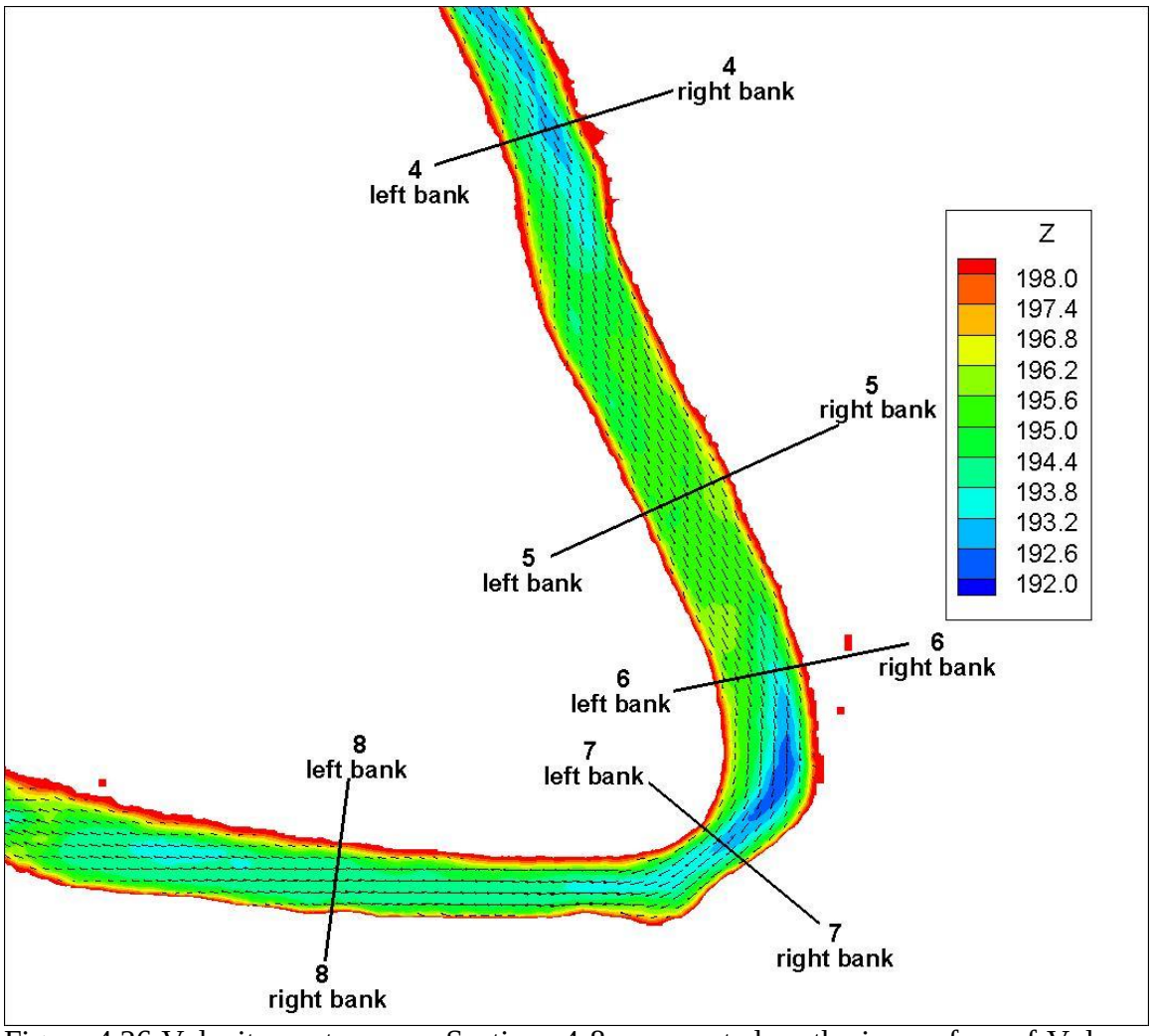

Figure 4.26 Velocity vectors near Sections 4-8 represented on the iso-surface of Volume Fraction of water equal to 0.9 for the 3-D solution of the flow in an 18-km river reach of the Iowa River near Iowa City. Velocity vectors were blanked at locations were the Volume Fraction of water was greater than 0.9.

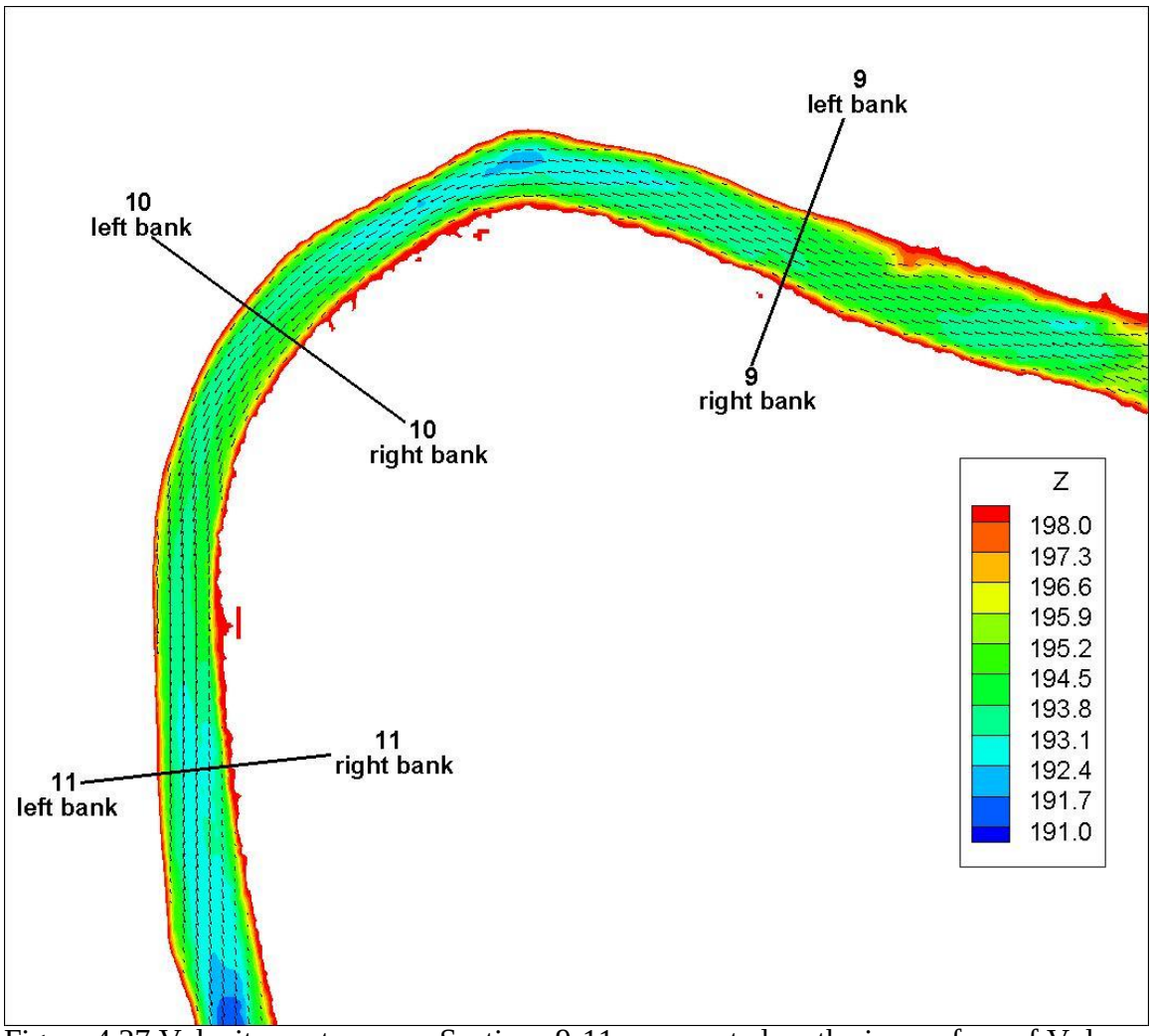

Figure 4.27 Velocity vectors near Sections 9-11 represented on the iso-surface of Volume Fraction of water equal to 0.9 for the 3-D solution of the flow in a 18-km river reach of the Iowa River near Iowa City. Velocity vectors were blanked at locations where the Volume Fraction of water was greater than 0.9.

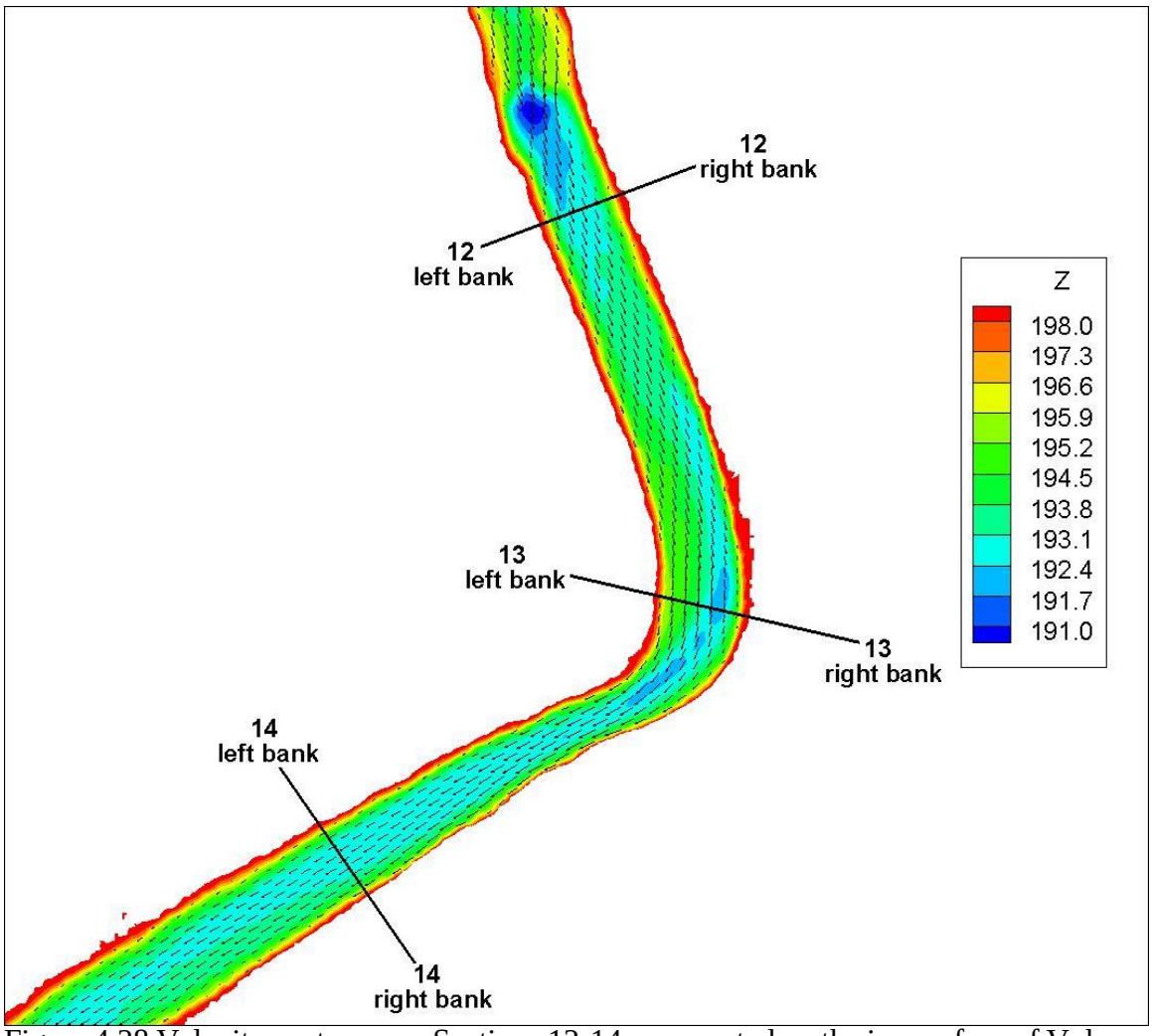

Figure 4.28 Velocity vectors near Sections 12-14 represented on the iso-surface of Volume Fraction of water equal to 0.9 for the 3-D solution of the flow in a 18-km river reach of the Iowa River near Iowa City. Velocity vectors were blanked for values of the Volume Fraction of water greater than 0.9.

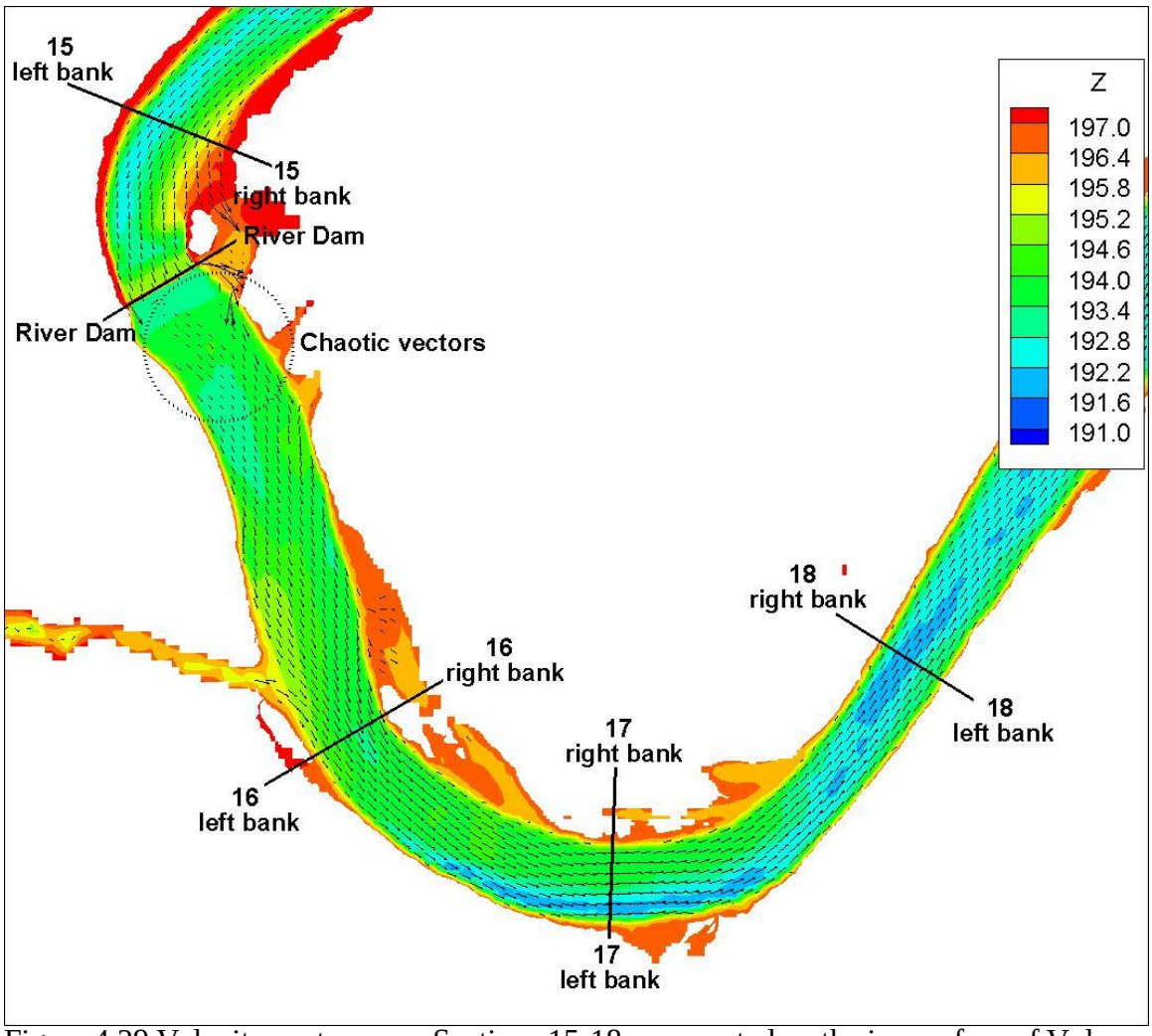

Figure 4.29 Velocity vectors near Sections 15-18 represented on the iso-surface of Volume Fraction of water equal to 0.9 for the 3-D solution of the flow in a 18-km river reach of the Iowa River near Iowa City. Velocity vectors were blanked for values of the Volume Fraction of water greater than 0.9.

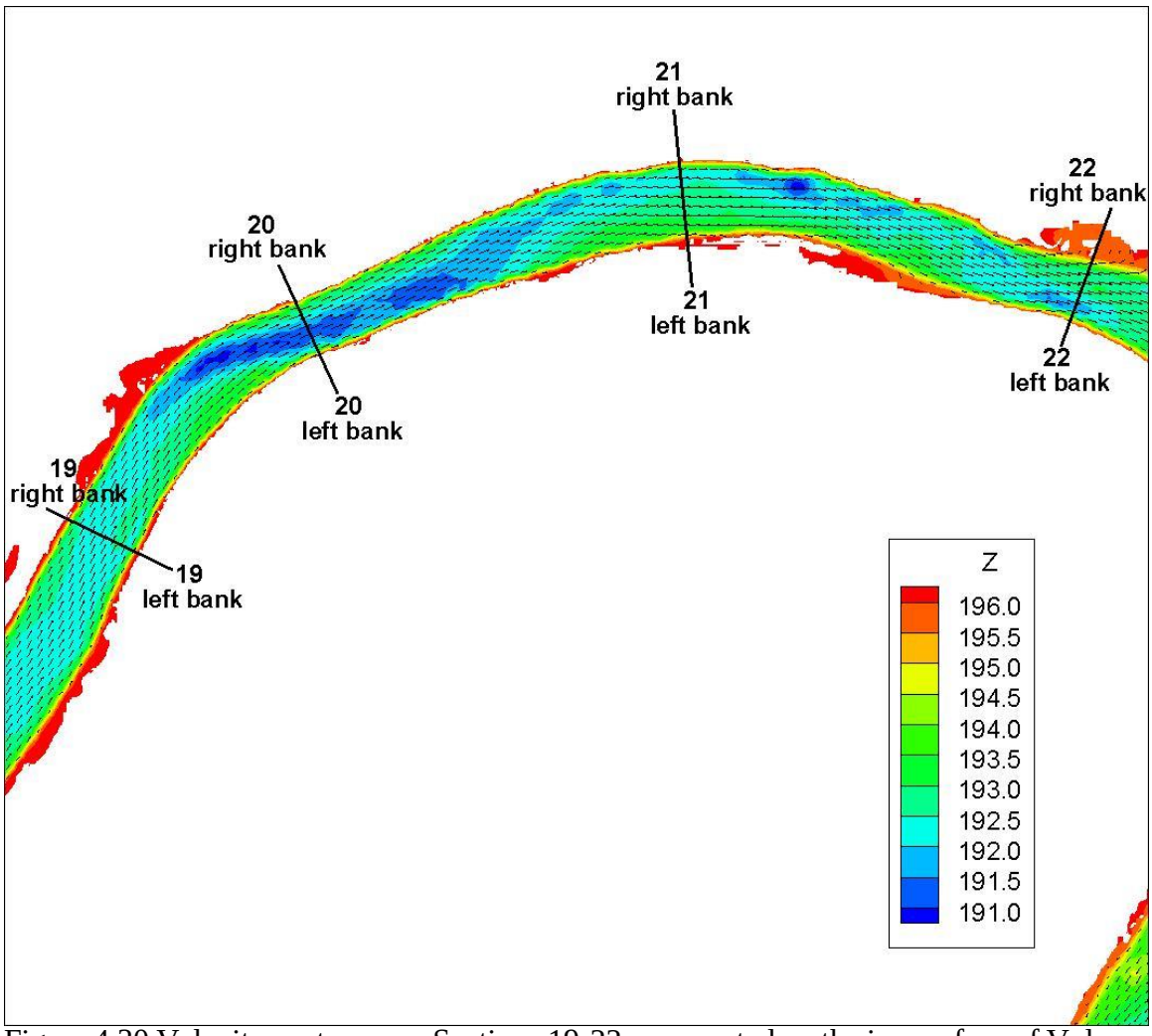

Figure 4.30 Velocity vectors near Sections 19-22 represented on the iso-surface of Volume Fraction of water equal to 0.9 for the 3-D solution of the flow in a 18-km river reach of the Iowa River near Iowa City. Velocity vectors were blanked for values of the Volume Fraction of water greater than 0.9.

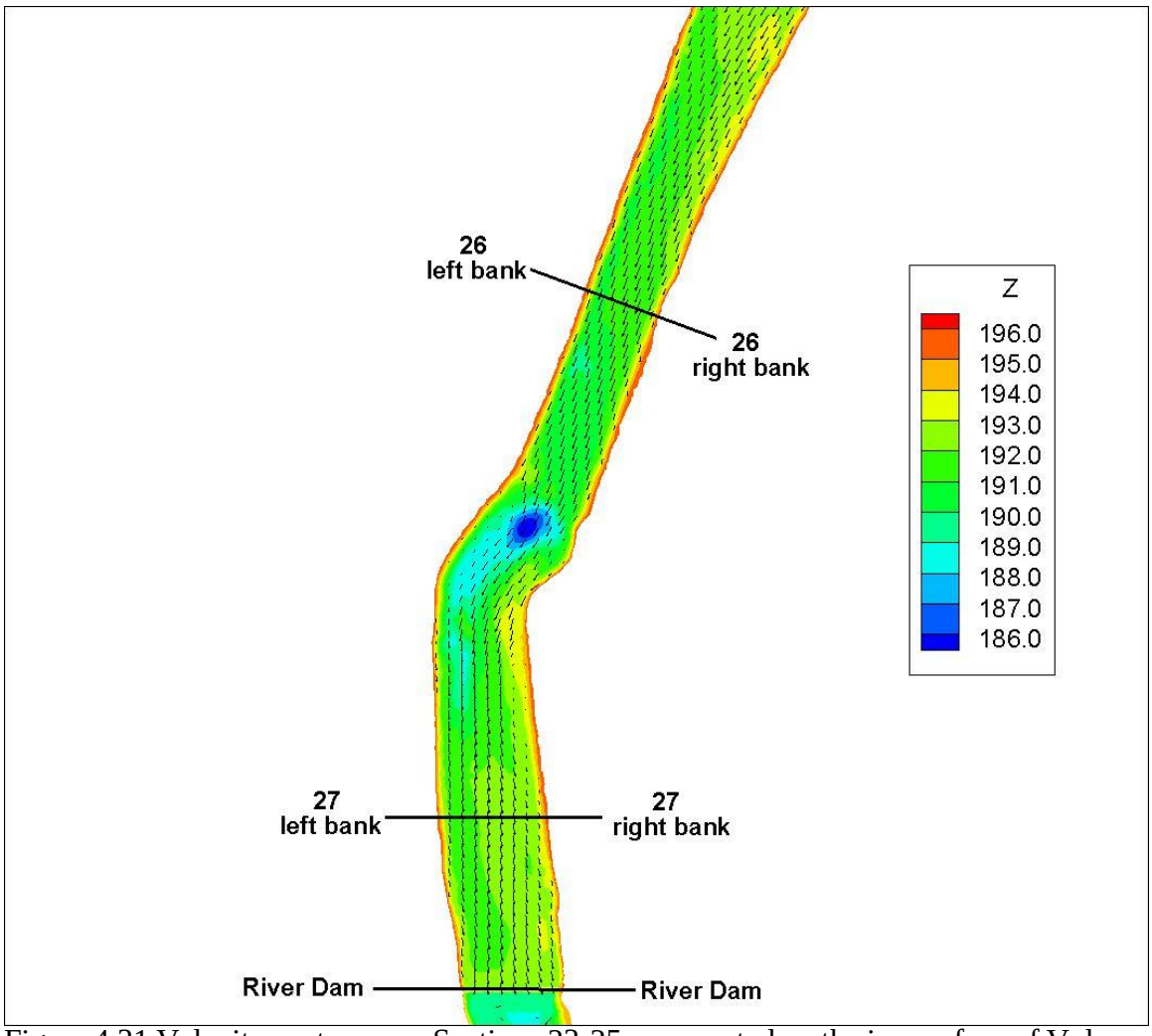

Figure 4.31 Velocity vectors near Sections 23-25 represented on the iso-surface of Volume Fraction of water equal to 0.9 for the 3-D solution of the flow in a 18-km river reach of the Iowa River near Iowa City. Velocity vectors were blanked for values of the Volume Fraction of water greater than 0.9.

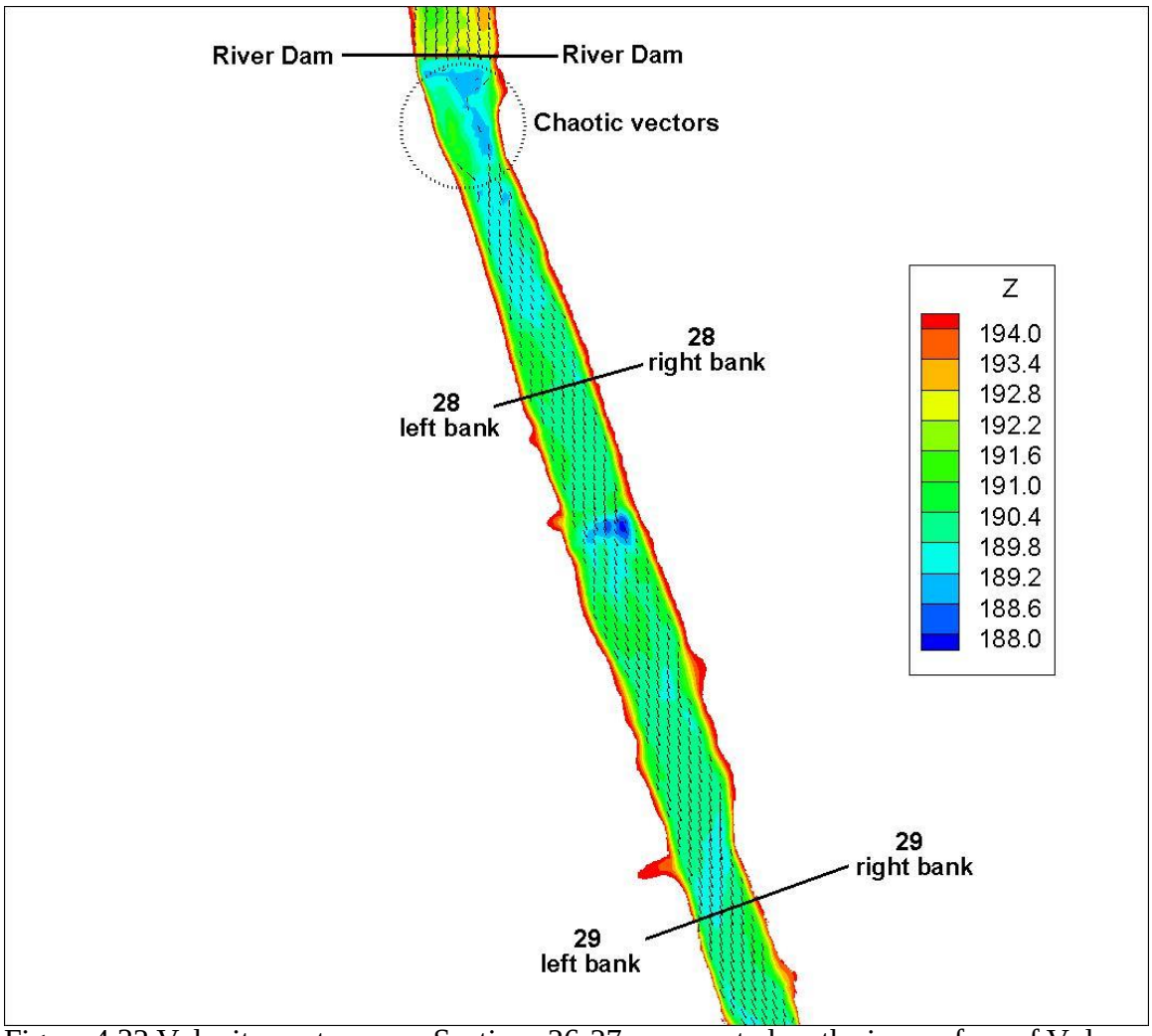

Figure 4.32 Velocity vectors near Sections 26-27 represented on the iso-surface of Volume Fraction of water equal to 0.9 for the 3-D solution of the flow in a 18-km river reach of the Iowa River near Iowa City. Velocity vectors were blanked for values of the Volume Fraction of water greater than 0.9.

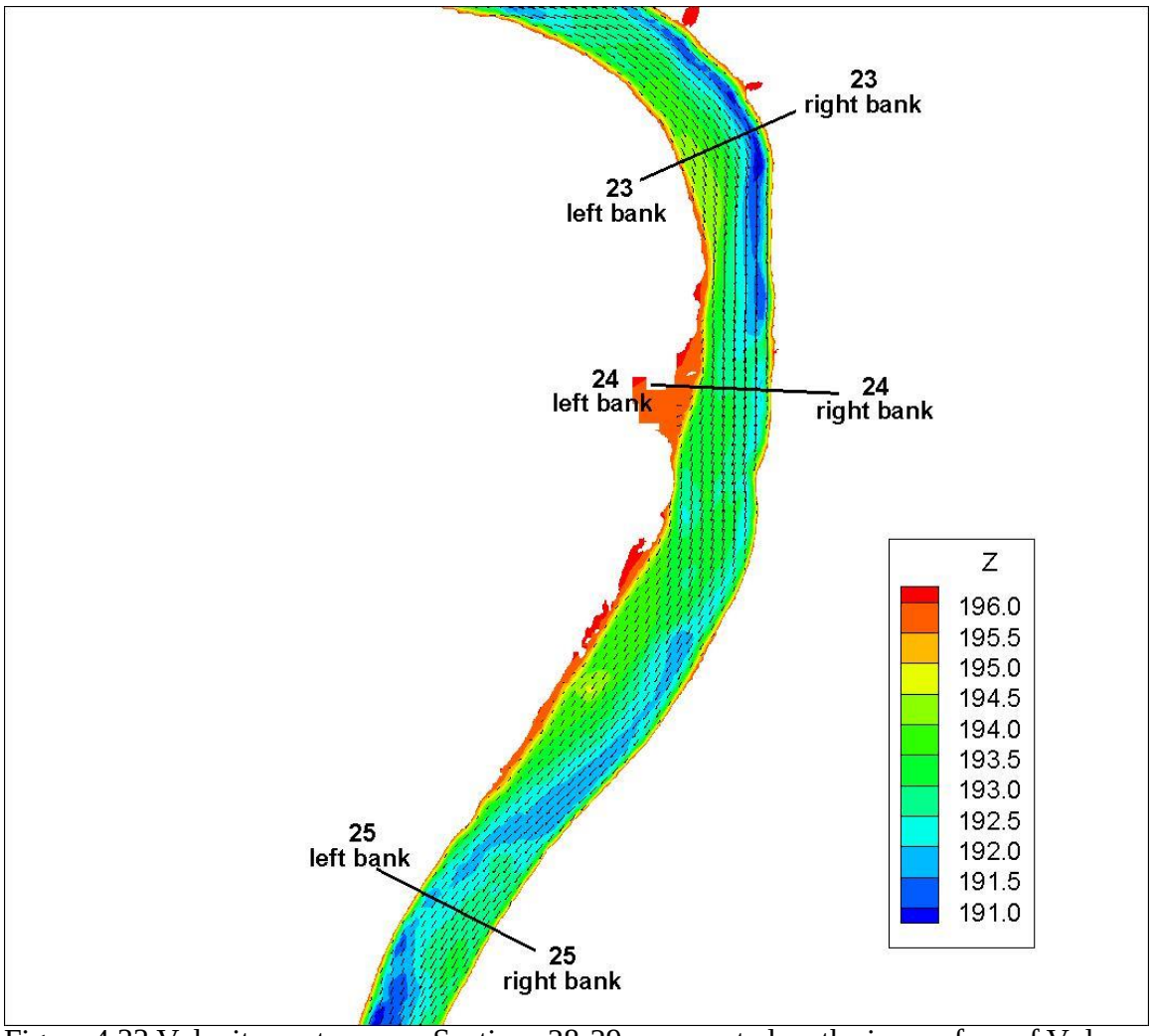

Figure 4.33 Velocity vectors near Sections 28-29 represented on the iso-surface of Volume Fraction of water equal to 0.9 for the 3-D solution of the flow in an 18-km river reach of the Iowa River near Iowa City. Velocity vectors were blanked for values of the Volume Fraction of water greater than 0.9.

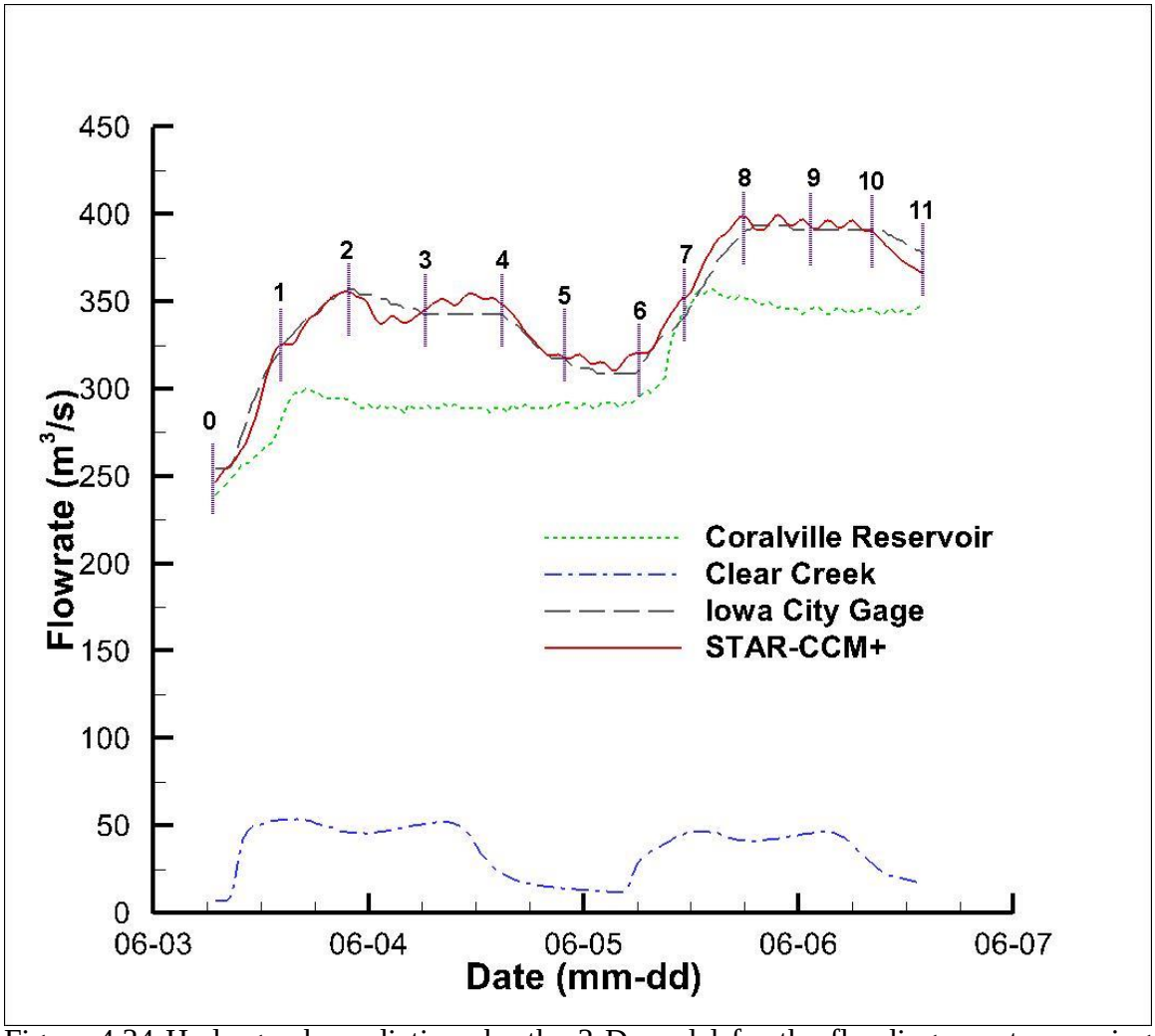

Figure 4.34 Hydrograph predictions by the 3-D model for the flooding event occurring from June 3rd, 2008 until June 6th, 2008. Predictions are compared with measured flow rates at the Iowa City Gage. Specific times for further analysis are specified as vertical lines labelled 0 through 11.

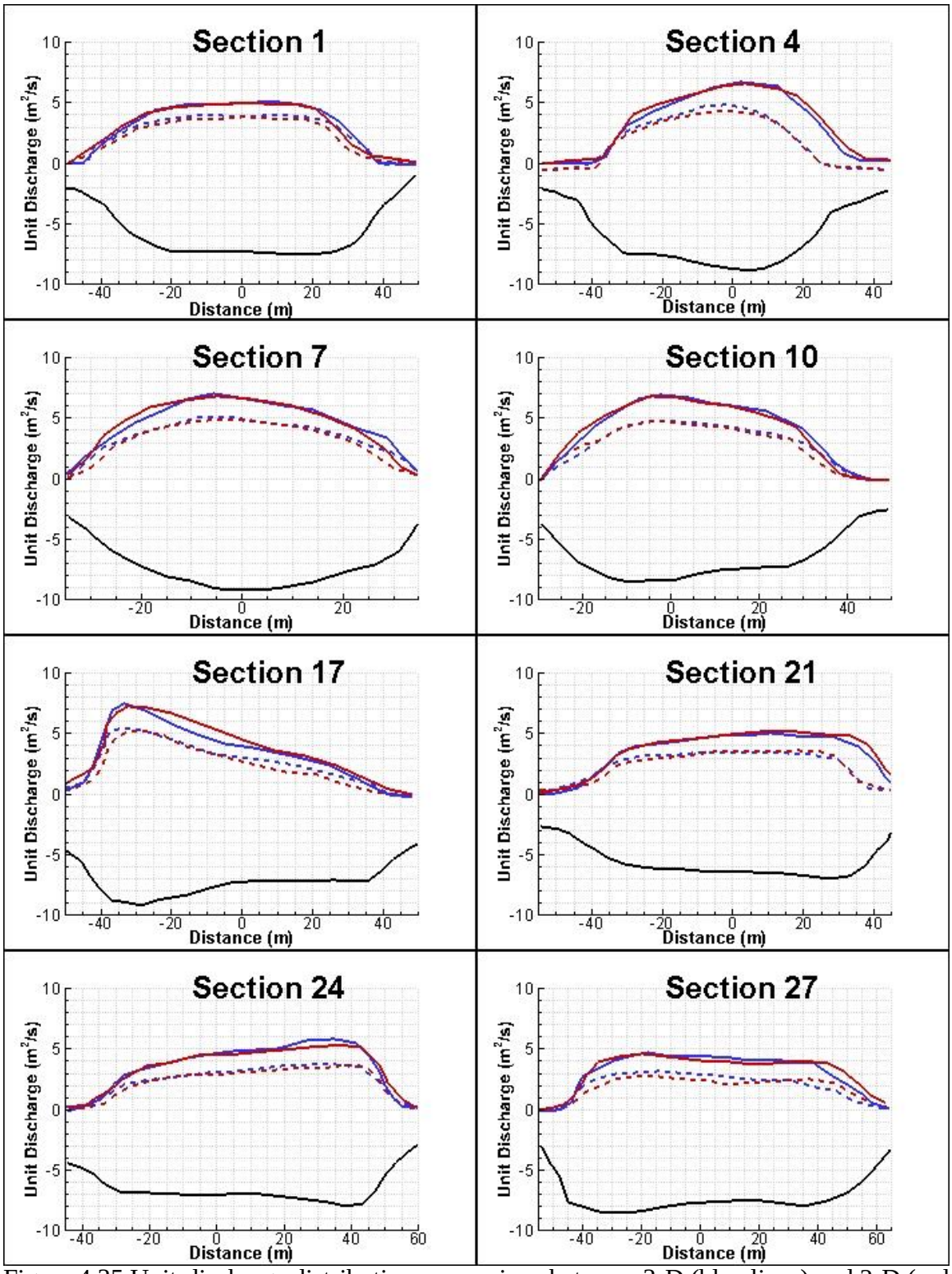

Figure 4.35 Unit-discharge distribution comparison between 3-D (blue lines) and 2-D (red lines) simulation results at initial conditions (dashed lines) and Time 8 (solid lines). Comparison is made at 8 cross sections that show good agreement between the 3-D and 2-D solutions.

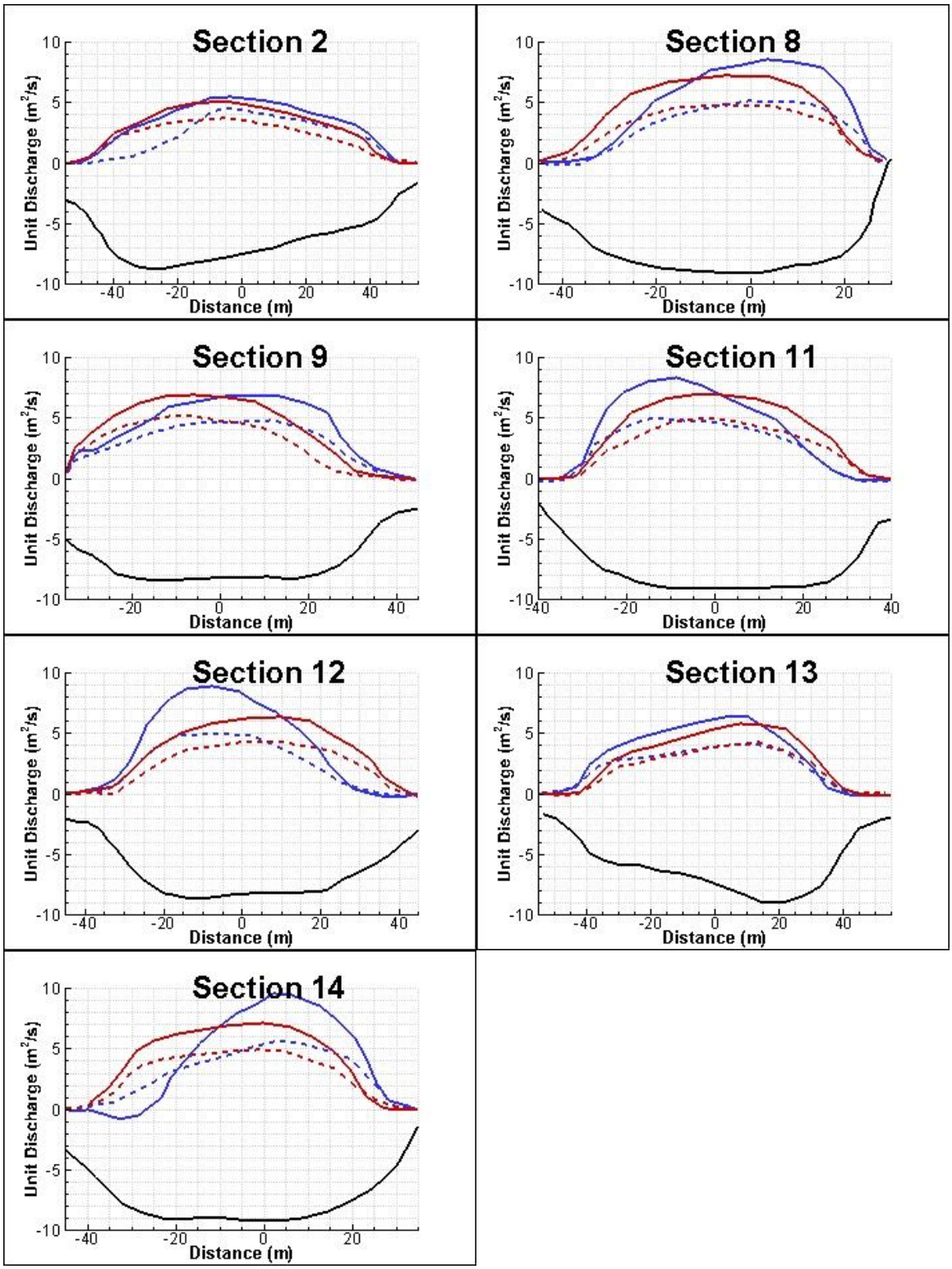

Figure 4.36 Unit-discharge distribution comparison between 3-D (blue lines) and 2-D (red lines) simulation results at initial conditions (dashed lines) and Time 8 (solid lines). Comparison is made at 7 cross sections that show bad agreement between 3D and 2D solutions.

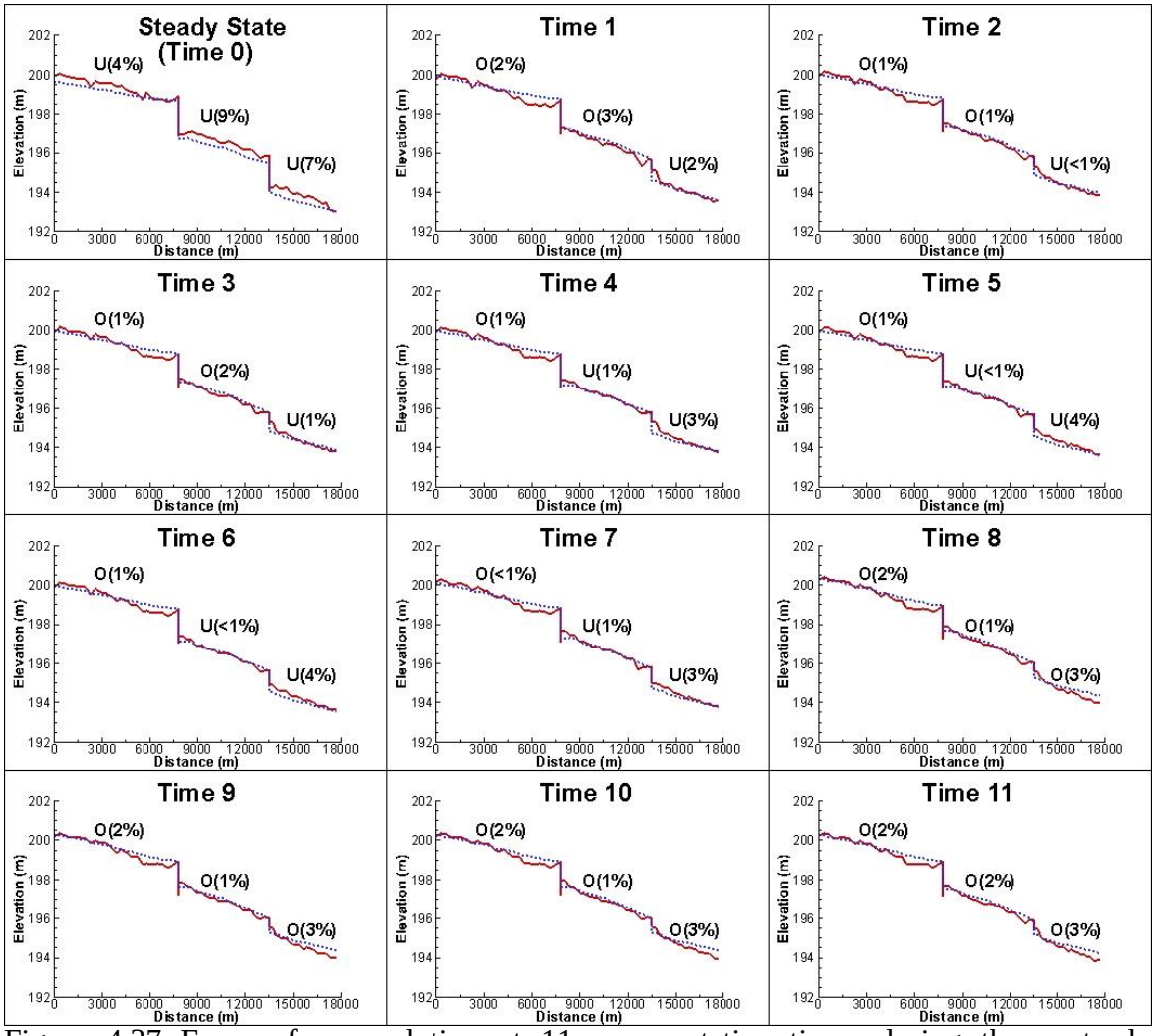

Figure 4.37 Free-surface evolution at 11 representative times during the unsteady hydrograph. Differences between the 3-D (Solid line) and 2-D (dashed line) solutions are shown for three regions: before the first dam, in between the first and second dam, and after the second dam. Errors are shown as percentage of the depth predicted by the 3-D model. O = Overestimate. U = underestimate.

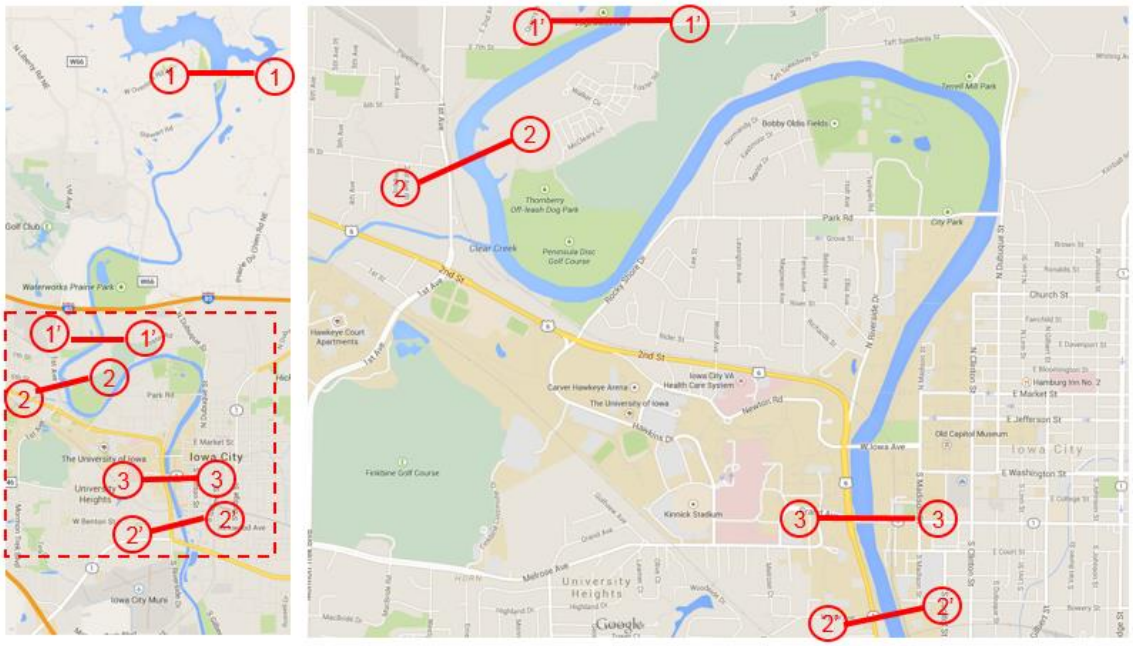

Figure 4.38 (a) Iowa River near Iowa City, Iowa, USA showing the flood control dam (1-1), the first river dam (2-2) and the second river dam (3-3). The start and end of the computational domain are shown in sections (1'-1') and (2'-2') respectively. (b) Close-up view showing the start of the computational domain (1'-1'), the end of the computational domain (2'-2') and the locations of the first river dam (2-2) and second river dam (3-3).

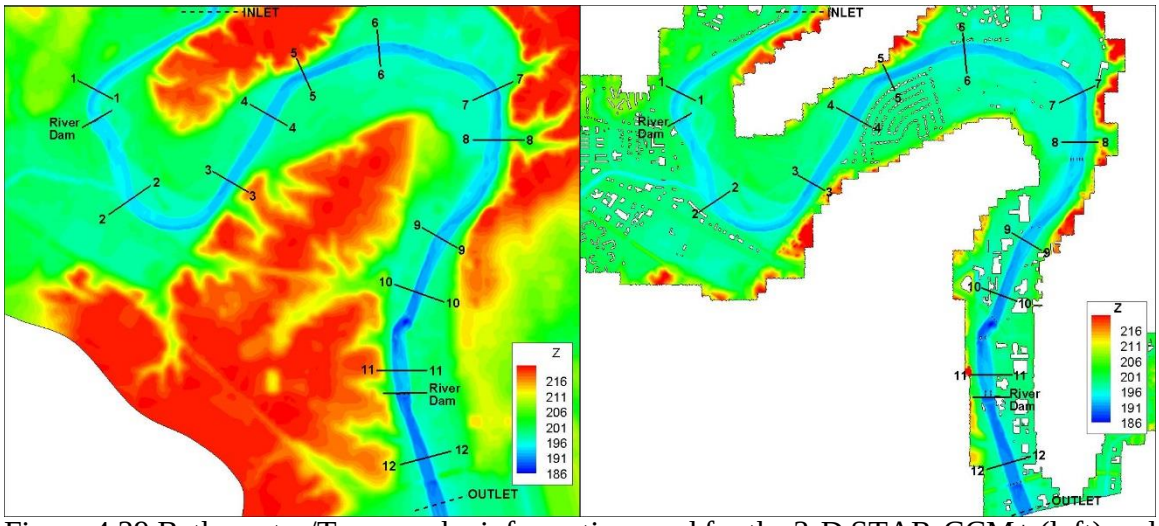

Figure 4.39 Bathymetry/Topography information used for the 3-D STAR-CCM+ (left) and 2D SRH-2D (right) simulations with locations of the 12 specified cross-sections for in-depth analysis.

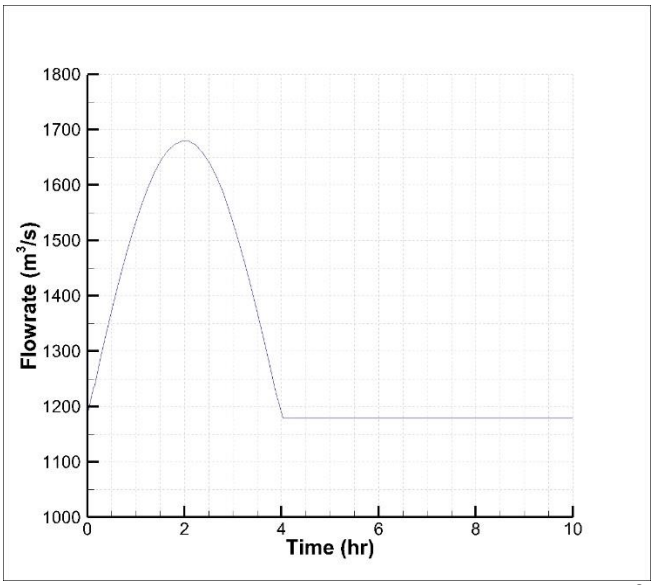

Figure 4.40 Sinusoidal hydrograph propagated into the 7-km reach of the Iowa River near Iowa City.

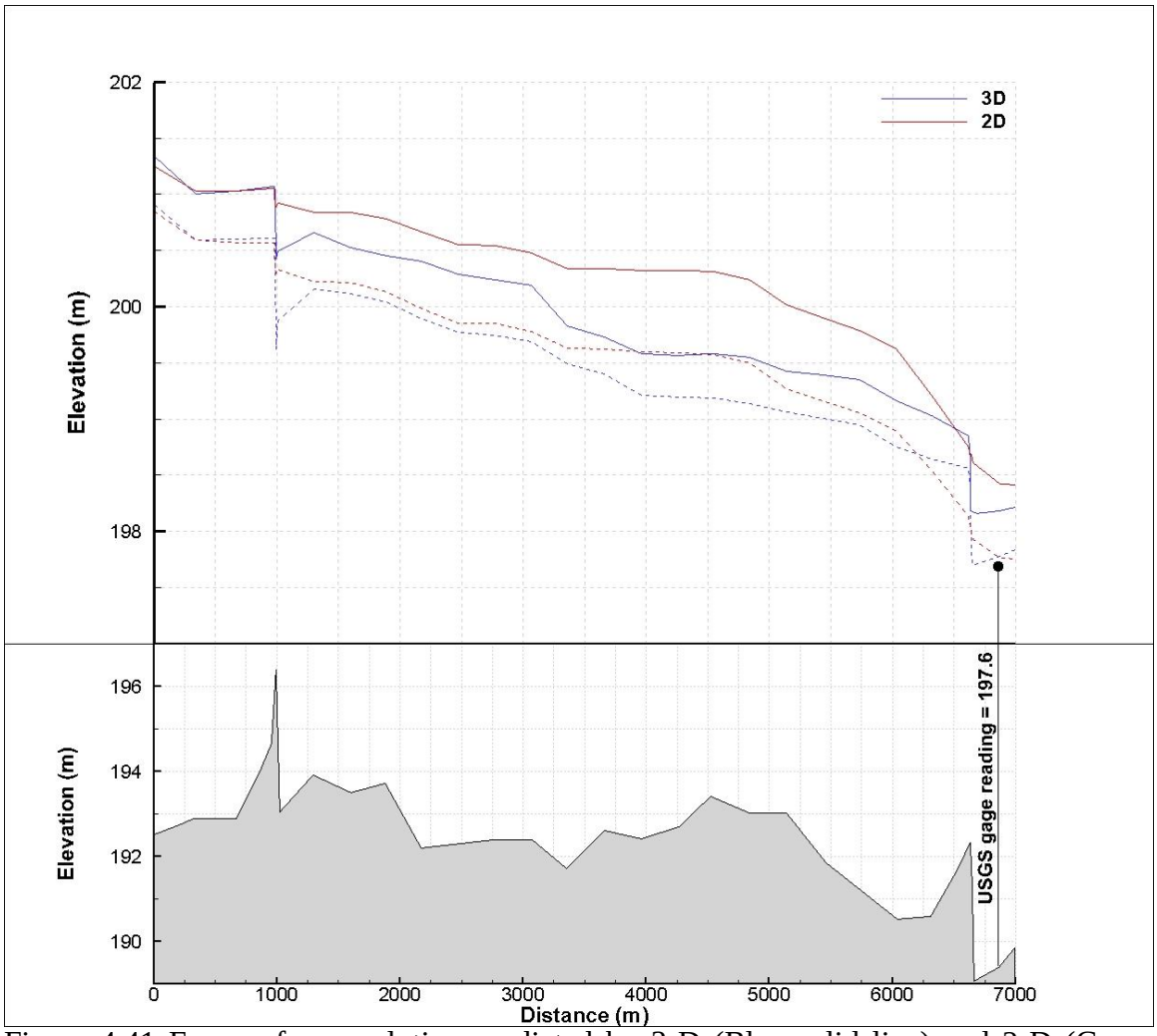

Figure 4.41 Free-surface evolution predicted by 3-D (Blue solid line) and 2-D (Green dashed line) simulations during the unsteady wave propagation into the 7-km reach of the Iowa River near Iowa City. Results are shown for specified times 1 through 4.

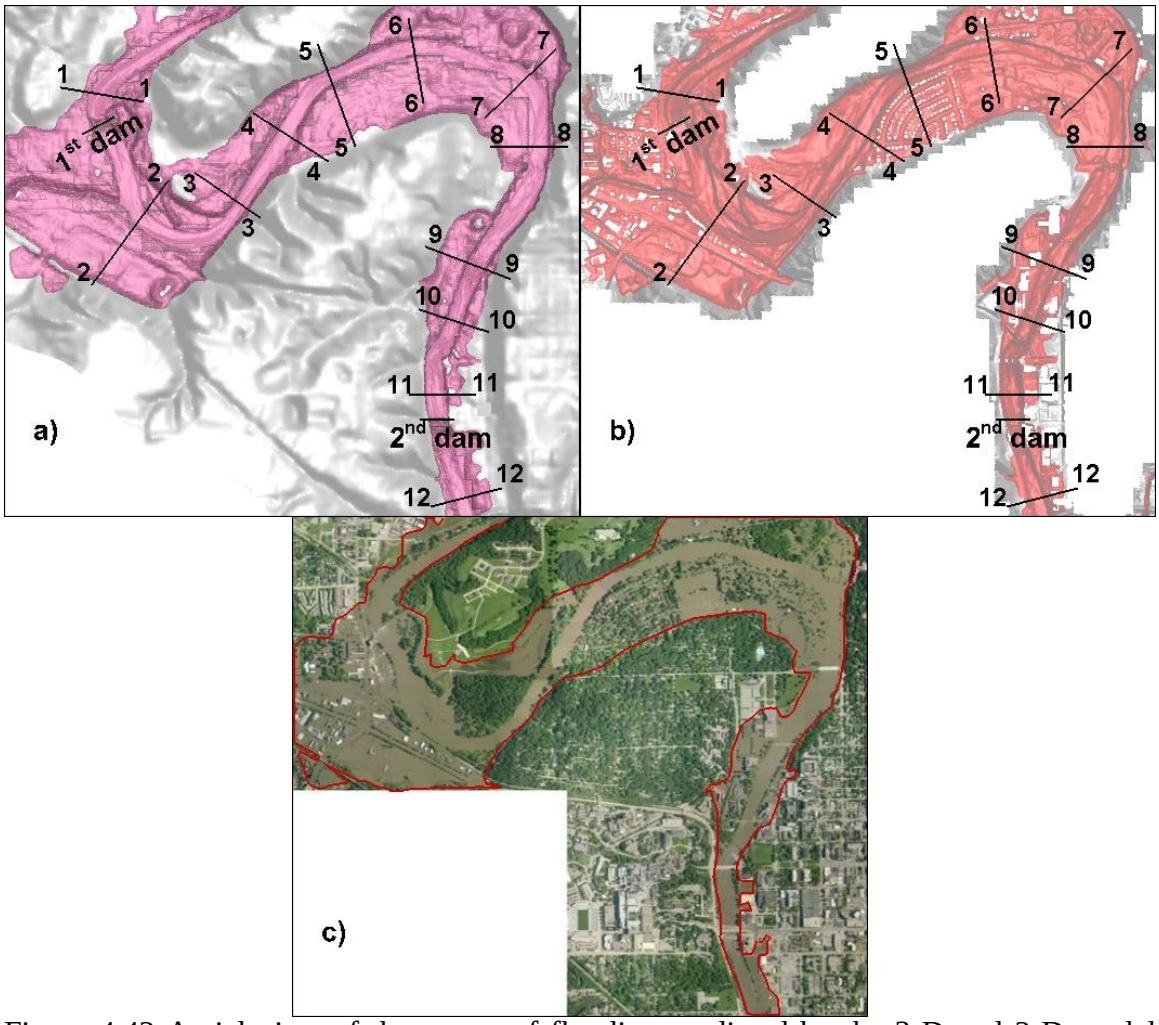

Figure 4.42 Aerial view of the extent of flooding predicted by the 3-D and 2-D model solutions at steady state and at the maximum extent of flooding during the unsteady wave propagation into the 7-km reach of the Iowa River near Iowa City.

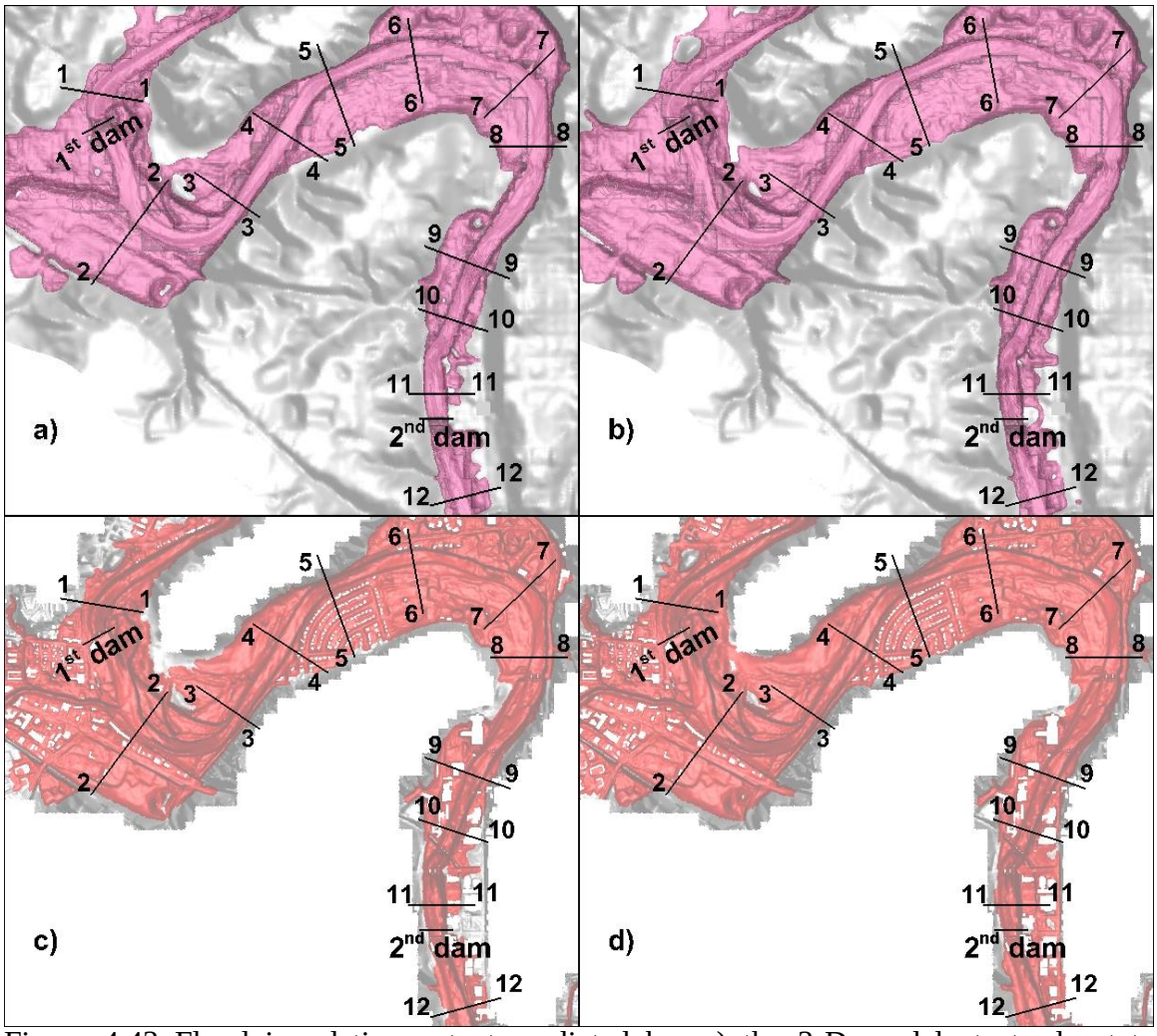

Figure 4.43 Flood inundation extent predicted by: a) the 3-D model at steady state conditions; b) the 3-D model at peak flood extent; c) the 2-D model at steady state conditions; and d) the 2-D model at peak flood extent.

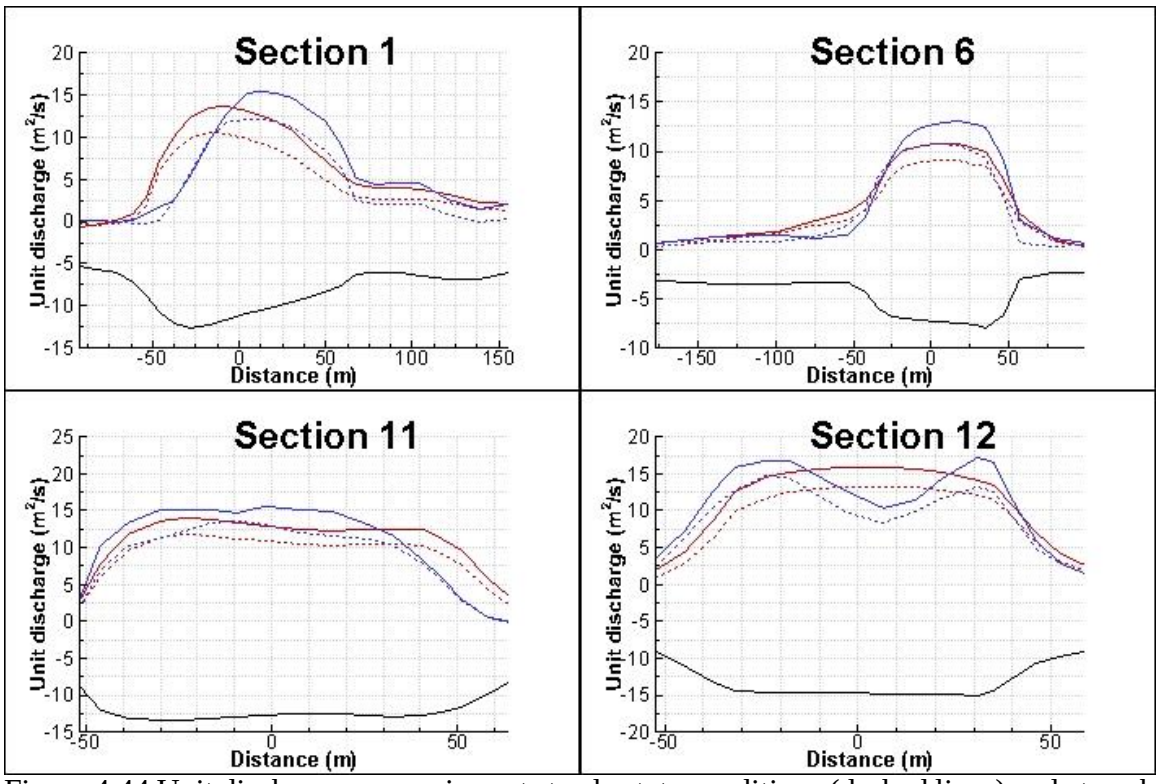

Figure 4.44 Unit discharge comparison at steady state conditions (dashed lines) and at peak flood extent (solid lines). Results are shown at the four cross sections that showed the most noticeable difference between the 3-D results (blue lines) and 2-D results (red lines).

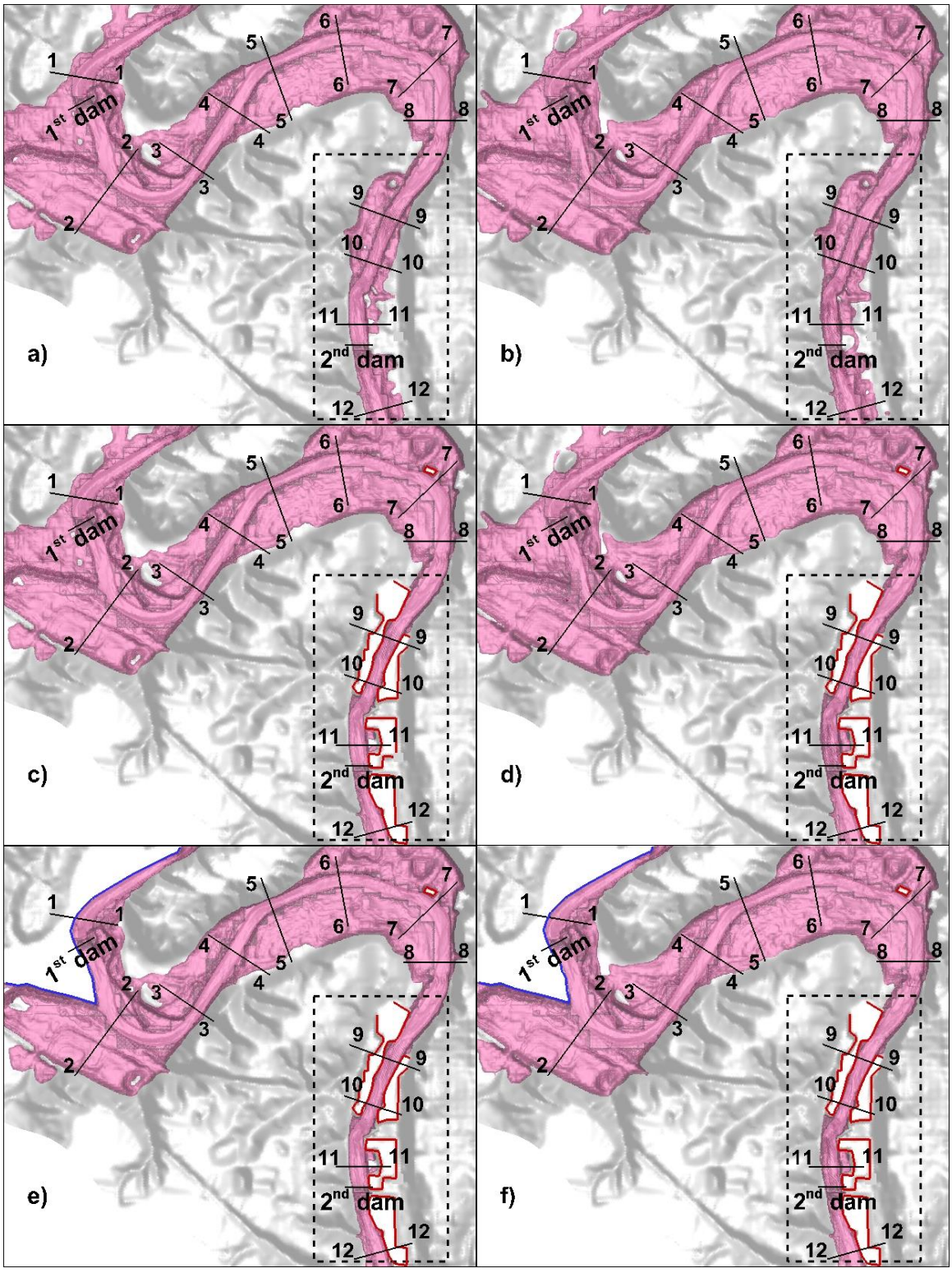
a)
b)
c)
d)
e)
f)
1st dam
2nd dam

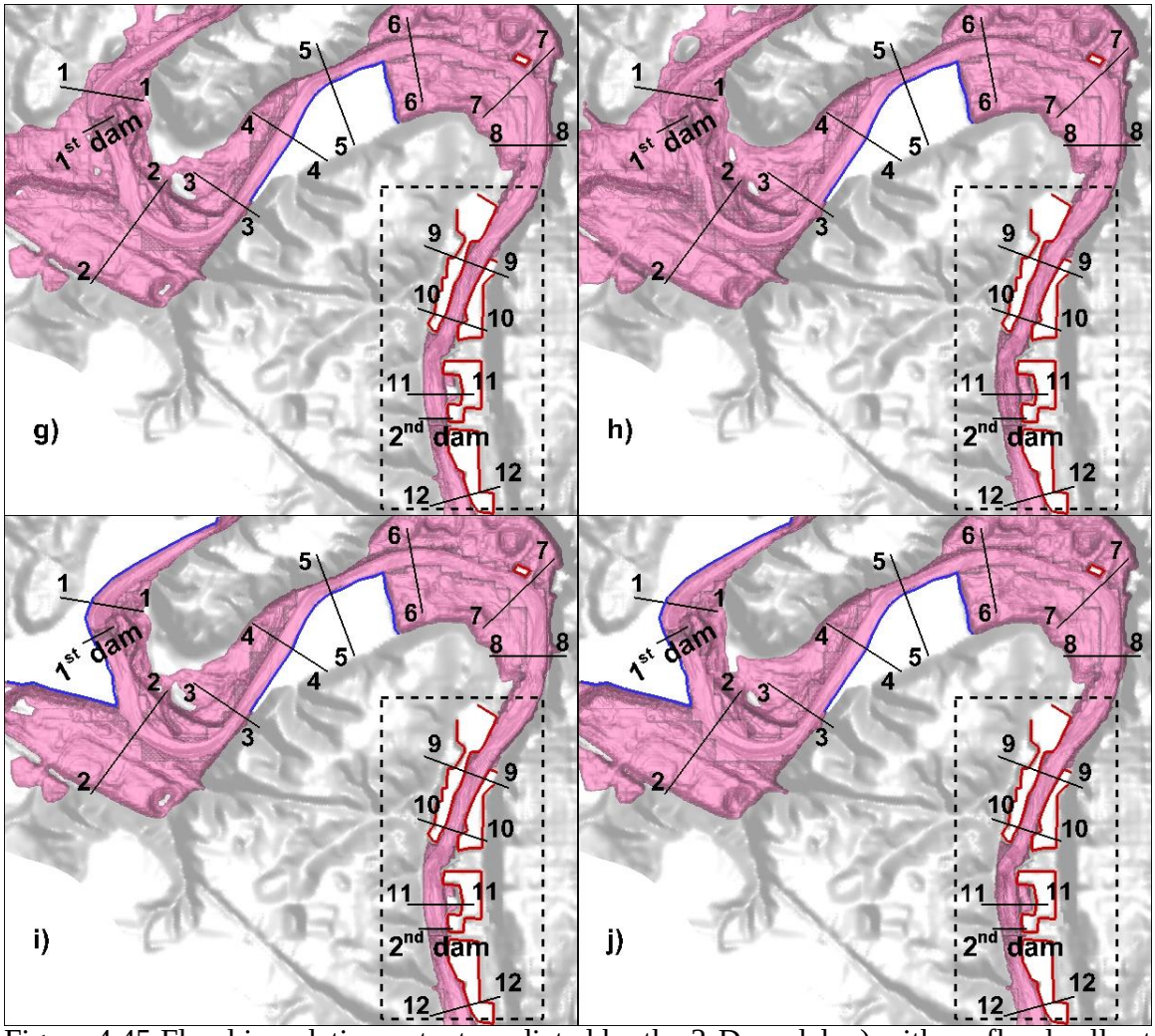

Figure 4.45 Flood inundation extent predicted by the 3-D model. a) with no floodwalls at steady state conditions; b) with no floodwalls at peak flood extent; c) with floodwalls, case scenario 1, at steady state conditions; d) with floodwalls, case scenario 1, at peak flood extent; e) with floodwalls, case scenario 2, at steady state conditions; f) with floodwalls, case scenario 2, at peak flood extent; g) with floodwalls, case scenario 3, at steady state conditions; h) with floodwalls, case scenario 3, at peak flood extent; i) with floodwalls, case scenario 4, at steady state conditions; and j) with floodwalls, case scenario 4, at peak flood extent.

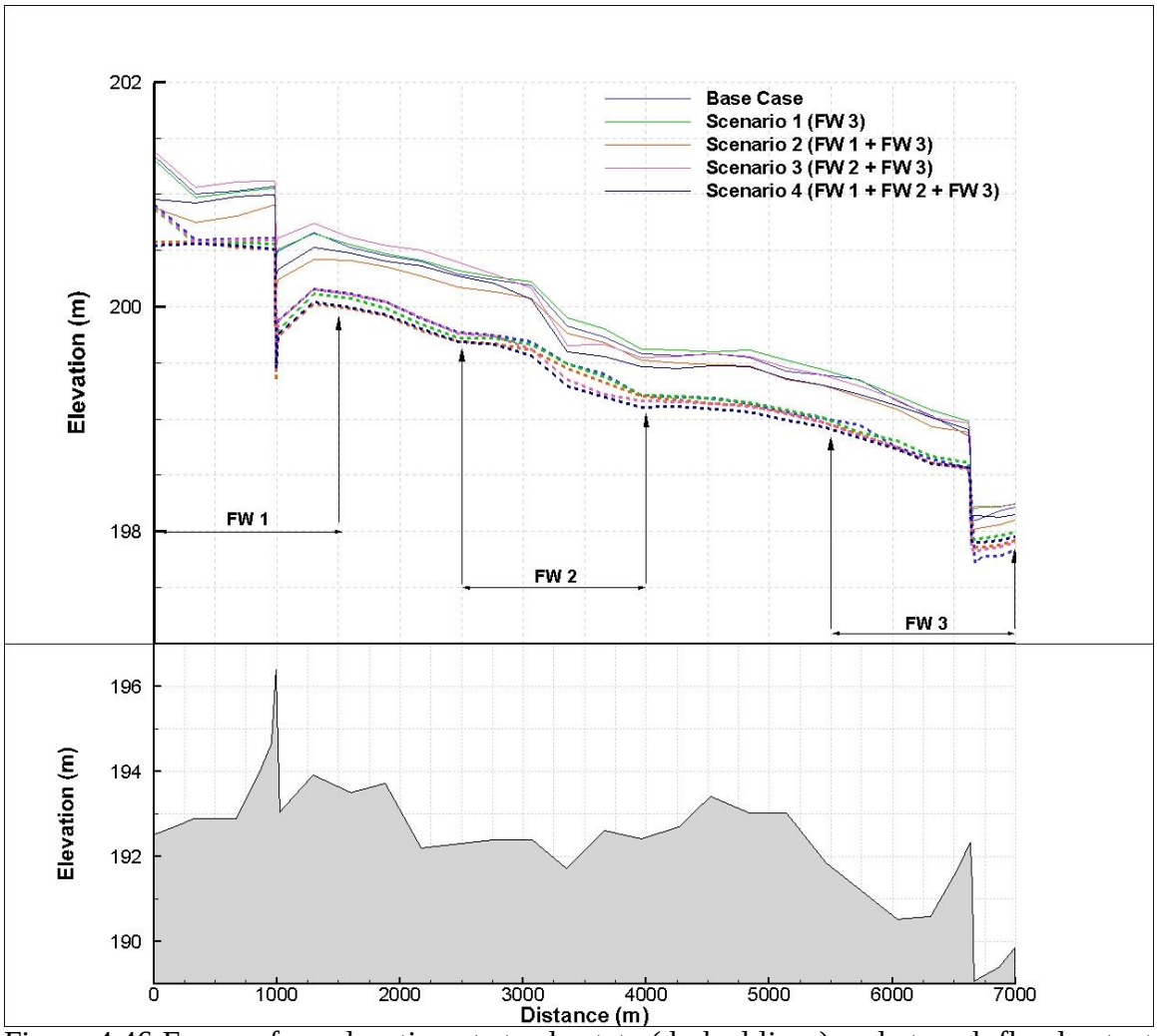

Figure 4.46 Free-surface elevation at steady state (dashed lines) and at peak flood extent (solid lines). Results are compared for the 3-D simulations with no flood walls (blue lines) and with floodwalls, case scenario 1 (green lines), case scenario 2 (orange lines), case scenario 3 (pink lines), and case scenario 4 (dark blue lines).

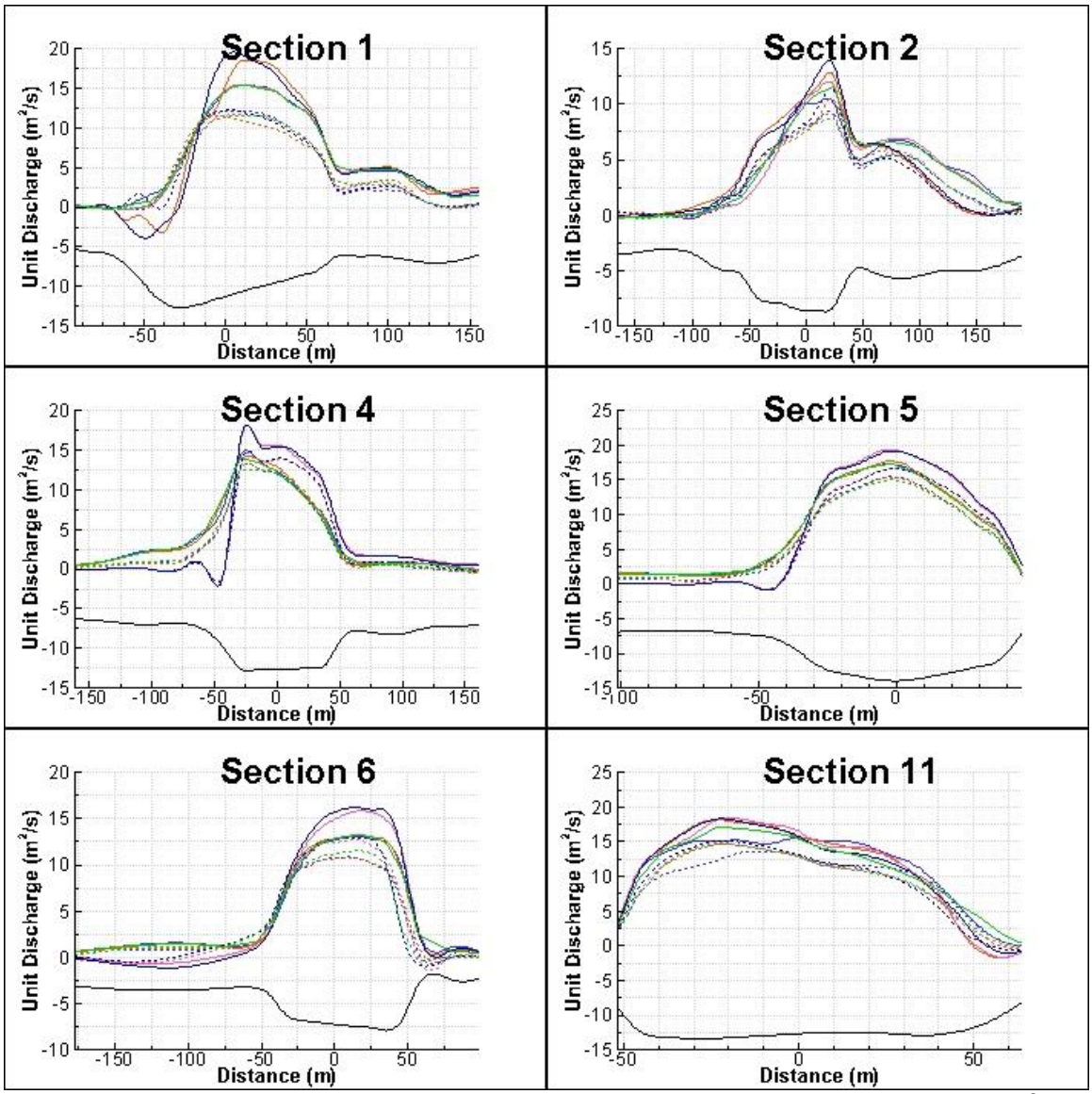

Figure 4.47 Unit discharge comparison at steady state (dashed lines) and at peak flood extent (solid lines). The profiles are compared at the six cross sections that showed the most noticeable difference between the 3-D simulations with no floodwalls (blue lines) and with floodwalls, case scenario 1 (green lines), case scenario 2 (orange lines), case scenario 3 (pink lines) and case scenario 4 (dark blue lines).

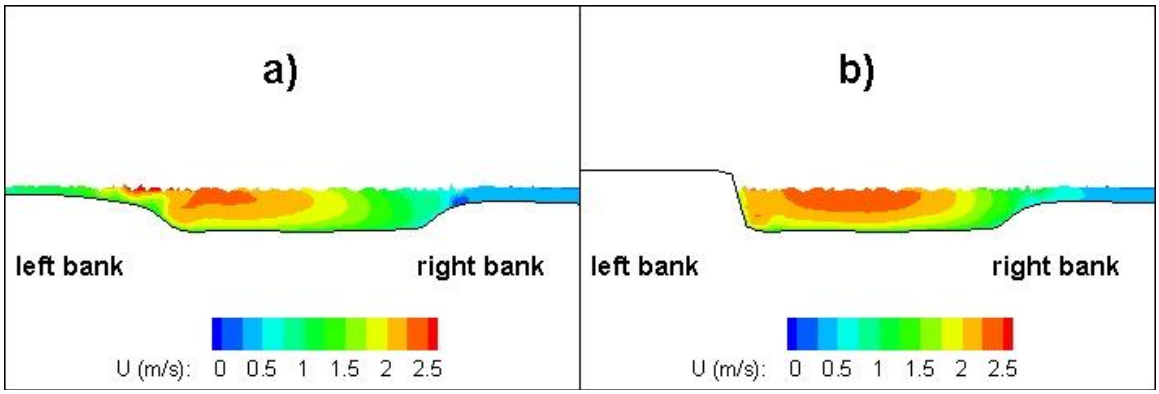

Figure 4.48 Streamwise velocity distribution at Section 4. Results are shown at steady state conditions for the cases: a) with no floodwalls; b) with floodwalls, case scenario 4.

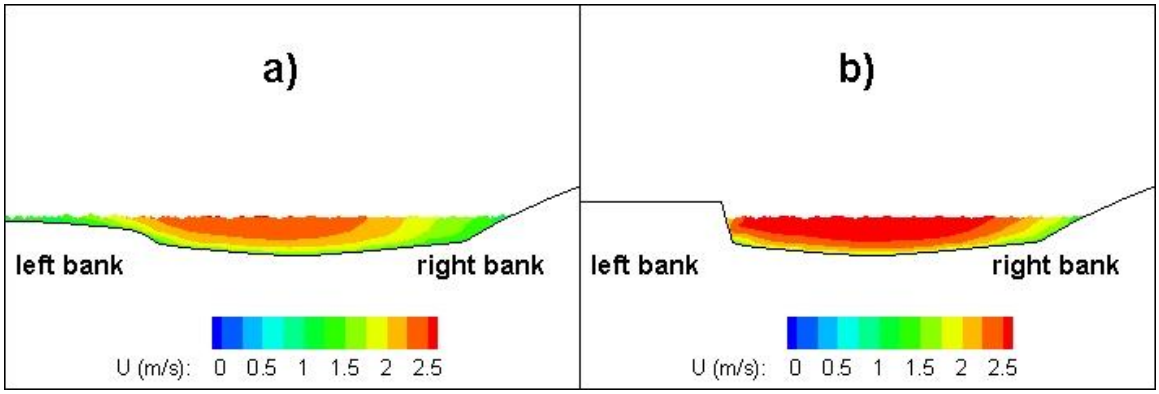

Figure 4.49 Streamwise velocity distribution at Section 5. Results are shown at steady state conditions for the cases: a) with no floodwalls; b) with floodwalls, case scenario 4.

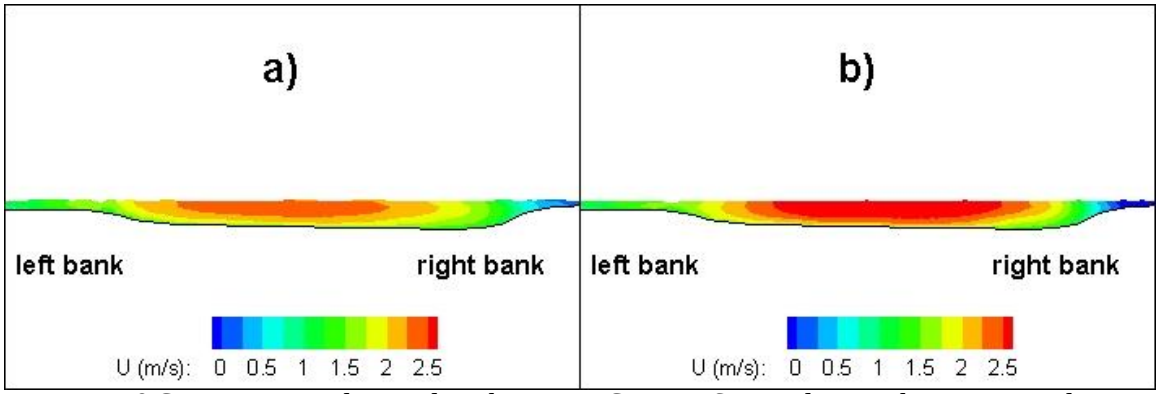

Figure 4.50 Streamwise velocity distribution at Section 6. Results are shown at steady state conditions for the cases: a) with no floodwalls; b) with floodwalls, case scenario 4.

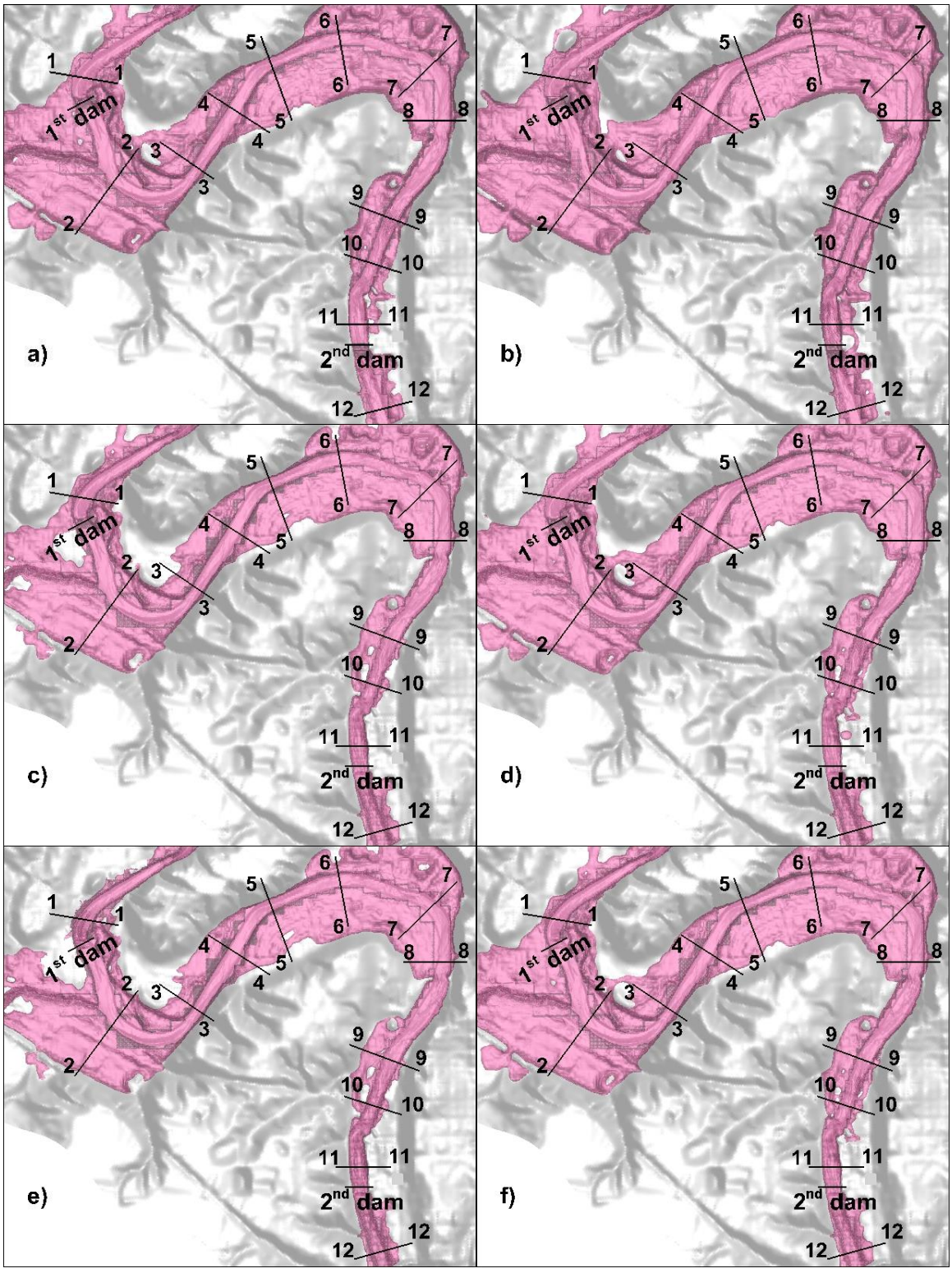
a)
b)
c)
d)
e)
f)
1st dam
2nd dam

Figure 4.51 Flood inundation extent predicted by the 3-D simulations. a) base case at steady state conditions; b) base case at peak flood extent; c) scenario 5 with removal of second dam at steady state conditions; d) scenario 5 with removal of second dam at peak flood extent; e) scenario 6 with removal of both dams at steady state conditions; and f) scenario 6 with removal of both dams at peak flood extent.

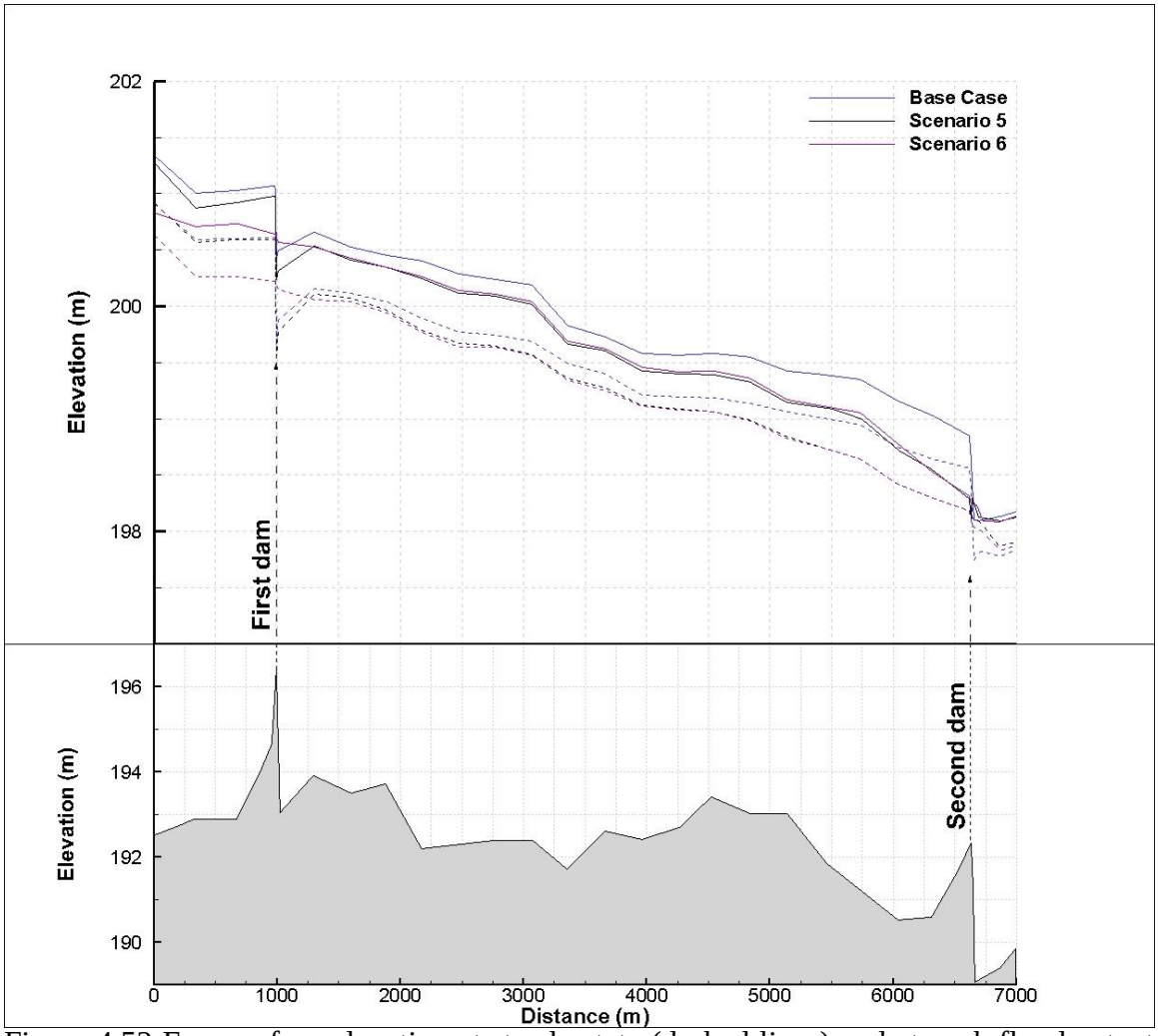

Figure 4.52 Free-surface elevation at steady state (dashed lines) and at peak flood extent (solid lines). Results are compared for the base case (blue line), scenario 5 with removal of second dam (black lines) and scenario 6 with removal of both dams (light purple lines).

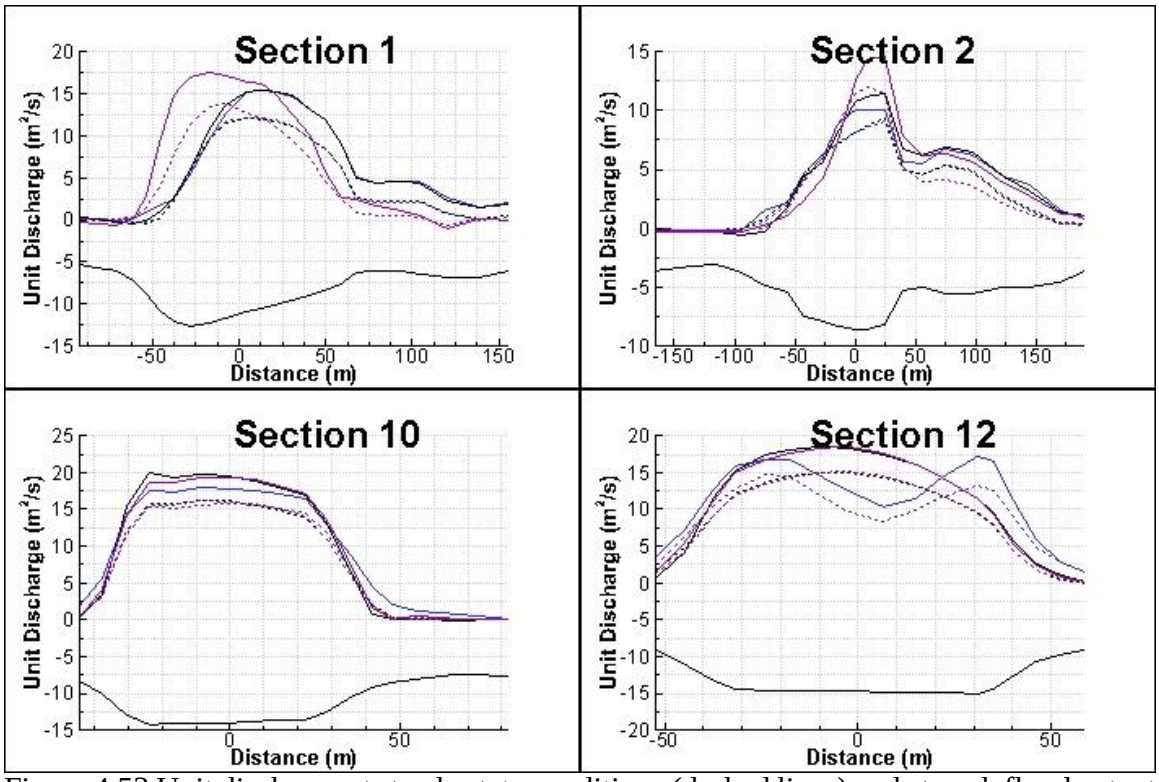

Figure 4.53 Unit discharge at steady state conditions (dashed lines) and at peak flood extent (solid lines). The profiles are compared at the three cross-sections that showed the most noticeable difference among the base case (blue lines), scenario 5 with removal of second dam (black lines) and scenario 6 with removal of both dams (light purple lines).

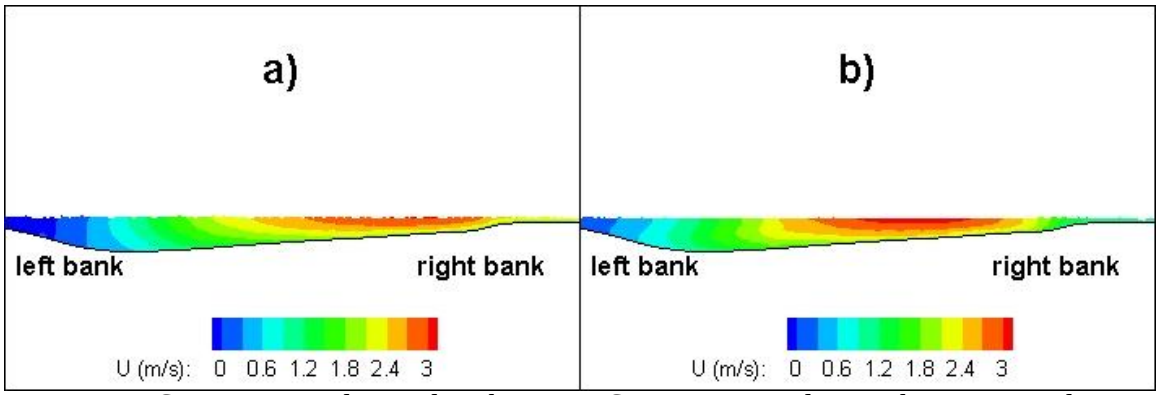

Figure 4.54 Streamwise velocity distribution at Section 1. Results are shown at steady state conditions for: a) Base Case; b) Scenario 6 with removal of both dams.

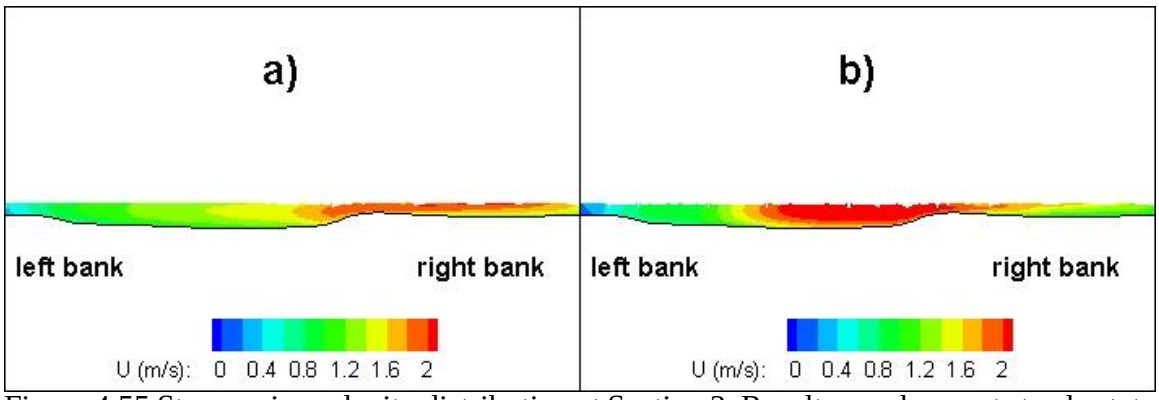

Figure 4.55 Streamwise velocity distribution at Section 2. Results are shown at steady state conditions for: a) Base Case; b) Scenario 6 with removal of both dams.

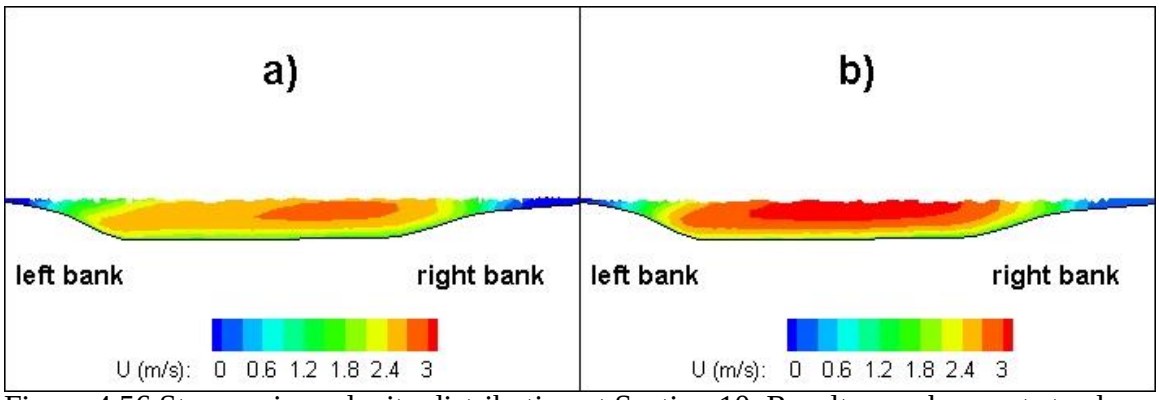

Figure 4.56 Streamwise velocity distribution at Section 10. Results are shown at steady state conditions for: a) Base Case; b) Scenario 6 with removal of both dams.

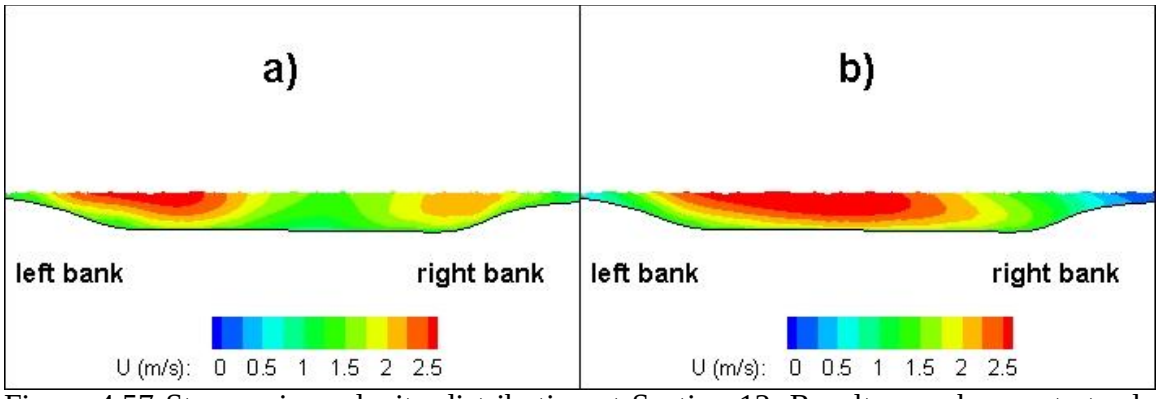

Figure 4.57 Streamwise velocity distribution at Section 12. Results are shown at steady state conditions for: a) Base Case; b) Scenario 6 with removal of both dams.

CHAPTER 5 ESTIMATION OF POTENTIAL FOR SEDIMENT EROSION DURING FLOODING EVENTS INCLUDING PRESSURE SCOUR EFFECTS

5.1 Introduction

Sediment transport plays a crucial role in most, for not saying all, of hydro-related environment. There is probably no better way to lay out its importance than to quote Garcia (1999):

Since the beginning of mankind, sedimentation processes have affected water supplies, irrigation, agricultural practices, flood control, river migration, hydroelectric projects, navigation, fisheries, and aquatic habitat. In the last few years, sediment also has been found to play an important role in the transport and fate of pollutants; thus sedimentation control has become an important issue in water quality management.

Several approaches have been proposed throughout the past decades to describe and quantify sediment transport phenomena (erosion, transportation, and deposition). These approaches can be classified as either deterministic or probabilistic (Juez et al., 2017). Examples of deterministically-based formulae to predict the sediment load are Meyer-Peter and Müller (1948), Nielsen (1992) and Wong (2003). Examples of probabilistic formulae are Einstein (1950) and Kalinske (1947). The common feature between these models is that they depend on the bed shear stress, making it one of the most important quantities to be determined. There are mainly two ways to determine the bed shear stress based on depth-averaged velocity profiles: Manning's based approach (Ven Te Chow, 1959) or Logarithmic Velocity profile approach (White, 1974). The bed shear stress, however, needs to be modified to include slope effects in order to be used in classical sediment transport formulae. It can be modified, for example, by using the method of Brooks (1963), Soulsby (1997) or Van Rijn (1989). It is known, however, that when the angle of repose is close to the bed angle, the corrected bed shear stress tends to

zero, which means the sediment transport capacity will go to infinity (Juez et al., 2017). A second approach is to connect the tractive force associated to the grain movements to the bed shear stress without modifying the critical bed shear stress (Wu, 2004; Wu et al. 2017), though extensive parameter calibration and tuning is needed to achieve realistic results (Juez et al., 2017). The final method is based on connecting how changes in near-bed hydraulics affect the force balance on individual grains (Kovacs and Parker, 1994; Parker, Seminara and Solari, 2003). The main drawback of this approach is its dependence on micro-scale theory, which limits its applicability to real scenarios (Juez et al., 2017).

Sediment transport can also affect existing infrastructure and should be considered in infrastructure design (e.g., bridges). According to the National Bridge Inventory, approximately 84% of bridges are built over streams (Mays, 2011). Most bridges experience problems with scour and bank erosion during their lifespan, especially during floods (Mays, 2011). For example, the 1993 flood in the Upper Mississippi River basin caused 23 bridge failures, with 21 failure modes related to scouring (Richardson and Davis, 2001). Failure modes are associated with their respective scour modes, such as pier scour, contraction scour, pressure scour, lateral bank migration, etc. For instance, pier scour develops around the bridge piers as a result of increased flow acceleration around their base. Contraction scour is caused by the sudden decrease of cross sectional area which increases the mean flow velocity in between piers or in between a pier and an abutment. As a result, erosion develops around the piers and abutments when the spacing between these hydraulic structures is not very large.

Pressure scour is only present during high flow conditions when the bridge deck becomes submerged. When the upstream free-surface elevation is higher than the bridge deck elevation, the flow experiences a vertical contraction, increasing the streamwise velocity in between the river bottom and the bridge deck. The potential for sediment erosion increases (Lyn, 2008) due to the flow underneath the bridge deck changing regime

from open channel flow to pressurized flow (pipe flow). Pressure scour has been studied both experimentally (Picek et al., 2007; Kumcu, 2017) and numerically (Shen et al., 2012), with emphasis on improving existing empirical equations for sediment transport such that they can be applied for pressurized flow regime, as well as predicting backwater effects upstream of the bridge deck and discharge over the deck. However, these modified formulas and approaches were shown to be only partially successful.

Several computational approaches have been developed to model sediment transport in common 1-D, 2-D or 3-D numerical models used in river engineering. 1-D models were the first to be developed. They are computationally fairly inexpensive, robust and relatively easy to use. Some examples of widely used 1-D sediment transport codes are HEC-RAS (USACE, 2016), MIKE11 (1999a) and SEDICOUP (Holly and Rahuel, 1990). The main assumptions in such 1-D (section-averaged) models are that flow is uniform in the cross section, pressure is hydrostatically distributed, turbulence can be accurately accounted using simplified resistance laws such as Manning's or Chezy formulas, and that the average channel bed slope is small. These models are able to predict long-term morphologic changes for large complex river networks. 2-D models, on the other hand, are better suited when the flow distribution varies significantly in the lateral direction. Some examples of 2-D models include MOBED2 (Spasojevic and Holly, 1990a), MIKE21 (DHI, 1999b), TELEMAC2D (Peltier et al., 1991). For example in the work of Zech et al, 2010 they were able to simulate a dam break scenario with moveable bed using a research 2D code, whereas in the work of Caviedes-Voullieme et. al., 2017 they were able to simulate bed-load transport to study channel flushing. These models can predict local changes in bathymetry, as well as long-term sediment load and morphologic changes. However, they often assume equilibrium in bed load transport. Finally, 3-D models solve the steady or unsteady RANS equations. Some examples of 3-D models are SUTRENCH-3D (Van Rijn, 1987) or CCHED3C (Wand and Adeff, 1986). Wu, Rodi and Wenka (2000) were able to accurately simulate flow and sediment transport in an 180° bend, whereas

Zeng et al. (2010) simulated equilibrium scour in S-shaped channel; both using a fully 3D CFD code. Such 3-D models are able to predict sediment transport, including non-equilibrium effects, with a higher degree of accuracy than 1-D and 2-D models given that such models use much less assumptions, especially in predicting the mean flow field and thus the bed shear stress distributions. 3D models are especially suited in channels with high degree of curvature, near hydraulic structures or obstructions such as piers, abutments, river dams, etc.

While a 3-D model with bed load transport and deformable bed should be ideal to study potential for scour in open channels and natural river reaches, the development of such a model is beyond the scope of this work. Rather, in the present chapter the potential for sediment entrainment is investigated using the hydrodynamics 3-D model at both steady state and unsteady conditions assuming no change in bathymetry. First, the sediment entrainment flux (instantaneous and cumulative) is estimated using the Du Boys formula, a FHWA approved equation used in practice. Second, bed shear estimates obtained using both Manning's and Logarithmic Velocity Profile methodologies are compared against bed shear estimates obtained based on the velocity field predicted by the 3-D model. Simulations with and without a bridge deck are included for some of the test cases analyzed in this chapter to assess the influence of pressure scour contribution to the total sediment erosion. The test cases include flow in a rectangular channel and flow in a reach of the Iowa River near Iowa City.

5.2 Flow in a straight rectangular channel

The first test case considered is a 1.5 km long rectangular channel with a bottom width of 60 m, total height of 10 m and a bed slope of 0.01%, as seen in Figure 5.1 a. Bed roughness was estimated using information on sediment data (e.g., d_{50}) available for the Iowa River near Iowa City. Strickler's formula (Strickler, 1923) was used to estimate the value of Manning's n coefficient. Strickler formula is shown below

$$n = \frac{1}{26} k_s^{1/6} \tag{5.1}$$

where k_s is the equivalent roughness height. The calculated Manning's n coefficient was estimated to be equal to 0.014.

Besides simulations with the brick deck present, corresponding simulations with no bridge deck were also conducted. The main reason was the need to isolate the contribution due to pressure scour to the potential for sediment entrainment. To isolate this effect one needs to know what is the potential for sediment entrainment for the case when no obstructions (bridge deck) are present in the channel.

The steady state condition was calculated for a discharge Q=200 m^3/s with n=0.014, giving an initial height of approximately 3 m (Figure 5.1 a). Once initial conditions (steady state) were established in the channel, a sinusoidal wave was propagated into the domain. The test cases were considered with a duration of the sinusoidal wave of 4 and 8 hours, respectively (Figure 5.2). The 8-hr wave test case was used to study hysteresis phenomena in the channel. This is discussed at the end of subsection 5.2.1.

Three cross sections were chosen for in-depth analysis. Their positions are shown in Figure 5.1 b for the computational domain containing the bridge deck. The actual streamwise locations are 990 m (Section 1), 1010 m (Section 2) and 1030 m (Section 3) downstream of the inlet. The section situated at 1010 m from the inlet section cuts through the middle of the bridge deck.

For both simulations without and with the bridge deck, the potential for sediment entrainment was calculated in each of the 3 cross sections using the DuBoys equation (DuBoys, 1879), shown below:

$$g_s = \psi \tau_0 (\tau_0 - \tau_c) \tag{5.2}$$

where g_s is the rate of sediment discharge per unit width of channel in lb/ft-s, τ_0 is the bed shear stress in psf, τ_c is the critical bed shear stress needed to start mobilizing bed material in psf, and ψ is the DuBoys coefficient in ft^3/lb-s . Both τ_c and ψ can be obtained from

a chart (Mays, 2011) and are dependent on the mean sediment size. It is important to mention that when τ_0 is less than τ_c, g_s becomes 0. For the present case, the estimated values of τ_c and ψ are 0.03 psf and 30 lb^3/lb-s. For consistency, all results were converted to SI units.

5.2.1 Base case: channel with no bridge deck

Figures 5.3a and 5.3c show the instantaneous and cumulative sediment entrainment calculated using the DuBoys equation at Sections 1 to 3. The local rate of sediment entrainment was integrated over the channel width (60 m). At the initial stages of the passage of the unsteady wave at those locations, negligible quantities of sediment are being mobilized. As the flowrate becomes higher, the mean velocity increases. Once the bed shear stress becomes larger than τ_0, the rate of sediment entrainment becomes nonzero. Once the flow rate starts decreasing at those locations, so does the bed shear stress and the sediment entrainment rate until the bed shear stress is too low to entrain sediment. This behavior is observed at the 3 cross sections. In fact, the three curves lie on top of each other in Figures 5.3a and 5.3c. This makes sense, no changes in the flow are expected between Sections 1 and 3 for the case the bridge deck is no present.

Given that the DuBoys formula is a function of the local bed shear stress, its accurate estimation is of critical importance. The bed shear stress can be estimated in two ways assuming that the depth-averaged velocity profiles are known. The first, and most common, approach is a Manning's based approach. Usually, the bed shear for uni-directional flow can be defined as:

$$\tau_b = c_f \rho \tilde{u}^2 \tag{5.3}$$

where c_f is a friction factor, ρ is the density of water, and $\tilde{u}$ is the depth-averaged streamwise velocity. The bed shear can also be calculated as:

$$\tau_b = \rho g h S_f \tag{5.4}$$

where h is the water depth and S_f is the friction slope. If both equations are combined, one arrives at a new relationship for the depth-averaged velocity:

$$\tilde{u} = \sqrt{\frac{g}{c_f}}\sqrt{hS_f} \tag{5.5}$$

The new expression can be compared to Manning's formula:

$$\tilde{u} = \frac{1}{n}h^{2/3}\sqrt{S_f} \tag{5.6}$$

which allows to estimate the friction factor, c_f, as:

$$c_f = \frac{n^2 g}{h^{1/3}} \tag{5.7}$$

Then, the bed shear stress can be calculated as:

$$\tau_b = \frac{n^2 g}{h^{1/3}}\rho\tilde{u}^2 \tag{5.8}$$

The bed shear stress can also be estimated assuming a logarithmic velocity profile (law of the wall assumption) using the following relationships:

$$u = \frac{u_\tau}{\kappa}\ln\frac{z}{z_0} \tag{5.9}$$

$$u_\tau = \sqrt{\frac{\tau_b}{\rho}} \tag{5.10}$$

$$z_0 = \frac{k_s}{30} \tag{5.11}$$

where u is the streamwise velocity as a function of x, y and z, u_τ is the bed friction velocity as a function of x and z, κ is the Von Karman constant (κ=0.41), z is the vertical direction from the rough bottom surface, z_0 is the distance from the bottom of the rough boundary at which the mean velocity is equal to to 0 and k_s is the equivalent roughness height. When dealing with the law of the wall, certain assumptions need to be made to relate the depth-averaged velocity ($\tilde{u}$) and the flow depth (D). It is commonly assumed that in an open channel of depth D the velocity equals the depth-averaged velocity at z= $0.4D$. Using this assumption and equation 5.9, one can relate the bed friction velocity, or equivalently the bed shear stress, to $\tilde{u}$, D and k_s.

$$u_\tau = \frac{\tilde{u}\kappa}{\ln\left[\frac{0.4D}{k_s/30}\right]} \tag{5.12}$$

Estimates of bed shear stress obtained with the two different methodologies just described are compared to estimations based on the velocity field predicted by the 3-D model. Figures 5.4a, 5.4c, and 5.4e show results the temporal variation of the bed shear stress at Sections 1 to 3 based on the 3-D model velocity profile and based on estimates obtained assuming a logarithmic velocity profile describes the variation of the streamwise velocity over the vertical. At all three cross section, the methodology to estimate the bed shear stress based on assuming a logarithmic velocity profile for the streamwise velocity is in excellent agreement with estimations based on the velocity field predicted by the 3-D model. The differences between the estimated values of the bed shear stress are less than 1% during the whole unsteady event.

Figures 5.5a, 5.5c and 5.5e show the temporal evolution of the bed shear stress as predicted by the 3-D model and estimates obtained using Manning's based methodology. Three different curves are presented for n=0.015, 0.020 and 0.025. The value of 0.015 is included since it is very close to the Manning coefficient estimated using the Strickler formula (n=0.014). Results are included for n=0.020 and 0.025 to visualize the variability of the results with varying n. The estimates are highly sensitive to the value of n. For example, choosing n=0.025 yields bed shear stress estimates of approximately 2.5 times the values predicted for n=0.015. Bed shear stress values estimated assuming n=0.015 are very close to values predicted based on velocity field predicted by the 3-D model. Knowing this information, one can use Strickler's formula to obtain a better approximation for the equivalent roughness.

Stage-Discharge relationships, also known as Rating Curves, are commonly used in engineering practice for flood monitoring and flood modeling (Dottori et al., 2009). During an unsteady event, it has been observed that Stage and Discharge is not unique

(e.g., stage values over the rising and falling limbs of the hydrograph are not the same for the same discharge), but rather this relationships resembles a closed loop over the duration of the unsteady event (e.g., see Qu and Graf, 2004). This non-unique relationship between stage and discharge during strongly unsteady events is referred to as hysteresis. Experimental investigations (Qu and Graf, 2004) have found that the position of the rising limb (increasing discharge) in the Stage – Discharge diagram is always situated below the falling limb (decreasing discharge) part of the diagram. Hysteresis effects are investigated for three pairs of important variables: Stage (Water elevation) vs. Discharge, Bed Shear Stress vs. Discharge and Bed Shear Stress vs. Stage (Water elevation). These diagrams are plotted in Figure 5.6. One should not that in terms of sediment transport what is really important is the relationship between stage and bed shear stress that controls local entrainment. However, bed shear stress cannot be measured directly in the field so the Stage-Discharge diagram is also used in calculations of sediment entrainment via the assumption that the bed shear stress scales with the mean velocity in the channel. The present simulation allows directly obtaining information on the variation of stage with the bed shear stress during unsteady events.

The Stage vs. Discharge diagram (Figure 5.6a) suggests that hysteresis effects are very small for the unsteady event simulated in this test case. The rising and falling limbs are very close to each other. Consistent with observations of hysteresis in the literature, the simulation predicts the falling limb is situated above the rising limb in the Stage vs. Discharge diagram.

A main finding is that hysteresis effects are quite significant in diagrams containing the bed shear stress, as can be seen from Figures 5.6b and 5.6c. Note also that the falling limb is situated beneath the rising limb in these diagrams. This implies that for a given flowrate, the bed shear stress is higher when the flowrate is increasing than when it is decreasing. The difference in the observed bed shear stress for a given flowrate can be as high as 30% between the falling and rising limbs. The differences are overall smaller in the

range of high flowrates (>1000 m^3/s) compared to the range of small flowrates. A similar behavior is observed in the Bed Shear Stress vs. Stage diagram. The difference in the observed bed shear stress for a given Stage can be as high as 30% but here the largest differences are observed for large water elevations (>4.2 m) in the channel.

The results in the diagrams containing the bed shear stress are physically sound. Experimental data show that during an unsteady event, for a given flowrate, the free-surface elevation is lower when the flowrate is increasing than when it is decreasing, a result confirmed by the present simulation. This implies that, for a given flowrate, the streamwise velocity would be higher when the flowrate is increasing than when it is decreasing. A higher velocity near the bed means a larger velocity gradient in the vertical direction, which means a higher the bed shear stress. So the higher bed shear stress should be observed when the flowrate is increasing. A final observation is that, since it is easier to measure free-surface elevations rather than flowrates, and the Bed Shear Stress vs. Stage diagram show very significant hysteresis effects, the most useful relationship to accurately estimate bed shear stress and sediment entrainment during unsteady events is the in Bed Shear Stress vs. Stage diagram. The other main conclusion is that small hysteresis effects in the Discharge vs. Stage diagram does not mean that hysteresis effects on the bed shear stress and sediment entrainment are negligible. Unfortunately direct estimation of bed shear stress and sediment entrainment during unsteady events in the field and even in the laboratory is not easy. Numerical simulations can offer a good alternative to quantitatively characterize these processes.

5.2.2 Modified case: channel containing a bridge deck

A bridge deck of 20 m x 60 m x 0.2 m (LxWxH) was introduced in the computational domain in the Modified Case. The center of the bridge deck was situated at a distance of 1010 m from the inlet section, as seen in Figures 5.1a and 5.1b. The distance between the channel bottom and the bridge deck was 4 m. The mesh around the bridge

deck was refined to accurately capture the flow around the structure (see Figure 5.1b). The purpose of including the bridge deck was to investigate the changes in the bed shear stress distributions and the (increase) of the potential for sediment entrainment due to potential pressure scour effects as the bridge deck becomes submerged over part of the unsteady event. A related goal was to quantify the errors in estimating the bed shear stress for such scenarios based on Log-law and Manning's law methods. The flow conditions in the Modified Case are the same as in the Base Case (Figure 5.2).

Figures 5.3b and 5.3d show the time history of the instantaneous and cumulative sediment entrainment flux at Sections 1, 2 and 3 for the Modified Case. A large amplification of the flux by about 15% is observed at Section 2, cutting through the bridge deck, compared to Section 1, located upstream of the bridge deck. This amplification is caused by the changes in the streamwise velocity profile in between the two sections in the Modified Case. Moreover, the velocity distribution below the bridge deck (e.g., at Section 2) is very different compared to the standard log-law distribution observed in the Base Case. The flow in this region is pressurized and the velocity profile resembles the one observed in a 2D channel with no-slip walls at the bottom and top surfaces.

Section 3, on the other hand, shows the highest potential for sediment entrainment. The values of the flux are by about 45% higher compared to those in Section 1. One should recall that the flux variation was about the same at the three sections in the Base Case. This behavior can be explained by the weir like behavior of the flow as it passes the bridge deck. The sudden drop of free-surface elevation makes the flow to plunge downwards downstream of the bridge deck. This increases the bed shear stress downstream of the bridge before the flow starts recovering toward uniform open channel flow. In the case of a loose bed channel, a scour hole will form right downstream of the bridge deck. Such scour holes were observed in the field (e.g., see Kumcu, 2017).

Even at Section 1 situated just upstream of the bridge deck, the flux of entrained sediment is not the same in the two simulations. In fact, the flux is lower in the Modified

Case because the bridge deck acts as a flow obstruction. The free-surface elevation rises, at least by an amount equal to the thickness of the bridge deck and a backwater effect is induced by the bridge deck upstream of it. The rise in the free-surface elevation at Section 1 increases the cross-sectional area at Section 1 compared to the Base Case. This means that the mean velocity and the bed shear stress are reduced compared to the Base Case, which explains the results in Figure 5.3b. Section 2 shows a similar variation of the flux as in the Base Case. This may look counter-intuitive since pressure scour is supposed to increase the bed shear stress and thus the capacity of the flow to entrain sediment in the Modified Case. The streamwise velocity distributions at Section 2 are shown in Figure 5.7 for the two cases. The total flowrate going below the bridge deck is 1400 m^3/s, which is the effective flowrate contributing to the bed shear stress in the Modified Case. By comparison, the total flowrate in the Base Case is 1600 m^3/s. So the two competing effects (pressurized flow conditions but lower discharge) result in a bed shear stress that is quite close to that predicted in the case where the bridge deck is not present. However, the effects of the pressurized flow regime beneath the bridge deck are felt downstream. The values of the flux at Section 3 in the Modified Case are larger than the ones predicted at Section 1 and 2 in the same case and also larger than the values recorded at Section 3 in the Base Case. This amplification is due to the weir-type flow forming over the bridge deck that advects higher-velocity flow toward the bed. Table 5.1 shows the amplification factors at the end of the wave propagation event for the downstream sections with respect to the upstream section (Section 1) and for each section in between the two cases.

Table 5.1 Potential for erosion amplification factors

	Amplification Factors in terms of potential for sediment entrainment	
Section	with respect to Section 1	with respect to the Base Case
1		-20%
2	15%	-2%
3	45%	25%

The main reason for the increase of the observed increase of the flux of sediment entrained from the bed between Sections 1, 2 and 3 is the increase of the bed shear stress over part of the time the wave passes over these sections. One important question is whether the simplified methods generally used to evaluate the bed shear stress in lower order (e.g., 2-D) models can provide an accurate description of the time variation of the bed shear stress near obstructions that force the flow to become pressurized over a small region.

The bed shear stress estimated based on the 3-D model velocity field are compared in Figures 5.4b, 5.4d and 5.4f to estimates obtained assuming a logarithmic velocity profile at Sections 1, 2, and 3 respectively. At Section 1, which is located upstream of the bridge deck, the estimate based on assuming a logarithmic velocity profile shows less than 2% error with respect to the estimate based on the 3-D velocity field. This means that at sections located at least one width of the bridge deck upstream from the bridge deck, the bed shear stresses during the unsteady event can be accurately estimated assuming a logarithmic velocity profile in the vertical direction.

At Section 2 situated beneath the bridge deck, bed shear stresses estimated assuming a log-law profiles underestimate by as much as 10% those predicted by the 3-D model. This is not surprising, as in these sections the flow is pressurized and the near-bed velocity gradient in the log-law fit is different from the one shown by the pressurized flow

profile at the same section. The underestimation given by the method based on the log-law at Section 3 is of the same order (10%), situated about one bridge deck width downstream of the bridge deck. This is due to the plunging component of the flow passing the bridge deck that modified the streamwise velocity profile in the vertical direction with respect to the log-law variation. It takes about 6 bridge deck widths for the log-law estimate to approach again the values predicted by the 3-D model. One should also mention that the errors given by the log-law based method to estimate bed shear stresses become very small even at Sections 2 and 3 at times when the bridge deck is not submerged.

Figures 5.5b, 5.5d and 5.5f compare the bed shear estimated assuming Manning's law applies with the values predicted by the 3-D model at Sections 1, 2 and 3, respectively. Similar to the Base Case, the bed shear stress values predicted based on Manning's formula are strongly dependent on the value of the Manning coefficient. The discussion bellow is based on predictions obtained using n=0.015, which agree well with 3-D model predictions for the Base Case. As expected, predictions based on Manning's formula are accurate at Section 1 in the Modified Case as the velocity profiles in this section remain close to those observed in a channel with no obstruction during the passage of the wave. Similar to what was observed in the method to estimate the bed shear stress based on the log law, Manning's based approach also underestimates by as much as 15% the bed shear stresses at Sections 2 and 3 during the times the bridge deck is submerged. Table 5.2 summarizes the maximum errors given by the two approximate methodologies to estimate bed shear stresses in regions influenced by the presence of the bridge deck.

Table 5.2 Bed Shear Stress estimates with respect to 3-D model predictions

	Error with respect to 3-D model results	
Section	Log-Law	Manning's law (n=0.015)
1	2%	2%
2	-8%	-16%
3	-10%	-14%

Next, a similar analysis is performed in a river reach with natural bathymetry to investigate if the main conclusions reached based on analysis of an idealized case hold for natural river reaches.

5.3 Flow in a 2 km reach of the Iowa River near Iowa City

The second test case considers a 2-km reach of the Iowa River near Iowa City. Except for the bridge deck, this is the same river reach and flow conditions used in the test case analyzed in Section 4.2., which also contains detailed information on the location and main features of the computational domain. The river reach bathymetry is shown in Figure 5.8. The main difference with respect to the test case discussed in Section 4.2 is the inclusion of a bridge deck right upstream of the river dam. The location and dimensions of the bridge deck are those of a bridge that exists in Iowa City, called *Burlington Street Bridge*. Figure 5.9 shows the bridge deck, which is now included in the computational domain. The mesh around the bridge deck was refined in a similar way as for the straight channel simulation containing a bridge deck.

One important observation is that significant 3-D effects can be experienced around regions experiences sudden changes in the bathymetry or regions containing large obstructions. In these regions the main assumptions made in methods to estimate the bed shear stress based on Manning's law or on assuming a logarithmic variation of the velocity

are violated. In the river reach analyzed in this section the bathymetry contains a large depression (scour hole) and a very shallow region upstream of the river dam. Additionally, the presence of the river dam makes the upstream and downstream regions of it to be disconnected from each other due to the hydraulic jump forming immediately downstream of the dam. As the flow goes over the dam, it accelerates while the flow depth decreases. This results in a large amplification of bed shear stresses over and immediately downstream of the dam. Regardless of the presence of the bridge deck, the flow downstream of the dam is mainly determined by the presence of the dam. So, pressure scour effects are expected to be important only upstream of the river dam. This is why most of the discussion focuses on analysis of the flow and potential for sediment entrainment at Section 1 situated at the bridge deck and Sections 2 and 3 situated 60 m and 120 m, respectively, upstream of Section 1 (see Figure 5.8).

The steady state was calculated for a discharge of approximately 200 m^3/s, similar to the straight rectangular channel case studied in Section 5.2. Once the initial conditions (steady state) were obtained, a sinusoidal wave was propagated into the domain. The duration of the unsteady part of the hydrograph was 4 hr (Figure 5.10). As for the test cases discussed in Section 5.1, two simulations were conducted. In one of them the bridge deck was not included (Base Case), while in the second one the bridge deck was included.

5.3.1 Base case: no bridge deck

Figures 5.11a and 5.11c show the instantaneous and cumulative sediment entrainment calculated using the DuBoys equation at Sections 1 to 3. The peak values of the sediment entrainment flux are comparable at the three sections. As opposed to the case of a straight channel with no dam, the temporal variation of the flux during the time the wave is passing the section is characterized by the presence of relatively high frequency oscillations. They are induced by the propagation of the backwater upstream of the river dam which creates sudden changes in the free-surface elevation. The high frequency

oscillations are not present in the temporal variation of the estimated volume of sediment entrained at these section. The total volume of entrained sediment at Sections 2 and 3 are only 12% and 15%, respectively, higher than that predicted at Section 1.

Figures 5.12a, 5.12c and 5.12e compare estimates of the (section-averaged) bed shear stress temporal variations at the three sections obtained based on the velocity field predicted by the 3-D model with those obtained assuming a logarithmic profile for the streamwise velocity. The method based on the log-law assumption gives predictions that are very close to those obtained based on the 3-D model, similar to what was observed in Section 5.2 for the straight rectangular channel with no dam. The maximum percentage difference between the two methods is about 7%. This value is higher than the one (0.5%) observed for the straight rectangular channel case, but this is expected given the much more complex bathymetry of the natural river reach and the presence of a dam close to the three cross sections where the bed shear stresses are compared.

Figures 5.13a, 5.13c and 5.13e compare estimates of the (section-averaged) bed shear stress temporal variations at the three sections obtained based on the velocity field predicted by the 3-D model with predictions obtained based using a simplified approach based on Manning's law. Results are shown for n=0.015, 0.020 and 0.025. Estimates obtained using n=0.015 replicate well the bed shear stress predictions based on the 3-D model at the three cross sections. The largest percentage difference is of the order of 8% and is observed at Section 3. One should also note that the optimum value of the Manning coefficient is not known in advance. For example, the recommended values of n for this particular reach of the Iowa River based on the calibrated 2-D model used in Chapter 5 are 0.030 for bankfull conditions and 0.035 for extreme flood events. Using such high values of n would lead to an overestimation of at least 3 times of the bed shear stress values predicted by the 3-D model.

As for the simplified straight channel test case, hysteresis effects were investigated for the natural river reach containing the dam. Results in Figure 5.14 are qualitatively

similar to those obtained in Figure 5.7 for the straight channel case in terms of the relative position of the rising and failing limbs in the three plots. Hysteresis effects are however more pronounced in the Stage vs. Discharge plot obtained for the natural river reach (Figures 5.14a and 5.6a). In the latter case, hysteresis effects become very small at high flowrates (>1300 m^3/s). This happens once the discharge is high enough that the floodplain becomes inundated. For this regime, a small increase of stage can lead to a significant increase in flowrate. The sudden reduction in hysteresis effects once the floodplain becomes inundated is also observed in the Bed Shear Stress vs. Flowrate and Bed Shear Stress vs. Stage plots in Figures 5.14b and 5.14c. However, hysteresis effects are quite pronounced at lower discharges, where for a given stage the difference in the bed shear stress values on the rising and falling limbs of the curve can be close to 25% of the mean value. Such differences are important to account for when trying to estimate sediment entrainment induced by a flood event in a natural river reach.

5.3.2 Effects of submerged bridge deck on flow and sediment erosion potential

The main purpose of including the bridge deck was to investigate pressure scour effects upstream of the dam and, in particular, how the potential for sediment entrainment during the flood wave propagation when the bridge deck becomes submerged is affected in this region. The bathymetry and hydrograph propagated through the river reach are the same as in the (base) case without a bridge deck.

The presence of the bridge deck affects the sediment entrained flux at all three sections compared to the base case. Figures 5.11b and 5.11d show that the largest amplification of the sediment entrainment flux among the three sections is observed at Section 1 located beneath bridge deck. In terms of the total volume of sediment entrained during the flood wave propagation, the entrainment at Section 1 is 60-70% bigger compared to that recorded at Sections 2 and 3 and close to 80% larger than the value

recorded at the same section in the base case. Meanwhile, the volume of sediment entrained at Sections 2 and 3 in this case is by about 15% smaller compared to the base case estimations. The significant decrease of the volume of sediment entrained at Sections 2 and 3 is mainly due to backwater effects. The increase of the free-surface elevation decreases the bed shear stress and the flux of sediment entrained at these locations during the time the bridge deck is submerged. Table 5.3 summarizes these findings

Table 5.3 Potential for erosion amplification factors

	Amplification Factors in terms of potential for sediment entrainment	
Section	with respect to upstream data (i.e. Section 2/3)	with respect to the Base Case (without bridge deck)
1	65%	80%
2		-15%
3		-15%

The sharp increase of the potential for erosion at Section 1 between the base case and the case with the bridge deck included is mainly a pressure scour effect. For the flow conditions considered in this test case, pressure scour effects beneath the bridge deck can account for about 50% of the total amount of bed material removed by the passage of the flood wave. The reasons for the large increase of the cross-sectional averaged bed shear stress in Section 1 during the times the bridge deck is submerged can be explained by comparing the distributions of the streamwise velocity in the two cases. From Figures 5.15 one can see that at peak flowrate (Q=1640 m^3/s) in Section 1, the core of high streamwise velocities extended toward the left side of the cross section in the simulation containing the bridge deck. The near bed velocity gradient over the right side of Section 1 is larger compared to that predicted in the simulation with no bridge deck (Figure 5.16).

Due to the significant effect of pressure scour on the potential for sediment entrainment beneath the bridge deck, one expects that the estimates of the bed shear stress obtained assuming a log-law velocity variation or Manning's law at Section 1 will be quite inaccurate, especially once the bridge deck becomes submerged. The time history of the bed shear stress in Figure 5.12b show that this is the case when the bed shear stress is estimated assuming the log-law is valid. Interestingly, the differences are quite small (within 5%) at Sections 2 and 3 despite backwater effects induced by the interaction of the bridge deck with the incoming wave.

In the case Manning's formula is used to estimate the bed shear stress during the propagation of the flood wave, the results are qualitatively similar to those observed for the log-law based method. Using n=0.015, the agreement with the bed shear stress directly estimated from the 3-D model velocity fields is excellent at Section 2 and quite good (within 8%) at Section 3. However, the Manning's based approach significantly underestimate the bed shear stress at Section 1. Differences as large as 30% are observed during the times the bridge deck becomes submerged. Table 5.4 summarizes the percentage error given by the log-law and Manning's law based methodologies to estimate bed shear stresses for the case when the bridge deck becomes submerged. Interestingly, an increase of Manning's coefficient by about 20% at Section 1 (n=0.018) will give very good agreement with the temporal variation of the bed shear stress predicted based on the 3-D velocity fields.

Table 5.4 Peak bed shear stress estimates errors during the flooding event

	Error with respect to 3-D model results	
Section	Log-Law	Manning's (n=0.015)
1	-25%	-30%
2	-5%	2%
3	~0%	-8%

5.4 Conclusions

The potential for sediment entrainment during a flooding event consisting of a sinusoidal wave was studied in the present chapter by considering two different domain configurations: an idealized geometry consisting of an open channel rectangular straight channel and a 2-km reach of the Iowa River containing a hydraulic dam. For both channel configurations simulations were performed without and with a bridge deck. In both cases the amplitude of the sinusoidal wave was large enough to submerge the bridge deck during part of the flooding event.

Significant pressure scour effects were induced beneath and/or around the bridge deck during the time it was submerged. Comparison of results conducted with and without the bridge deck allows estimating the contribution of pressure scour to the potential for sediment entrainment associated with the passage of the flood wave. For the conditions considered in the test case in which the flow in a 2 km reach of Iowa River was simulated, results showed that pressure scour during the time the bridge deck was submerged can contribute as much as 50% to the total volume of sediment entrained by the flooding event at locations where pressure scour effects are the largest. For the case of the idealized channel, pressure scour effects were found to increase by as much as 25% the sediment entrainment flux at sections situated immediately downstream of the channel and to decrease it by up to 20% at sections situated upstream of the channel, where backwater flow effects were significant during the times the bridge deck was submerged.

Such estimations are impossible to obtain using standard depth-averaged codes, as the main assumptions associated with using such simplified models are violated once an obstruction becomes submerged and the flow in between the bed and that obstruction becomes pressurized. In this regard, fully 3-D non-hydrostatic models are the only way to correctly model the flow and obtain information on the erosive capacity of the flow in regions where the flow becomes pressurized. Given that in many practical applications 2-D models or hydrostatic 3-D model are used to predict flow in natural rivers even for cases when the flow locally changes regime during a flood event, the chapter also discusses the errors associated with using law-of-the-wall assumptions and/or Manning's formula based methods to estimate the bed shear stress during flood events, including in regions where the flow can become pressurized. One empirical fix may be to locally increase the Manning coefficient in regions where the flow becomes pressurized over the time interval where these conditions are observed. Significant research is still needed to find a consistent methodology to propose amplification factors for different geometries and configurations, since the amplification factors is a function of many variables. Estimations based on Manning's formula were also found to be highly sensitive to the value of the Manning coefficient. This highlights even more the need for correct calibration of 1-D and 2-D models used to predict flood wave propagation.

Several suggestions can be made to improve results obtained using 2D depth-averaged codes. If the 2D code asks for both the Manning coefficient and the equivalent bed roughness values as input, the Manning coefficient should be used to calibrate the free-surface elevation predicted by the 2-D model using available experimental/field data, while the equivalent roughness value should be used to provide bed shear stress estimates, since it was found that estimations of the bed shear stress based on the log-law approach better replicate the values predicted by the 3D model.

The present simulations conducted with no bridge deck were also used to estimate hysteresis effects. Normally hysteresis effects are described in terms of the relationship

between stage and discharge and served to more accurately quantify discharge during unsteady events such as those associated with flood wave propagation. However, knowledge of hysteresis effects via the stage-discharge relationship is not sufficient to also lead to an accurate estimation of sediment entrainment induced by the unsteady events, because of nonlinearity between discharge and sediment entrainment flux. The availability of the 3-D flow fields during the unsteady event and the possibility to directly estimate the bed shear stress allowed studying the relationship between the bed shear stress and the stage during the considered flood propagation event. These hysteresis effects were important, as over part of the range of recorded discharges during the flood event the difference between the bed shear stress values corresponding to the falling and rising limbs of the hydrograph was close to 25% of the mean bed shear stress value at a given stage. In the case of the 2-km reach of the Iowa River, hysteresis effects affecting the bed shear stress were more important at relatively low stages and flow rates when the flow remained confined in the main channel.

In the case of the straight channel, hysteresis effects affecting the bed shear stress and sediment entrainment flux were relatively important for all the range of discharges observed during the flooding event. Hysteresis effects for both the discharge and the bed shear stress were not influenced in a significant way by the duration of the flood event (a sinusoidal flood wave of same peak discharge was used in both cases corresponding to a 4-hr wave and a 8-hr wave). One should also note that for this test case hysteresis effects on the bed shear stress were very strong even though hysteresis effects on the discharge were relatively small. This highlights even more the importance of directly measuring or estimating hysteresis effects on the bed shear stress if a main goal is to be able to estimate sediment entrainment and transport during a flood event.

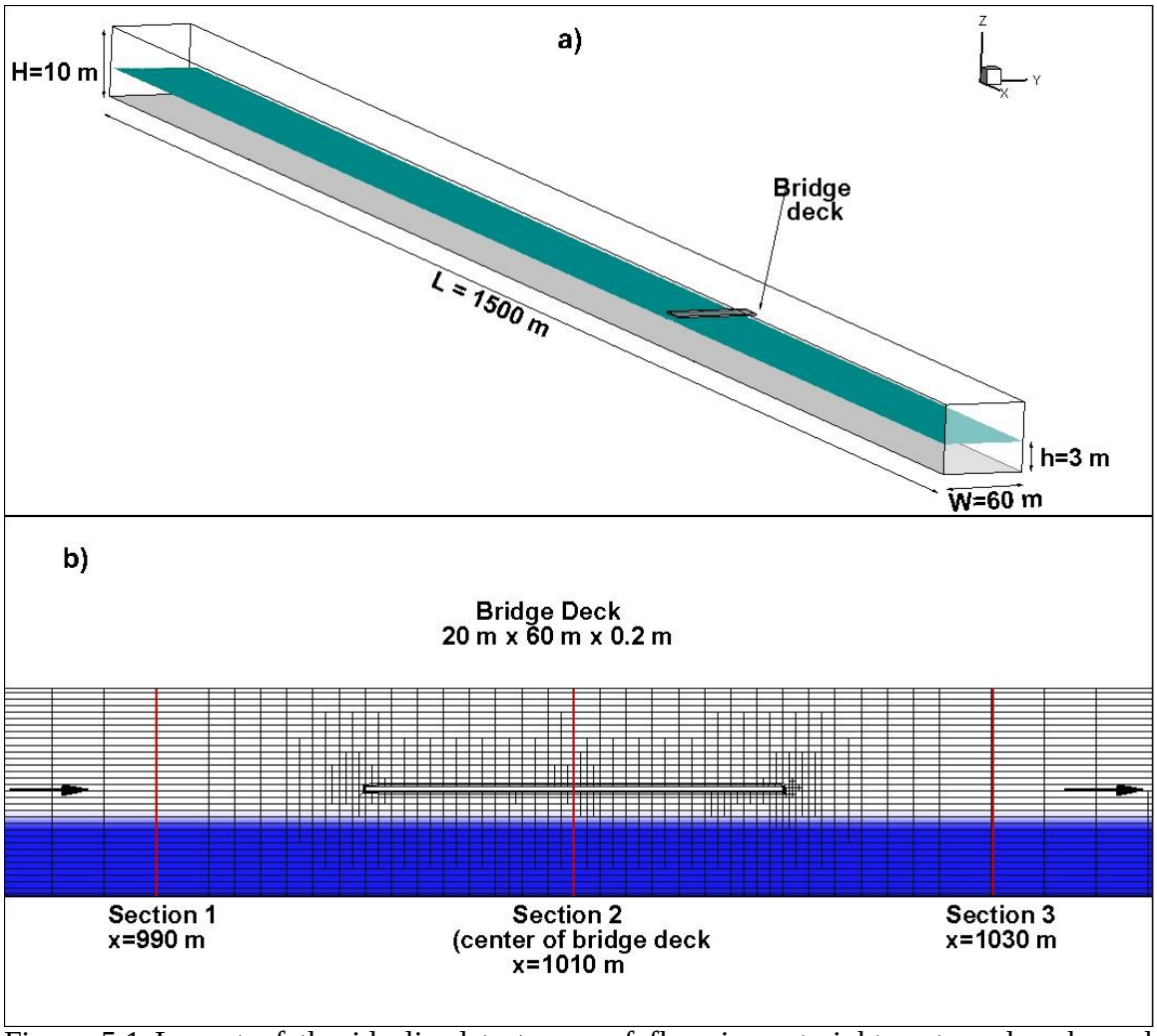

Figure 5.1 Layout of the idealized test case of flow in a straight rectangular channel containing a bridge deck. a) Sketch of the computational domain showing location of the bridge deck. b) Computational mesh in a streamwise-vertical plane, near the bridge deck. Also shown are the positions of three cross sections where the solution is analyzed.

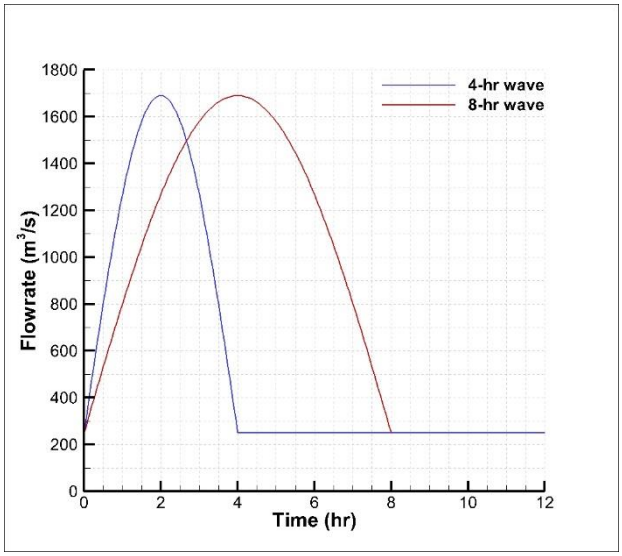

Figure 5.2 Inlet hydrographs in the idealized test case.

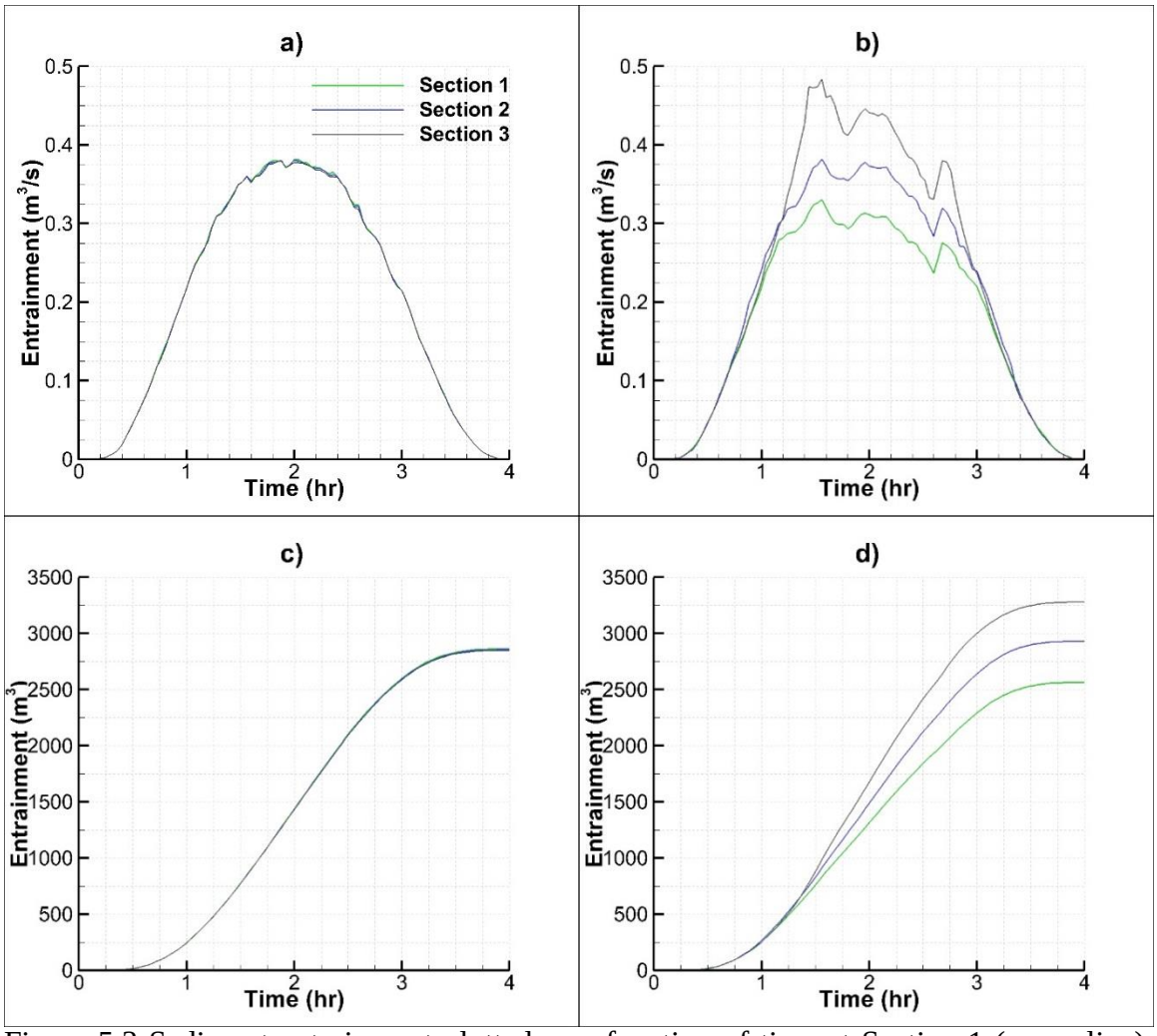

Figure 5.3 Sediment entrainment plotted as a function of time at Section 1 (green line), Section 2 (blue line) and Section 3 (black line) for the idealized test case. a) Flux of entrained sediment for the idealized case with no bridge deck; b) Flux of entrained sediment for the idealized case with the bridge deck; c) Volume of entrained sediment for the idealized case with no bridge deck; d) Volume of entrained sediment for the idealized case with the bridge deck.

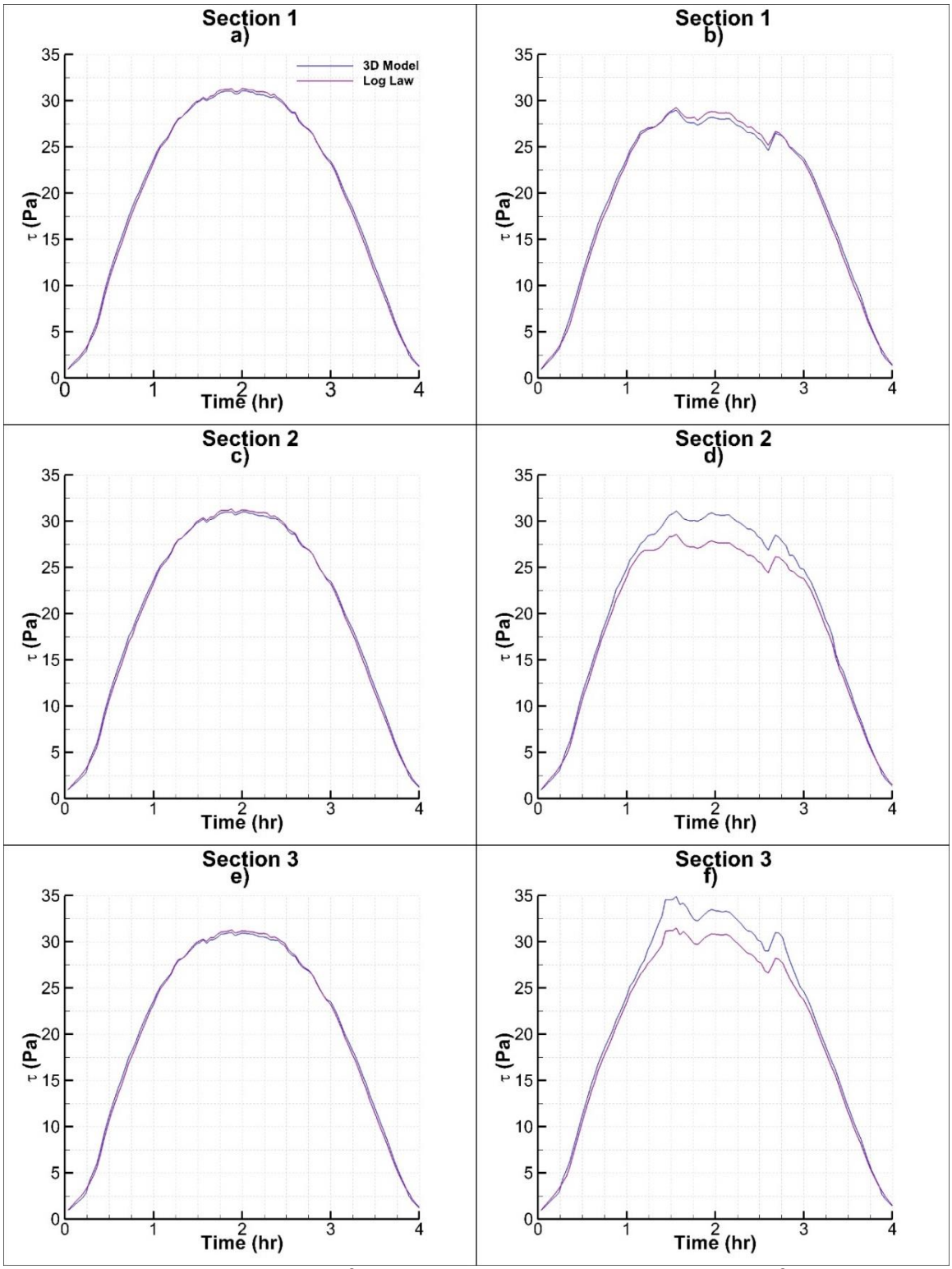

Figure 5.4 Temporal variation of bed shear stress at Sections 1, 2 and 3 for the idealized test case. 3D numerical predictions (blue lines) are compared with those obtained assuming a logarithmic streamwise velocity profile (purple line). Frames a, c and e show results for the idealized test case with no bridge deck. Frames b, d, and f show results for the idealized test case with the bridge deck.

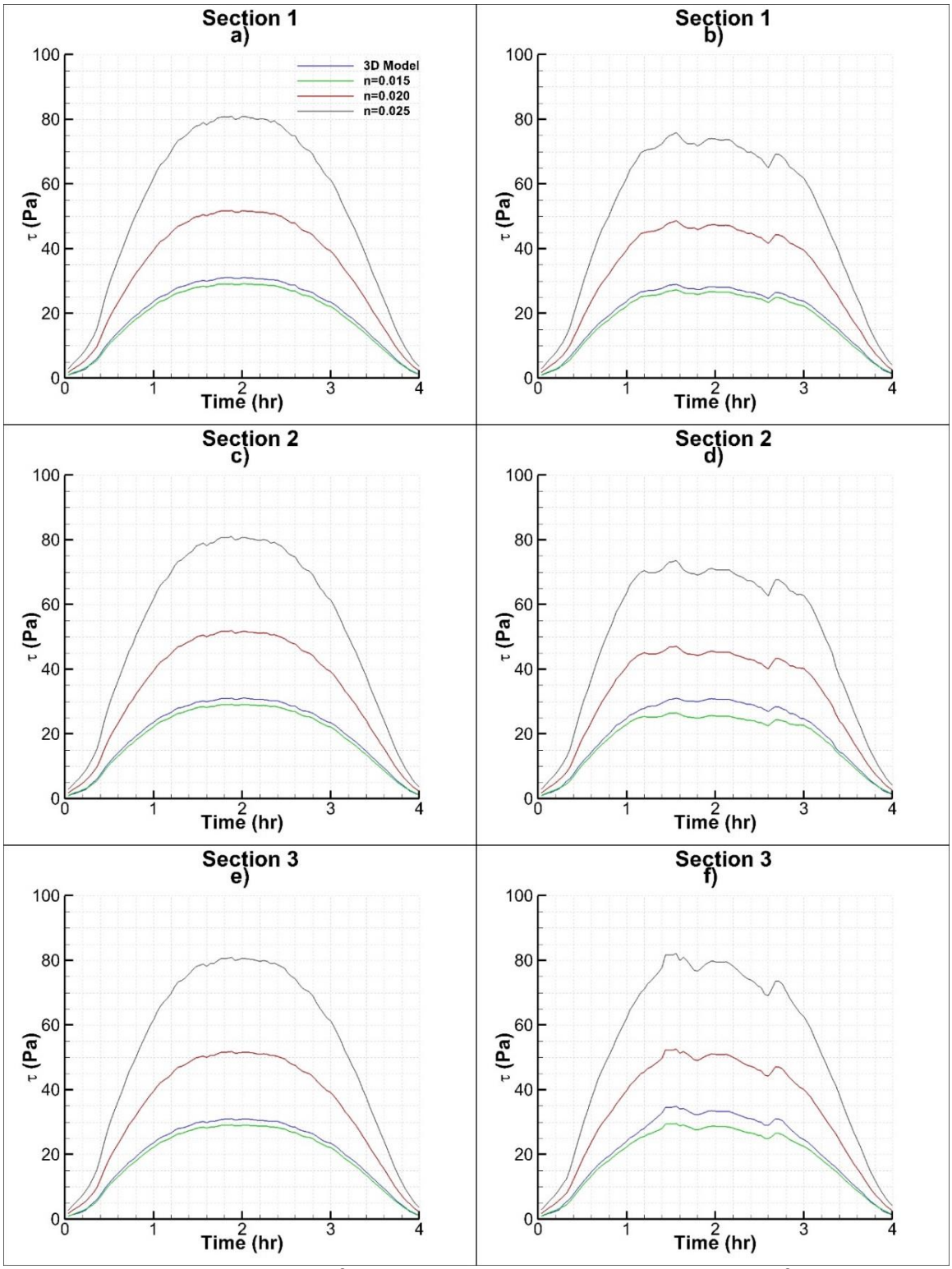

Figure 5.5 Temporal variation of the bed shear stress at Sections 1, 2 and 3 for the idealized test case. Estimations based on the 3-D numerical predictions (blue lines) are compared with those obtained assuming n=0.015 (green line), n=0.020 (red line) and n=0.025 (black line). Frames a, c, and e show results for the idealized test case with no bridge deck. Frames b, d, and e show results for the idealized test case with the bridge deck.

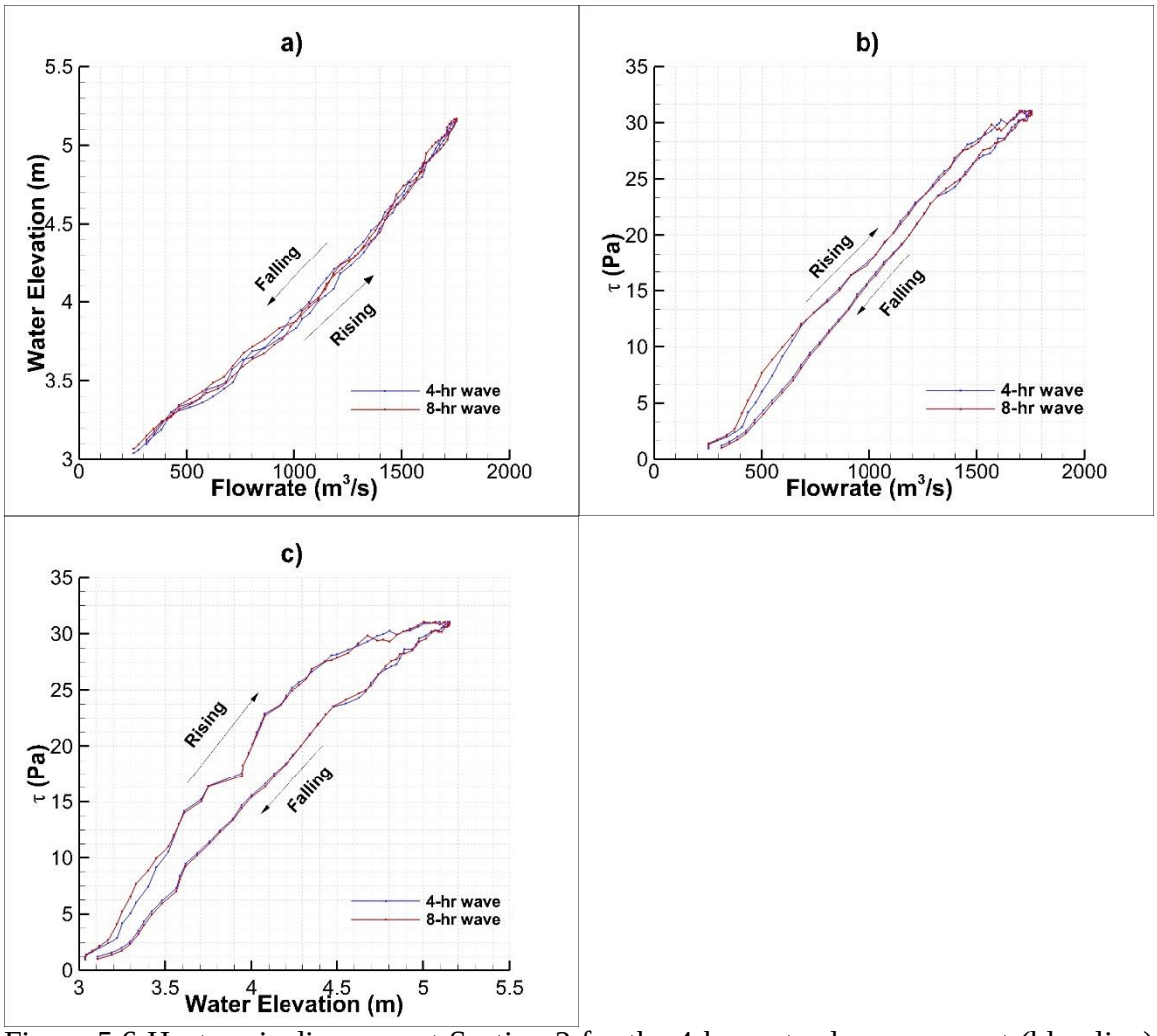

Figure 5.6 Hysteresis diagrams at Section 2 for the 4-hr unsteady wave event (blue line) and the 8-hr unsteady wave event (red lines) in the idealized test case with no bridge deck. The inlet hydrographs are shown in Figure 5.2. a) Stage vs. Flowrate; b) Bed Shear Stress vs. Flowrate; and c) Bed Shear Stress vs. Stage.

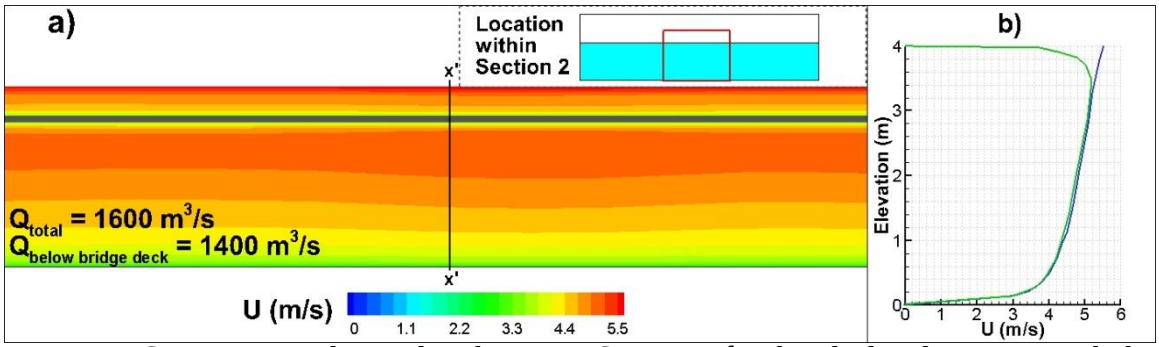

Figure 5.7 Streamwise velocity distribution at Section 2 for the idealized test case with the bridge deck (gray region).

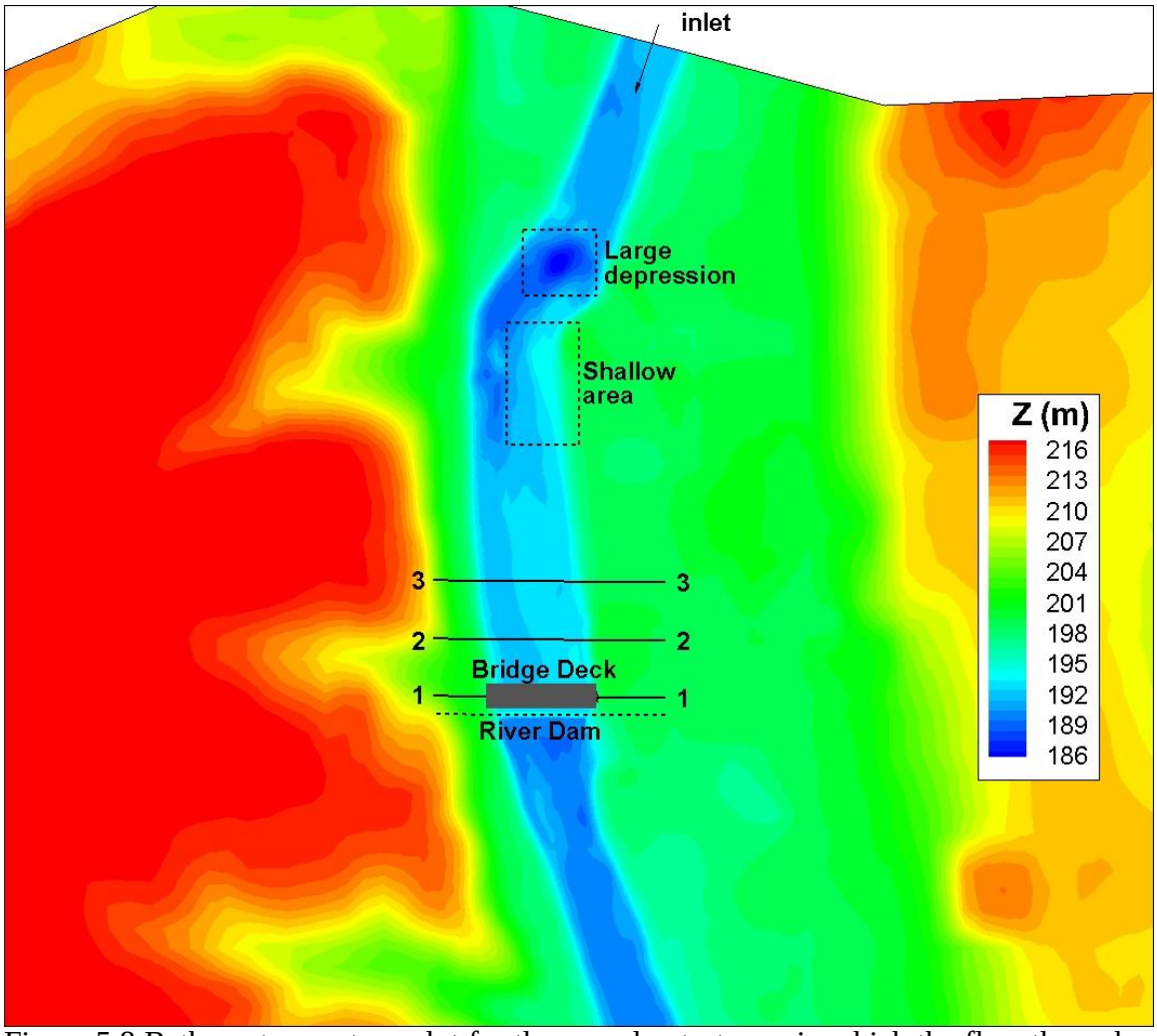

Figure 5.8 Bathymetry contour plot for the complex test case in which the flow through a 2-km reach of the Iowa River near Iowa City is simulated. The reach contains a dam and a bridge deck situated slightly upstream of the dam (dashed line). The picture shows elevation, Z (m).

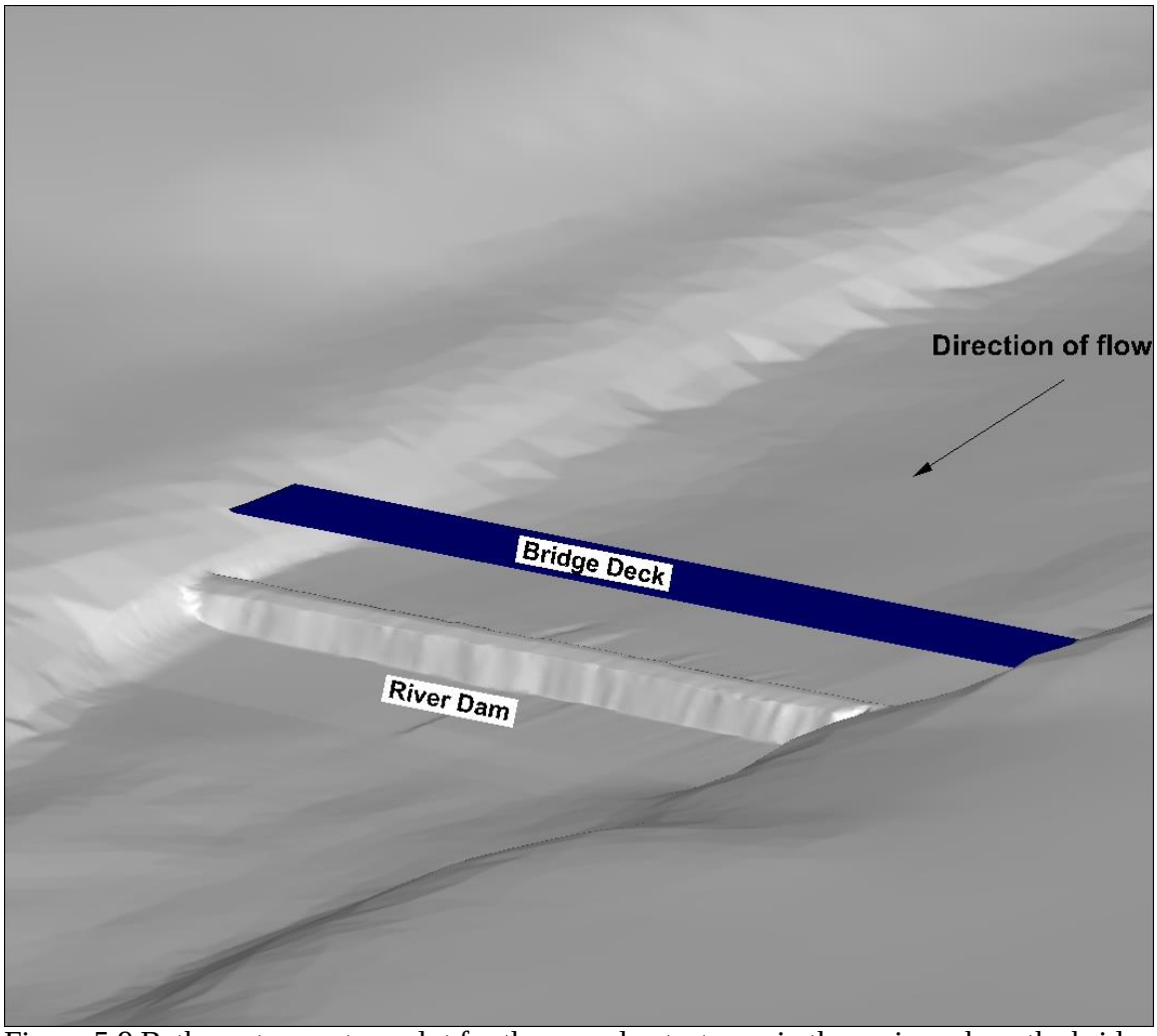

Figure 5.9 Bathymetry contour plot for the complex test case in the region where the bridge is present. The bridge deck is shown in blue.

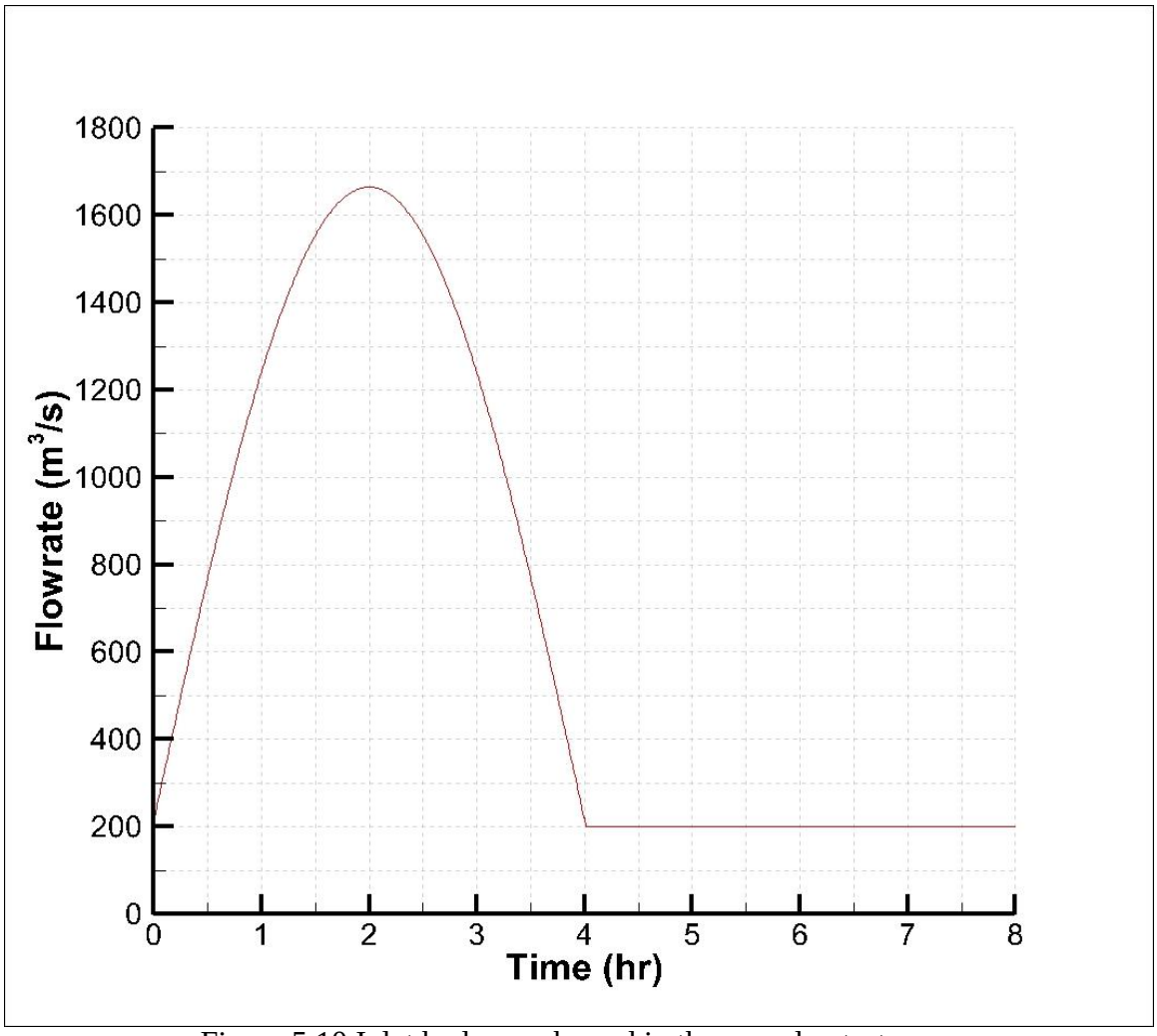

Figure 5.10 Inlet hydrograph used in the complex test case.

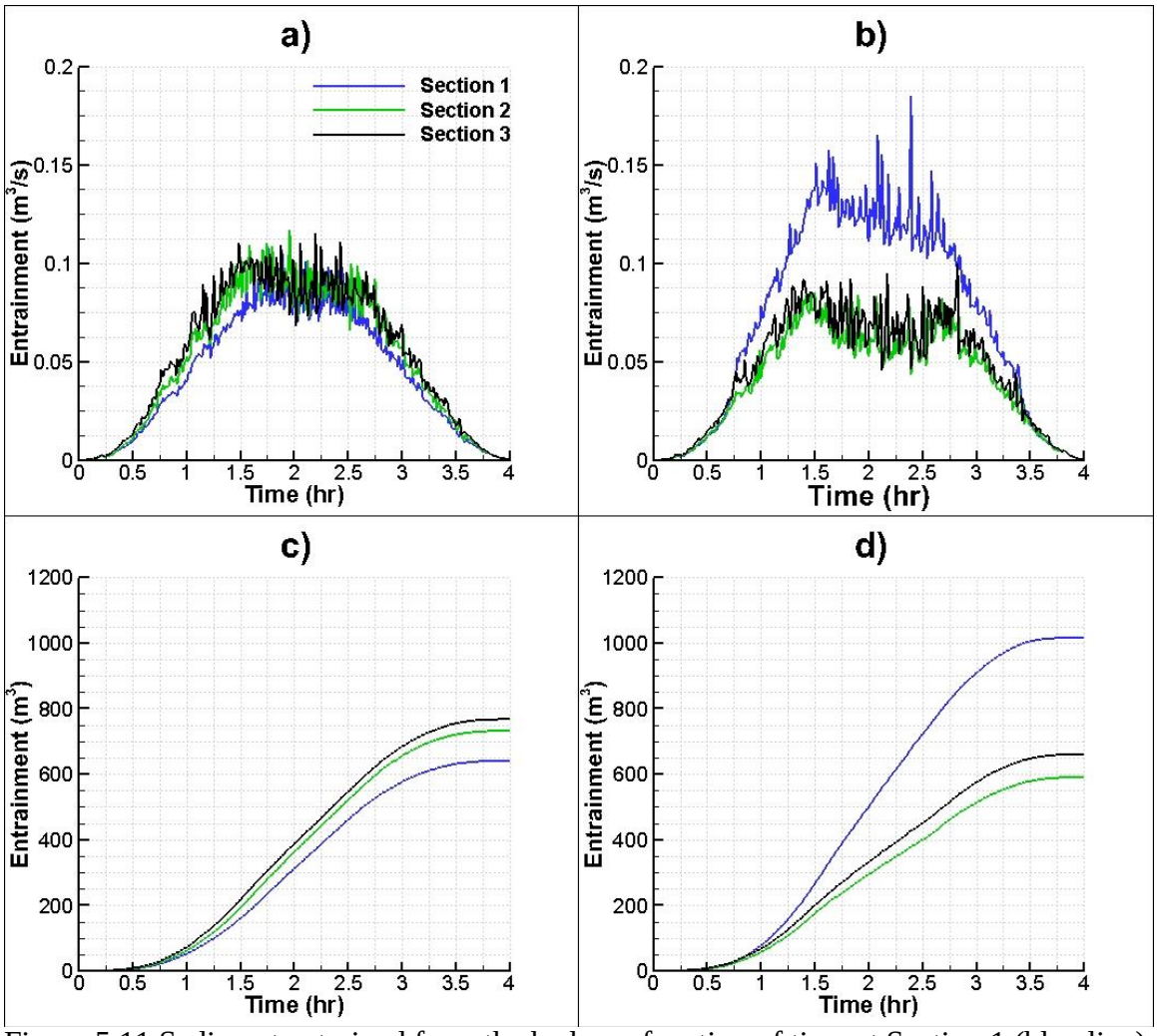

Figure 5.11 Sediment entrained from the bed as a function of time at Section 1 (blue line), Section 2 (green line) and Section 3 (black line) for the complex test case. a) Flux of entrained sediment for the case with no bridge deck; b) Flux of entrained sediment for the case with the bridge deck; c) Volume of entrained sediment for the case with no bridge deck; and d) Volume of entrained sediment for the case with the bridge deck.

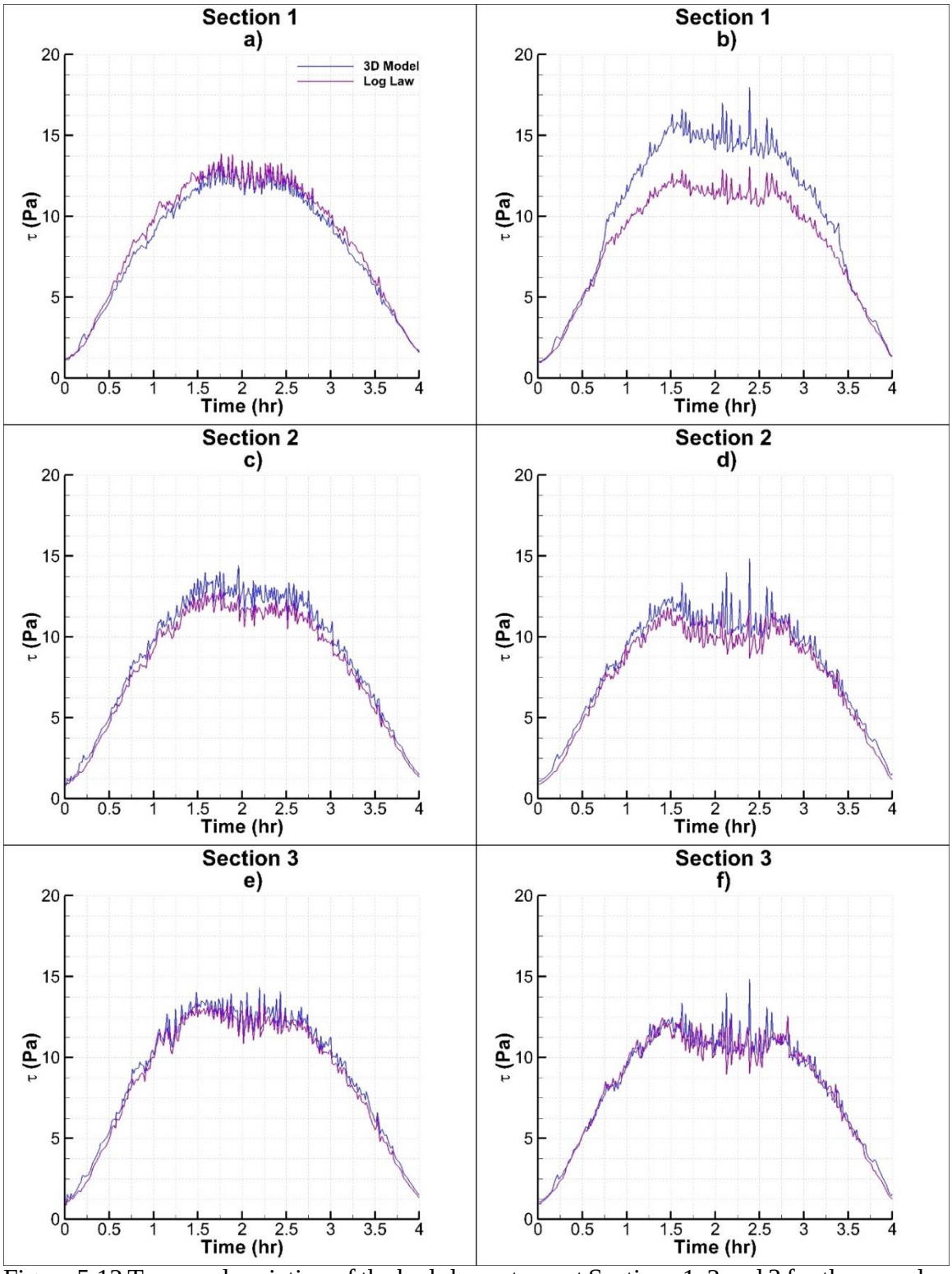

Figure 5.12 Temporal variation of the bed shear stress at Sections 1, 2 and 3 for the complex test case. Estimations based on 3-D numerical predictions (blue line) are compared to those obtained assuming a logarithmic streamwise velocity profile (purple line). Frames a, c and e show results for the test case with no bridge deck. Frames b, d, and e show results for the test case with the bridge deck present.

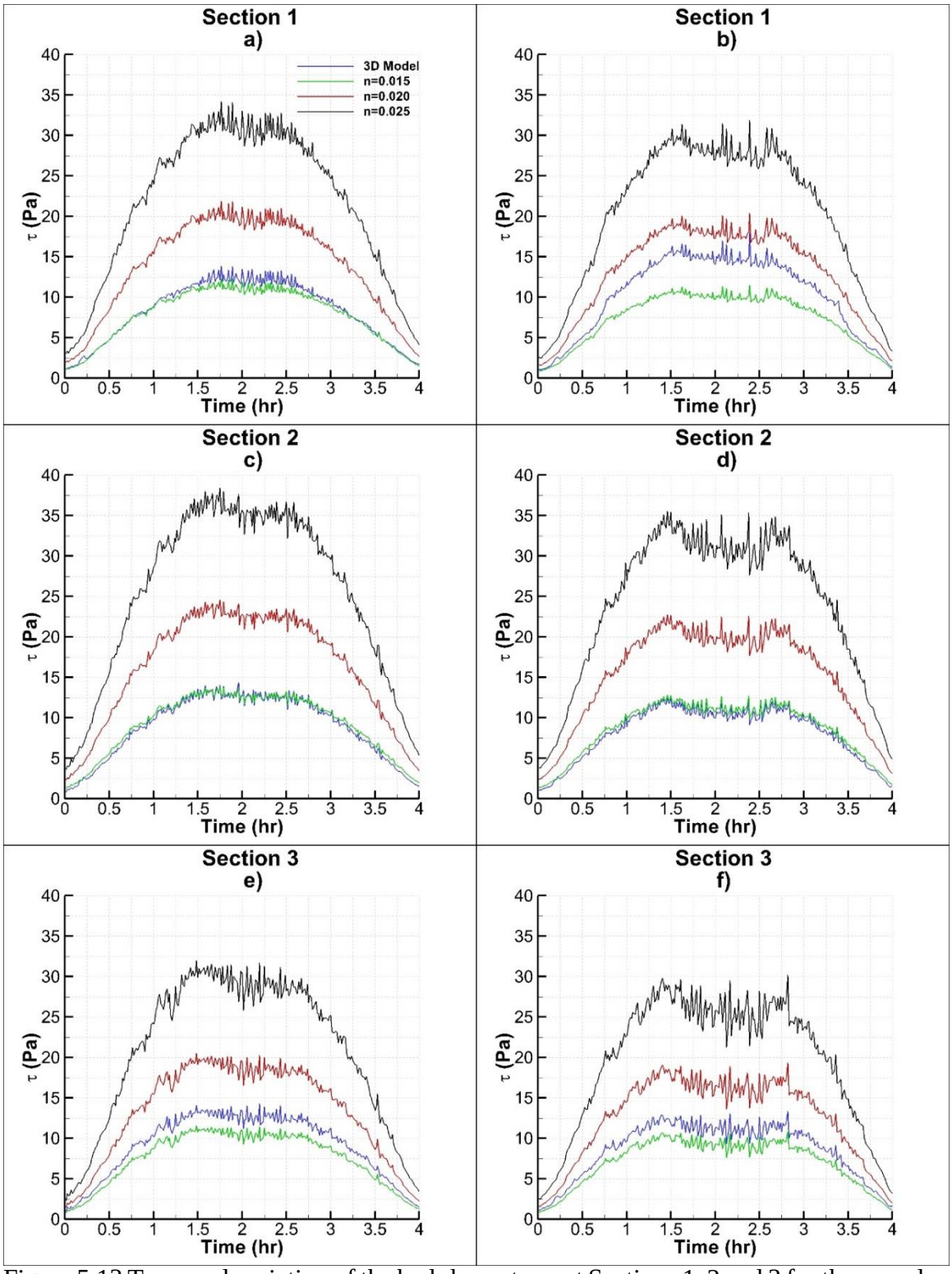

Figure 5.13 Temporal variation of the bed shear stress at Sections 1, 2 and 3 for the complex test case. Estimations based on the 3-D numerical predictions (blue lines) are compared to those obtained assuming n=0.015 (green line), n=0.020 (red line) and n=0.025 (black line). Frames a, c, and e show results for the test case with no bridge deck. Frames b, d and f show results for the test case with the bridge deck present.

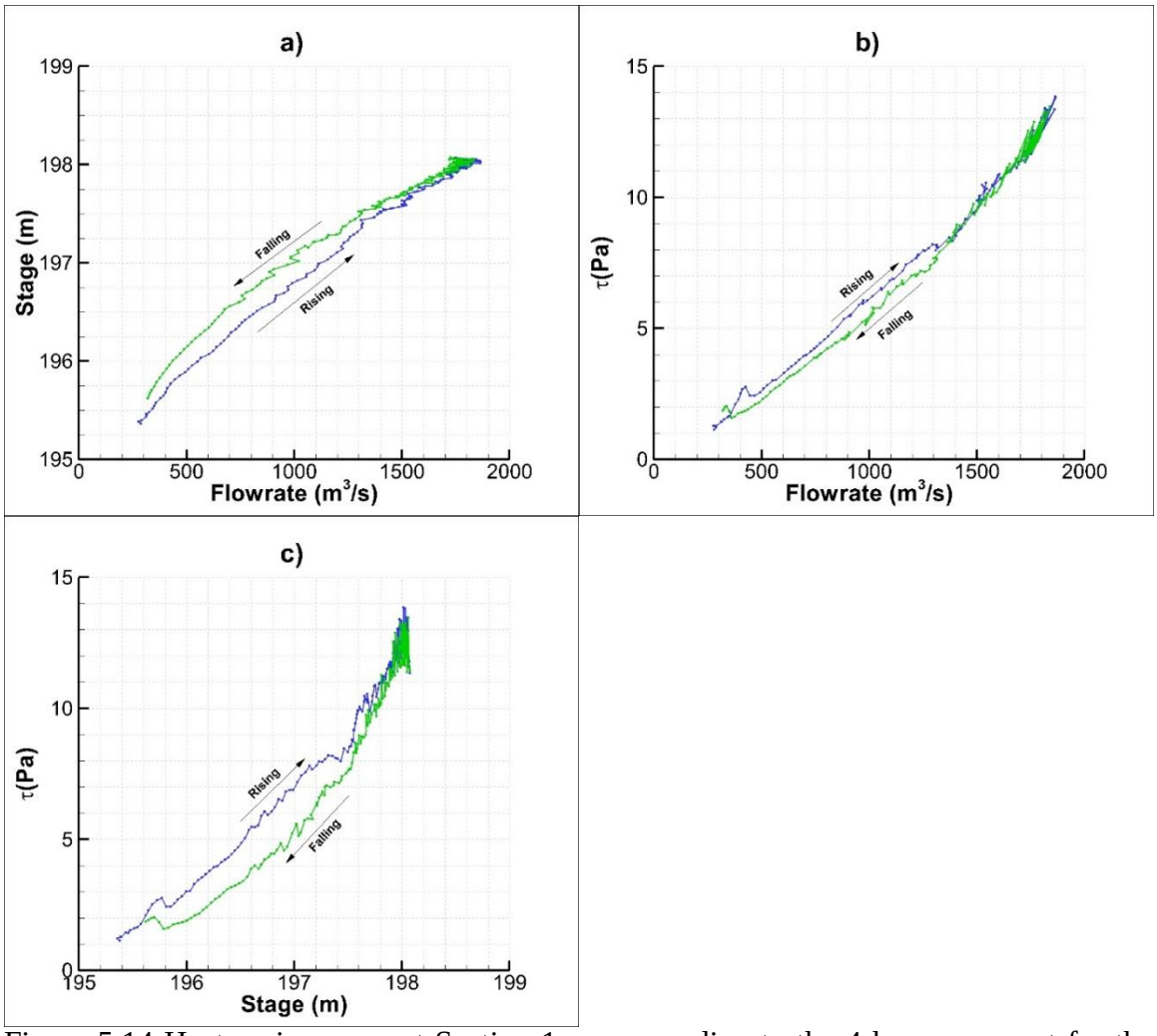

Figure 5.14 Hysteresis curves at Section 1 corresponding to the 4-hr wave event for the complex test case with no bridge deck. The inlet hydrograph is shown in Figure 5.10. a) Stage vs. Flowrate; b) Bed Shear Stress vs. Flowrate; and c) Bed Shear Stress vs. Stage. The rising and falling limbs are shown in blue and green colors respectively.

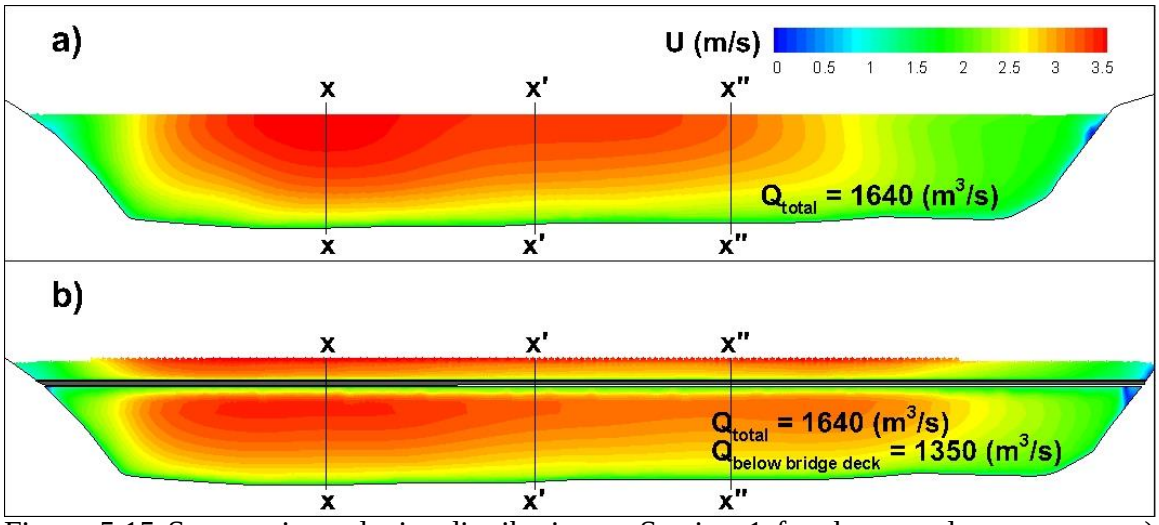

Figure 5.15 Streamwise velocity distribution at Section 1 for the complex test case. a) Simulation with no bridge deck; b) Simulation with the bridge deck (gray region).

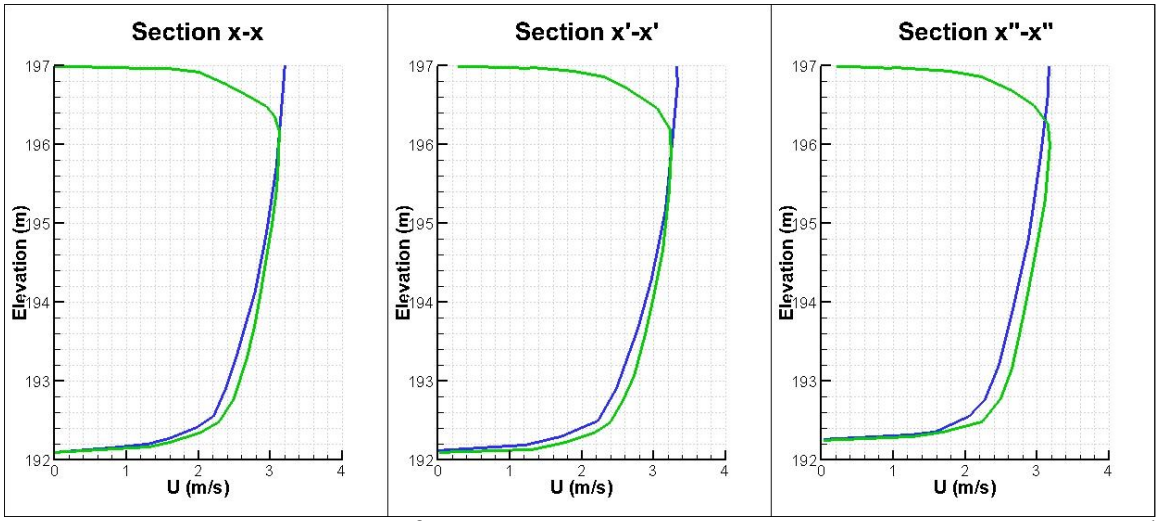

Figure 5.16 Vertical variation of streamwise velocity at spanwise locations x-x, x'-x' and x''-x'' in Section 1 (See Figure 5.15) for the complex test case. The velocity profiles in between the bed and the bottom of the bridge deck are shown for the simulation with no bridge deck (blue line) and the simulation with the bridge deck (green line).

CHAPTER 6 APPLICATION OF DEVELOPED 3-D MODEL IN IMPROVING PREDICTION OF DAM BREAK FLOODS

6.1 Introduction

Dam break floods are floods caused by the sudden structural collapse of a dam. In the rare eventuality of a dam break, the flood may have catastrophic consequences. Some examples include the Malpasset dam failure in 1959 in France that caused approximately $70 million in losses (Biscarini, 2016), and the Samarco Dam failure in 2015 in Brazil that caused the death of 19 people and $5 billion in recovery work (BBC news, 2016).

Dam break flood modeling is commonly done using either 1-D or 2-D models. Due to highly non-hydrostatic pressure distribution right downstream of the dam breach, both types of modeling approaches fail to predict the correct flood wave propagation (CADAM, 2000). The application of a fully 3-D model for realistic dam break floods is practically non-existent. The only example is the recent study of Biscarini (2016) who developed a 3-D model to simulate the Malpasset dam break flood event.

In the present chapter, the developed 3-D model with VOF capabilities is applied to simulate two realistic dam break events. The first test case simulates the sudden break of the Coralville Dam, which is located upstream of Iowa City, Iowa. The second test simulates the sudden break of the Saylorville Dam, which is located upstream of Des Moines, Iowa. In both case, a thorough comparison between results obtained with the newly developed 3-D model and with a calibrated 2-D model that is routinely used for this type of applications is performed. The differences between the predictions of the two models in terms of flood propagation speed, hydrographs at representative cross sections, free-surface elevation and unit-discharge profiles are analyzed. Using the 3-D model results as a target, a methodology is presented to calibrate 2-D models to improve their performance.

6.2 Coralville Dam break flood

6.2.1 Set up of 3-D and 2-D model simulations

The Coralville Dam is a flood-protection dam located upstream of Iowa City, Iowa and was built in 1958. It has a total capacity of approximately 570 million m^3 and it contains an emergency spillway that becomes active once the water level reaches an elevation of 217 m. The highest water level ever recorded was 219 m on June 15, 2008 during the peak of the 2008 flood in the US Midwest. Figure 6.1 shows the location of the Coralville dam with respect to Iowa City. Figure 6.2 shows a close-up view of the dam and its main features (e.g., the emergency spillway).

Due to the large computational extent of the region affected by the dam breaking, the mesh had to be optimized significantly in order to mesh the whole domain using a reasonable number of computational cells. The domain was split in 3 subparts: the Coralville Lake, the transition part connecting the lake with the Iowa River, and the 18-km reach of the Iowa River and its floodplain near Iowa City. The Coralville Lake was meshed with polyhedral cells. The average cell size was around 100 m in the horizontal plane. A minimum of 30 cells were used to resolve the flow in the vertical direction (Figure 6.3). The transition part, located right downstream of the lake, was meshed with a much higher resolution in the horizontal directions. The average cell size near the bed was 0.3125 m near the bed. The cell size was increasing progressively to a maximum cell size of 1.25 m close to the top of the computational domain (Figures 6.3 and 6.4). Finally, the mesh in the 18-km reach of the Iowa River was meshed with a resolution of approximately 1.25 m in the main channel and of 20 m over the floodplain (Figure 6.4). This mesh resolution is close to that used in the test cases discussed in Chapter 4, Section 3. The total number of cells was approximately 18 million.

In terms of initial conditions for the 3-D model, the lake was initially filled up to an elevation of 219 m, corresponding to the highest ever recorded water elevation, as to

propagate the largest dam break flood that could have occurred in the history of the Coralville Dam. The flow in the 18-km reach of the Iowa River was initialized using the steady state conditions calculated in Chapter 4, Section 3, corresponding to a flowrate of 245 m^3/s. At the start of the simulation (time t=0 s), the column of water inside the Coralville Lake is allowed to collapse freely into the downstream areas (transition part and the 18-km reach of the Iowa River).

Results of the dam break 3-D simulation will be compared to those predicted by the 2-D depth averaged model that was already used in Chapter 4 Section 3. The boundary conditions for the 2-D model are similar to the ones employed in Chapter 4 with one exception. Based on the findings of Biscarini et al. (2010) and CADAM (2000), calibrated 2-D depth-averaged models tend to underestimate the flood wave propagation speed and fail to predict the peak flowrates caused by the wave propagation as well as the time when the peak flowrates are reached. Due to these reasons, the computational domain in the 2-D simulation does not include the dam and transition region, where 3-D effects are expected to be important. Setting up the 2-D simulation this way increases the chances the 2-D model to accurately predict the flood wave propagation in the region situated downstream of the dam. The hydrograph predicted by the 3-D simulation in a section situated downstream of the dam is specify as the inlet boundary condition for the 2-D model simulation. This approach guarantees that at the location of the inlet in the 2-D model simulation, both computational models predict the same flowrates during the simulation time.

The time step was calculated based on a preliminary estimate of the dam break flood wave propagation speed. A Froude number, which is in fact the nondimensional front velocity, can be calculated using the theory proposed by Benjamin (1968) for gravity currents. For a current containing water and advancing in a surrounding air environment, an expression for the Froude number can be derived as a function of the height of the column of water, h, and the total height of the domain of interest, H (Benjamin, 1968):

$$Fr = \left[\frac{\left(2 - \frac{h}{H}\right)\left(1 - \frac{h}{H}\right)}{\left(1 + \frac{h}{H}\right)} \right]^{1/2} \tag{6.1}$$

For a very shallow environment, $\frac{h}{H} \to 0$. In this limit, the Froude number approaches $\sqrt{2}$ .The Froude number is defined as:

$$Fr = \frac{U}{\sqrt{gD}} \tag{6.2}$$

where U is the characteristic velocity or floodwave propagation speed in the present case, D is a characteristic length scale and g is the gravitational acceleration. Assuming that the characteristic length scale is the depth of the column of water at the face of the dam and assuming Fr= $\sqrt{2}$, one obtains:

$$U = \sqrt{2}\sqrt{gD} \tag{6.3}$$

Using this velocity and assuming CFL=0.2, similar to the other simulations conducted in natural river reaches, the time step can be calculated. The time step was estimated to be 0.05 s.

6.2.2 Comparison between 3-D and 2-D model (Version 0) results

In this subsection the main features of the flood wave propagation, as predicted by the 3-D model, are discussed. Also shown is comparison with the simulation performed using the previously calibrated 2-D model (Version 0). The main variable that was calibrated in the 2-D model was the Manning's coefficient. In Version 0, seven different values of this coefficient are used to specify the roughness over the different parts of the computational domain. These values were obtained based on preliminary calibration of the 2-D model when applied to calculate various flooding events in the same reach of the Iowa River.

Figure 6.5 shows snapshots of the evolution of the flood wave as predicted by the 3-D and 2-D model simulations at 6 time instances: 250 s, 500 s, 750 s, 1000s, 2500 s and

11625 s after the collapse of the dam (t=0 s). Both solutions predict a gravity current shape for the flood wave as it advances. The flood wave in the 2-D model is lagging behind the flood wave predicted by the 3-D model. This finding is in agreement with what was observed in previous applications of 2-D models for this type of problems (CADAM, 2000).

Figure 6.6a the total flooded area predicted by the two models as a function of time. The 3-D model inundates faster than the 2-D model. The temporal rate of increase of the inundated area is 7 km^2/hr in the 3-D model simulation and 5.9 km^2/hr in the 2-D simulation, which corresponds to a 15% underprediction by the 2D model. After about 1 hr from the dam break, the rate of increase of the inundated area is about the same in both solutions. The peak flood extent is reached at 2.75 hrs after the collapse of the dam in the 3-D model solution and at 3.25 hrs in the 2-D model solution. This corresponds to a 20% overestimation of the time to peak flood extent of the 2-D model with respect to the 3-D model predictions. The error of the 2-D model solution with respect to the 3-D model prediction is plotted as a function of time in Figure 6.7. The error in terms of flooded area ranges from -15% to 6%. On average, the 2-D model solution is underestimating by 6% the flooded area with respect to the 3-D model results.

Figure 6.8 shows the free-surface elevation along the centerline of the main channel of the Iowa River art peak flood extent. Starting from the 2nd river dam and until the end of the computational domain the 3-D model and 2-D model Version 0 simulations predict a very similar profile. However, upstream of the 2nd dam, the differences between the predictions by the two models become more noticeable. For instance, close to the inlet section, the differences are close to 3 m, which corresponds to a 20% error with respect to the local depth predicted by the 3-D model (~15 m). The differences are, most likely, due to the roughness parametrization in the calibrated 2-D model, which uses a relatively large value of the Manning's coefficient in the regions where the 1st and 2nd dams are situated.

Moreover, the bathymetry in the region the two dams are present is not fully consistent with the construction blueprints of the two dams.

Figure 6.9 shows the unit discharge distribution at peak flood extent. Qualitatively, both solutions look very similar. The regions of high unit discharge are present at approximately the same locations inside the computational domain in the two simulations. Still, there are some differences. The 2-D model predicts two 'generic' regions of relatively high unit discharge. The first one is situated over the main channel of the Iowa River. The other one corresponds to regions uniting deeper parts of the flow once the floodplain becomes inundated and the flow tends to follow a shorter path in between the deeper regions. Solutions predicted with St. Venant solvers tend to force the flow through the deepest parts of the domain, consistent with Manning's equation. The capacity of such model to account for phenomena that tend to deviate the flow from following deepest regions is quite limited given the inability of such models to account for secondary currents and shallow mixing layers developing at the interface between the main channel and its floodplain. When applied to a realistic river environment, it means that the regions of high unit discharge would tend to be situated over the deepest regions which align with the location of the main channel. The 3D model, on the other hand, can capture secondary flow and 3-D effects especially as the floodplain starts being inundated. Maybe the most obvious effect is that close to the free surface some of the flow changes direction from being oriented more or less along the centerline of the main channel to being oriented in a lateral direction with respect to the centerline. This effect is more pronounced in regions where large high curvature meanders are present. Another difference in the distributions of the unit discharge in the two simulations is that the region of high unit discharge predicted by the 3-D model looks more uniform compared to the one predicted by the 2-D model, in the sense that the transverse variations in the values of unit discharge are less sharp compared to those observed in the 2-D model simulation.

At peak flood extent, 22 cross sections were selected along the river reach to perform a more quantitative analysis of unit discharge distribution at peak flow extent and of the hydrograph. The hydrograph comparison is very relevant since it provides a new metric to evaluate the propagation speed of the flood wave. Figure 6.10 shows the hydrographs predicted by the 3-D model and 2-D model simulations at 6 representative cross sections. Here, only the comparison between the 3-D model simulation and the 2-D model Version 0 simulation is discussed. The 3-D model predicts a faster increase of the flowrate compared to the 2D model until the peak levels are reached at each cross section. This finding is consistent with the temporal variation of the inundated area in Figure 6.6a. The more downstream the cross section is situated, the larger the difference between the times the peak flow rate is reached in the 2-D model and 3-D model simulations. For example, the difference is close to 0.7 hr at section 9 and close to 2 hrs at sections 15 and 18. The difference in time was taken as the difference between the time it took the 2-D model to reach its corresponding peak flowrate and the time it took the 3-D model to reach its peak flowrate. However, a similar analysis can be performed comparing the time it took both models to reach the peak flowrate captured by the 3-D model. This analysis was not performed since at some cross sections the 2-D model did not reach the peak flowrate captured by the 3-D model, and in the cross sections that it did, it would yield the same conclusions as the ones obtained from the aforementioned analysis performed.

It was found that 15 out of 22 cross sections showed good agreement between the unit discharge profiles predicted by the 3-D model and 2-D model simulations. The hydrographs for several sections where good agreement was observed are shown in Figure 6.11. Figure 6.12 shows the hydrographs at four cross sections where poor agreement was observed between the two simulations. For example, Section 4 is located in the region where the flow transitions from being mainly situated over the main channel to a region where the 3D model predicts most of flow is advected over the floodplain. By contrast, the 2-D model predicts high values of the unit discharge over the main channel, followed by

reduced values of the unit discharge on the floodplain next to the main channel. This is followed by an increase of the unit discharge to peak values that are close to those predicted by the 3-D model in the region situated over the floodplain where incoming flow is advected mostly from upstream over the shallower regions. Section 9 is located right downstream from a bridge contraction (Figure 6.13), in a region where the flow expands and 3-D effects are important. The unit discharge distribution predicted by the 2-D model at section 9 is very different from the one predicted by the 3-D model. In particular the 2-D model severely underpredicts the peak unit discharge in the main channel. It then predicts a much slower decay of the unit discharge away from the banks of the main channel compared to the 3-D model simulation. Section 13 is located in the middle of a high curvature part of the channel. The secondary flow leads to a redistribution of the unit discharge in the cross section that is not captured by the 2-D model. Section 17 is located close to the 2nd river dam. As expected, the flow is highly three dimensional right downstream of the dam. Most of the differences in the unit discharge predictions are observed over the part of the floodplain situated next to the main channel. Significant 3-D effects are induced in this region because of the mixing layer generated by the difference in depth-averaged velocities, bed roughness and flow depths. This explains why the 2-D model overestimates by about 30% the amount of flow advected over the main channel part of the cross section.

Consistent with other studies, the calibrated 2-D models failed to accurately capture the speed of propagation of the flood. The hydrographs predicted by the 2-D model showed a longer time for the discharge to reach peak values compared to the 3-D model. The 2-D model also predicted higher free-surface elevations compared to the 3-D model. While the 2-D model predictions of the unit discharge profiles were in many regions in good agreement with the 3-D model predictions, significant differences were observed in regions where 3-D effects are expected to be important.

6.2.3 Recalibration of 2-D model based on 3-D model results

The next subchapter will propose a simple way to improve the predictions of 2-D model based on the 3-D model predictions via recalibration of the Manning coefficient values prescribed over the main channel and the flood plain. Based on Manning's equation, the roughness coefficient is inversely proportional to the discharge. Since the 2-D depth-averaged simulation using the 2-D model with the original calibration underestimated the speed of the flood wave, the Manning's coefficient needs to be decreased over part or the whole domain.

Three additional simulations were performed using the 2-D model. In the 2-D Model – Version 0 simulation, 7 different values were used for the Manning's coefficient throughout the computational domain based on the original calibration. In the 2-D model Version 1 simulation the Manning coefficient in the main channel was decreased from 0.035 to 0.015, while its values in the other parts of the domain were left unchanged with respect to Version 0. This modification was based on the estimation of the value of the Manning coefficient based on the equivalent roughness height used in the 3-D simulation of flow in the reach of the Iowa River discussed in Chapter 5. In the 2-D model Version 1 simulation the Manning coefficient is set equal to 0.015 over the whole domain. In the 2-D model Version 3 simulation the Manning coefficient in each of the subregions defined in Version 0 is multiplied by 0.43, which is the ratio between the value of the Manning coefficient in the main channel based on the roughness used in the 3-D simulation (n=0.015) and the corresponding value used in Version 0 (n=0.035). Table 6.1 shows the different Manning's coefficients used for all versions of the 2-D model.

Table 6.1 Manning's coefficient for the different versions of the 2-D model for the Coralville Dam Break

	2-D Model			
	Version 0	Version 1	Version 2	Version 3
River Channel	0.035	0.015	0.015	0.015
Field	0.040	0.040	0.015	0.017
Woods	0.120	0.120	0.015	0.051
Pavement	0.013	0.013	0.015	0.006
Low Density Development	0.050	0.050	0.015	0.021
Medium Density Development	0.075	0.075	0.015	0.032
High Density Development	0.100	0.100	0.015	0.043

Figure 6.6 compare the inundation extent as a function of time predicted by the 3-D model with those predicted by the 2-D model simulations. Compared to the original model set up, Version 1 better predicts the rate of increase of the inundated area during the initial stages of the flood wave generated by the dam break, as the difference with the 3-D predictions decays from 15% underestimation to about 11%. However, Version 1 predictions are not closer to the 3-D model predictions than Version 0 predictions during the later stages of the propagation of the flood wave. Version 2 predicts a faster rate of increase of the inundated area during the initial stages compared to the 3-D model predictions (14% increase). During the later stages of the propagation of the flood wave, Version 2 predictions remain quite close to the 3-D model prediction. Finally, Version 3 follows very closely the 3-D model prediction of the temporal variation of the inundated area over the first 2.5 hrs of the flood wave propagation.

All 2-D simulations predict a larger peak flood extent compared to the 3-D model. However, the difference is less than 5%. Figure 6.7 shows the percentage difference between the 2-D and 3-D model predictions of the flood inundation extent as a function of time. The differences predicted by Version 1 simulation range from -10% to 2%, compared to the -15% to 6% range predicted Version 0. Versions 2 and 3 predict differences with the 3-D model ranging from -2% to 9% and from -6% to 5%, respectively (Table 6.2). The

time-averaged percentage difference predicted by Version 2 and 3 (1.4% and -1.7%) are significantly lower than those predicted by the other versions (~6%).

Table 6.2 Comparison of percentage difference between 2-D model and 3-D model predictions of the flooded area as a function of time

	Range of percentage difference	**Average percentage difference**
2D-Version 0	[-15% - 6%]	-6%
2D-Version 1	[-10% - 2%]	-6%
2D-Version 2	[-2% - 9%]	1.4%
2D-Version 3	[-6% - 5%]	-1.7%

Figure 6.8 shows the free-surface elevation along the centreline of the main channel of the Iowa River at peak flood extent. Downstream of the second river dam, the predictions of 2-D model simulations are close to each other and also close to the 3-D model prediction. However, upstream of the 2nd river dam, significant differences are observed among the various 2-D model predictions. Version 1 predicts a free-surface profile that is very similar to the one predicted by version 0. Version 2, on the other hand, predicts a free-surface profile that is very close to the one predicted by the 3-D model over the whole river reach. Version 3 also shows a significant improvement compared to versions 1 and 2, in terms of its agreement with the 3-D model prediction.

Figure 6.10 compares the hydrographs predicted by the 2-D model and 3-D model simulations at 6 representative cross sections. Compared to the agreement observed for version 0, version 1 shows only slightly better agreement with the 3-D model hydrographs during the initial stages of the flood wave propagation, when the flow rate increases rapidly. This is explained by the smaller value of the Manning's coefficient in the main channel in version 1 (0.015) compared to version 0 (n=0.035) which allows water to move faster in the main channel. The hydrographs predicted by versions 2 and 3 show much

better agreement with the corresponding 3-D hydrographs compared to the one observed for versions 0 and 1.

Despite the fact that versions 2 and 3 accurately predict the hydrographs and the rate of increase of the flooded area, some significant differences are sometimes observed between the 2-D model and 3-D model predictions of the unit discharge profiles (Figure 6.11 and 6.12). Overall, one cannot say that versions 2 and 3 predict more accurately the unit discharge profiles at the analysed sections compared to versions 0 and 1. Still, the level of agreement with the 3-D model is acceptable.

6.3 Saylorville Dam break flood

Saylorville Dam is a flood protection dam located upstream of the City of Des Moines. The dam was built in 1977. It backs up water from the Des Moines River before the city of Des Moines. The highest water level ever recorded was 272 m, which occurred on July 11, 1993 during the Great Flood of 1993 that affected the US Midwest. Figure 6.14 shows the location of the Saylorville dam with respect to the city of Des Moines. Figure 6.15 shows a close-up view of the Saylorville dam.

The physical size of computational domain is larger than the one used in the Coralville Dam break simulation. The length of the Des Moines River downstream of the Saylorville Dam included in the computational domain is 34 km, compared to the 18 km length of the Iowa River in the computational domain used to simulate the failure of the Coralville Dam. Additionally, there are two tributaries feeding into the Des Moines River: Beaver Creek and the Raccoon River. The computational domain includes an 8-km long reach of the Beaver Creek and a 27-km long reach of the Raccoon River. The total number of computational cells was close to 40 million.

In the 3-D model simulation, the lake was initially filled up to an elevation of 272 m, corresponding to the highest ever recorded water elevation in the lake. The areas situated downstream of the dam did not contain any water at the start of the simulation. The column

of water inside the Saylorville Lake is allowed to collapse freely into the downstream areas, which generates a flood wave. All the other boundary conditions and simulation set up procedures are identical to the ones used in the 3-D simulation of the Coralville dam break up. The 3-D simulation was ran with a time step corresponding to a CFL number equal to 0.2. Due to the very large computational cost associated with this dam break simulation, the solution was only calculated until 3.75 hrs (13500 s) after the dam break occurred.

HEC-RAS 2D was used to perform the 2-D simulations because a calibrated model for this region was available from the Iowa Flood Center. The 2-D simulation using the calibrated Manning's coefficients for the Des Moines River is referred to as version 0. The boundary conditions used in this 2-D model are of the same types as the ones used to set up the 2-D simulations of the Coralville Dam break (see Section 6.2). A hydrograph was recorded based on the 3-D simulation results at the location situated immediately downstream of the dam, where the computational domain starts in the 2-D simulations. This hydrograph was then used to specify the water elevation and discharge at the inlet boundary for the 2-D simulations.

Figure 6.16 shows snapshots of the evolution of the flood wave generated by the dam break at 6 time instances (t=250 s, 500 s, 1000 s, 2000s, 400 s and 13500 s) in the 3-D and 2-D (version 0) simulations. The flood wave predicted by the 2-D model is lagging behind the one predicted by the 3-D model. This finding is consistent with what was observed in Section 6.2 for the Coralville Lake dam break simulations.

The temporal evolutions of the flooded area predicted by the 3-D and 2-D version 0 simulations are compared in Figure 6.17a. Fairly significant differences are observed in the predicted values of the average rate of increase of the flooded area at different stages of the flood wave propagation in the two simulations. During the initial stages (t<0.5 hrs), the rate of increase of the inundated area predicted by the 3-D model is 59 km^2/hr, while that predicted by the 2-D model version 0 is 48 km^2/hr. This corresponds to an 18% underprediction by the 2-D model, which is comparable to the underprediction observed in

the Coralville Lake dam break simulation (15% over the initial stages using another calibrated 2-D model). Between t=0.5 hrs and t=1.25 hrs, the rate of increase predicted by the two models are comparable (10 km^2/hr vs 12 km^2/hr). While the 2-D simulation reaches a regime where the rate of increase of the inundated area is close to 10km2/hr until the end of the simulation, the rate of increase is subject to much stronger variations (between 5 km^2/hr and 22 km^2/hr) in the 3-D simulation.

Figure 6.18 quantifies the percentage difference between the 2-D model simulations and the 3-D model. For the version 0 simulation, the 2-D model underestimates the inundated area at all times (error range is -70% to -5%). The error is less than 15% for t>0.5 hrs. The large differences observed over the initial stages are attributed to 3-D non-hydrostatic effects that appear to be very strong even if the 2-D model does not try to simulate the flow inside the lake and at the location of the dam where the flood wave is forming, a phenomenon that is tougher to accurately simulate using a 2-D depth averaged model. Since the solution did not reach peak inundation extent at the final time of simulation (t=3.5 hrs) it is not possible to get an estimate by what amount of time the 2-D model underestimates the time at which the peak flood extent is observed.

Figure 6.19 compares the free surface profiles along the main channel of the Des Moines River at t=3.75 hrs. The (calibrated) 2-D model version 0 predictions are very close to the 3-D model prediction. Close to the inlet the differences are of the order of 1 m for a channel depth of approximately 10 m, meaning an error of approximately 10%. At a distance of about 15 km (section 6-6 in Figure 6.16), the free-surface elevation drops because of the local bathymetry features over the flood plain which redirects most of the incoming flow toward the main channel. Downstream of this constriction, the free surface elevations predicted by the two simulations are very close to each other. Due to the fact that the flood wave in the 2-D version 0 simulation does not propagate as fast as in the 3-D simulation, the front of the wave stops at around 27 km at t=3.5 hrs in Figure 6.19.

A total of 16 cross sections were chosen along the centerline of the main channel of the Des Moines River to perform a more quantitative analysis of the predicted hydrographs and unit discharge distribution at peak flow extent. The locations of these cross sections are shown in Figure 6.16. Figure 6.20 compares the hydrographs at cross sections 2, 4, 6, 8, 10 and 12. Consistent with results in Figure 6.17a, the 3-D simulation predicts a faster increase of the flowrate at these sections compared to the 2-D model version 0 simulation during the initial stages of the hydrograph. The further the cross section is located with respect to the dam, the more noticeable these differences are. At Section 2 both simulations show a similar increase of the flowrate during the initial stages and a similar value of the time to peak and corresponding discharge. At Section 8, the flowrate in the 2-D version 0 simulation starts increasing 0.2 hrs after that happens in the 3-D simulation. The difference in the time to peak is about the same and the peak discharge is smaller by about 10% in the 2-D simulation. The trend continues at Section 12, where the time difference is close to 0.4 hrs and the peak discharge is about 20% smaller compared to the value predicted by the 3-D simulation.

In terms of unit discharge profiles, it was found that 13 out of 16 cross sections showed good agreement between the two simulations. Figure 6.21 shows the unit discharge profiles in the cross section at 6 sections that showed good agreement between the 3-D and the 2-D version 0 simulations. Figure 6.22 shows the same information at three cross sections that showed poor agreement between the two simulation results. Generally, these sections were situated in regions where 3-D effects (e.g., increased flow non-uniformity in the vertical direction, strong cross-flow secondary motions) are expected to be significant. For example, Section 2 is located in a shallow region where the flow is expanding laterally. While the 3-D model predicts a fairly uniform increase of unit discharge from the left floodplain to the right floodplain, the 2-D version 0 simulation predicts a sharp increase of the unit discharge over the main channel compared to the values observed on the two floodplains. This behavior has also been observed in the 2-D simulation of the Coralville

Lake dam break and is due to the tendency of 2-D solvers to force the flow predominantly over the deepest regions of the domain. Significant 3-D effects are also expected at the other 2 cross sections for which results are shown in Figure 6.22. Section 10 is located in the middle of a curved region of the main channel of the Des Moines River. Section 12 is located around the location where the cross-section of the Des Moines River reduces significantly. In both of these cross sections, the 3-D simulation predicts a much higher peak unit discharge compared to the 2-D version 0 simulation.

6.3.1 Improvement of 2D depth-averaged results

Similar to the approach used in Section 6.2, additional modifications will be implemented in the 2-D model to try to obtain a better agreement with the 3-D simulation. As decreasing only the value of the Manning's coefficient in the main channel (version 1) was shown in Section 6.2.1 not to lead to a significant improvement, only simulations in which the Manning coefficients were specified in a way similar to what was done in versions 2 and 3 were performed. Table 6.3 shows the Manning's coefficients for the versions of the 2-D models being used for this analysis.

Table 6.3 Manning's coefficient for the different versions of the 2-D model for the Saylorville Dam Break

	2-D Model		
	Version 0	*Version 2*	*Version 3*
River Channel	0.035	0.015	0.015
Barren Land	0.090	0.015	0.039
Cultivated Crops	0.037	0.015	0.016
Deciduos forest	0.100	0.015	0.043
High Intensity Development	0.150	0.015	0.064
Medium Intensity Development	0.100	0.015	0.043
Low Intensity Development	0.050	0.015	0.021
Development - Open Space	0.020	0.015	0.009
Emergent wetlands	0.045	0.015	0.019
Evergreen forest	0.110	0.015	0.047
Hay/Pasture	0.033	0.015	0.014
Herbaceuous	0.034	0.015	0.015
Mixed forest	0.100	0.015	0.043
open water	0.020	0.015	0.009
Shrub/Scrub	0.050	0.015	0.021
Woody wetlands	0.100	0.015	0.043

In the 2-D version 2 simulation the Manning coefficient in set to 0.015 over the full domain. In the 2-D version 3 simulation, the Manning coefficient used in the version 0 simulation are multiplied by the ratio (0.43) between the calibrated Manning coefficient value in the main channel (n=0.035) and the value estimated based on the equivalent roughness (n=0.015).

Figure 6.17 compares the temporal evolution of the inundation area between the 3-D model prediction and the various 2-D simulations. During initial stages of the flood wave

propagation (t<0.5 hrs), the rate of the increase of the inundated area in the 2-D version 2 simulation is very close to that shown by the 3D model, which is a first improvement compared to version 0 results (Figure 6.17b). The agreement between the 2-D version 2 and 3-D simulations remains very good until t=2.25 hrs. At larger times, the 2-D version 2 simulations overpredicts the total inundated area but the differences are less than 10%. The temporal variation of the inundated area predicted by the 2-D version 3 simulation shows even better agreement with the one predicted by the 3-D simulation (Figure 6.17c). The agreement remains very good until the end of the simulation. Figure 6.18 characterizes in a more quantitative way how close the inundated region predicted by the three 2-D simulations is to the 3-D prediction during the flood wave propagation (0<t<3.5 hrs). All versions predict large errors over the first couple of minutes of the wave propagation. These errors are probably unrelated to the Manning coefficient values specified in the 2-D model. However, for t>0.5 hrs version 0 underestimates by up to 20% the inundated area predicted by the 3-D simulation, while version 2 overestimates it by up to 12%. Clearly, for the Saylorville Lake version 3 gives the most accurate results during the simulated time as the difference varies between -6% and 6%. Table 6.4 summarizes the performance of the three 2-D simulations in predicting the temporal evolution of the inundated area.

Table 6.4 Comparison of percentage difference between 2-D model and 3-D model predictions of the flooded area as a function of time

	Range percentage difference	**Average percentage difference**
2D-Version 0	[-70% - -5%]	-16% (16%)
2D-Version 2	[-60% - 10%]	2% (6%)
2D-Version 3	[-70% - 13%]	-3% (4%)

In terms of the free-surface elevation predictions along the centreline of the main channel of the Des Moines river at t=3.5 hrs, the 2-D version 2 and 3 simulations show very good agreement with the 3-D simulation at all locations, something that is not the case for the 2-D version 0 simulation. The hydrographs predicted by the 2-D version 2 and 3 simulations are also in better agreement with the ones predicted by t eh 3-D simulation. Version 2 tends to overpredict slightly the peak flow rate, but overall the discharge at all six cross sections shown in Figure 6.20 starts increasing at about the same time in the 2-D versions 2 and 3 and in the 3-D simulations. The peak discharge is also reached at about the same time in the three simulations. So, the analysis of the hydrographs barely favours version 3. As for the analysis conducted for the Coralville Lake, the predictions of the unit discharge profiles by the 2-D version 2 and 3 simulations are not necessarily more accurate than those of the 2-D version 0 simulation (see Figures 6.21 and 6.22). Overall the unit discharge profiles predicted by the three 2-D simulations show a similar level of agreement with the profiles predicted by the 3-D simulation.

6.4 Conclusions

In this chapter the 3-D model was extended and applied to predict he propagation of flood waves generated by the sudden collapse of a dam. These type of problems are characterized by sudden changes in the free surface elevation, especially during the initial stages of the flow. Two realistic dam break scenarios were simulated and results were compared to those given by two 2-D depth averaged models currently used by the Iowa Flood Center to predict floods in the state of Iowa. The 2-D simulations using the calibrated values of the Manning coefficient in the region where the flood occurred underpredicted the speed of propagation of the flood wave and the area inundated by the flood. Significant differences were observed for the hydrographs at different cross sections situated along the path of the flood and in the free surface elevation with respect to the 3-D predictions. Using the Manning coefficient value corresponding to the mean value of the equivalent bed

roughness used in the 3-D simulation, one was able to improve the agreement between the 3-D and the 2-D model predictions when the calibrated values of the Manning coefficient in the different regions of the computational domain were rescaled by the ratio between the calibrated value of the Manning coefficient in the main channel and the value corresponding to the equivalent roughness height used in the 3-D model.

Based on the results presented in this chapter, some recommendations are proposed to improve the performance of numerical predictions of dam break induced floods for realistic large-domain applications.

1. The reservoir located upstream of the dam as well as regions situated some distance downstream of the dam should be simulated using a 3-D code given that the flood wave propagation is subject to important 3-D effects and large accelerations during the initial stages of the dam break.
2. A hydrograph from the 3-D simulation should be collected at the inlet of the computational domain used in the 2-D model simulation. The inlet of the computational domain used in the 2-D simulation should be situated inside the 3-D computational domain. This hydrograph will be used to specify the inlet boundary conditions in the 2-D simulation.
3. Even if the 2-D model was calibrated for a certain region, it is a good idea to try to recalibrate the model using information on the equivalent roughness height in the main rivers present in the computational domain (the procedure should be similar to the one adopted to set up the 2-D version 3 simulations). The 3-D computational domain should contain the upstream part of the 2-D domain, such that one can identify which 2-D simulations gives the best agreement with the 3-D simulation over the common part of the two computational domains.

4. Preliminary tests should be performed to insure the time stepping errors in the 3-D simulations are not significant. Generally, running the 3-D simulation with a CFL number less than 0.2 is sufficient to avoid large time stepping errors.

Both 3-D dam break simulations were performed on the Titan HPC cluster at the Oak Ridge National lab. Each simulation used around 2500 processor for a mesh of around 20-30 million cells. A scalability study showed that this number of processors gave the optimum performance for the CFD model used and for the grid sizes employed in the simulations (Figure 6.23). This corresponds to about 10,000 grid points per processor for the Titan HPC cluster. However, this number may be very different on other PC Clusters using a different architecture.

Figure 6.1 Aerial view of region affected by the break of the Coralville Dam. The region includes the Coralville Lake and Iowa City.

Figure 6.2 Close-up view of the Coralville Dam, including the main dam and the emergency spillway.

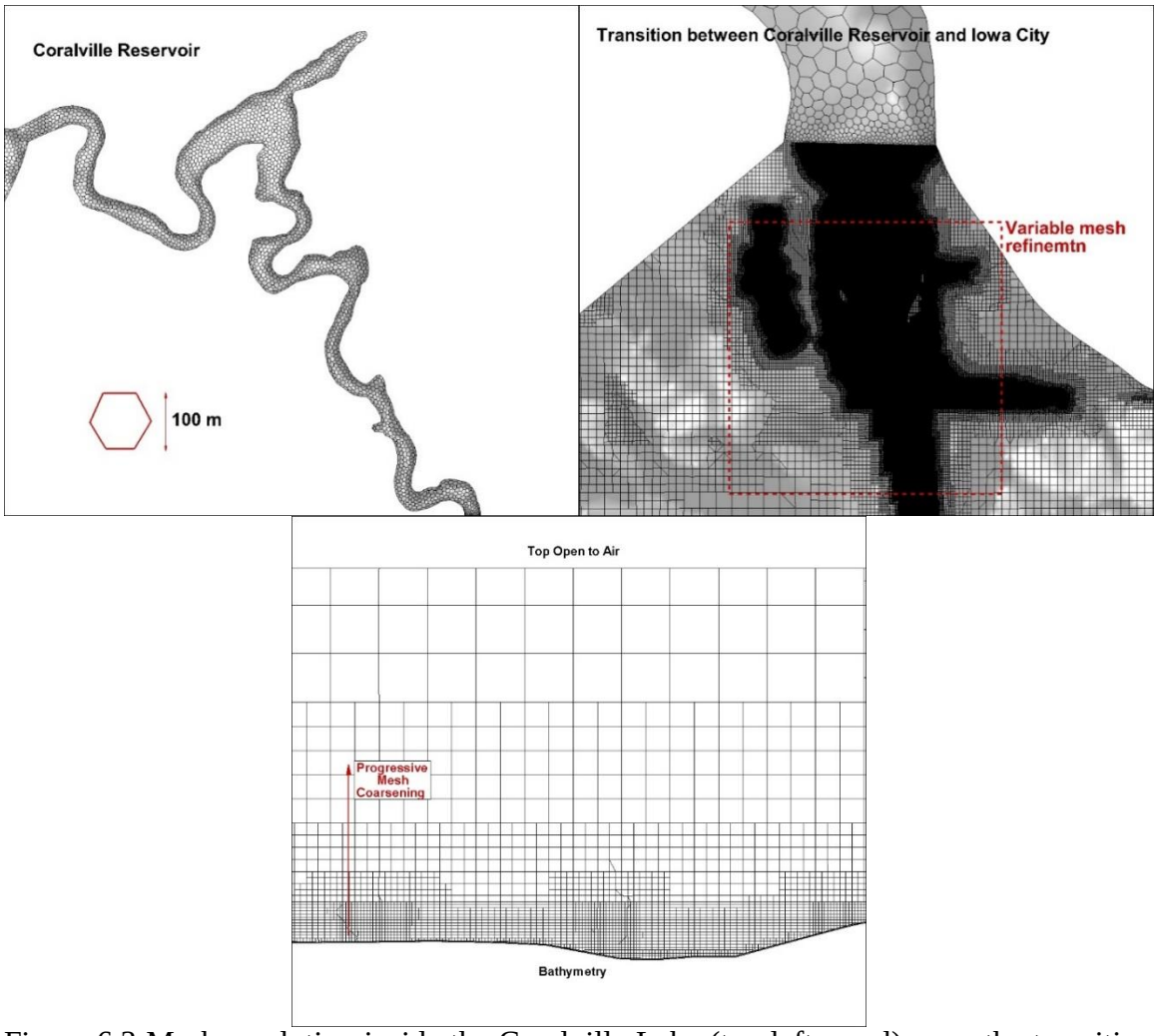

Figure 6.3 Mesh resolution inside the Coralville Lake (top left panel), near the transition between the Coralville Lake and Iowa City (top right panel), and along the vertical direction inside the main channel of the river (bottom panel).

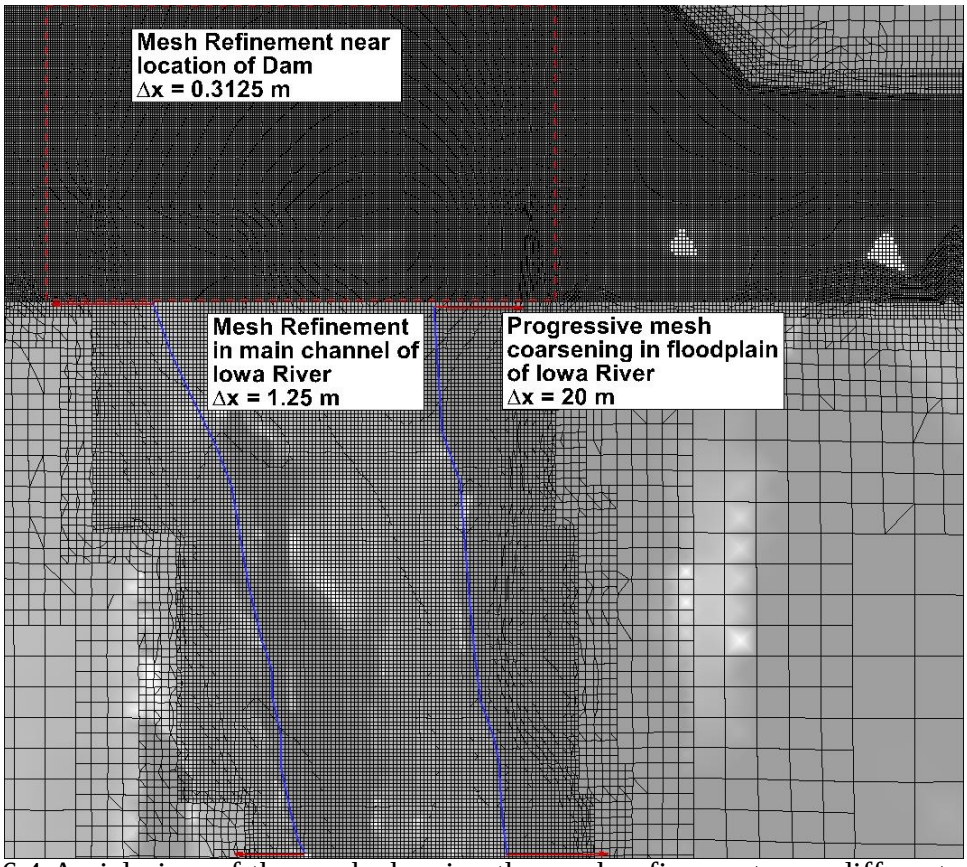

Figure 6.4 Aerial view of the mesh showing the mesh refinement near different areas of interest. These areas include regions located close to the dam, in the main channel and over the floodplain of the Iowa River.

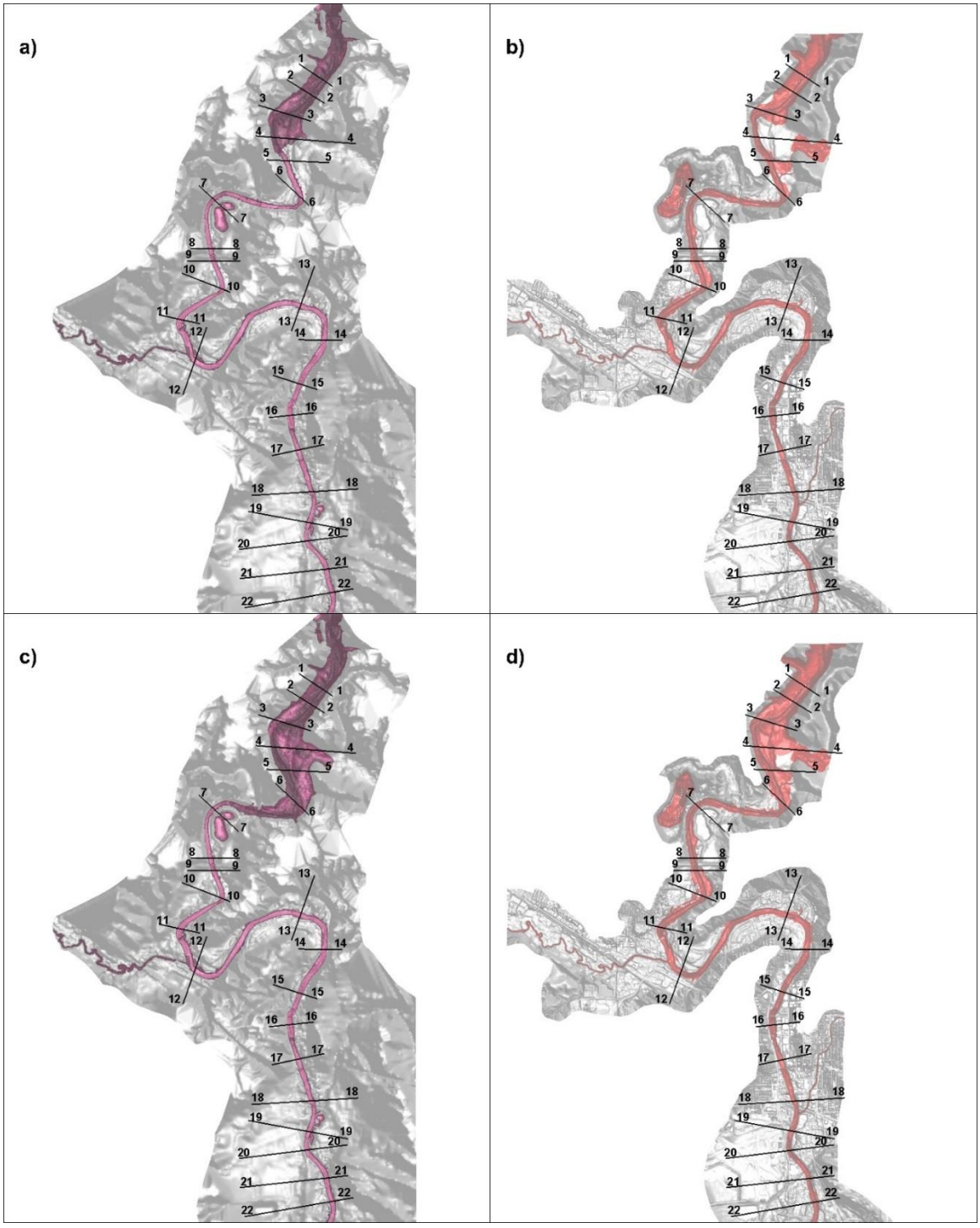
a)
b)
c)
d)

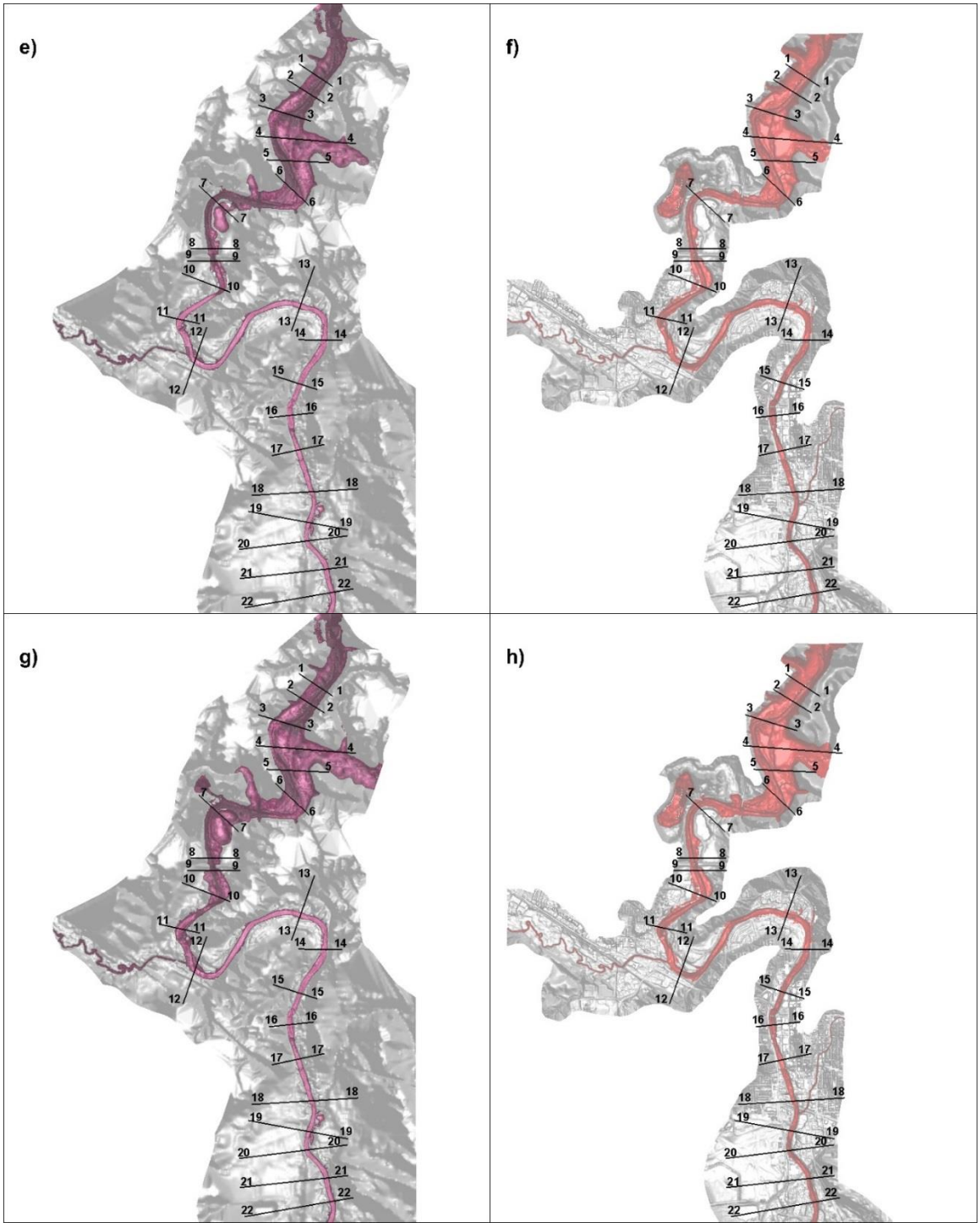
e)
f)
g)
h)

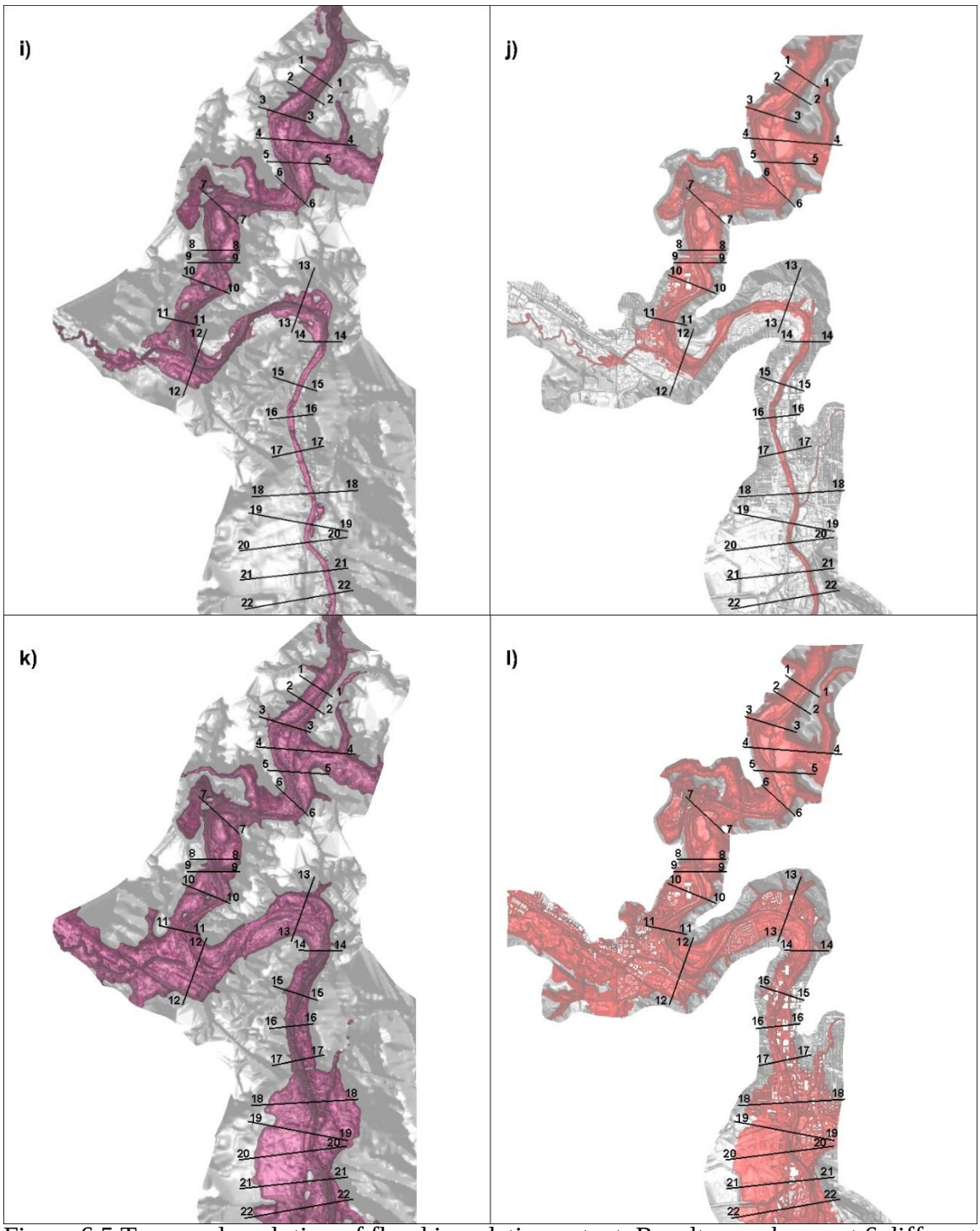

Figure 6.5 Temporal evolution of flood inundation extent. Results are shown at 6 different times after the collapse of the Coralville Dam. A) 3-D model, t=250 s; b) 2-D model, t = 250 s; c) 3-D model, t = 500 s; d) 2-D model, t = 500 s; e) 3-D model, t = 750 s; f) 2D model, t = 750 s; g) 3-D model, t = 1000 s; h) 2-D model, t = 1000 s; i) 3-D model, t = 2500 s; j) 2-D model, t = 2500 s; k) 3-D model, t = 11625 s; l) 2-D model, t = 11625 s.

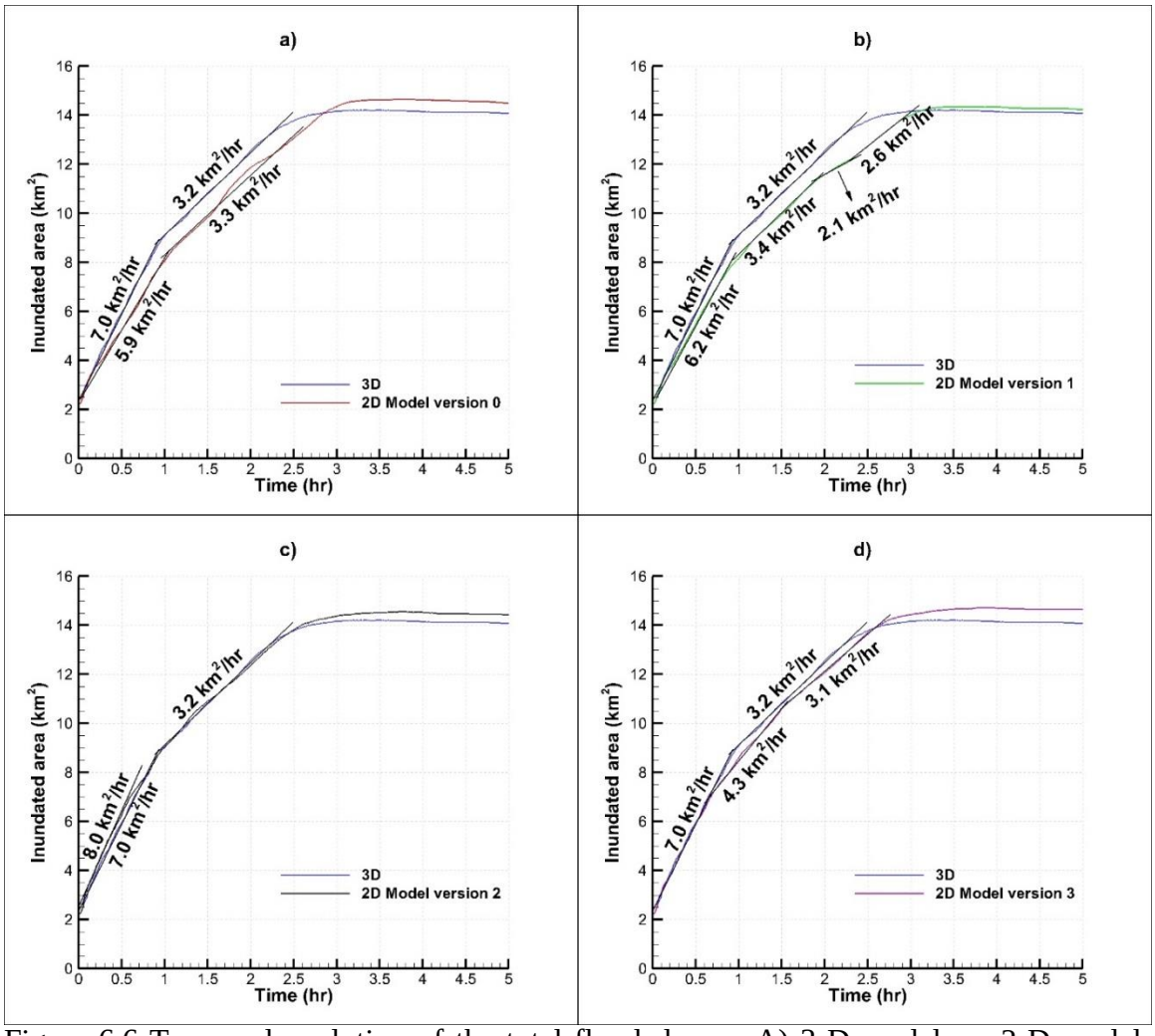

Figure 6.6 Temporal evolution of the total flooded area. A) 3-D model vs. 2-D model-version 0; b) 3-D model vs. 2-D model-version 1; c) 3-D model vs. 2D model-version 2; and d) 3-D model vs. 2-D model version 3.

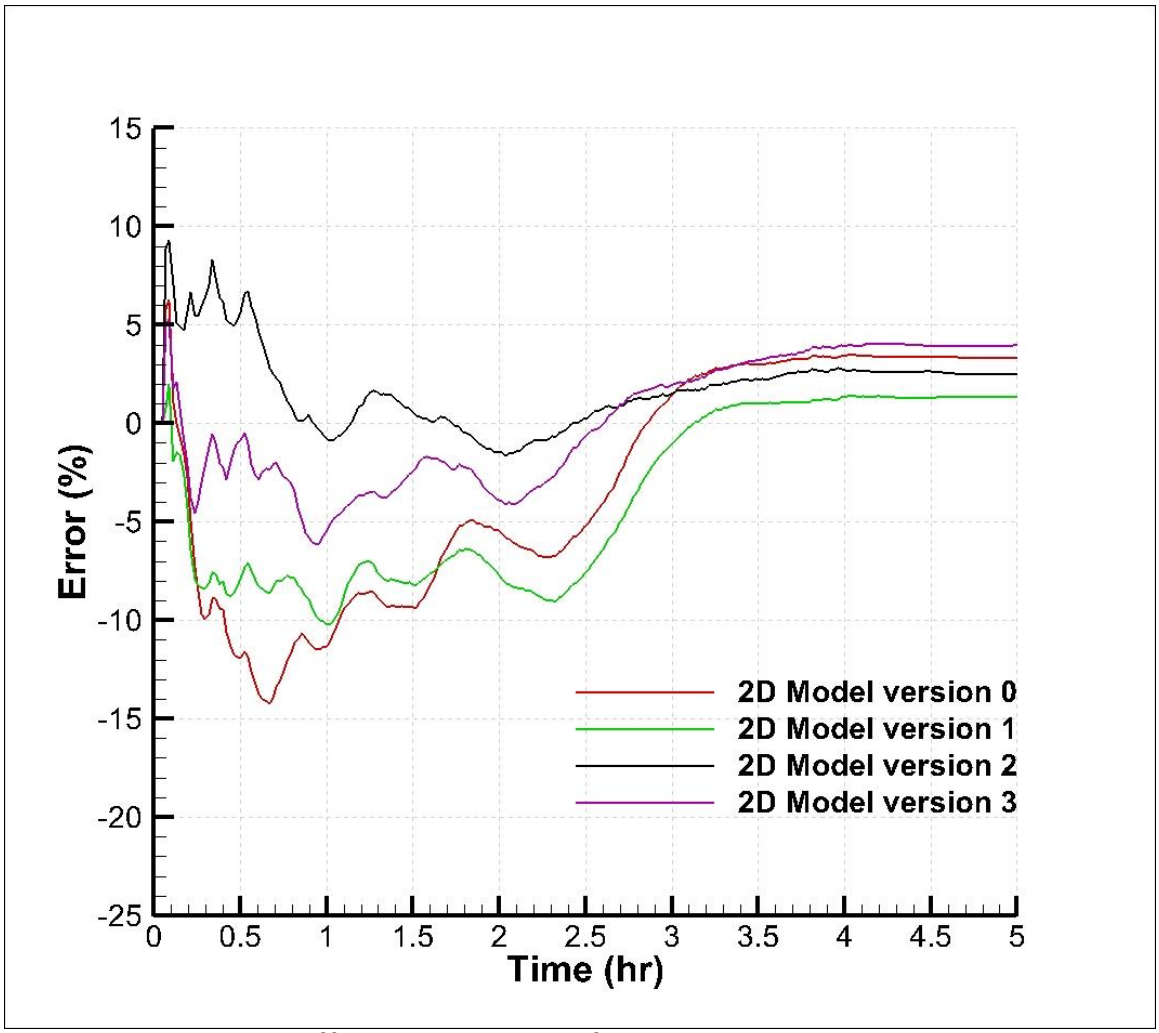

Figure 6.7 Percentage difference between the flood inundation extent predicted by the 2-D simulations with respect to the 3-D simulation predictions. Results are shown for the 2-D model-version 0 (red line), 2-D model-version 1 (green line), 2-D model-version 2 (black line) and 2-D model-version 3 (purple line). The error is calculated with respect to the 3-D model predictions.

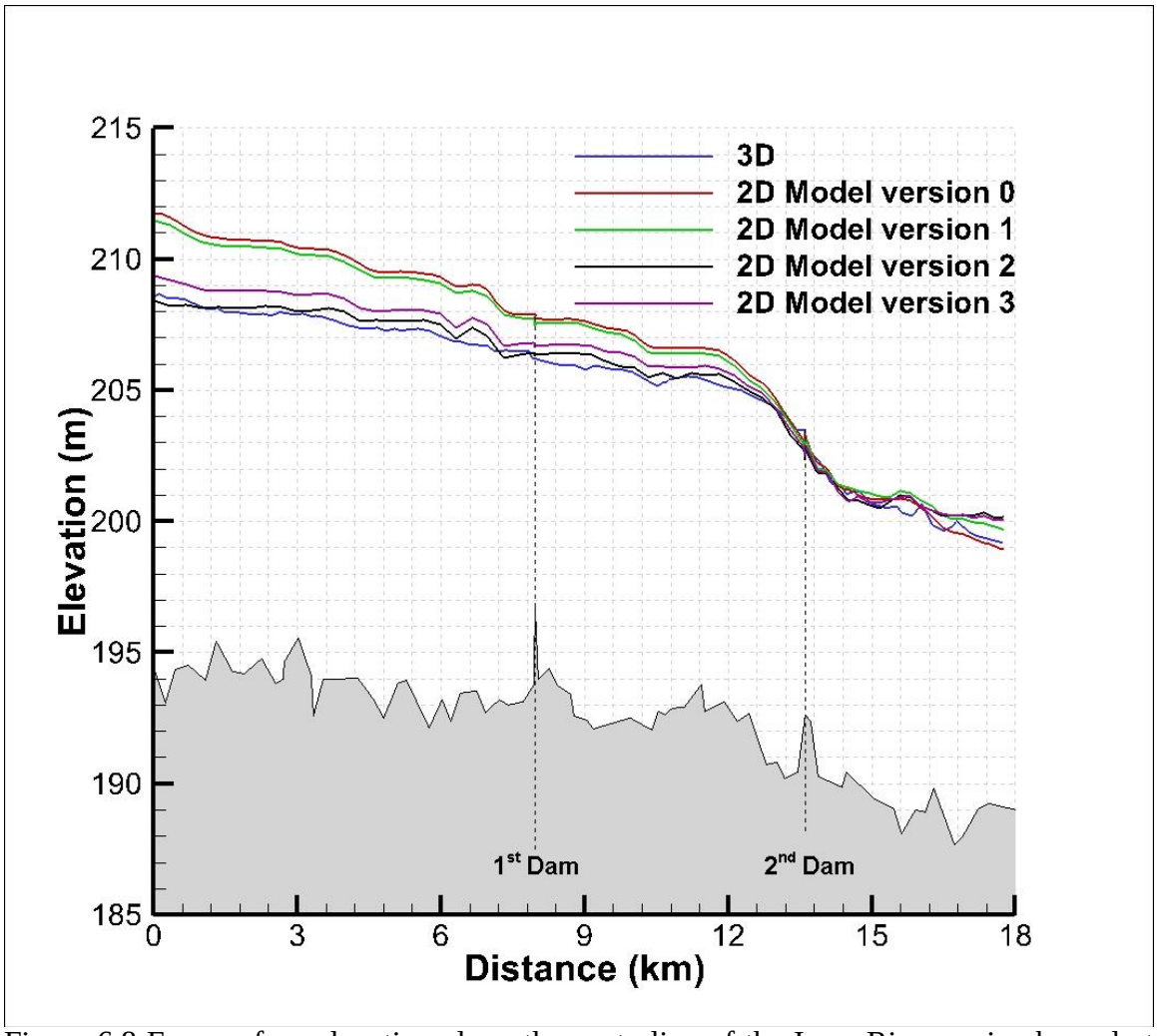

Figure 6.8 Free-surface elevation along the centerline of the Iowa River main channel at peak flood extent. Comparison between predictions given by the 3-D model (blue line), 2-D model-version 0 (red line), 2-D model-version 1 (green line), 2-D model-version 2 (black line), and 2-D model-version 3 (purple line).

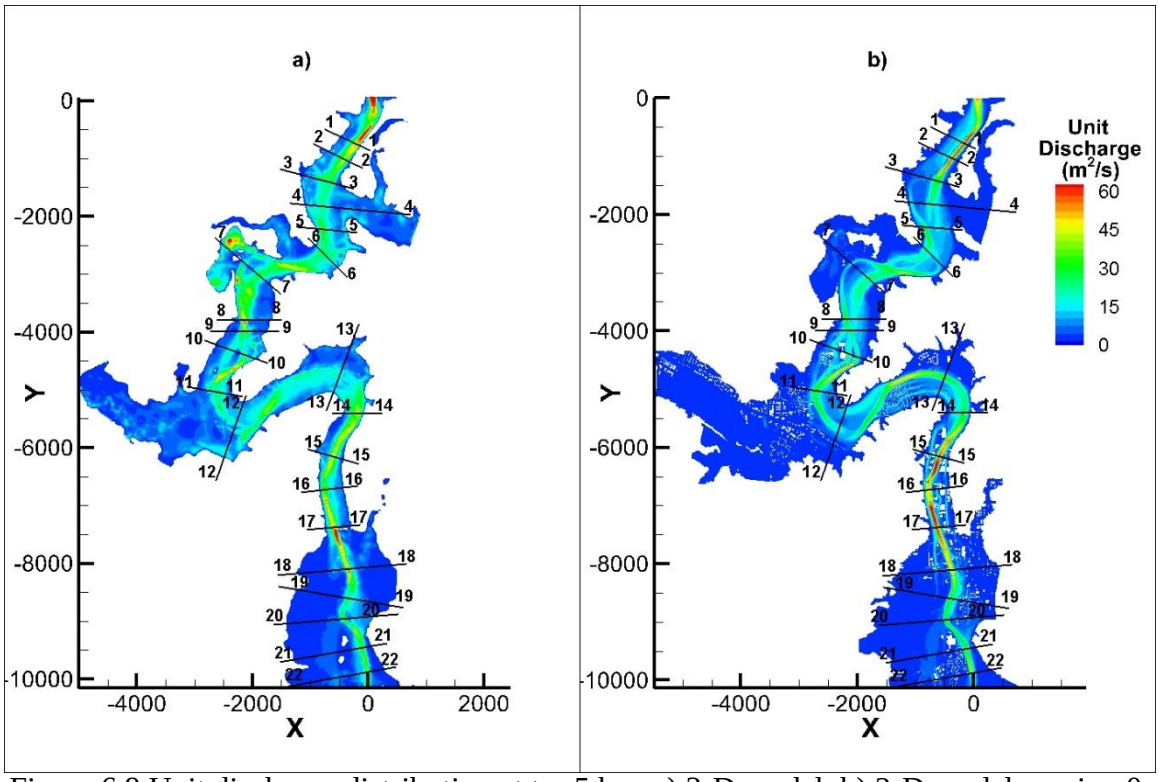

Figure 6.9 Unit discharge distribution at t = 5 hrs. a) 3-D model; b) 2-D model-version 0.

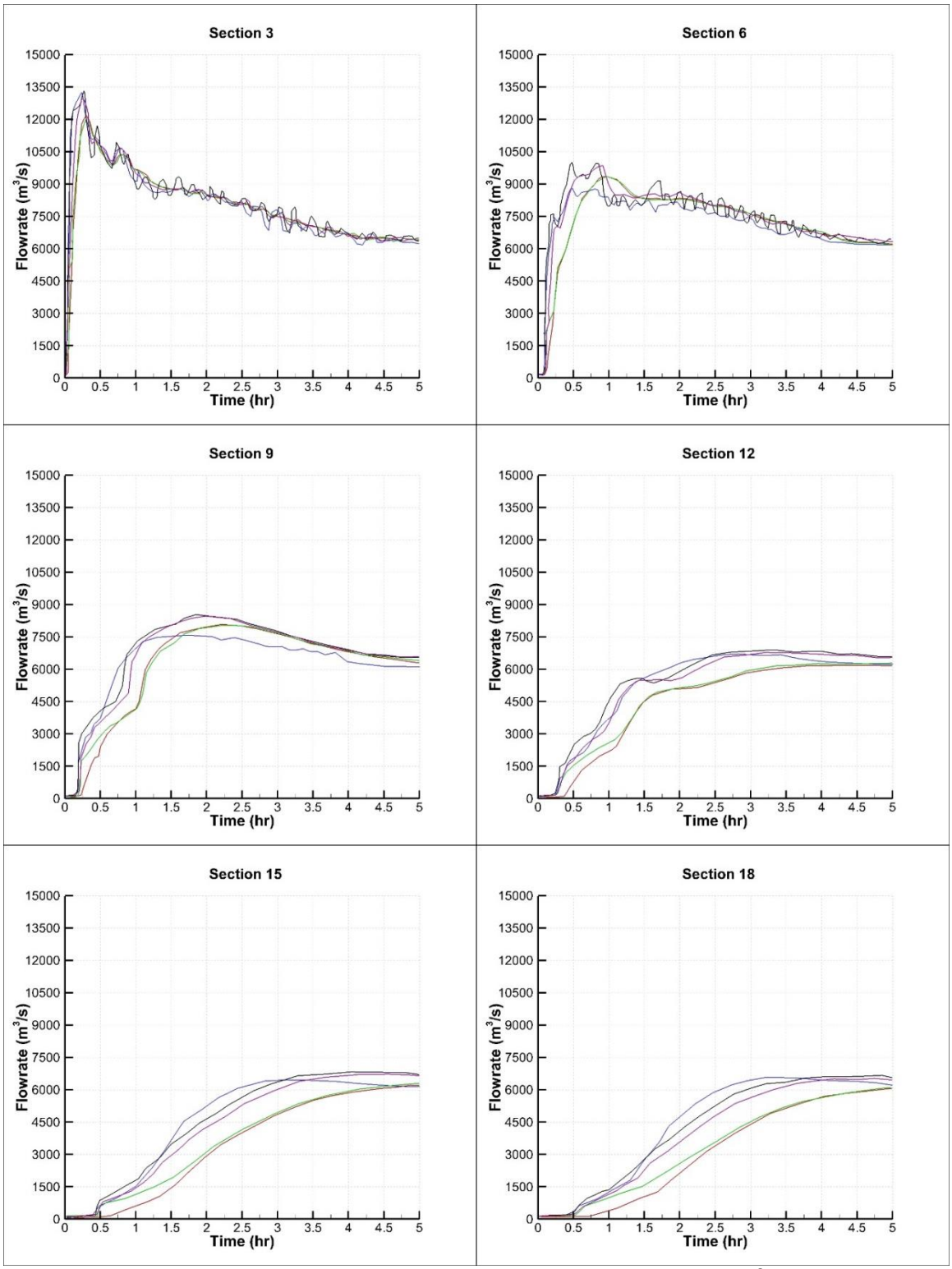

Figure 6.10 Hydrograph at representative cross sections. The positions of the cross sections are shown in Figure 6.9. Results are shown for the 3-D model (blue line), 2-D model-version 0 (red line), 2-D model-version 1 (green line), 2-D model-version 2 (black line) and 2-D model-version 3 (purple line).

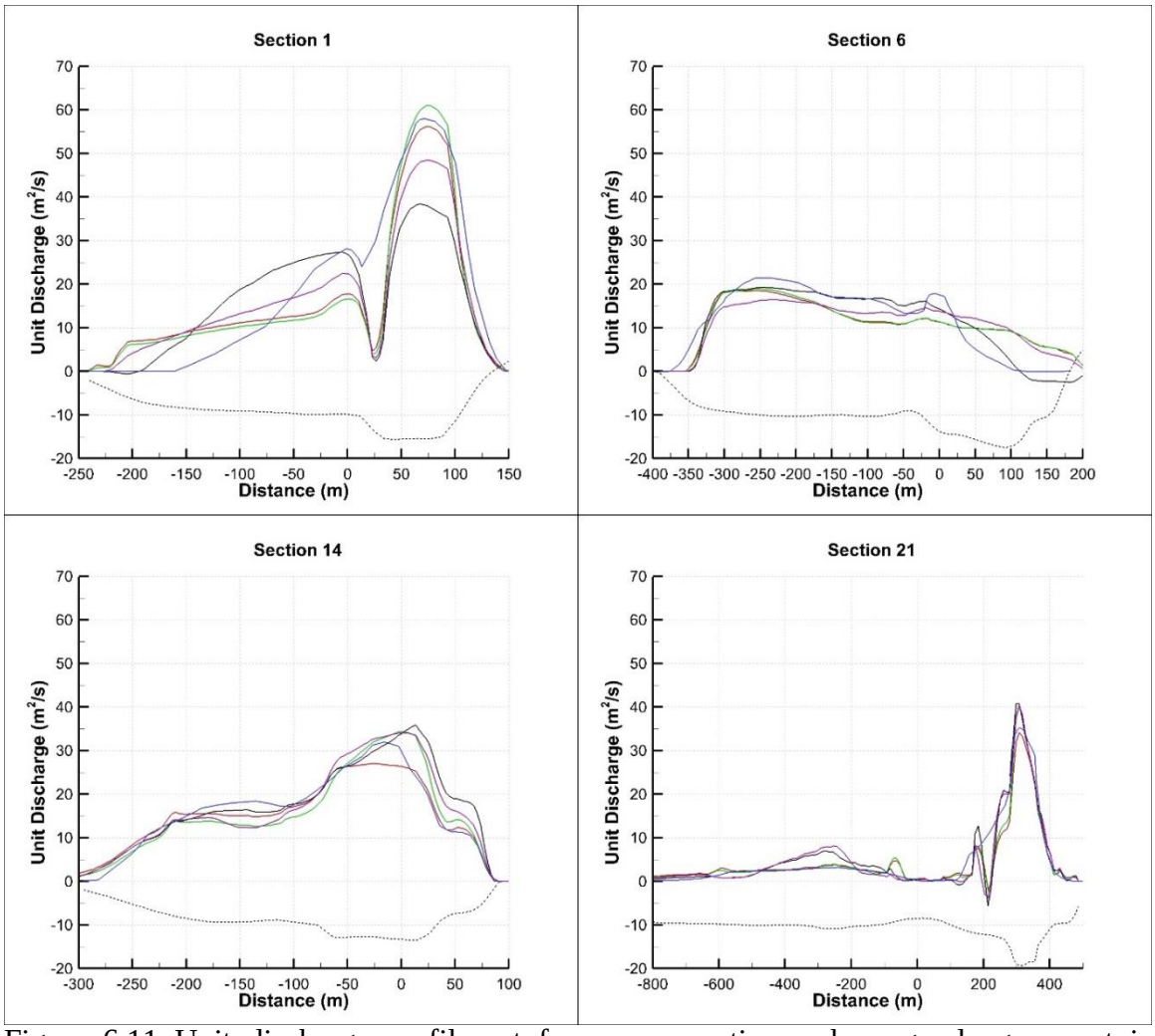

Figure 6.11 Unit discharge profiles at four cross sections where good agreement is observed between the predictions given by the 3-D model (blue line) and the 2-D model-version 0 (red line). Additionally, results obtained using the 2-D model-version 1 (green lines), 2-D model-version 2 (solid black lines) and 2-D model-version 3 (purple lines) are shown. The dashed black lines show the bathymetry in the cross section.

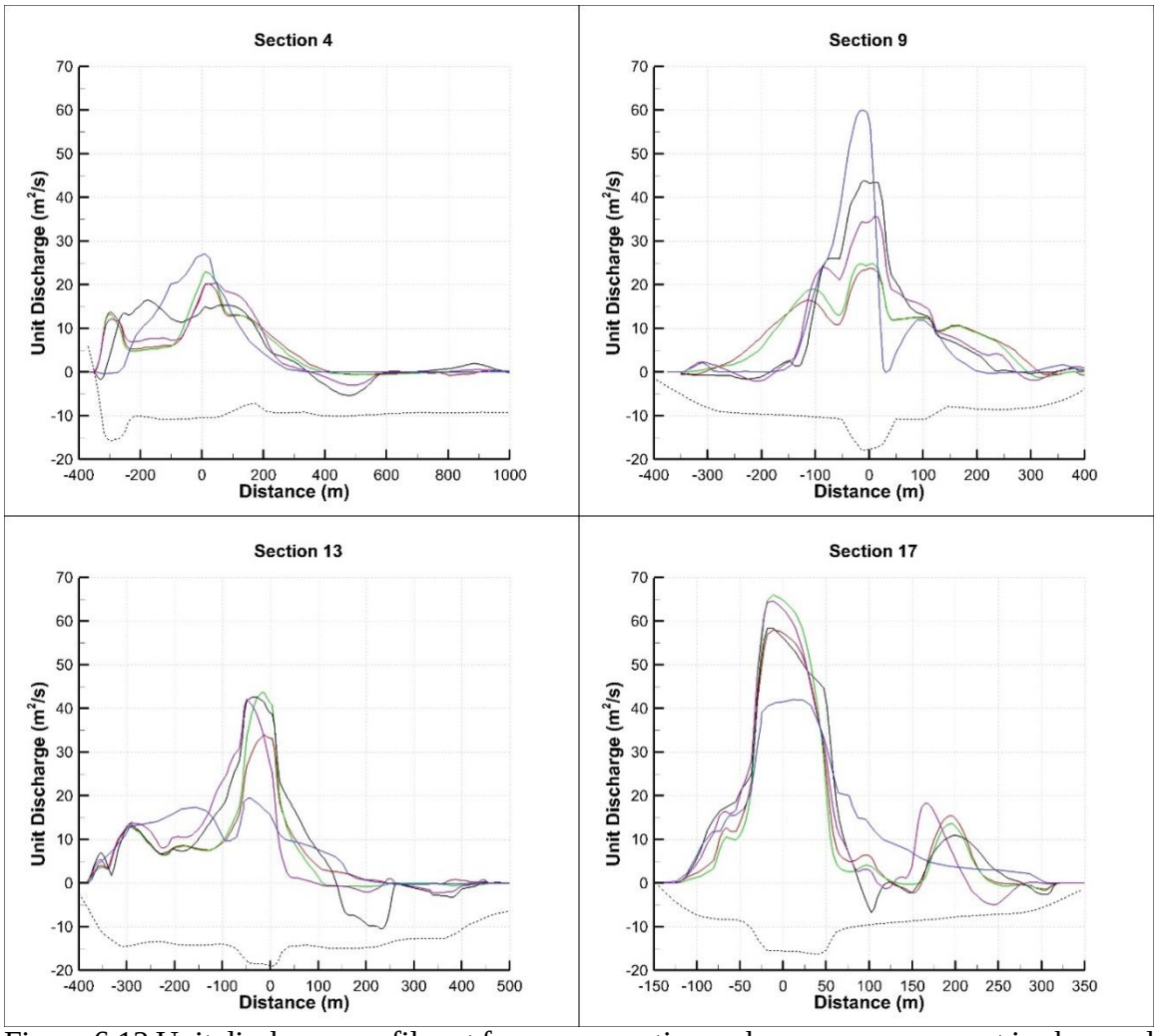

Figure 6.12 Unit discharge profiles at four cross sections where poor agreement is observed between the predictions of the 3-D model (blue lines) and the 2-D model-version 0 (red lines). Additionally, results obtained using the 2-D model-version 1 (green lines), 2-D model-version 2 (black lines) and 2-D model-version 3 (purple lines) are shown. The dashed black lines show the bathymetry in the cross section.

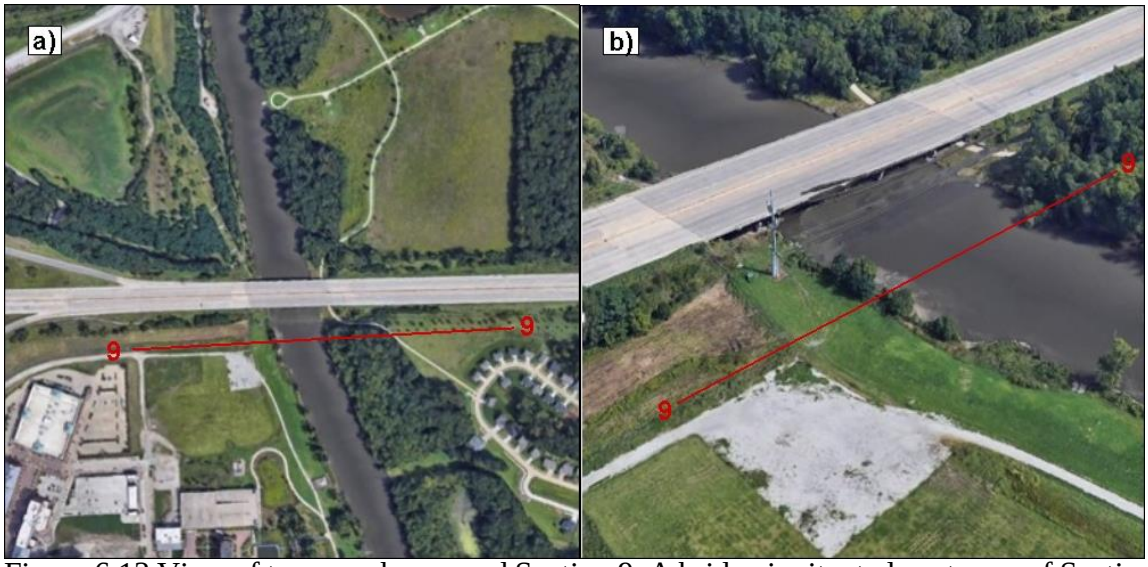

Figure 6.13 View of topography around Section 9. A bridge is situated upstream of Section 9. The two pictures are taken from different directions.

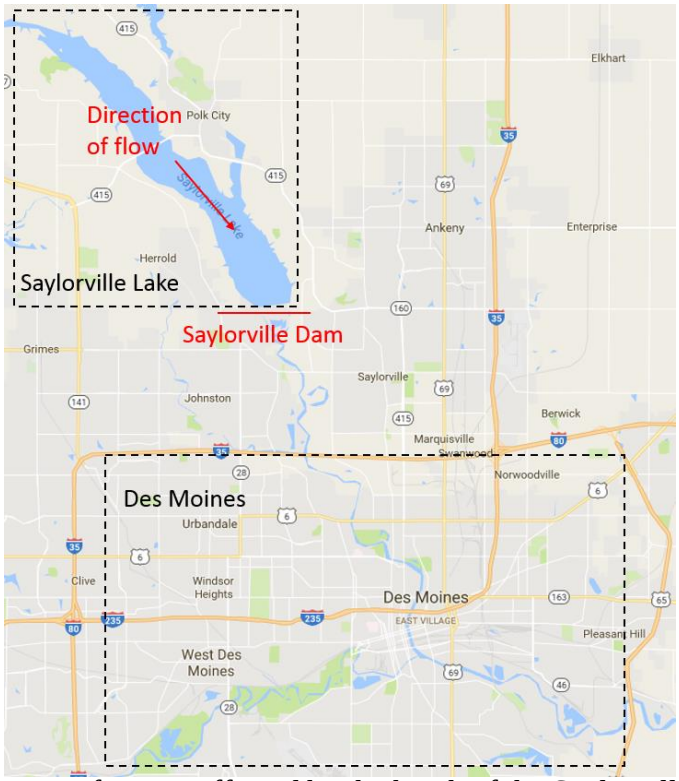

Figure 6.14 Aerial view of region affected by the break of the Saylorville Dam. The region includes the Saylorville Lake and the City of Des Moines.

Figure 6.15 Close-up view of the Saylorville Dam.

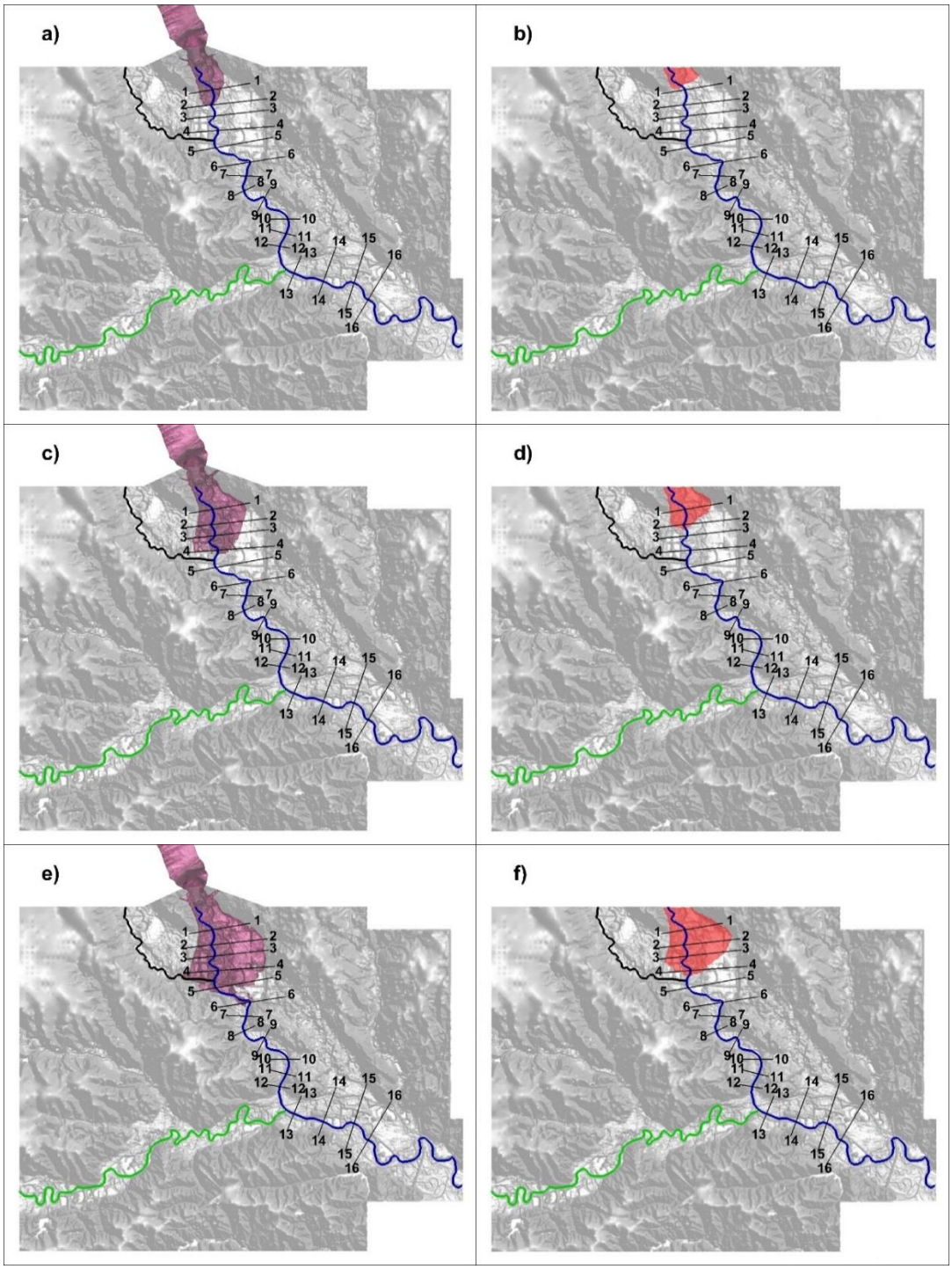
a)
b)
c)
d)
e)
f)

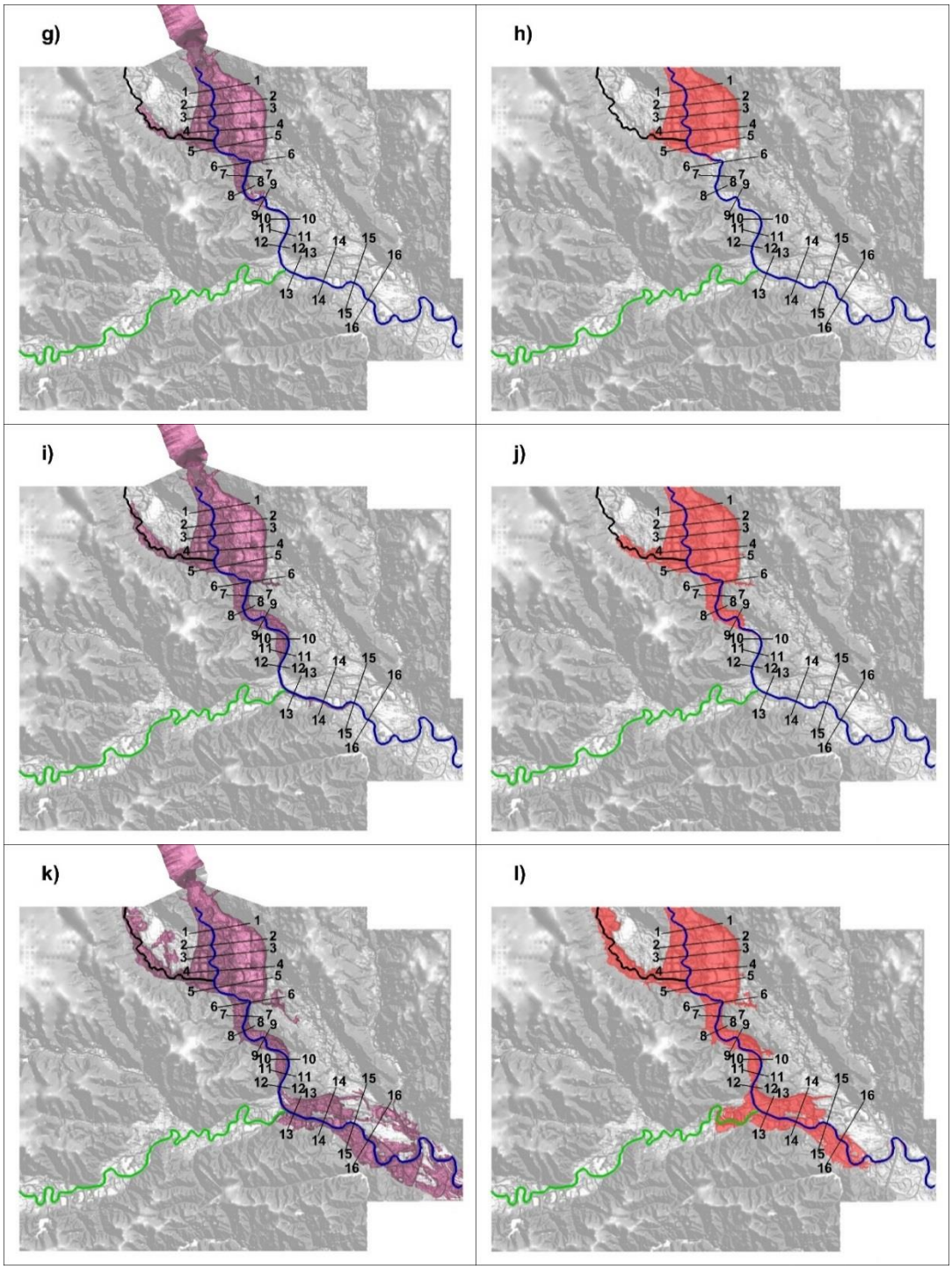

Figure 6.16 Temporal evolution of flood inundation extent. Results are shown at 6 different times after the collapse of the Saylorville Dam. a) 3-D model, t = 250 s; b) 2-D model, t = 250 s; c) 3-D model, t = 500 s; d) 2-D model, t = 500 s; e) 3-D model, t = 1000 s; f) 2-D model, t = 1000 s; g) 3-D model, t = 2000 s; h) 2-D model, t = 2000 s; i) 3-D model, t = 4000 s; j) 2-D model, t = 4000 s; k) 3-D model, t = 13500 s; l) 2-D model, t = 13500 s. The Des Moines River, Beaver Creek and the Raccoon River are shown in blue, black and green, respectively.

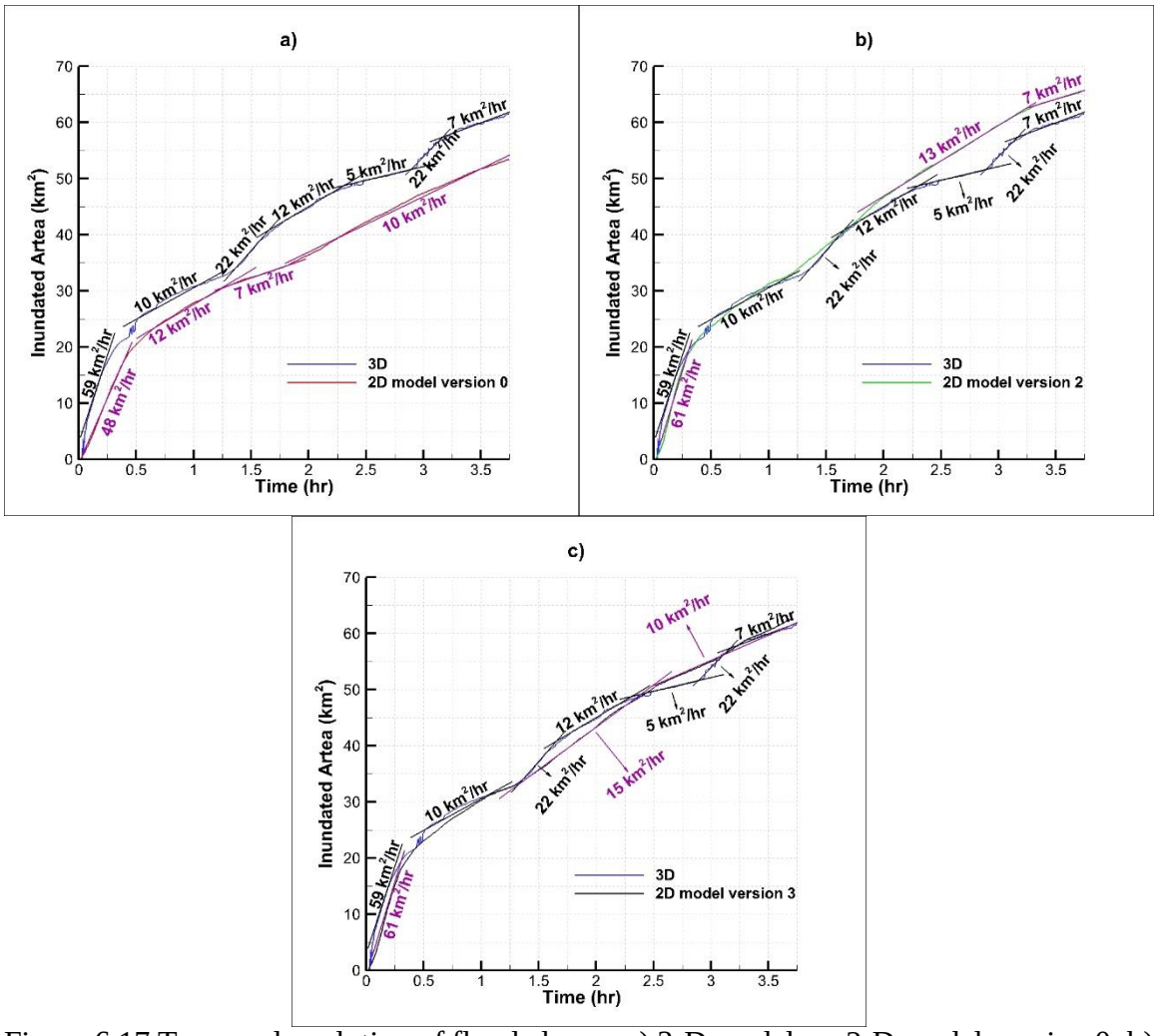

Figure 6.17 Temporal evolution of flooded area. a) 3-D model vs. 2-D model-version 0; b) 3-D model vs. 2-D model-version 2; c) 3-D model vs. 2-D model-version 3.

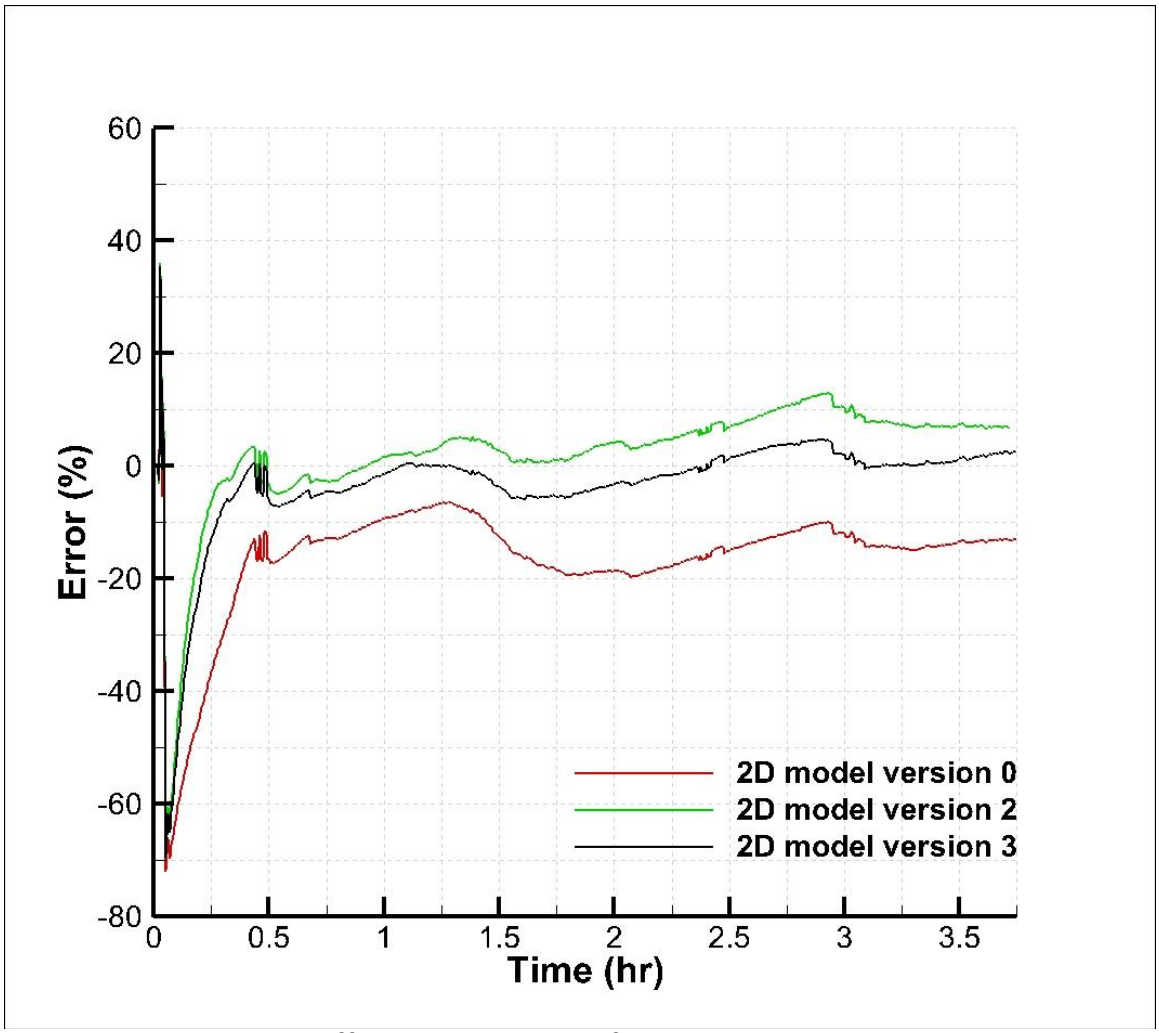

Figure 6.18 Percentage difference between the flood inundation extent predicted by the 2-D simulations with respect to the 3-D simulation predictions. Results are shown for the 2-D model-version 0 (red line), 2-D model-version 2 (green line) and 2-D model-version 3 (black line).

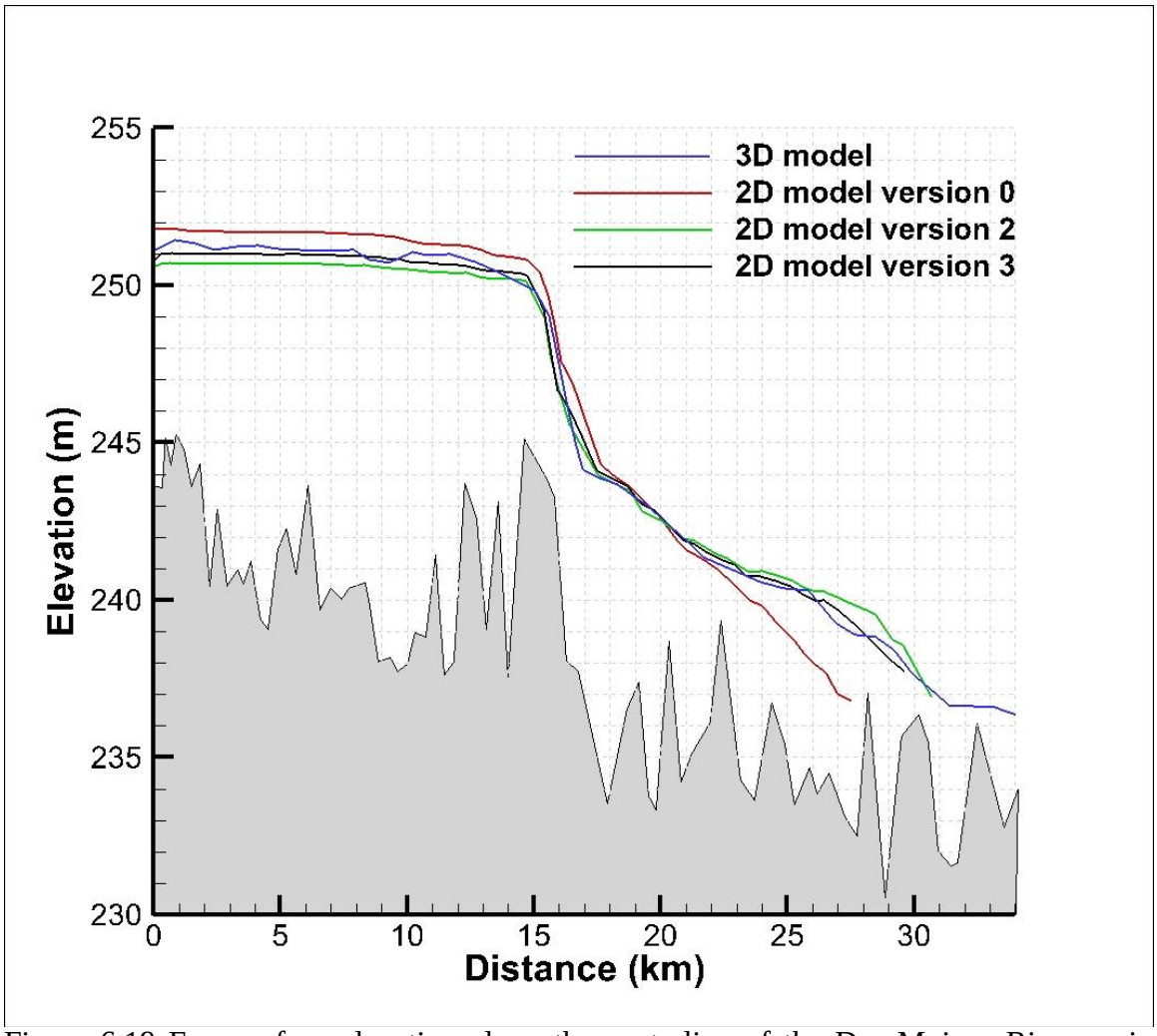

Figure 6.19 Free-surface elevation along the centerline of the Des Moines River main channel at t=3.75 hrs. Comparison between predictions given by the 3-D model (blue line), 2-D model-version 0 (red line), 2-D model-version 2 (green line) and 2-D model-version 3 (black line).

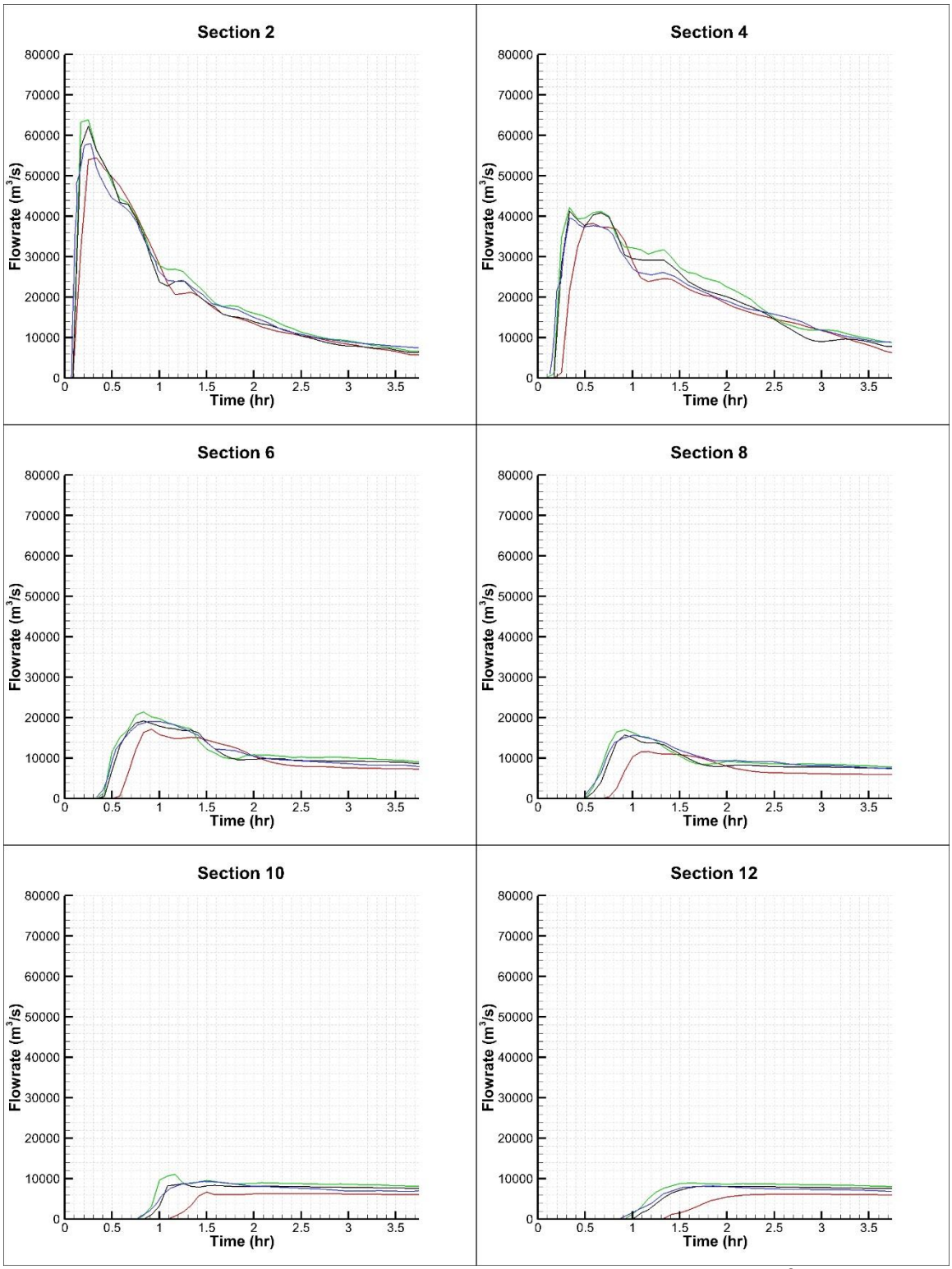

Figure 6.20 Hydrograph at representative cross sections. The positions of cross sections are shown in Figure 6.16. Results are shown for the 3-D model (blue line), 2-D model-version 0 (red line), 2-D model-version 2 (green line) and 2-D model-version 3 (black line).

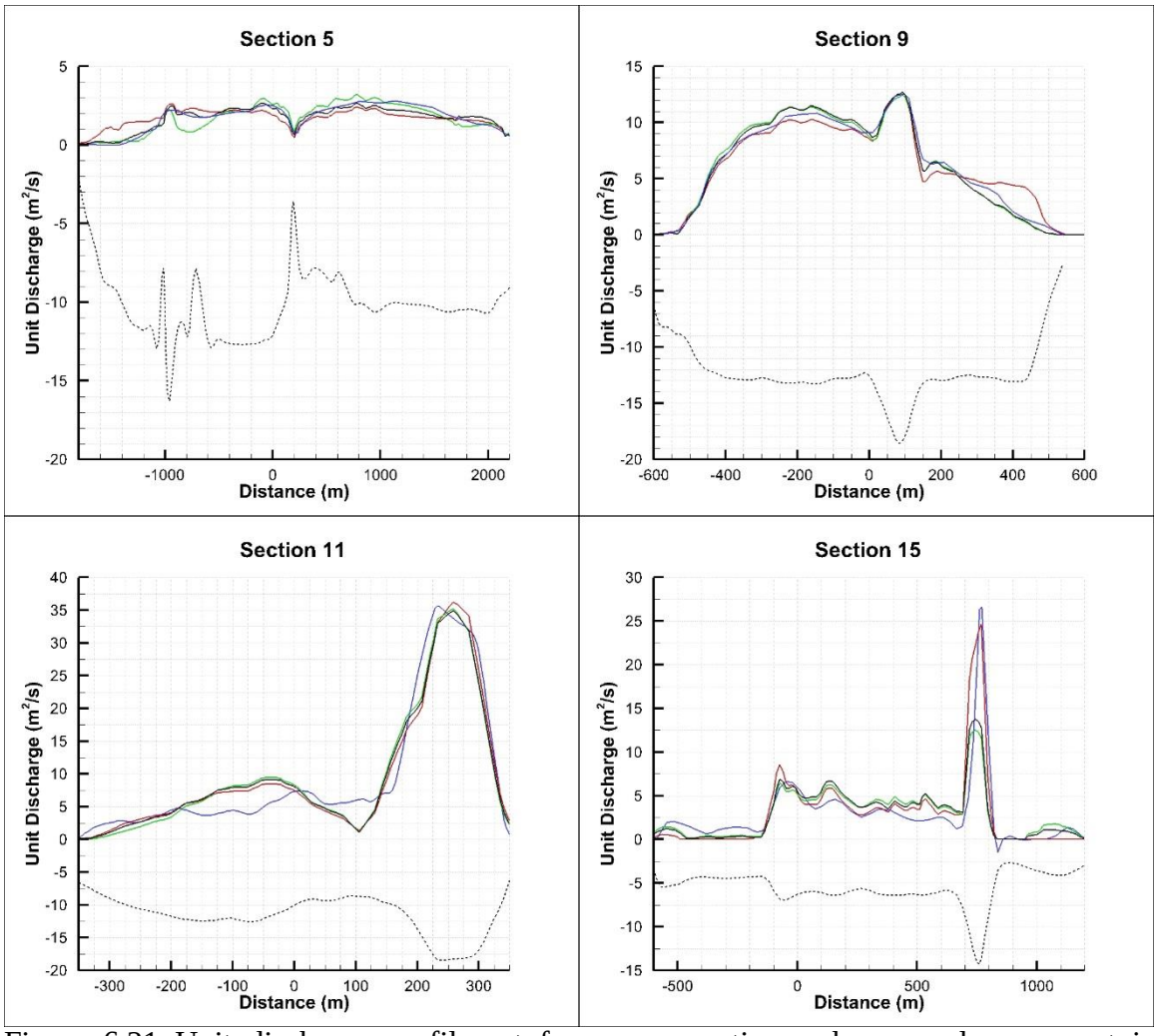

Figure 6.21 Unit discharge profiles at four cross sections where good agreement is observed between the predictions given by the 3-D model (blue line) and 2-D model-version 0 (red line). Additionally, results obtained using the 2-D model-version 2 (green lines) and 2-D model-version 3 (solid black lines) are shown. The dashed black lines show the bathymetry in the cross section.

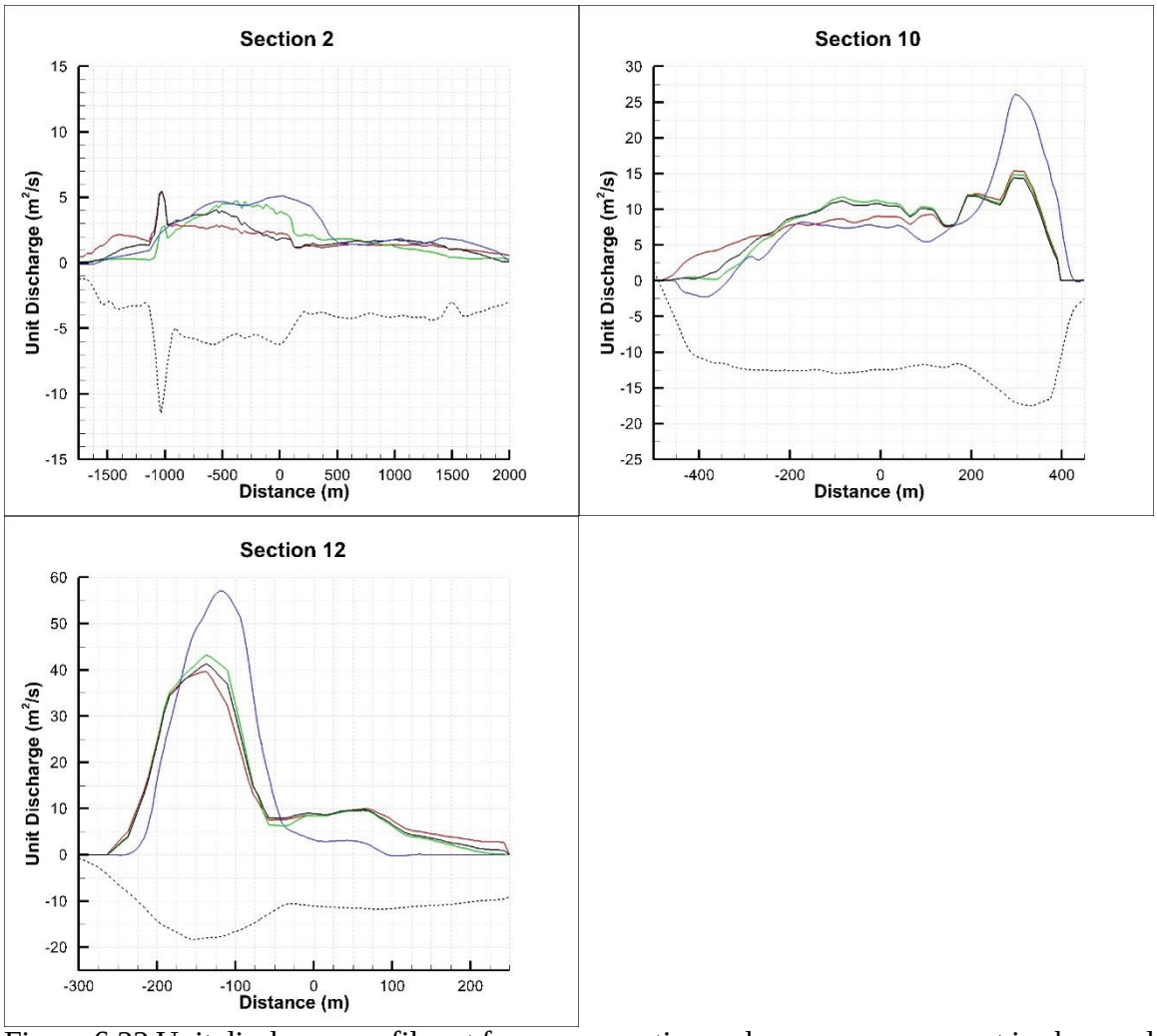

Figure 6.22 Unit discharge profiles at four cross sections where poor agreement is observed between predictions given by the 3-D model (blue line) and 2-D model-version 0 (red line). Additionally, results obtained using the 2-D model-version 2 (green lines) and 2-D model-version 3 (solid black lines) are shown. The dashed black lines show the bathymetry in the cross section.

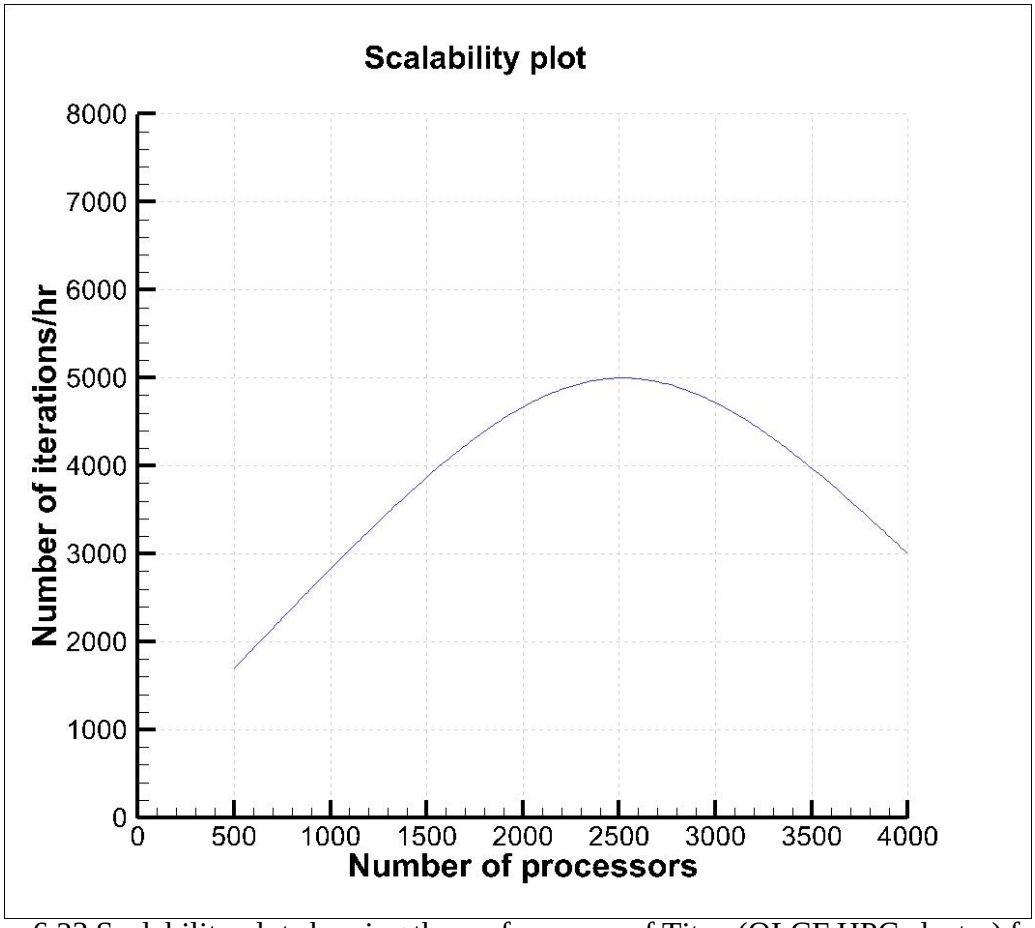

Figure 6.23 Scalability plot showing the performance of Titan (OLCF HPC cluster) for the dam break simulation for the Saylorville Dam test case.

CHAPTER 7 CONCLUDING REMARKS AND FUTURE WORK

A fully 3D RANS non-hydrostatic model with deformable free-surface capabilities was developed within an existing CFD code to simulate flood propagation in natural river environments. This is one of the first applications of time accurate RANS for this type of problems. The study reported in-depth validation of the model followed by its applications for several important classes of applications in river engineering and hydrology (flood propagation in river reaches and over their floodplains, investigation of pressure scour effects when the flow becomes pressurized over part of the domain, floods induced by a dam break). The study also compares the capabilities of the 3-D model with that of standard 2-D depth averaged models routinely used by agencies and research groups to predict flood propagation in natural river environments.

7.1 Concluding remarks

The proposed 3-D URANS model was first validated for several test cases of increasing complexity that tested the different features of the model that are critical to accurately predict flood propagation in natural environments. It was found that the 3-D model was able to reproduce results obtained in the laboratory experiments with a high level accuracy that was as good as or better than that of calibrated 2-D depth-averaged codes. Not surprisingly, the largest differences between 3-D and 2-D model predictions for these cases was observed in regions where 3-D effects (e.g., strong secondary cross-stream currents, strong vertical nonuniformity of the flow in the dominant direction) are expected to be important (e.g., high curvature reaches, near hydraulic structures, near flow expansion/contraction and near main channel/floodplain transition).

Once validated, the 3-D model was used as an engineering tool to aid in deciding on the most effective design to implement a flood protection measure that may be under consideration by the authorities in charge of protecting against flood hazard and flood mitigation. As an example, the effectiveness of placing a number of floodwalls at different

locations and of several dam removal strategies to diminish the negative effects of an incoming flood wave approaching Iowa City were investigated and recommendations were made on what should be the most effective flood protection measure among the ones considered.

One of the possible criticism of using a 3-D models to predict flood propagation in real environments is that such models computationally very expensive and simulations take a very long physical time to complete compared to state-of-the-art calibrated 2-D codes. Though this is a similar criticism to that voiced when the transition was made 10-20 years ago from using 1-D models to using 2-D models, it is true that at the present time 3-D models are very expensive compared to 2-D models and they cannot be used to simulate floods occurring over very large domains and long floods (e.g., with a hydrograph of the order of 1 months as was the case for the largest floods occurring in the US Midwest). However, the increase in computer power and advances in numerical algorithms will make such simulations possible in the not so far future. Meanwhile, there are several way in which 3-D simulations that are already feasible today can provide critical information for improving our flood modeling capabilities, despite the afore mentioned limitations in terms of the time and domain size that can be simulated for field scale applications.

For example, such simulations can be used as a numerical experiment based on which the predictive capabilities of lower order (2-D and 1-D) models can be assessed. This is important, given that even test cases of flood propagation in the laboratory generally provide only a limited amount of data for validation. Data obtained from observations of floods occurring in real environments is even scarcer because of the hazard associated with collecting data during the floods. 3-D numerical simulations can be depth averaged, thus providing a full data set for validation and eventual recalibration of lower order model. Several examples were given in the present study. Another possible use of 3-D simulations is in the framework of a hybrid 2D-3D or even 1D-2D-3D approach to simulate floods in natural environments where higher order models are used over smaller regions where the

flow is more complex. Such approaches are already used in flood modeling in many commercial codes where one can build a 1-D model of the whole domain but then switch to a 2-D model in regions where the accuracy of the 1-D model is expected to be insufficient. Based on the results of the present study, one can argue that a 3-D model should be used in dam break flows around the hydraulic structure that fails (dam, levee, etc), given that the flow is strongly three dimensional and the flow accelerations are very high. Downstream of that region one can switch to a 2-D model.

Maybe the strongest argument in using 3-D non-hydrostatic models is related to problems where the flow locally changes regime during the flood event (e.g., around locations where bridges, culverts or other hydraulic structures that limit the vertical expansion of the flow as the discharge increases are present). Once the flow becomes pressurized, a 2-D model is of no use. The problem is not only that around the region where the flow is becoming pressurized the predictions of 2-D models will be wrong, but that the failure to account for the changes in the flow around those regions may result in large errors in prediction of the flow event over large parts or most of the domain that is simulated. An important class of problems for river engineering where a change in the flow regime occurs is related to applications where pressure scour effects are present. Pressure scour can be a main contributor to local scour in rivers. Given that most of the scour around hydraulic structures (e.g., bridge piers, abutments) occurs during flood events, more precisely during the times when the flowrate is close to its peak values), accurate quantification of scour requires as a prerequisite being able to estimate the bed shear stresses around the hydraulic structure during the flooding event, including at times when the flow around the structure is pressurized. Using a 3-D model is the only way to obtain this critical information.

The present study included a test case where the flow became pressurized close to the location of a bridge at close to peak flow conditions when the bridge deck becomes submerged. Besides estimating the increase in the erosive potential of the flow during the time the flow becomes pressurized (once that happens the velocity profile is not anymore

logarithmic along the vertical direction, a main assumption in any 2-D or 1-D model), it was also possible to isolate the effects of pressure scour on the erosive capability of the flow by conducting simulations with and without the bridge present and calculating the maximum erosion that can occur locally in the two cases. In a good approximation, the difference can be attributed to pressure scour effects. Another issue that these series of 3-D simulations allowed investigating are hysteresis effects on the bed shear stress. While, hysteresis effects in the relationship between the stage and the discharge during flood propagation in open channels are well known and received lots of attention, the present study showed that such effects are also present in the relationship between the bed shear stress and the discharge. Moreover, significant hysteresis effects can be observed for the bed shear stress even for cases when hysteresis effects are close to negligible in the stage-discharge relationship. Given that estimation of the erosive capability of the flow during floods relays on accurate estimation of the bed shear stress that is the main variable controlling the flux of entrained sediment, accounting for hysteresis effects in the bed shear stress-discharge relationship is critical for being able to predict erosion induced by the passage of a flood wave over an erodible boundary.

The present 3-D model was also successfully applied to predict flood wave propagation induced by the sudden failure of two dams situated in the vicinity of two cities in the state of Iowa. 2-D simulations of the same dam-break events were found to underestimate the speed of the wave both in terms of flooding extent and flowrates as a function of time and to overestimate the free-surface elevation compared to the 3-D simulation. These findings are consistent with those of other studies reported in the literature where 2-D models underestimated the speed of propagation of the flood wave. In the test cases investigated in this study, this happened even if the computational domain used in the 2-D simulation did not contain the dam and its immediate vicinity, where 3-D effects are expected to be important, and the hydrograph specified at the inlet of the computational domain was taken from the corresponding 3-D simulations that included the

lake and the dam. Using the 3-D results, a methodology was proposed to recalibrate the Manning coefficients used to specify roughness in 2-D simulations such that the 2-D predictions can become closer to the 3-D simulation results.

7.2 Future work

As already mentioned, the main challenge of using 3-D models for routine predictions of flood propagation in natural systems is the associated computational cost and resources required to perform the needed simulations. Besides improvements in hardware which results in a speed up of the code, new developments in numerical schemes, code parallelization algorithms should result in a significant increase of their computational efficiency. The success of the 3-D simulations presented in this study to simulate flooding phenomena occurring in idealized and natural environments was due in great part to being able to generate a high quality mesh in critical parts of the domain. This process was very time consuming and required advanced skills in mesh generation. Though most CFD solvers offer automatic mesh generation options, these algorithms are not sufficiently adapted to be used for problems involving flooding over natural terrain. As such, improvement in numerical algorithms to solve the URANS equations with free-surface tracking algorithms on parallel computing platforms and automatic mesh generation should make the object of future research.

In all the simulations performed in this study the bathymetry was assumed to be fixed and not to evolve during the simulation. Most flood events take place over erodible boundaries. Moreover, most of the erosion of the bed occurs during the flood events when the discharge is much larger than the one observed under normal flow conditions. This is especially true around hydraulic structures present in the rivers, where most of the local scour and in some cases pressure scour take place during the times the times high flow conditions are observed in the river channel. As such, future research should be directed toward conducting 3-D numerical simulations with sediment transport that can capture the

bed morphology changes induced during the flood. Future research should also try to quantify the effect of hysteresis on sediment entrainment from the bed and the errors made when hysteresis effects are ignored in more simplified approaches that try to estimate sediment entrainment in river reaches. Such simulations where besides the bridge deck the bridge piers and abutments are included in the computational domain should allow direct estimation of scour induced by the passage of the flood wave in waterways containing bridges.

Development of nested and hybrid modeling approaches integrating 1-D, 2-D and 3-D modeling approaches in various parts of the computational domain should be a main direction for future research in flood modeling and in particular in problems including failure of hydraulic structures that generate a flood wave whose evolution (e.g., dam break, levee breach), at least during its initial stages is subject to strong 3-D effects. The developed model can be easily used to simulate floods induced by levee breach. Such events are known to generate even more significant 3-D effects, as the wave flood propagation direction is generally not perpendicular to the levee. Predictions using 3-D models should be much more accurate than those obtained using 2-D models for this important class of problems. Development of strategies to recalibrate 2-D and 1-D models based on 3-D simulations should also result in more accurate predictions using the lower order models. This can be achieved by performing a systematic series of dam/levee break simulations by changing a defined set of parameters, such as curvature of the downstream channel, ratio between floodplain/main channel widths, width/depth ratio and/or roughness parameters. Such results can then be extrapolated to hypothetical realistic dam/levee break scenarios.

REFERENCES

Balabel, A. (2015). "Numerical Simulation of Turbulent Dam-Break Flow Using the Level Set Method." *International Journal of Modern Physics and Applications,* 1 (3), 112-117

Bates, P.D. and De Roo, A.P.J. (2000). "A simple raster-based model for flood inundation simulation." *Journal of Hydrology,* 236, 54-77

Bates, P., Trigg, M., Neal, J., and Dabrowa, A. (2013) "LISFLOOD-FP User Manual, code release 5.9.6"

Benjamin, T. B. (1968). "Gravity currents and related phenomena." *Journal of Fluid Mechanics,* 31 (2), 209-248

Biscarini, C., Di Francesco, S., and Manciola, P. (2010). "CFD modelling approach for dam break flow studies." *Hydrology and Earth System Sciences,* 14, 705-718

Biscarini, C., Di Francesco, S., Rifoldi, E., and Manciola, P. (2016). "On The Simulation of Floods in a Narrow Bending Valley: The Malpasset Dam Break Case Study." *Water,* 8, 545

Blanckaert, K. (2002). "Secondary currents measured in sharp open-channel bends." *Proceedings River Flows Conference,* Louvain, Belgium (Bousmar, D. and Zech, Y. eds), Vol. 1, 117-125. Balkema.

Brooks, N. (1963) "Discussion of boundary shear stresses in curved trapezoidal channels." *Journal of Hydraulic Division of American Society of Civil Engineering,* 89(3), 327-333

CADAM 2000. Concerted action on dambreak modeling. Final Report SR 571, HR Wallingford UK.

Carrica, P.M., Wilson, R.V. and Stern, F. (2007). "An Unsteady Single-Phase Level Set Method for Viscous Free SurfaceFlows." *International Journal for Numerical Methods in Fluids,* 53, 229-256

Casas, A., Benito, G., Thorndycraft, V.R., and Rico, M. (2006). "The topographic data source of digital terrain models as a key element in the accuracy of hydraulic flood modelling." *Eartch Surface Processes and Landforms,* 31, 444-456

Caviedes-Voullieme, D., Morales-Hernandez, M., Juez, C., Lacasta, A., and Garcia-Navarro, P. (2017). "Two-dimensional Numerical Simulation of Bed-Load Transport of a Finite-Depth Sediment Layer: Applications to Channel Flushing." *Journal of Hydraulic Engineering,* 143(9), 04017034-1 – 04017034-16

Chen, H.C., and Yu, K. (2009) "CFD simulations of wave-current body interactions including greenwater and wet deck slamming." *Advances in Computational Fluid Dynamics,* 35 (5), 970-980

Choi, S.U., and Paik, J. (2001). "Performance test of high resolution schemes for 1D dam break problem." *KSCE Journal of Civil Engineering,* 5 (3), 273-280

Dalrymple, R. A., and Rogers, B. D. (2006). "Numerical modeling of water waves with the SPH method." *Coastal Engineering,* 53, 141-147

De Maio, A., Savi, F. and Sclafani, L. (2004). "Three-dimensional Mathematical simulation of Dambreak Flow." *Proceeding of IASTED conferences - Environmental Modelling and Simulation.* St. Thomas, US Virgin Island.

DHI (Danish Hydraulic Institute) (2007). "MIKE FLOOD. 1D-2D Modelling User Manual"

DHI (Danish Hydraulic Institute) (2009a). "Mike 11. A modelling System for Rivers and Channels Reference Manual"

DHI (Danish Hydraulic Institute) (2009b). "Mike 21. User Manual Reference Guide"

DHI (Danish Hydraulic Institute) (2011). "MIKE SHE User Manual Volume 2: Reference Guide"

Dhondia, J.F., and Stelling, G.S. (2002), "Application of One Dimensional – Two Dimensional Integrated Hydraulic Model for Flood Simulation and Damage Assessment." *Hydroinformatics,* 1-12

Dottori, F., Martina, M. L. V., and Todini, E. (2009). "A dynamic rating curve approach to indirect discharge measurement." *Hydrology and Earth System Sciences,* 13, 847-863

DuBoys, P. (1879). "The Rhone and Streams with Moveable Beds," *Annales des ponts at chausses,* Section 5, Vol. 18, 141-195

Einstein, H. (1950). "The bed-load function for sediment transportation in open channel flows." Washington, DC: United States Department of Agriculture. Soil Conservation Service.

Endreny, T., Lautz, L. and Siegel, D. I. (2011) "Hyporheic flow path response to hydraulic jumps at river steps: Flume and hydrodynamic models." *Water Resources Research,* 47

Fennema, R. J. and Chaudhry, M. H. (1990). "Explicit methods for two-dimensional transient free-surface flows." *Journal of Hydraulic Engineering,* 116 (8), 1013-1034

Ferrand, M., Laurence, D., Rogers, B. Violeau, D. and Kassiotis, C. (2013). "Unified semi-analytical wall boundary conditions for inviscid, laminar or turbulent flows in the meshless SPH method." *International Journal for Numerical Methods in Fluids,* 71, 476-504

Floryan, J.M., and Rasmussen, H. (1989) "Numerical Methods for viscous flows with moving boundaries." *Applied Mechanics Reviews,* 42 (12), 323-341

Frank, E.A., Ostan, A., Coccato, M., and Stelling, G.S. (2001). "Use of an integrated one-dimensional/two-dimensional hydraulic modeling approach for flood hazard and risk mapping." *River Basin Management* by R.A., Falconer and W.R. Blain, 99-208. Southhampton, UK: WIT Press, 2001

Fu, X. L., Li, D. M. and Jin, G. Y. (2007). "Calculation of flow field and analysis of spawning sites for Chinese sturgeon in the downstream of Gezhouba Dam." *Journal of Hydrodynamics,* 19 (10), 78-83

Garcia, M. (1999). "Sedimentation and Erosion Hydraulics." *Hydraulic Design Handbook*

Gomez-Gesteira, M., Cerqueiro, D., Crespo, C. and Dalrymple, R. A. (2005). "Green water overtopping analyzed with a SPH model." *Ocean Engineering,* 32, 223-238

Hervouet, J.-M. (2000). "A high resolution 2-D dam-break model using parallelization." *Hydrological Processes,* 13, 2211-2230

Hirt, C.W., Cook, J. L. and Butler, T.D. (1970). "A Lagrangian method for calculating the dynamics of an incompressible fluid with free surface." *Journal of Computational Physics*, 5, 103-124

Hirt, C.W., Amsdem, A. A., and Cook, J. L. (1974). "An arbitrary Lagrangian-Eularian computing method for all speeds." *Journal of Computational Physics,*14, 227-253

Hirt, C. W. and Nichols, B. D. (1981). "Volume of fluid (VOF) methods for the dynamics of free boundaries." *Journal of Computational Physics*, 39, 201-225

Holly, F. M., and Rahuel, J. L. (1990) "New numerical/physical framework for mobile-bed modeling. Part I." *Journal of Hydraulic Research,* 28(4), 401-416

Horrit, M.S., and Bates, P.D. (2002). "Evaluation of 1-D and 2-D numerical models for predicting river flood inundation." *Journal of Hydrology,* 268, 87-89

Hunter, N.M., Bates, P.D., Horritt, M.S., and Wilson, M.D. (2007). "Simple spatially-distributed models for predicting flood inundation: A review." *Geomorphology,* 90, 208-225

Juez, C., Soares-Frazao, S., Murillo, J., and Garcia-Navarro, P. (2017). "Experimental and numerical simulation of bed load transport over steep slopes." *Journal of Hydraulic Engineering,* 55:4, 455-469.

Kalinske, A. A. (1947). "Movement of sediment as bed load in rivers." *Transactions of American Geophysical Union.* 28, 615-620.

Kelecey, F. J. and Pletcher, R. H. (1997). "The development of a free surface capturing approach for multidimensional free surface flows in closed containers." *Journal of Computational Physics,* 138, 939-980

Kang, S., Lightbody, A., Hill, C. and Sotiropoulos, F. (2011). "High-resolution numerical simulation of turbulence in natural waterways." *Advances in Water Resources,* 34 (1), 98-113

Kang, S. and Sotiropoulos, F. (2012). "Numerical modeling of 3D turbulent free surface flow in natural waterways." *Advances in water resources,* 40, 23-36

Kao, H. M., and Chang, T. J. (2012). "Numerical modeling of dambreak-induced flood and inundation using smoothed particle hydrodynamics." *Journal of Hydrology,* 448, 232-244

Kovacs, A. and Parker, G. (1994). "A new vectorial bedload formulation and its application to the time evolution of straight river channels." *Journal of Fluid Mechanics,* 267, 153-183

Kumcu, S. Y. (2016) "Steady and unsteady pressure scour under bridges at clear-water conditions." *Canadian Journal of Civil Engineering,* 43(4), 334-342

Liang, R., Liao, Z. and Liang, S. (2011). "Solving Dam Break Problem considering wall adhesion." *Microgravity Science Technology,* 23, 49-57

Lucy, L. (1977). "A Numerical approach to the Testing of Fusion Process." *Journal of Astronomy*, 82, 1013-1024

Lyn, D. (2008). "Pressure-Flow Scour: A Reexamination of the HEC-18 Equation." *Journal of Hydraulic Engineering,* 134(7), 1015-1020

Ma, L., Ashworth, P. J., Best, J. L., Elliot, L., Ingham, D. B. and Whitcombe, L. J. (2002). "Computational fluid dynamics and the physical modelling of an upland urban river." *Geomorphology*, 44, 375-391

Mambretti, S., Larcan, E., and De Wrachien, D. (2008). "Theoretical and experimental analysis of debris flow: rheology and two-phase modelling." *Irrigation and Drainage*, 57 (5), 555-570

Martin, J. C. and Moyce, W. J. (1952) "An experimental study of the collapse of lquid columns on a rigid horizontal plate." *Philosophical Transactions of the Royal Society of London. Series A, Mathematical and Physical Sciences,* 244, 312-324

Mays, L. *Water Resources Engineering*, Hoboken, New Jersey, John Wiley & Sons, 2011, Print.

Meselhe, E.A. and Sotiropoulos, F. (2000). "Three-dimensional numerical model for open-channels with free-surface variations." *Journal of Hydraulic Research,* 38 (2), 115-121

Meyer-Peter, E., and Muller, R. (1948). "Formulas for bedload transport." *2nd IAHR congress,* Stockholm pp. 39-64

Milly, P.C.D., Wetherald, R.T., Dunne, K.A., and Delworth, T.L. (2002). "Increasing risk of great floods in a changing climate." *Nature,* 415(6871), 514-517

Mohammed, T.A., Said, S., Baradie, M.Z., and Basri, S. (2006). "One Dimensional simulation of Flood Levels in a Tropical River System Using HEC-2 Model" *Proceedings of the Joint International Conference on Computing and Decision Making in Civil Engineering*. Montreal, Canada.

Musser, J.W. and Dryer, T.R. (2005). "Two-dimensional Flood-Inundation Model for the Flint River at Albany, Georgia." *Proceedings of the 2005 Georgia Water Resources Conference,* April 25-27, 2005: University of Georgia, Athens, Georgia

Nielsen, P. (1992). "Coastal bottom boundary layers and sediment transport." *AdvancedSeries on Ocean Engineering*. Singapore: World Scientific.

Noh, W. F. and Woodward, P. (1976). "SLIC (simple line interface calculation)". In van der Vooren and P. Zandbergen (Eds.), *Lecture notes in Physics,* 59, 330-340. Springer-Verlag

Omer, C.R., Nelson, E.J., and Zundel, A.K. (2003). "Impact of varied data resolution on hydraulic modeling and floodplain delineation." *Journal of the American Water Resources Association*, 39, 467-475

Osher, S. and Sethian, J. (1988). "Fronts propagating with curvature-dependent speed: algorithms based on Hamilton-Jacobi formulations." *Journal of Computational Physics*, 79, 12-49

Ozmen-Catagay, H. and Kocaman, S. (2011). "Dam-break flow in the presence of obstacle: Experiment and CFD simulation." *Engineering Applications of Computational Fluid Mechanics*, 5 (4), 541-552

Ozmen-Catagay, H., Kocaman, S. and Guzel, H. (2014). "Investigation of dam-break flood waves in a dry channel with a hump." *Journal of Hydro-environment Research*, 8 (3), 304-315

Pappenberger, F.P., Matgen, P., Beven, K.J., Jean-Baptiste, H., Pfister, L. and Fraimont, P. (2006). "Influence of uncertain boundary conditions and model structure on flood inundation predictions." *Advances in Water Resources*, 1430-1449

Peltier, E., Duplex, J., Latteux, B., Pechon, P., and Chaussonb, P. (1991). "Finite element model for bed-load transport and morphological evolution." *Computer Modelling in Ocean Engineering 91*, Balkema, Rotterdam, The Netherlands.

Picek, T., Havlik, A., Mattas, D., and Mares, K. (2010) "Hydraulic calculation of briudges at high water stages." *Journal of Hydraulic Research*, 45(3), 400-406

Prakash, M., Rothauge, K. and Cleary, P. W. (2014). "Modelling the impact of dam failure scenarios on flood inundation using SPH." *Applied Mathematical Modelling*, 38, 5515-5534

Qu, Z., and Graf, W. H. (2004). "Flood hydrographs in open channels." *Water Management*, 157, 45-52

Rebollo, L. L., De Blas, M., Diaz, R., Marivela, R. (2010). "Hydrodynamic verification with SPH of under gate flow in the Alarcon spillway (Spain)." *First European IAHR Congress*, Edinburgh, United Kingdom.

Richardson, E. V., and David, S. R. (2001). "Evaluating Scour at Bridges." 4th Edition, Hydraulic Engineering Circular No. 18, Publication No. FHWA NHI 01-001, Federal Highway Administration, U.S. Department of Transportation, Washington, D.C.

Rodriguez, J. F., Bombardelli, F. A., Garcia, M. H., Frothingham, K. M., Rhoads, B. and Abad, J. D. (2004). "High-resolution Numerical Simulation of Flow through a Highly Sinuous River Reach." *Water Resources Management*, 18, 177-199

Sauer, V.B. and Meyer, R.W. *Determination of Error in Individual Discharge Measurements*. Open-File Report, Norcross, Georgia: U.S. Geological Survey, 1992.

Seminara, G., Solari, L. and Parker, G. (2002). "Bed load at low Shields stress on arbitrarily sloping beds: Failure of the Bagnold hypothesis." *Water Resources Research*, 38(11), 31-1 – 31-16

Shen, Y.M., Ng, C.O. and Zhenag, Y.H. (2004). "Simulation of wave propagation over a submerged bar using the VOF method with a two-equation k-ε turbulence modeling." *Ocean Engineering*, 31, 87-95

Shen, J., Shan, H., Suaznabar, O., Xie, Z., Bojanowski, C., Lottes, S., and Kerenyi, K. (2012) "Submerged-flow bridge scour under clear-water conditions." *6th International conference on Scour and Erosion*, Paris, France (pp. 755-760)

Singh, J., Altinakar, M.S., and Ding, Y. (2011). "Two-dimensional numerical modeling of dam-break flows over natural terrain using a central explicit scheme." *Advances in Water Resources*, 34, 1366-1375

Soarez-Frazao, S. (2002). "Dam-break induced flows in complex topographies. Theoretical, numerical and experimental approaches" (PhD. Dissertataion). Louvain-la-Neuve: Universita catholique de Louvain. Civil Engineering Department, Hydraulics Division, 116 (8)

Soarez-Frazao, S. and Zech, Y. (2002). "Dam Break in channels with 90° bend." *Journal of Hydraulic Engineering*, 128 (11), 956-968

Soulsby, R. (1997). "Dynamics of marine sands: A manual for practical applications." London: Thomas Telford

Spasojevic, M., and Holly, F. M., Jr. (1990a). "2-D evolution in natural waterscourses - New simulation approach." *Journal of Waterway, Port, Coastal, and Oceans Engineering*, 116(4), 425-443

Strickler, A. (1923) Beiträge zur Frage der Geschwindigheitsformel und der Rauhigkeitszahlen für Ströme, Kanale und geschlossene Leitungen. *Mitteilungen des Eidgenössischen Amtes für Wasserwirtschaft* (16 pp.).

Sussman, M., Smereka, P., and Osher, S. (1994) "A level set approach for computing solutions to incompressible two-phase flows." *Journal of computational physics*, 114, 146-159

Syme, W.J., Pinnel, M.G., and Wicks, J.M. (2004). "Modelling Flood Inundation of Urban Area in the UK using 2D / 1D Hydraulic Models." *Proceedings of the 8th National Conference on Hydraulics in Water Engineering*, The Institution of Engineers, Australia.

US Army Corps of Engineers (2006). "Hydrologic Modeling System HEC-HMS: User's Manual"

US Army Corps of Engineers. (2010) "HEC-RAS River Analysis System. Hydraulic Reference Manual. Version 4.1"

Van Rijn, L. (1987). "Mathematical modeling of morphological processes in the case of suspended sediment transport." *Delft Hydraulics Communication No. 382*, June.

Van Rijn, L. (1989) *Handbook sediment transport by currents and waves.* Delft: Delft Hydraulics communication.

Ven Te Chow. *Open Channel Hydraulics*, Caldwell, New Jersey, McGraw Hill Education, 1959, Print.

Verwey, A. (2001) "Latest Development in Floodplain Modelling -1D/2D/ Integration." *Conference on Hydraulics in Civil Engineering.*

Violeau, D., Buvat, C., Abed-Meraim, K. and De Nanteuil, E. (2007). "Numerical modelling of boom and oil spill with SPH." *Coastal Engineering,* 2007, 54 (12) 895-913

Violeau, Damien. *Fluid Mechanics and the SPH Method: Theory and Applications*, Oxford, Oxford University Press, 2012, Print.

Wagner, C.R., Mueller, D.S., and USGS. *Calibration and Validation of a Two-Dimensional Hydrodynamic Model of the Ohio River, Jefferson County, Kentucky.* Water Resources Investigations Report 01-4091 (2001).

Wang, S. S. Y., and Adeff, S. E. (1986). "Three-dimensional modeling of river sedimentation processes." *Proc. Third International Symposium on River Sedimentation,* The University of Mississippi, March 31 – April 4, 1496-1505

White, F. *Viscous Fluid Flow*, Boston, Massachusetts, McGraw Hill Education 1974, Print.

Wong, M. (2003). "Does the bedload transport relation of Meyer-Peter and Muller fits its own data"" *30th IAHR-Congress,* Thessaloniki pp. 12-20

Wu, W., Rodi, W., and Wenka, TY. (2000). "3D numerical modeling of flow and sediment transport in open channels." *Journal of Hydraulic Engineering.* 126(1), 4-15

Wu, W. (2004). "Depth-averaged two-dimensional numerical modeling of unsteady flow and nonuniform sediment transport in open channels." *Journal of Hydraulic Engineering,* 130(10), 1013-1024

Wu, W., Wang, S., Jia, T., and Robinson, K. (1999). "Numerical simulation of two-dimensional headcut migration." *International water resources engineering conference,*Seattle, WA (pp. 45-53).

Xanthopoulos, T., and Koutias, C. (1976). "Numerical Simulation of a two dimensional flood wave propagation due to dam failure." *Journal of Hydraulic Research*, 14 (4), 321-331

Yang, C., Lin, B., Jiang, C. and Liu, Y. (2010). "Predicting near-field dam-break flow and impact force using a 3D model." *Journal of Hydraulic Research*, 48 (6), 784-792

Yang, X. F. and Liu, M. B. (2013). "Numerical modeling of oil spill containment by boom using SPH." *Science China-Physics, Mechanics and Astronomy*, 56, 315-321

Yen, C. L. (1967). "Bed configuration and characteristics of subcritical flow in a meandering channel." PhD. Thesis, The University of Iowa, Iowa City, Iowa.

Young, D. L. (1982). "Time-dependent multi-material flow with large fluid distortion." In K. W. Morton and M. J. Baines (Eds.), *Numerical Methods for Fluid Dynamics,* 273-285, Academic.

Zech, Y., Soarez-Frazao, S., and Spanwine, B. (2008). "Dam-break induced sediment movement: Experimental approaches and numerical modeling." *Journal of Hydraulic Research,* 46(2), 176-190

Zeng, J., Constantinescu, S. G., and Weber, L. (2010). "3D Calculations of Equilibrium Conditions in Loose-Bed Open Channels with Significant Suspended Sediment load." *Journal of Hydraulic Engineering,* 136, 557-571

Zeng, J., Constantinescu, G., Weber, L. J. (2007) “Fully 3D non-hydrostatic model to compute flow, sediment transport and bed morphology changes for alluvial open channel bends” (Doctoral Dissertation). IIHR-Technical Report No 462.

Zhang, H., Youssef, H., Long, N.D., and Kahawita, R. (1992). “A 1-D numerical model applied to dam-break flow on dry beds.” *Journal of Hydraulic Research,* 30 (2), 211-224

Zhang, M., Hao, Z., Zhang, Y. and Wu, W. (2013). “Numerical simulation of solitary and random wave propagation through vegetation based on VOF method.” *Acta Oceanologica Sinica*, 32 (7) , 38-46

“Samarco Dam failure in Brazil ‘caused by design flaws’” *BBC News,* 30 August, 2016. Web. 10 August, 2017.